Universiteit
Leiden
The Netherlands

Multimodal visualization of adult stem cells in inner ear and brain pathology

Schomann, T.

Citation

Schomann, T. (2019, May 16). *Multimodal visualization of adult stem cells in inner ear and brain pathology*. Retrieved from https://hdl.handle.net/1887/72413

Version:	Not Applicable (or Unknown)
License:	Leiden University Non-exclusive license
Downloaded from:	https://hdl.handle.net/1887/72413

Note: To cite this publication please use the final published version (if applicable).

Cover Page

Universiteit Leiden

The following handle holds various files of this Leiden University dissertation:
http://hdl.handle.net/1887/72413

Author: Schomann, T.
Title: Multimodal visualization of adult stem cells in inner ear and brain pathology
Issue Date: 2019-05-16

Multimodal Visualization of Adult Stem Cells in Inner Ear and Brain Pathology

PROEFSCHRIFT

Ter verkrijging van de graad Doctor aan de Universiteit Leiden,
op gezag van Rector Magnificus Prof. mr. C. J. J. M. Stolker,
volgens besluit van het College voor Promoties
te verdediging op donderdag 16 mei 2019
klokke 10:00 uur

door

Timo Schomann

Geboren te Verl, Duitsland in 1986

Promotor	Prof. dr. ir. J. H. M. Frijns
Copromotores	Dr. M. A. Huisman Dr. L. Mezzanotte (Erasmus Medical Center)
Promotiecommissie	Prof. dr. P. P. G. van Benthem Prof. dr. C. W. G. Löwik (Erasmus Medical Center) Dr. L. van der Weerd Dr. J. C. M. J. de Groot Prof. dr. S. M. van der Maarel Prof. em. dr. J. J. Grote

All rights reserved. No part of this publication may be reproduced, stored in a retrieval system of any nature, or transmitted in any form or by any means, electronic, mechanical, photocopying, recording or otherwise, including a complete or partial transcription, without the prior written permission of the copyright owner.

ISBN: 978-94-6380-298-7

Layout by: T. Schomann
Printed by: ProefschriftMaken || www.proefschriftmaken.nl
Cover by: T. Schomann

This thesis was financially supported by: Carl Zeiss B.V., ChipSoft B.V., EmiD audiologische apparatuur, FUJIFILM VisualSonics, Inc., GCON, LBB van der Heijden-Sweere VOF, MED-EL, Meditop Medical Products B.V., Oticon Medical, Percuros B.V., and Phonak.

Table of contents

Chapter 1	General introduction	5
Chapter 2	Isolation, expansion and neural differentiation of stem cells from human plucked hair: A further step towards autologous nerve recovery	27
Chapter 3	Lentiviral transduction and subsequent loading with nanoparticles do not affect cell viability and proliferation in hair-follicle-bulge-derived stem cells *in vitro*	49
Chapter 4	Neuronal differentiation of hair-follicle-bulge-derived stem cells co-cultured with mouse cochlear modiolus explants	77
Chapter 5	Imaging bioluminescent exogenous stem cells in the intact guinea pig cochlea	101
Chapter 6	Ouabain does not induce selective spiral ganglion cell degeneration in guinea pigs	131
Chapter 7	Multimodal imaging of hair follicle bulge-derived stem cells in a mouse model of traumatic brain injury	163
Chapter 8	General discussion	191
Appendix	Summary in Dutch	202
	List of abbreviations	203
	List of publications	206
	Curriculum vitae	207
	Acknowledgements	207

Chapter 1

General introduction

Hearing, development, anatomy and physiology

Hearing is one of the five senses of perception in humans and most other vertebrates. In the process of hearing, sound pressure waves are converted into electrical signals, that are propagated by neurons to the brain where these signals are subsequently processed.

During embryonic development the structures of the inner ear arise from the otic placode, an ectodermal thickening in the head region of the embryo.

The otic placode, like other neurogenic placodes, develops at the border of the neural plate [1]. All epibranchial neurogenic placodes originate in a common pre-placodal region slightly more lateral than the neural crest (NC) and form discrete areas of columnar epithelium derived from non-neural ectoderm [2]. During development, these placodes give rise to neuroepithelium in the sensory organs of the vertebrate.

The olfactory epithelium in the nose is generated by the olfactory placode and the lens of the eye is produced by cells of the lens placode (or optic placode). Similarly, the audiovestibular system originates from the otic placode. Together with the NC, the otic placode also contributes to the peripheral nervous system of the respective sensory organ. The otic placode invaginates and undergoes a complex morphogenesis into the inner ear [3, 1].

The fully mature hearing organ consists of three major parts: the outer ear, the middle ear, and the inner ear (Fig. 1). The outer ear consists of the pinna (or auricle; Fig. 1A) and the external auditory meatus (or outer ear canal; Fig. 1B), which focus sound, an audible mechanical wave of pressure and displacement, and conduct it to the tympanic membrane (or eardrum; Fig. 1C). In the middle ear, sound waves are propagated and transformed through vibrations of the comparatively large, low-impedance tympanic membrane to the smaller, high-impedance oval window of the cochlea (impedance increase: 18.75 times in humans) by means of the three auditory ossicles (Fig. 1D): the malleus (hammer; impedance increase: 2.1 times in humans), incus (anvil), and stapes (stirrup) [4]. The auditory ossicles function as an acoustic impedance transformer that converts sound energy from low-impedance air to the high-impedance cochlear fluids (Fig. 1E) [5]. This is achieved by a piston-like movement of the stapes' footplate in the oval window, which generates pressure

waves that travel through the fluid-filled compartments of the cochlea. In humans, the total transformer ratio of the middle ear amounts to 82.5 times, which also includes the 2.1-times velocity decrease (2.1^2 = 4.4 times) [4].

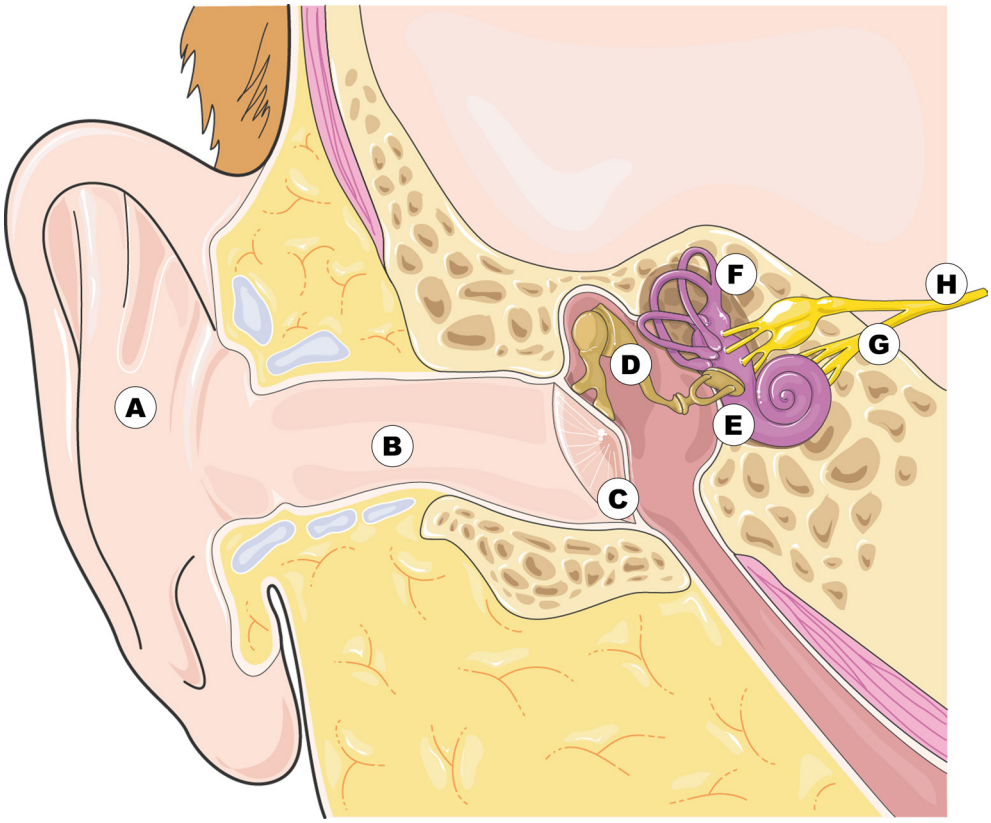

Fig. 1: The ear. **A:** pinna (auricle), **B:** external auditory meatus (ear canal), **C:** tympanic membrane (eardrum), **D:** auditory ossicles: the malleus (hammer), incus (anvil), and stapes (stirrup), **E:** cochlea, **F:** vestibular system, **G:** auditory nerve, **H:** vestibulocochlear nerve. Picture adapted from "Ear" [6].

The cochlea is a snail-shaped, bony structure that houses the neurosensory organ of hearing (organ of Corti) and forms one of the two major structures of the inner ear. The other major apparatus of the inner ear is the vestibular system, containing the organs of balance (Fig. 1F).

In humans, the cochlea coils approximately 2.5 turns around its central axis, while in other mammals the number of turns slightly varies. The cochlea in mice has 2 turns and in guinea pigs it has approximately 4 turns (Fig. 2A). In humans and other mammals, the cochlea consists of three fluid-filled compartments: the scala vestibuli,

scala tympani and scala media (Fig. 2B). The scala vestibuli spirals upwards to the helicotrema at the apex of the cochlea, where it is connected to the scala tympani which conversely spirals downwards. Both compartments are broad near the base and become more narrow towards the apex. They are filled with perilymph, which is characterized by a high sodium concentration (~140 mM) and low levels of potassium (4-5 mM) and resembles the electrolyte composition of the cerebrospinal fluid. In between these two perilymph-filled scalae, the scala media (or cochlear duct) is located. It is filled with endolymph, which has low levels of sodium (~1 mM) and a high potassium concentration (~150 mM). The scala media contains the organ of Corti, which houses the sensory receptors of hearing, the cochlear hair cells, i.e., one row of inner hair cells (IHCs) and three to four rows of outer hair cells (OHCs), and other highly specialized cells, such as Deiters' cells, Hensen's cells and Claudius' cells (Fig. 2C).

In the scala vestibuli, the traveling pressure wave, which is generated by the movement of the stapes, causes a vibration of the perilymphatic fluid towards the round window [4]. This initiates a displacement on the basilar membrane from base to apex, whereby pattern and positioning of the wave depends upon the frequency of the stimulus. In response to the vibrations of the basilar membrane, the entire organ of Corti is moved up and down [7]. Depending on the frequency, the location of maximal displacement of the basilar membrane is different and relies on its physical mechanics and the composition of the cochlear fluids [5]. At the base of the cochlea, high-frequency stimuli lead to a maximal displacement of the basilar membrane, since it possesses a lower mass and higher stiffness than in the more apical regions [7, 5]. Consequently, low-frequency stimuli lead to maximal displacement towards the apex of the cochlea.

The displacement of the basilar membrane pushes the stereocilia of the OHCs against the tectorial membrane [4]. Due to this tension on the tips of the stereocilia, the stereocilia deflect, whereupon the mechanoelectrical transduction channels open leading to depolarization of the hair cells through influx of potassium from the endolymph [8]. This depolarization results in a release of the neurotransmitter glutamate at the base of the hair cells that evokes an action potential in the synapses of the innervating afferent spiral ganglion neurons (SGNs). After binding of the neurotransmitters to the respective membrane receptors in the synapse, the individual neurons depolarize and an electrical signal is generated.

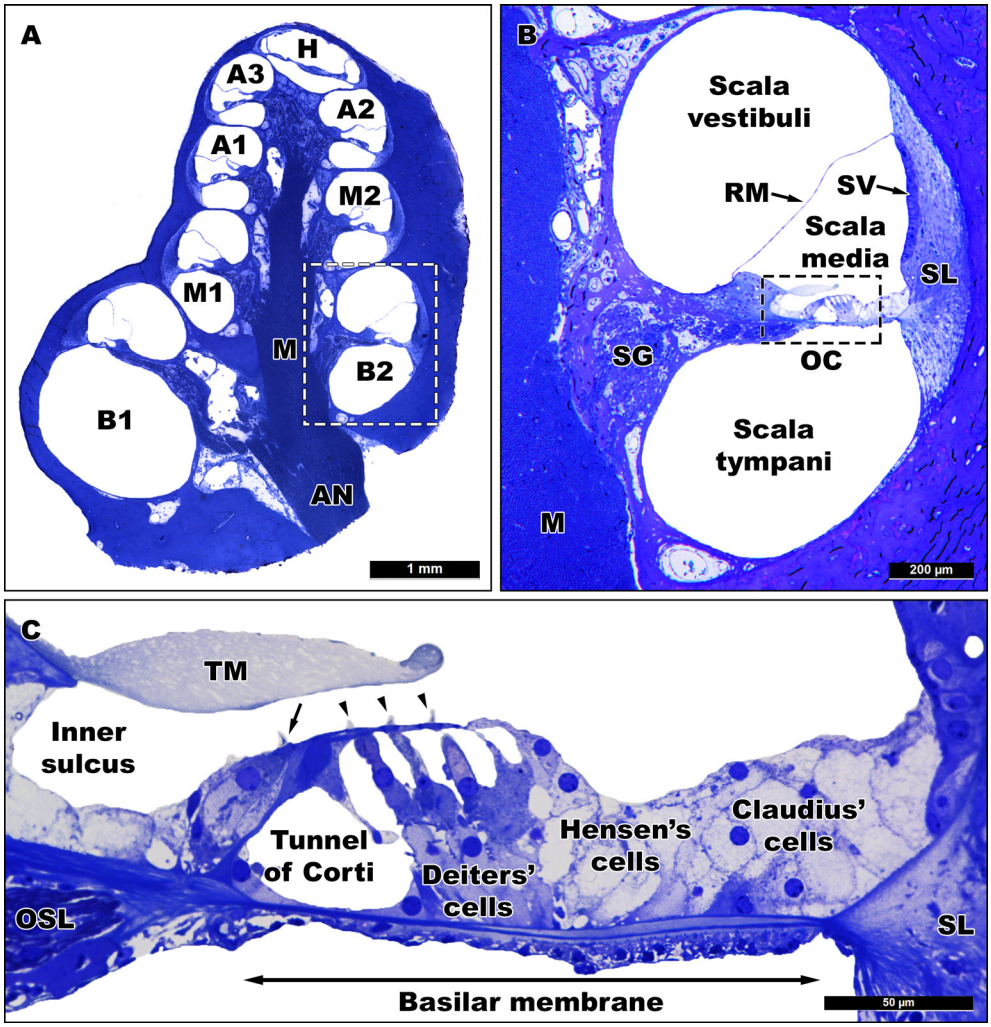

Fig. 2: The guinea pig cochlea and organ of Corti. **A:** Midmodiolar section of a guinea pig cochlea showing all eight scalae. M = modiolus; AN = auditory nerve; B1 = lower basal turn; B2 = upper basal turn; M1 = lower middle turn; and M2 = upper middle turn; A1, A2 and A3 = three apical turns; H = helicotrema. **B:** The upper basal turn (B2) and its scalae. RM = Reissner's membrane; OC = organ of Corti; SG = spiral ganglion; M = modiolus; SL = spiral ligament; SV = stria vascularis. **C:** The organ of Corti contains different highly specialized cells, such as the cochlear hair cells, Deiters' cells, Hensen's cells, Claudius' cells, and the inner sulcus. The organ of Corti is located on the basilar membrane and contains inner hair cells (arrow) and outer hair cells (arrowheads). OSL = osseous spiral lamina; SL = spiral ligament; TM = tectorial membrane.

Small voltage changes are propagated by the SGNs, which form the cochlear nerve within the modiolus. Outside the cochlea, the cochlear nerve joins the vestibular nerve to form the vestibulocochlear nerve, which ends in the brain stem (Fig. 1H). Next, the nerve fibers enter the cochlear nucleus. The signal is then transferred to the trapezoid body, the superior olivary complex, the lateral lemniscus, the inferior colliculus and medial geniculate nucleus before reaching the primary auditory cortex in the brain (Fig. 3).

The propagation of the electrical signal through the neural tracts of the auditory pathway can be measured from relatively large distances using superficial electrodes in humans or subdermal needle electrodes in animals. The time window to record this electrical activity is within milliseconds after the auditory stimulus. Acoustically-evoked auditory brainstem responses (aABRs) can be used to measure and record the propagation of the electrical signal, which gives an indication about the hearing capability of living mammals [9]. The measurements do not require active participation of the subject and are thus a reliable proxy for auditory function in human infants and animals during sleep or anesthesia [10, 11].

After electrical activity is evoked by a broadband acoustic click stimulus, its propagation can be recorded by means of aABR and subsequently visualized as a series of waves using non-invasive or minimally invasive electrodes within 10 milliseconds [12-14]. The first five dominant peaks (I-V) of these waves are evaluated in cats and guinea pigs (Fig. 3A). In these animals, wave I (P1-N1) consists of the first positive peak (P1) and the first negative peak (N1) and represents the combined distal and proximal part of the auditory nerve (Fig. 3B) [15-20]. Waves II-V are generated in the different nuclei in the auditory brainstem [21-23]. The ipsilateral cochlear nucleus generates wave II (P2-N2), while wave III (P3-N3) reflects the activity of the contralateral superior olivary complex and medial nucleus of the trapezoid body. Wave IV represents the combined activity of superior olivary complex and lateral lemniscus (P4-N4) and wave V arises from lateral lemniscus and inferior colliculus (P5).

Recordings of aABRs can help to estimate sensorineural hearing loss (SNHL) by finding the lowest intensity level, at which wave V is present and replicable. SNHL can result from a variety of factors, such as genetic disorder, prolonged exposure to loud noise, ototoxic drug treatment, or simply as a result of ageing, causing degeneration

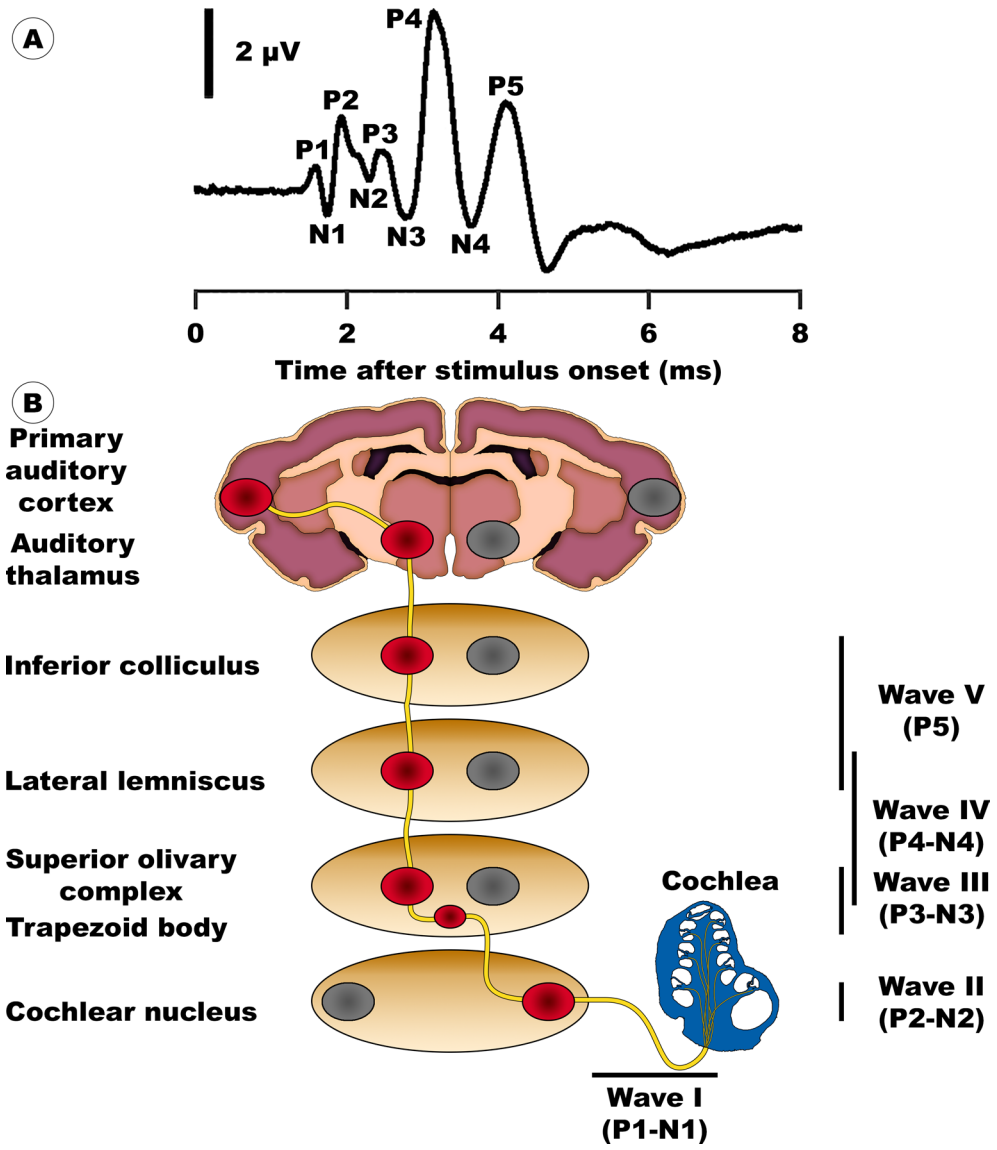

Fig. 3: Schematic drawing of the origin of ABR waves in the guinea pig. **A:** Representation of example of ABR waves with peaks (P) and troughs (N) as measured in a guinea pig. **B:** Waves I – V are generated by the activity of the auditory nerve (yellow), while passing through different areas of the auditory system to deliver the signal to the auditory cortex.

of hair cells and auditory neurons [24]. The degree of neuronal degeneration is of particular significance for hearing-impaired patients. Early on, in ageing or noise-exposed ears, the synapses between the cochlear hair cells and the SGNs degenerate at first and so-called hidden hearing loss develops, which does not affect hearing thresholds but could impair speech understanding in noisy environment [25, 26]. However, once SNHL is diagnosed, affected patients face a rather limited range of therapeutic options, amongst them conventional hearing aids in mild cases or bone-anchored hearing devices and cochlear implants (CIs) in severe cases.

Regarding SNHL, CIs help many hearing-impaired people by partially restoring their sensation of hearing by means of bypassing part of the peripheral auditory system, i.e. the hair cells. The surgically inserted electrode of the CI generates action potentials within the remaining nerve fibers of the spiral ganglion by direct electrical stimulation of the SGNs. Despite considerable progress in CI technology in the past 20 years, there is variability in the performance between individual CI users. Previous studies have suggested that this might be caused by an auditory neuropathy spectrum disorder, which creates site-specific variations of stimulus-dependent activation of neurons [27-29].

Another reason could be an increased distance between the electrodes of the CI and the peripheral projections (dendrites) of the SGNs, which would impair stimulation of the neurons [27, 30-32]. Hence, limiting these variations and increasing the efficiency of the CI is an important aim of current research. Several different approaches have been recently investigated, such as a combination of CI implantation with (neuro) trophic growth factors or stem cell (SC) therapy to improve the hearing of SNHL patients.

Stem cell therapy

Cell-based therapy may counteract the effect of cochlear nerve degeneration [33], although it has to be taken into consideration that, in patients with disabling hearing loss, stem cells will lack (neuro)trophic support of hair cells and perhaps also of non-sensory cells (Fig. 4A-C). Different types of SCs could be applied to support and regenerate the auditory nerve and thereby reducing the distance between CI and

nerve fibers (Fig. 4D). A healthy population of SCs could support the auditory nerve by differentiating into neurons and/or glial cells, which then interact with and help repair the degenerating auditory nerve (Fig. 4E). Another mechanism could be through paracrine effects by stimulation of angiogenesis or support of the microenvironment by reduction of inflammation as shown in other models [34, 35].

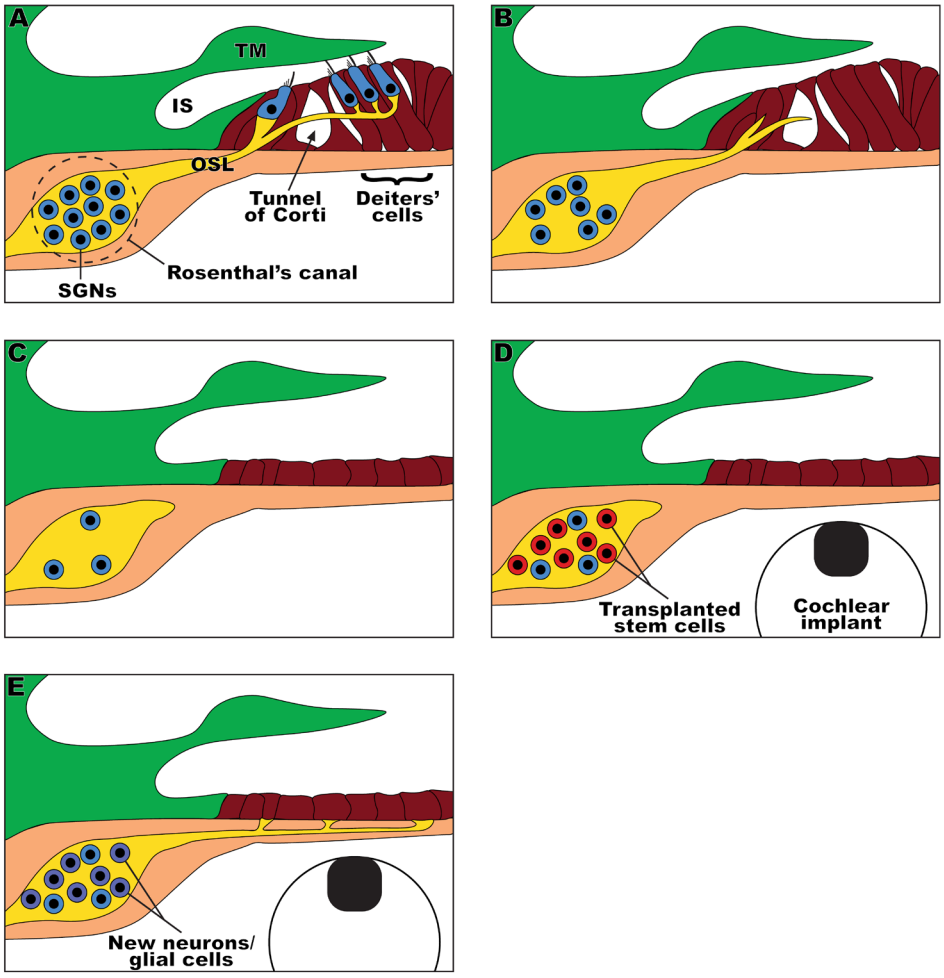

Fig. 4: Schematic drawing of organ of Corti pathology and possible stem cell-based regenerative therapy. **A:** Normal situation with intact inner and outer hair cells (blue), which are innervated by the peripheral projections (dendrites) of the efferent spiral ganglion neurons (SGNs; yellow). TM = tectorial membrane; IS = inner sulcus; OSL = osseous spiral lamina. **B:** Early pathology after damage. Inner and outer hair cells are lost and the amount of SGNs is decreased. **C:** Advanced pathology of the organ of Corti after damage. Organ of Corti is degenerated and replaced by flat epithelium. **D:** Implantation of cochlear implant and transplantation of stem cells (red). **E:** Stem cells support the degenerated nerve fibers and possibly differentiate into new neurons and/or glial cells (purple). This could lead to outgrowth of new nerve fibers and reduce the neural gap with the CI.

For future clinical applications, it would be ideal to have suitable autologous SCs to avoid transplant rejection. Cell-based therapy using stem cells from the neural crest (NC) may represent an attractive therapeutic option [2]. As explained earlier, the NC develops in close proximity to the cranial sensory placodes and interacts with, among others, the otic placode during embryogenesis [36-41, 1]. In addition, gene expression patterns in NC and the otic placode are similar to each other during development [2]. At an early stage of neurulation, the neural plate border is a stripe adjacent to the neural plate and the ectoderm, which co-expresses pre-neural and non-neural ectodermal markers [42-44]. Within the neural plate border region, precursors for neural, NC, epidermal and placodal cells remain interspersed [45, 37]. Similar to the placodal cells, NC cells arise between the newly formed ectoderm and the neural tube in vertebrates after neurulation. This was first described by Wilhelm His in the developing chick embryo as the intermediate cord ('Zwischenstrang') in 1868 [46]. From this tissue, embryonic NC cells migrate out and give rise to several ectodermal and mesodermal cell types in the vertebrate organism [47, 48]. When the first three streams migrate out from the NC, epibranchial progenitor cells converge to form distinct placodes. This suggests a role of NC migration in the individualization of otic and epibranchial placodes in sub-dividing the posterior pre-placodal region [49, 1].

During their migration NC cells undergo developmental restrictions. However, it is generally accepted that populations of NC-derived stem cells (NCSCs) can be found within various niches throughout the adult body where they retain the capacity for self-renewal and multi-lineage differentiation [50, 51].

In the adult human body, populations of NCSCs can be found in various, easily accessible locations, such as teeth, inferior turbinate, and the palate [52-55]. Their developmental ability to differentiate into glial cells and neurons is conserved during adulthood [51, 56].

As shown by various studies, SCs from the NC can, furthermore, be found in both mouse and human hair follicles [57-61], of which the latter can be easily harvested using minimally invasive techniques. Differentiation of SCs derived from the hair follicle into smooth muscle cells, melanocytes, keratinocytes, osteocytes, and chondrocytes as well as glial cells, and, most importantly, neurons has been indicated in earlier studies [62-66]. In this thesis, we will investigate if hair follicle bulge-derived

SCs (HFBSCs) are able to migrate and differentiate into glial and neuronal cells *in vitro* (Chapters 2-4). Depending on these findings, NCSCs – and especially the relatively immune-privileged HFBSCs – might represent promising candidates for autologous SC therapies [67-69].

Due to the easy harvesting, efficient isolation and their *in vitro* differentiation potential, HFBSCs have advantages over SCs from other origins, such as neural progenitor cells or embryonic SCs. Nevertheless, the novelty of this type of stem cell in the field of regenerative therapy and particularly of inner ear cell-based therapy requires investigation of the differentiation and migration potential in the living animal, such as the mouse or the guinea pig.

The animal model and deafening

Guinea pigs have been used as experimental animals for centuries, which gave rise to the expression 'guinea pig' in English in the sense of a human experimental subject. Guinea pigs and humans share many biological similarities, such as a similar immune system, which led Robert Koch to discover in an 1882 study with guinea pigs that tuberculosis is caused by the bacterium *Mycobacterium tuberculosis* [70]. In addition, vitamin C was discovered in guinea pigs by means of nutritional deficiency, since guinea pigs like humans – and in contrast to most other animals – are incapable of endogenous synthesis of vitamin C, which leads to scurvy-like symptoms [71].

Moreover, the structure of the cochlea of guinea pigs is comparable to that of humans, demonstrating a more similar hearing range when compared to that of, e.g., mice, rats, gerbils, and cats. Therefore, guinea pigs have long been a preferred animal model in the field of hearing research. The anatomy of the guinea pig middle ear, allowing easy access to the round window and thus to the cochlea, further adds to its suitability. Another advantage of this animal model is the fact that the guinea pig permits xenogeneic transplants without induction of an immune rejection [72].

Altogether, these advantages are in favor of the guinea pig for cell-based regenerative therapy in the auditory system. Therefore, this could enable tracking of mouse-derived

HFBSCs after their implantation into the cochleas of deafened animals, in order to monitor their long-term survival, proliferation, and differentiation into functional SGNs. As explained earlier, SGNs are afferent neurons, that transmit electric signals encoding sound from the cochlear hair cells to the brain. They are classified as type-I (myelinated) SGNs - making up 90-95% of the total SGN population – and type-II (unmyelinated) SGNs (5-10%). Type-I SGNs innervate the inner hair cells within the organ of Corti, which are the primary sound receptors and, as such, are responsible for the sensation of hearing.

A potent drug for the induction of deafness is the selective Na^+/K^+-ATPase inhibitor ouabain (g-strophanthin), which has been reported to selectively destroy the type-I SGNs in certain species of rodent cochleas, while leaving type-II SGNs and cochlear hair cells unharmed. Contrary to deafening methods that are based upon systemic application of ototoxic drugs, this method uses local (i.e., deposition on RWM) instillation of the drug in order to bypass the blood-cochlea barrier. The advantage of this application approach is that ouabain does not interfere with the production of chemotactic growth factors of the hair and supporting cells. These growth factors may support survival of transplanted stem cells and may also direct peripheral projections of the newly formed neurons to the organ of Corti [73, 74].

The denervation effect of ouabain was initially observed in many studies using Mongolian gerbils [75-79] and was subsequently observed to occur as well in the cochlea of other rodent species, such as mice [80-84], rats [85-87], but also in cats [88], in a dose-dependent way.

However, comparably little is known about the effect of ouabain upon the guinea pig inner ear. Only two (contradictory) studies have described the morphological effect of local application of ouabain upon the SGNs in the guinea pig cochlea [89, 73]. It is hence necessary to evaluate if ouabain can be used for selective deafening of guinea pigs and subsequent regenerative stem cell therapy (Chapter 6).

Multimodal visualization

Following transplantation, it is necessary to track the transplanted cells in the living animal. Long-term follow-up studies of implanted cells give a closer insight into their survival, distribution in the inner ear and, ultimately, to their contribution to the regeneration of damaged structures.

Visualization of mammalian cells is used in a broad field of research: Investigation of engrafted cells, tracking of cancer cells in the mammalian organism, and the homing capacity of stem cells [90, 91]. Therefore, a range of different labeling techniques for mammalian cells has been developed, such as (i) genetic manipulation using a viral vector to introduce one or more reporter molecules (fluorescent or bioluminescent), and (ii) loading with superparamagnetic iron oxide (SPIO) and/or fluorescent nanoparticles, which enables multimodal imaging, but label the cells only temporarily.

More specifically, these labeling techniques enable imaging with different modalities, such as fluorescence imaging (FLI), bioluminescence imaging (BLI), and magnetic resonance imaging (MRI). Each one of these approaches has advantages and disadvantages and requires different imaging equipment. Multimodal imaging combining two or more of the above-mentioned modalities, offers the possibility of minimizing the potential drawbacks of using one single modality. This approach allows to make use of the modality-specific strengths and will help to optimize and complete the comprehension of graft behavior.

One approach to visualize cells is the use of naturally occurring fluorescent molecules, such as the green fluorescent protein (GFP), which can be used for both fluorescence microscopy and imaging. GFP was first described by Shimomura and colleagues in 1962 during the isolation of the bioluminescent protein aequorin from the luminous hydrozoan jellyfish *Aequorea victoria* as a byproduct [92, 93]. Since then, GFP and its numerous variants have become widely used tools for biological imaging in biochemistry and cell biology [93, 94]. Apart from jellyfish, other species were discovered expressing GFP-like proteins [95, 96]. Among these species are two copepod families in the class of Crustacea (phylum Arthropoda), which are known for expressing such GFP-like proteins, namely the *Pontellidae* and the *Aetideidae* [95, 97]. Advantages of copepod GFP (copGFP; λ_{ex}: 482nm, λ_{em}: 502nm) over other GFP variants are a high fluorescence quantum yield, which is more stable at a wide

range of temperatures (including 37°C, i.e. human body temperature) and features faster folding and post-translational maturation rates, resulting in rapid availability of the protein after transduction [98]. In addition, green fluorescence can be detected in copGFP-expressing cells during cell culture and in histological sections using conventional fluorescence microscopy. However, copGFP is not suitable for *in vivo* detection due to the low penetration depth of the excitation and emission light [92-94, 97].

This drawback of copGFP can be obviated by the use of expression of bioluminescent proteins, such as click beetle luciferase or firefly luciferase. Firefly luciferase and its visualization in single mammalian cells was first demonstrated by Hooper and colleagues [99]. As a result, visualization of cells using BLI became suitable for *in vitro* and *in vivo* studies. The firefly luciferase is an adenosine triphosphate (ATP)-dependent oxidoreductase, which specifically converts the substrate D-luciferin into oxyluciferin in the presence of molecular O_2, resulting in a bioluminescent signal emitting at a wavelength of 425–550 nm [100-102]. One of the most red-shifted naturally-occurring luciferases is derived from the head lanterns of the railroad worm, *Phrixothrix hirtus*, with λ_{em}= 628 nm, which corresponds to (dark) orange [103]. The blue light-emitting luciferases Renilla and Gaussia are ATP-independent, but require coelenterazine as a substrate [104]. Furthermore, the blue-bioluminescent bacterial luciferase lux from *Photorhabdus luminescens* functions independent of substrate by auto-induction of luminescence [105-107]. Despite the fact that codon-optimized versions of lux were recently published, it remains difficult to express *P. luminescens* in mammalian cells [108, 109, 102].

Nonetheless, light in this range (blue to green) is particularly well-absorbed by tissue chromophores, such as (oxy-)hemoglobin, melanin and cytochromes in mammalian tissue, which leads to impracticality of these luciferases for *in vivo* imaging [110, 111]. However, the codon-optimized *Photinus pyralis* luciferase (Luc2) possesses major advantages in comparison to the wildtype luciferases, such as a high photon flux and an emission peak of 560 nm at 25°C [112]. At 37°C, a thermally induced shift towards 612 nm, which is above the light absorption spectrum of mammalian tissue, makes Luc2 a valuable tool for *in vivo* BLI [113]. Therefore, it is suitable for visualization of viable exogenous stem cells in the intact guinea pig cochlea using molecular optical imaging.

The lentiviral Luc2-copGFP reporter gene construct, which stably integrates into the genome of mammalian cells by means of viral transduction, leads to constitutive expression of Luc2 and copGFP at equimolar ratio, allowing FLI and BLI. Both imaging techniques, however, do not provide detailed anatomical information, nor do they enable visualization of transplanted cells. MRI, on the other hand, allows *in vivo* assessment of the exact location of transplanted cells, when loaded with SPIO nanoparticles and their migration within the host after engraftment. For dynamic evaluation of the migration of transplanted cells in deep tissue during *in vivo* experiments, SPIO nanoparticles have advantages due to their large signal contrast change [114]. Moreover, after sacrificing the animal, they can also be detected in histological sections using light and electron microscopy [115, 116].

Two examples of contrast-enhancing SPIO nanoparticles are ferumoxytol and NEO-STEM. Ferumoxytol is an U.S. Food and Drug Administration (FDA)-approved iron preparation for the treatment of anemia in chronic kidney disease [117]. With a straightforward cell-loading approach ferumoxytol effectively labels cells for *in vivo* MRI through formation of self-assembling nanocomplexes in the presence of heparin and protamine. NEO-STEM™ TMSR50 nanoparticles contain a magnetic core and a red-fluorescent dye, which allows visualization of nanoparticles using both MRI and FLI. The silica shell of NEO-STEM™ TMSR50 nanoparticles is biocompatible and resistant to degradation.

In conclusion, the fluorescent protein copGFP can be used to assess the transduction efficiency, for monitoring transduced cells *in vitro*, and in histological sections using conventional fluorescence microscopy. *In vivo*, viable cells can be detected by means of emitted light from the bioluminescent Luc2 after engraftment. This allows non-invasive long-term monitoring of cell viability and survival, while MRI of SPIO nanoparticle-loaded cells can be used to obtain additional anatomical information.

Aims and outline of this thesis

The general aim of this thesis is to investigate the feasibility of multimodal imaging techniques for the visualization of exogenous stem cells, i.e., HFBSCs, in the living animal. Due to the novelty of HFBSCs in this field of research, a series of proof-of-principle experiments have been undertaken *in vitro*, *ex vivo*/*in situ*, and *in vivo*:

Objective 1: *The isolation, expansion and neural differentiation of stem cells from human plucked hair* (Chapter 2).
This chapter examines whether HFBSCs still possess the immunophenotype of NCSCs and neural differentiation potential after isolation and expansion. In addition, it is investigated whether these cells support cryopreservation and tolerate needle shear-stress.

Objective 2: *Rule out the possible cytotoxic effects of lentiviral transduction and subsequent loading with nanoparticles on cell viability and proliferation of HFBSCs* in vitro (Chapter 3).
Prior to application of HFBSCs *in vivo*, the possible risk of negative effects of lentiviral transduction and loading with SPIO nanoparticles needs to be ruled out to obtain and maintain a viable cell population for cell-based regenerative therapy.

Objective 3: *Investigate the neuronal differentiation potential of HFBSCs in co-culture with modiolus explants from adult mice* (Chapter 4).
This chapter focuses on three key factors to ensure successful application of HFBSCs in cell-based therapy *in vivo*: (i) to ascertain the migratory character of the cells, (ii) to monitor their incorporation into damaged cochlear tissue lacking supportive growth factors from hair cells, and (iii) to assess their capability to undergo differentiation within a neural phenotype after integration into the modiolus explant.

Objective 4: *The feasibility of BLI for the visualization of transduced cells after engraftment in the intact guinea pig cochlea* (Chapter 5).
After excluding negative effects of the labeling methods, it is essential to assure that it is possible to image the labeled cells by means of BLI after transplantation in the inner ear of the guinea pig. This is particularly challenging since the cochlea of the guinea pig (our experimental animal model) is embedded within a bony otic capsule consisting of compact bone with a high mineral density, the bulla may block signal

detection during molecular FLI and BLI.

Objective 5: *Determine if the ototoxic drug ouabain results in selective degeneration of type-I SGNs in guinea pigs* (Chapter 6).
Due to two conflicting papers, we decide to re-investigate the ototoxic effect of ouabain application via the round window membrane of the cochlea and to study the validity of this protocol in the guinea pig.

Objective 6: *Multimodality imaging of HFBSCs in a mouse model of traumatic brain injury* (Chapter 7).
In this chapter we aim to establish that HFBSCs keep their neural differentiation potency after transplantation *in vivo*, and to investigate i) whether HFBSCs integrate into the brain, ii) whether they differentiate, and if so into which type of cell, and iii) whether they do not form extracellular matrix *in vivo*.

In Chapter 8, the results of our studies are discussed and future experiments will be considered, based upon the results presented in this thesis, to visualize HFBSCs in the cochlea of the guinea pig.

References

1. Steventon, B., Mayor, R., and Streit, A., Neural crest and placode interaction during the development of the cranial sensory system. Dev. Biol., 2014. **389**: pp. 28-38.
2. Huisman, M.A. and Rivolta, M.N., Neural crest stem cells and their potential application in a therapy for deafness. Front. Biosci. (Schol. Ed.), 2012. **4**: pp. 121-132.
3. Chen, J. and Streit, A., Induction of the inner ear: Stepwise specification of otic fate from multipotent progenitors. Hear. Res., 2013. **297**: pp. 3-12.
4. Pickles, J.O., *An introduction to the physiology of hearing*. Vol. Fourth Edition. 2013: Brill. 460 pages.
5. Kim, J. and Koo, M., Mass and stiffness impact on the middle ear and the cochlear partition. J. Audiol. Otol., 2015. **19**: pp. 1-6.
6. SMART, Servier Medical Art is licensed under CC BY 3.0. Les Laboratoires Servier: http://smart.servier.com.
7. Oghalai, J.S., The cochlear amplifier: Augmentation of the traveling wave within the inner ear. Curr. Opin. Otolaryngol. Head Neck Surg., 2004. **12**: pp. 431-438.
8. Pan, L. and Zhang, M., Structures of Usher syndrome 1 proteins and their complexes. Physiology, 2012. **27**: pp. 25-42.
9. Mulsow, J. and Reichmuth, C., The binaural click-evoked auditory brainstem response of the California sea lion (*Zalophus californianus*). J. Acoust. Soc. Am., 2013. **133**: pp. 579-586.
10. Burkard, R.F., Eggermont, J.J., and Don, M., *Auditory evoked potentials: Basic principles and clinical application*. 2007: Lippincott Williams & Wilkins. 731 pages.
11. Kraus, N. and Nicol, T., *Auditory evoked potentials*, in *Encyclopedia of neuroscience*, M.D. Binder, N. Hirokawa, and U. Windhorst, Editors. 2009, Springer Berlin Heidelberg. pp. 214-218.
12. Jewett, D.L. and Williston, J.S., Auditory-evoked far fields averaged from the scalp of humans. Brain, 1971. **94**: pp. 681-696.
13. Lev, A. and Sohmer, H., Sources of averaged neural responses recorded in animal and human subjects during cochlear audiometry (Electro-Cochleogram). Arch. klin. exp. Ohr.-, Nas.- u. Kehlk.-Heilk., 1972. **201**: pp. 79-90.
14. Huang, C.M., A comparative study of the brain stem auditory response in mammals. Brain Res., 1980. **184**: pp. 215-219.
15. Buchwald, J.S. and Huang, C., Far-field acoustic response: Origins in the cat. Science, 1975. **189**: pp. 382-384.
16. Achor, L.J. and Starr, A., Auditory brain stem responses in the cat. I. Intracranial and extracranial recordings. Electroencephalogr. Clin. Neurophysiol., 1980. **48**: pp. 154-173.
17. Wada, S.I. and Starr, A., Generation of auditory brain stem responses (ABRs). I. Effects of injection of a local anesthetic (procaine HCl) into the trapezoid body of guinea pigs and cat. Electroencephalogr. Clin. Neurophysiol., 1983. **56**: pp. 326-339.
18. Wada, S.I. and Starr, A., Generation of auditory brain stem responses (ABRs). III. Effects of lesions of the superior olive, lateral lemniscus and inferior colliculus on the ABR in guinea pig. Electroencephalogr. Clin. Neurophysiol., 1983. **56**: pp. 352-366.
19. Wada, S. and Starr, A., Anatomical bases of binaural interaction in auditory brain-stem responses from guinea pig. Electroencephalogr. Clin. Neurophysiol., 1989. **72**: pp. 535-544.
20. Dehmel, S., Eisinger, D., and Shore, S.E., Gap prepulse inhibition and auditory brainstem-evoked potentials as objective measures for tinnitus in guinea pigs. Front. Syst. Neurosci., 2012. **6**: pp. 1-15.
21. Ingham, N.J., Thornton, S.K., Comis, S.D., and Withington, D.J., The auditory brainstem response of aged guinea pigs. Acta Otolaryngol., 1998. **118**: pp. 673-680.
22. Yost, W.A., *Fundamentals of hearing: An introduction*. 2007: Academic Press.
23. Knipper, M., Van Dijk, P., Nunes, I., Ruttiger, L., and Zimmermann, U., Advances in the neurobiology of hearing disorders: recent developments regarding the basis of tinnitus and hyperacusis. Prog. Neurobiol., 2013. **111**: pp. 17-33.
24. Lang, H., *Loss, degeneration, and preservation of the spiral ganglion neurons and their processes*, in *The primary auditory neurons of the mammalian cochlea*, A. Dabdoub, *et al*., Editors. 2016, Springer New York: New York, U.S.A. pp. 229-262.
25. Liberman, M.C., Epstein, M.J., Cleveland, S.S., Wang, H., and Maison, S.F., Toward a differential diagnosis of hidden hearing loss in humans. PLoS ONE, 2016. **11**: pp. e0162726.
26. Wu, P.Z., Liberman, L.D., Bennett, K., de Gruttola, V., O'Malley, J.T., and Liberman, M.C., Primary neural degeneration in the human cochlea: Evidence for hidden hearing loss in the aging ear. Neuroscience, 2018.
27. Briaire, J.J. and Frijns, J.H.M., The consequences of neural degeneration regarding optimal cochlear implant position in scala tympani: A model approach. Hear. Res., 2006. **214**: pp. 17-27.
28. Pickles, J.O., *An introduction to the physiology of hearing*. Vol. Third Edition. 2008.
29. Sherman, C. Closing the gap between cochlear implants and natural hearing. 2014 [cited 2018/03/06]; Available from: http://dana.org/News/Closing_the_Gap_Between_Cochlear_Implants_and_Natural_Hearing/.
30. Briaire, J.J., Cochlear implants: From model to patients, in Department Othorhinolaryngology. 2008, Leiden University Medical Center (LUMC), Leiden University: Leiden. pp. 281.
31. Stephen, J.O.L., Rachael, R.R., and Hugh, J.M., Principles of design and biological approaches for improving the selectivity of cochlear implant electrodes. J. Neural Eng., 2009. **6:** pp. 055002.
32. Pinyon, J.L., Tadros, S.F., Froud, K.E., AC, Y.W., Tompson, I.T., Crawford, E.N., Ko, M., Morris, R., Klugmann, M., and Housley, G.D., Close-field electroporation gene delivery using the cochlear implant electrode array enhances the bionic ear. Sci. Transl. Med., 2014. **6**: pp. 233ra54.
33. Nayagam, B.A., Human stem cells ameliorate auditory evoked responses in a model of neuropathy. Stem Cell Res. Ther., 2012. **3**: pp. 44.
34. Lemmens, R. and Steinberg, G.K., Stem cell therapy for acute cerebral injury: What do we know and what will the future bring? Curr. Opin. Neurol., 2013. **26**: pp. 617-625.
35. Hasan, A., Deeb, G., Rahal, R., Atwi, K., Mondello, S., Marei, H.E., Gali, A., and Sleiman, E., Mesenchymal stem cells in

the treatment of traumatic brain injury. Front. Neurol., 2017. **8**: pp. 1-15.
36. Verwoerd, C.D., van Oostrom, C.G., and Verwoerd-Verhoef, H.L., Otic placode and cephalic neural crest. Acta Otolaryngol., 1981. **91**: pp. 431-435.
37. Streit, A., Extensive cell movements accompany formation of the otic placode. Dev. Biol., 2002. **249**: pp. 237-254.
38. Bhattacharyya, S. and Bronner-Fraser, M., Hierarchy of regulatory events in sensory placode development. Curr. Opin. Genet. Dev., 2004. **14**: pp. 520-526.
39. Kuriyama, S. and Mayor, R., Molecular analysis of neural crest migration. Philos. Trans. R. Soc. Lond., B, Biol. Sci., 2008. **363**: pp. 1349-1362.
40. Ladher, R.K., O'Neill, P., and Begbie, J., From shared lineage to distinct functions: The development of the inner ear and epibranchial placodes. Development, 2010. **137**: pp. 1777-1785.
41. Groves, A.K. and LaBonne, C., Setting appropriate boundaries: Fate, patterning and competence at the neural plate border. Dev. Biol., 2014. **389**: pp. 2-12.
42. Streit, A. and Stern, C.D., Establishment and maintenance of the border of the neural plate in the chick: Involvement of FGF and BMP activity. Mech. Dev., 1999. **82**: pp. 51-66.
43. Litsiou, A., Hanson, S., and Streit, A., A balance of FGF, BMP and WNT signalling positions the future placode territory in the head. Development, 2005. **132**: pp. 4051-62.
44. McCabe, K.L. and Bronner-Fraser, M., Molecular and tissue interactions governing induction of cranial ectodermal placodes. Dev. Biol., 2009. **332**: pp. 189-195.
45. Kozlowski, D.J., Murakami, T., Ho, R.K., and Weinberg, E.S., Regional cell movement and tissue patterning in the zebrafish embryo revealed by fate mapping with caged fluorescein. Biochem. Cell Biol., 1997. **75**: pp. 551-562.
46. His, W., *Untersuchungen über die erste Anlage des Wirbelthierleibes: Die erste Entwickelung des Hühnchens im Ei*. Leipzig : F.C.W. Vogel, 1868: pp. 1-292.
47. Yoshida, S., Shimmura, S., Nagoshi, N., Fukuda, K., Matsuzaki, Y., Okano, H., and Tsubota, K., Isolation of multipotent neural crest-derived stem cells from the adult mouse cornea. Stem Cells, 2006. **24**: pp. 2714-2722.
48. Le Douarin, N.M., Calloni, G.W., and Dupin, E., The stem cells of the neural crest. Cell Cycle, 2008. **7**: pp. 1013-1019.
49. Theveneau, E., Steventon, B., Scarpa, E., Garcia, S., Trepat, X., Streit, A., and Mayor, R., Chase-and-run between adjacent cell populations promotes directional collective migration. Nat. Cell Biol., 2013. **15**: pp. 763-772.
50. Kruger, G.M., Mosher, J.T., Bixby, S., Joseph, N., Iwashita, T., and Morrison, S.J., Neural crest stem cells persist in the adult gut but undergo changes in self-renewal, neuronal subtype potential, and factor responsiveness. Neuron, 2002. **35**: pp. 657-669.
51. Kaltschmidt, B., Kaltschmidt, C., and Widera, D., Adult craniofacial stem cells: Sources and relation to the neural crest. Stem Cell Rev., 2012. **8**: pp. 658-671.
52. Fernandes, K.J., McKenzie, I.A., Mill, P., Smith, K.M., Akhavan, M., Barnabe-Heider, F., Biernaskie, J., Junek, A., Kobayashi, N.R., Toma, J.G., Kaplan, D.R., Labosky, P.A., Rafuse, V., Hui, C.C., and Miller, F.D., A dermal niche for multipotent adult skin-derived precursor cells. Nat. Cell Biol., 2004. **6**: pp. 1082-1093.
53. Techawattanawisal, W., Nakahama, K., Komaki, M., Abe, M., Takagi, Y., and Morita, I., Isolation of multipotent stem cells from adult rat periodontal ligament by neurosphere-forming culture system. Biochem. Biophys. Res. Commun., 2007. **357**: pp. 917-923.
54. Widera, D., Zander, C., Heidbreder, M., Kasperek, Y., Noll, T., Seitz, O., Saldamli, B., Sudhoff, H., Sader, R., Kaltschmidt, C., and Kaltschmidt, B., Adult palatum as a novel source of neural crest-related stem cells. Stem Cells, 2009. **27**: pp. 1899-1910.
55. Hauser, S., Widera, D., Qunneis, F., Müller, J., Zander, C., Greiner, J., Strauss, C., Lüningschrör, P., Heimann, P., Schwarze, H., Ebmeyer, J., Sudhoff, H., Araúzo-Bravo, M.J., Greber, B., Zaehres, H., Schöler, H., Kaltschmidt, C., and Kaltschmidt, B., Isolation of novel multipotent neural crest-derived stem cells from adult human inferior turbinate. Stem Cells Dev., 2012. **21**: pp. 742-756.
56. Liu, J.A. and Cheung, M., Neural crest stem cells and their potential therapeutic applications. Dev. Biol., 2016. **419**: pp. 199-216.
57. Sieber-Blum, M. and Grim, M., The adult hair follicle: Cradle for pluripotent neural crest stem cells. Birth Defects Res. C. Embryo Today, 2004. **72**: pp. 162-172.
58. Yu, H., Fang, D., Kumar, S.M., Li, L., Nguyen, T.K., Acs, G., Herlyn, M., and Xu, X., Isolation of a novel population of multipotent adult stem cells from human hair follicles. Am. J. Pathol., 2006. **168**: pp. 1879-1888.
59. Krejci, E. and Grim, M., Isolation and characterization of neural crest stem cells from adult human hair follicles. Folia. Biol. (Praha), 2010. **56**: pp. 149-157.
60. Yu, H., Kumar, S.M., Kossenkov, A.V., Showe, L., and Xu, X., Stem cells with neural crest characteristics derived from the bulge region of cultured human hair follicles. J Invest Dermatol 2010. **130**: pp. 1227-36.
61. Liu, F., Zhang, C., and Hoffman, R.M., Nestin-expressing stem cells from the hair follicle can differentiate into motor neurons and reduce muscle atrophy after transplantation to injured nerves. Tissue Eng. Part A, 2014. **20**: pp. 656-662.
62. Sieber-Blum, M., Grim, M., Hu, Y.F., and Szeder, V., Pluripotent neural crest stem cells in the adult hair follicle. Dev. Dyn., 2004. **231**: pp. 258-269.
63. Amoh, Y., Li, L., Katsuoka, K., Penman, S., and Hoffman, R.M., Multipotent nestin-positive, keratin-negative hair-follicle bulge stem cells can form neurons. Proc. Natl. Acad. Sci. USA, 2005. **102**: pp. 5530-5534.
64. El Seady, R., Huisman, M.A., Löwik, C.W., and Frijns, J.H.M., Uncomplicated differentiation of stem cells into bipolar neurons and myelinating glia. Biochem. Biophys. Res. Commun., 2008. **376**: pp. 358-362.
65. Amoh, Y., Kanoh, M., Niiyama, S., Hamada, Y., Kawahara, K., Sato, Y., Hoffman, R.M., and Katsuoka, K., Human hair follicle pluripotent stem (hfPS) cells promote regeneration of peripheral-nerve injury: An advantageous alternative to ES and iPS cells. J. Cell Biochem., 2009. **107**: pp. 1016-1020.
66. Clewes, O., Narytnyk, A., Gillinder, K.R., Loughney, A.D., Murdoch, A.P., and Sieber-Blum, M., Human epidermal neural crest stem cells (hEPI-NCSC)-characterization and directed differentiation into osteocytes and melanocytes. Stem Cell Rev., 2011. **7**: pp. 799-814.

67. Paus, R., Nickoloff, B.J., and Ito, T., A 'hairy' privilege. Trends Immunol., 2005. **26**: pp. 32-40.
68. Sieber-Blum, M. and Hu, Y., Epidermal neural crest stem cells (EPI-NCSC) and pluripotency. Stem Cell Rev., 2008. **4**: pp. 256-260.
69. Greiner, J.F., Hauser, S., Widera, D., Muller, J., Qunneis, F., Zander, C., Martin, I., Mallah, J., Schuetzmann, D., Prante, C., Schwarze, H., Prohaska, W., Beyer, A., Rott, K., Hutten, A., Golzhauser, A., Sudhoff, H., Kaltschmidt, C., and Kaltschmidt, B., Efficient animal-serum free 3D cultivation method for adult human neural crest-derived stem cell therapeutics. Eur. Cell Mater., 2011. **22**: pp. 403-419.
70. Koch, H.H.R., Die Aetiologie der Tuberculose. Berliner Klinische Wochenschrift, 1882. **15**: pp. 221-230.
71. Holst, A. and Frolich, T., Experimental studies relating to "Ship-beri-beri" and scurvy. J. Hyg. (Lond), 1907. **7**: pp. 634-671.
72. Regala, C., Duan, M., Zou, J., Salminen, M., and Olivius, P., Xenografted fetal dorsal root ganglion, embryonic stem cell and adult neural stem cell survival following implantation into the adult vestibulocochlear nerve. Exp. Neurol., 2005. **193**: pp. 326-333.
73. Cho, Y.B., Cho, H.H., Jang, S., Jeong, H.S., and Park, J.S., Transplantation of neural differentiated human mesenchymal stem cells into the cochlea of an auditory-neuropathy guinea pig model. J. Korean Med. Sci., 2011. **26**: pp. 492-498.
74. Chen, W., Jongkamonwiwat, N., Abbas, L., Eshtan, S.J., Johnson, S.L., Kuhn, S., Milo, M., Thurlow, J.K., Andrews, P.W., Marcotti, W., Moore, H.D., and Rivolta, M.N., Restoration of auditory evoked responses by human ES-cell-derived otic progenitors. Nature, 2012. **490**: pp. 278-282.
75. Schmiedt, R.A., Okamura, H.O., Lang, H., and Schulte, B.A., Ouabain application to the round window of the gerbil cochlea: A model of auditory neuropathy and apoptosis. J. Assoc. Res. Otolaryngol., 2002. **3**: pp. 223-233.
76. Lang, H., Schulte, B.A., and Schmiedt, R.A., Ouabain induces apoptotic cell death in type I spiral ganglion neurons, but not type II neurons. J. Assoc. Res. Otolaryngol., 2005. **6**: pp. 63-74.
77. Wang, L.E., Cao, K.L., Yin, S.K., Wang, Z., and Chen, Z.N., Cochlear function after selective spiral ganglion cells degeneration induced by ouabain. Chin. Med. J., 2006. **119**: pp. 974-979.
78. Qu, J., Gan, Y.N., Xie, K.L., Liu, W.B., Wang, Y.F., Hei, R.Y., Mi, W.J., and Qiu, J.H., Inhalation of hydrogen gas attenuates ouabain-induced auditory neuropathy in gerbils. Acta Pharmacol. Sin., 2012. **33**: pp. 445-451.
79. Bourien, J., Tang, Y., Batrel, C., Huet, A., Lenoir, M., Ladrech, S., Desmadryl, G., Nouvian, R., Puel, J.L., and Wang, J., Contribution of auditory nerve fibers to compound action potential of the auditory nerve. J. Neurophysiol., 2014. **112**: pp. 1025-1039.
80. Kilpatrick, L.A., Samuvel, D.J., Zhu, J., Smythe, N., and Lang, H., Ouabain-induced auditory nerve degeneration in congenic Ly5.1 mice. J. Otol., 2011. **6**: pp. 19-28.
81. Kilpatrick, L.A., Zhu, J., Lee, F.S., and Lang, H., Role of stromal cell-derived factor-1 expression in the injured mouse auditory nerve. Otolaryngol. Head Neck Surg., 2011. **145**: pp. 1007-1015.
82. Lang, H., Li, M., Kilpatrick, L.A., Zhu, J., Samuvel, D.J., Krug, E.L., and Goddard, J.C., Sox2 up-regulation and glial cell proliferation following degeneration of spiral ganglion neurons in the adult mouse inner ear. J. Assoc. Res. Otolaryngol., 2011. **12**: pp. 151-171.
83. Yuan, Y. and Chi, F., Dynamic changes in hair cell ribbon synapse induced by loss of spiral ganglion neurons in mice. Chin. Med. J. (Engl), 2014. **127**: pp. 1941-1946.
84. Yuan, Y., Shi, F., Yin, Y., Tong, M., Lang, H., Polley, D.B., Liberman, M.C., and Edge, A.S., Ouabain-induced cochlear nerve degeneration: Synaptic loss and plasticity in a mouse model of auditory neuropathy. J. Assoc. Res. Otolaryngol., 2014. **15**: pp. 31-43.
85. Fu, Y., Ding, D., Jiang, H., and Salvi, R., Ouabain-induced cochlear degeneration in rat. Neurotox. Res., 2012. **22**: pp. 158-169.
86. Qu, J., Huang, H., Wang, J., Mi, W.J., Qiao, L., and Qiu, J.H., Detrimental effects of ouabain on cochlear spiral ganglion cells in rats. Chin. J. Otorhinolaryngol. Head Neck Surg., 2012. **47**: pp. 926-930.
87. Wang, X., Wang, Y., Ding, Z.J., Yue, B., Zhang, P.Z., Chen, X.D., Chen, X., Chen, J., Chen, F.Q., Chen, Y., Wang, R.F., Mi, W.J., Lin, Y., Wang, J., and Qiu, J.H., The role of RIP3 mediated necroptosis in ouabain-induced spiral ganglion neurons injuries. Neurosci. Lett., 2014. **578**: pp. 111-116.
88. Kim, B.Y., Bae, W.Y., Kim, J.-R., and Lee, T.H., Damage of spiral ganglion cell induced by ouabain application in cat. Korean J. Otorhinolaryngol. Head Neck Surg., 2014. **57**: pp. 589-595.
89. Hamada, M. and Kimura, R.S., Morphological changes induced by administration of a Na+,K+-ATPase inhibitor in normal and hydropic inner ears of the guinea pig. Acta Otolaryngol., 1999. **119**: pp. 778-786.
90. Edinger, M., Sweeney, T.J., Tucker, A.A., Olomu, A.B., Negrin, R.S., and Contag, C.H., Noninvasive assessment of tumor cell proliferation in animal models. Neoplasia, 1999. **1**: pp. 303-310.
91. Kim, D.E., Schellingerhout, D., Ishii, K., Shah, K., and Weissleder, R., Imaging of stem cell recruitment to ischemic infarcts in a murine model. Stroke, 2004. **35**: pp. 952-957.
92. Shimomura, O., Johnson, F.H., and Saiga, Y., Extraction, purification and properties of aequorin, a bioluminescent protein from the luminous hydromedusan, Aequorea. J. Cell. Comp. Physiol., 1962. **59**: pp. 223-239.
93. Tsien, R.Y., The green fluorescent protein. Annu. Rev. Biochem., 1998. **67**: pp. 509-544.
94. Shaner, N.C., Steinbach, P.A., and Tsien, R.Y., A guide to choosing fluorescent proteins. Nat. Methods, 2005. **2**: pp. 905-909.
95. Shagin, D.A., Barsova, E.V., Yanushevich, Y.G., Fradkov, A.F., Lukyanov, K.A., Labas, Y.A., Semenova, T.N., Ugalde, J.A., Meyers, A., Nunez, J.M., Widder, E.A., Lukyanov, S.A., and Matz, M.V., GFP-like proteins as ubiquitous metazoan superfamily: evolution of functional features and structural complexity. Mol. Biol. Evol., 2004. **21**: pp. 841-850.
96. Masuda, H., Takenaka, Y., Yamaguchi, A., Nishikawa, S., and Mizuno, H., A novel yellowish-green fluorescent protein from the marine copepod, Chiridius poppei, and its use as a reporter protein in HeLa cells. Gene, 2006. **372**: pp. 18-25.
97. Hunt, M.E., Scherrer, M.P., Ferrari, F.D., and Matz, M.V., Very bright green fluorescent proteins from the pontellid copepod Pontella mimocerami. PLoS ONE, 2010. **5**: pp. e11517.
98. Evdokimov, A.G., Pokross, M.E., Egorov, N.S., Zaraisky, A.G., Yampolsky, I.V., Merzlyak, E.M., Shkoporov, A.N., Sander, I., Lukyanov, K.A., and Chudakov, D.M., Structural basis for the fast maturation of Arthropoda green fluorescent protein.

EMBO Rep., 2006. **7**: pp. 1006-1012.
99. Hooper, C.E., Ansorge, R.E., Browne, H.M., and Tomkins, P., CCD imaging of luciferase gene expression in single mammalian cells. J. Biolumin. Chemilumin., 1990. **5**: pp. 123-130.
100. Green, A.A. and McElroy, W.D., Crystalline firefly luciferase. Biochim. Biophys. Acta, 1956. **20**: pp. 170-176.
101. Contag, C.H. and Bachmann, M.H., Advances in *in vivo* bioluminescence imaging of gene expression. Annu. Rev. Biomed. Eng., 2002. **4**: pp. 235-260.
102. Mezzanotte, L., Que, I., Kaijzel, E., Branchini, B., Roda, A., and Löwik, C., Sensitive dual color *in vivo* bioluminescence imaging using a new red codon optimized firefly luciferase and a green click beetle luciferase. PLoS ONE, 2011. **6**: pp. e19277.
103. Viviani, V.R., Bechara, E.J., and Ohmiya, Y., Cloning, sequence analysis, and expression of active Phrixothrix railroad-worms luciferases: Relationship between bioluminescence spectra and primary structures. Biochemistry, 1999. 38: pp. 8271-8279.
104. Tannous, B.A., Kim, D.E., Fernandez, J.L., Weissleder, R., and Breakefield, X.O., Codon-optimized *Gaussia* luciferase cDNA for mammalian gene expression in culture and *in vivo*. Mol. Ther., 2005. **11**: pp. 435-443.
105. Frackman, S., Anhalt, M., and Nealson, K.H., Cloning, organization, and expression of the bioluminescence genes of *Xenorhabdus luminescens*. J. Bacteriol., 1990. **172**: pp. 5767-5773.
106. Contag, C.H., Contag, P.R., Mullins, J.I., Spilman, S.D., Stevenson, D.K., and Benaron, D.A., Photonic detection of bacterial pathogens in living hosts. Mol. Microbiol., 1995. **18**: pp. 593-603.
107. Wilson, T. and Hastings, J.W., Bioluminescence. Annu. Rev. Cell Dev. Biol., 1998. **14**: pp. 197-230.
108. Patterson, S.S., Dionisi, H.M., Gupta, R.K., and Sayler, G.S., Codon optimization of bacterial luciferase (*lux*) for expression in mammalian cells. J. Ind. Microbiol. Biotechnol., 2005. **32**: pp. 115-123.
109. Close, D.M., Patterson, S.S., Ripp, S., Baek, S.J., Sanseverino, J., and Sayler, G.S., Autonomous bioluminescent expression of the bacterial luciferase gene cassette (*lux*) in a mammalian cell line. PLoS ONE, 2010. **5**: pp. e12441.
110. Wilson, B.C., Jeeves, W.P., and Lowe, D.M., *In vivo* and *post mortem* measurements of the attenuation spectra of light in mammalian tissues. Photochem. Photobiol., 1985. **42**: pp. 153-162.
111. Mezzanotte, L., Fazzina, R., Michelini, E., Tonelli, R., Pession, A., Branchini, B., and Roda, A., *In vivo* bioluminescence imaging of murine xenograft cancer models with a red-shifted thermostable luciferase. Mol. Imaging Biol., 2010. **12**: pp. 406-414.
112. Mezzanotte, L., Aswendt, M., Tennstaedt, A., Hoeben, R., Hoehn, M., and Löwik, C., Evaluating reporter genes of different luciferases for optimized *in vivo* bioluminescence imaging of transplanted neural stem cells in the brain. Contrast Media Mol. Imaging, 2013. **8**: pp. 505-513.
113. Welsh, D.K. and Noguchi, T., Cellular bioluminescence imaging. Cold Spring Harb. Protoc., 2012. **2012**: pp. 852-866.
114. Sykova, E. and Jendelova, P., In vivo *tracking of stem cells in brain and spinal cord injury*, in *Progr. Brain Res.*, T.W. John and I.R.M. Andrew, Editors. 2007, Elsevier. pp. 367-383.
115. Jendelova, P., Herynek, V., DeCroos, J., Glogarova, K., Andersson, B., Hajek, M., and Sykova, E., Imaging the fate of implanted bone marrow stromal cells labeled with superparamagnetic nanoparticles. Magn. Reson. Med., 2003. **50**: pp. 767-776.
116. Bulte, J.W. and Kraitchman, D.L., Iron oxide MR contrast agents for molecular and cellular imaging. NMR Biomed., 2004. **17**: pp. 484-499.
117. Rosner, M.H. and Bolton, W.K., Ferumoxytol for the treatment of anemia in chronic kidney disease. Drugs Today (Barc), 2009. **45**: pp. 779-786.

Chapter 2

Isolation, expansion and neural differentiation of stem cells from human plucked hair: A further step towards autologous nerve recovery

Cytotechnology, 2016

Vol. **68** (5): pp. 1849-1858

C.G. Gho, T. Schomann, S.C. de Groot, J.H.M. Frijns, M.N. Rivolta, M.H.A. Neumann, M.A. Huisman

Abstract

Stem cells from the adult hair follicle bulge can differentiate into neurons and glia, which is advantageous for the development of an autologous cell-based therapy for neurological diseases. Consequently, bulge stem cells from plucked hair may increase opportunities for personalized neuroregenerative therapy. Hairs were plucked from the scalps of healthy donors, and the bulges were cultured without prior tissue treatment. Shortly after outgrowth from the bulge, cellular protein expression was established immunohistochemically. The doubling time was calculated upon expansion, and the viability of expanded, cryopreserved cells was assessed after shear stress. The neuroglial differentiation potential was assessed from cryopreserved cells. Shortly after outgrowth, the cells were immunopositive for nestin, SLUG, AP-2α and SOX9, and negative for SOX10. Each bulge yielded approximately 1×10^4 cells after three passages. Doubling time was 3.3 (± 1.5) days. Cellular viability did not differ significantly from control cells after shear stress. The cells expressed class III β-tubulin (TUBB3) and synapsin-1 after 3 weeks of neuronal differentiation. Glial differentiation yielded KROX20- and MPZ-immunopositive cells after 2 weeks. We demonstrated that human hair follicle bulge-derived stem cells can be cultivated easily, expanded efficiently and kept frozen until needed. After cryopreservation, the cells were viable and displayed both neuronal and glial differentiation potential.

Introduction

During the last decade, the interest in autologous stem cells has increased considerably, especially regarding the development of individualized therapies [1]. However, the procurement of autologous somatic stem cells for human therapeutic purposes is still limited. In addition, somatic stem cell potency is restricted, and multipotent rather than pluripotent [1]. Reprogramming somatic cells into induced pluripotent stem cells by the forced expression of certain genes is being explored but is controversial, since they are often tumorigenic and may initialize a T-cell-dependent immune response in syngeneic recipients [2-4].

For these reasons, the use of other types of autologous somatic stem cells is currently under investigation, such as bone marrow stem cells in a curative treatment for ischemic heart patients and cerebral infarction [5, 6], already showing some promising results. One of the risks with this approach is that stem cells may follow their innate biological inclination irrespective of the tissue or organ into which they have been grafted. This was demonstrated by the finding that autologous bone marrow stem cells can produce extracellular matrix after engraftment into the brain [7, 8].

An alternative strategy could involve the use of neural crest-derived stem cells (NCSCs). They are appropriate for autologous cell-based therapy in many diseases, as they can be derived from adult tissue and can give rise to many cell types from ectodermal and mesodermal lineages. NCSCs from adult tissue (aNCSCs) are nononcogenic and possess a broad regenerative potential [9]. In culture, aNCSCs retain their neural crest potential to differentiate into a variety of cells including adipocytes, chondrocytes, neurons, glia, osteocytes, and muscle cells [9]. Minimally invasive, easily accessible sources for NCSCs are the olfactory sheath, palate, dental pulp and the hair follicle bulge [9].

We consider the hair follicle to be the most easily accessible option [10]. It has been reported that hair follicle bulge-derived NCSCs (HFBSCs) from human adults still possess neural crest characteristics such as multipotency [11-15]. This multipotency is of particular use in the area of neuroregeneration, given that hair follicle stem cells can promote the functional recovery of injured peripheral and central nerves [16, 12, 13, 17]. Hence, autologous HFBSCs are potentially suitable

for therapeutic application in a broad range of neurological disorders such as ALS, Alzheimer's disease and stroke. They also may be used in cell-based therapies for sensory neurological diseases such as those for ocular or inner ear regeneration [10, 18]. If HFBSCs could be harvested from plucked hairs, their practical utilization for autologous stem cell therapy would increase immensely. We therefore aimed to establish that:

1. Follicular stem cells, migrated out of the bulge from plucked hair follicles, are nestin-positive and possess a neural crest stem cell immunophenotype. Moreover, due to the cytotoxic nature of proteases, we intend to minimize the enzymatic treatments of tissue and cells [19].

2. HFBSCs can be used for transplantation purposes, because they can be expanded easily and remain viable after cryopreservation and needle shear stress.

3. These stem cells are suitable as a source for future neural regenerative medicine in the patient, i.e. they can be stored frozen while keeping their neural and glial differentiation capacity.

Materials and methods

Specimen

Plucked hairs from healthy donors were obtained from the occipital area of the scalp. The hairs were removed with depilation forceps. All human material was handled according to the Dutch Medical Treatment Agreement Act (Dutch Civil Code, Book 7, Section 7.7.5, article 7:467; http://www.dutchcivillaw.com/legislation/dcctitle7777.htm). Intact hair follicles (HFs) in the anagen phase were selected under a dissection microscope and placed in DMEM/Ham's F-12 1:1 (Biochrom AG, Berlin, Germany) containing 1% GlutaMAX (100x; Life Technologies, Carlsbad, CA, USA) and 1% Antibiotic Antimycotic Solution (100x; Sigma-Aldrich, St. Louis, MO, USA) (Fig. 1A). The HFs were processed the next morning.

Isolation and cultivation of HFBSCs

Isolation of HF stem cells was according to Sieber-Blum *et al*. [11] with minor changes. Briefly, connective tissue (if present) was removed from the HF and the bulge-containing area was dissected out just below the sebaceous gland and well above the bulb (Fig. 1A). Then, a longitudinal section along the tissue of the bulge was made, to cause the tissue to unfold. During these procedures, care has to be taken to avoid dehydration of the HF. Before the start of the culture, tissue culture 12-well plates (TPP; Trasadingen, Switzerland) were coated with poly-D-lysine (PDL; Sigma-Aldrich) diluted in sterile demi water (1:10) at 37°C and 5% CO_2 for 1 h. Then the PDL solution was removed and the wells air-dried under sterile conditions. Prior to usage, the PDL matrix was rehydrated with basic growth medium (BGM, 37°C, 30 min). BGM consisted of DMEM/Ham's F-12 1:1, containing 1% GlutaMAX, 1% Antibiotic Antimycotic Solution, supplemented with 10% fetal bovine serum Gold (FBS; Life Technologies), 2% B-27 Supplement without vitamin A (50x; Life Technologies), 1% N-2 MAX Media Supplement (100x; R&D Systems, Minneapolis, MN, USA), recombinant human Fibroblast Growth Factor-basic (rhFGF-basic; 20 ng/ml; R&D Systems), and recombinant human Epidermal Growth Factor (rhEGF; 20 ng/ml; R&D Systems). After rehydration, the BGM was poured out of the wells, and one HF-bulge was placed in each well. The HFs were carefully pressed on the bottom of the well using a forceps. Subsequently, three incubation periods in a small

drop of medium allowed the HF to attach to the matrix. Incubation was done at 37°C and 5% CO_2 for 75 min. If necessary, some medium was added. Finally, 500 µl of freshly prepared BGM was added cautiously. The primary culture was established by the outgrowth of HF stem cells from the bulge, usually at 8-10 days after the start of the culturing. After 1 week of culturing, a complete medium change was performed, followed by replacement of half of the medium every other day. Three to four days after the start of outgrowth, the HF bulge was removed and some of the cultures were fixed with 1% formaldehyde in PBS (FA) for immunohistochemical analysis of neural crest markers.

Expansion and cryopreservation

After removal of the bulge, cells were grown to 60-70% confluence and enzymatically detached using pre-warmed 0.05% trypsin-EDTA (Life Technologies) at 37°C for precisely 2 min. Trypsinization was stopped by the addition of DMEM/HAM's F-12 1:1 supplemented with 10% FBS. The cells were centrifuged at 280×*g* for 10 min, and the cell pellet was suspended in 1 ml BGM. After cell counting (Logos Biosystems, Anyang-City, Korea), the cells were seeded at expansion density (2.5×10^3 cells per cm^2) in a PDL-coated dish and allowed to expand until 60-70% confluence. In general, cells were passaged three to four times. Each period of time prior to passaging was about 1 week. Doubling times were calculated at passages 2 and 3, using the site: Roth V. 2006 Doubling Time Computing, Available from: http://www.doubling-time.com/compute.php [20].

In addition, a portion of the cells was frozen at -80°C at a concentration of 1×10^6 cells/ml in 90% FBS with 10% dimethyl sulfoxide (Sigma-Aldrich). After storage and thawing, the cells were suspended in 5 ml BGM, centrifuged, collected, suspended in BGM, carefully triturated, seeded at expansion density, and cultured at 37°C and 5% CO_2.

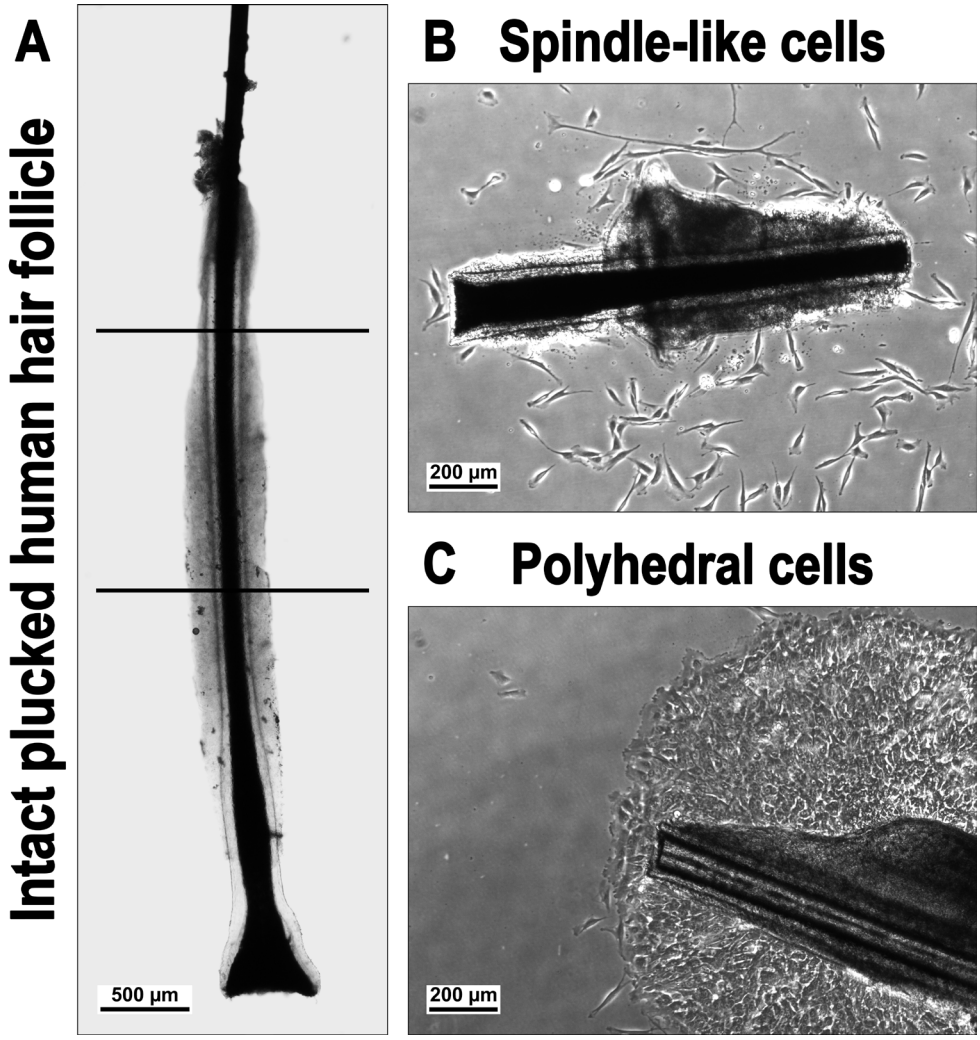

Fig. 1: **A:** Hair follicle with an intact inner and outer root sheath. Only the upper half of the follicle was used (between lines; scale bar 500 µm). **B:** HF and cells with spindle-like morphology, at day 2 of outgrowth. The outer root sheath is curled (scale bar 200 µm). **C:** HF and tightly clustered cells with an epithelial appearance (sheets of flattened polyhedral cells; scale bar 200 µm).

Simulation of the transplantation procedure: ejection of cells

After cryopreservation, cells were cultured at 37°C and 5% CO_2. After 1 week cells were enzymatically detached and centrifuged at 280×*g* for 10 min. They were suspended at a density of ~4.0 × 10^6 cells/ml in BGM medium and carefully triturated.

Subsequently, 10 µl of the cell suspension was loaded into a 100 µl syringe with a 30 gauge needle and injected into a 1 ml Eppendorf tube using a programmable syringe pump (Prosense, Oosterhout, The Netherlands); settings: diameter 4.699 mm-rate 0.5 ml/min. Both cultured and cryopreserved cells were subjected to shear stress. Viability was assessed using the trypan blue test. Trypan blue staining is based on the principle that live cells possess intact cell membranes that exclude the dye, whereas dead cells do not [21]. A 1:1 dilution of cell suspension and 0.4% trypan blue was incubated for 2 min at room temperature. Next, the stained cells were counted using a Neubauer haemocytometer chamber and calculated using the following formula:

$$\text{Vital cell rate } (\%) = \frac{\text{number of vital cells}}{\text{number of vital cells} + \text{number of dead cells}} \times 100$$

Cells that had been cultured but not injected served as controls.

Statistical analysis

The paired, two-tailed Student's *t* test was used to estimate the difference between the control and injected cells. The unpaired, two-tailed Student's *t* test was used to estimate the difference between control cells and both cryopreserved and injected cryopreserved cells.

Neural differentiation of HFBSCs

Following outgrowth, expansion, and cryopreservation of HFBSCs, 2.5×10^5 cells in 500 µl of BGM were seeded per well of a 12-well plate. The cells were seeded via the side into PDL-coated wells containing PDL-coated cover glasses (Thermo Scientific, Waltham, MA, USA). It was essential in all the described procedures to prevent the cover glass sticking to the bottom of the well. Prior to PDL coating, the cover glasses were etched in 85% phosphoric acid (Merck Millipore, Darmstadt, Germany) for 12 h [22]. Subsequently, acid-treated cover glasses were rinsed extensively in ultrapure water and subjected to a graded series of 70, 90, and 96% ethanol. Cover glasses were stored in 96% ethanol. The 12-well plates and etched cover glasses were coated separately with PDL as described previously. After seeding, the cells were cultured at 37°C and5 % CO_2, while their settlement underneath the cover glass

was observed daily. When an appropriate density was achieved, i.e., 5 to 10 cells in one field of view (FOV, 10× magnification, an area of ~3.5 mm^2), differentiation was induced by removal of 250 µl medium and replacement with 300 µl cAMP-containing induction medium (IM) [23]. IM consisted of DMEM/Ham's F-12 1:1 supplemented with 1.5 mM cAMP (Sigma-Aldrich), 1% glutamax (Life Technologies), 10 ng/ml NGF, 10 ng/ml GDNF, 10 ng/ml BDNF (all from R&D Systems) and 2% B27 + VitA (Life Technologies). If the appropriate density was not achieved, half of the medium was replaced with fresh BGM every other day. After IM was added, the cultures were allowed to differentiate for at least 60 h without disturbance due to opening of the incubator or observation of the cells. Subsequently, 250 µl medium was removed and again substituted with 300 µl IM. Thereafter, the medium was replenished with IM every other day. Cultures were observed for morphological changes on a daily basis. If no neuronal morphologies appeared after 7 days of differentiation, the culture underwent another period without disturbance in IM, and the above-mentioned differentiation procedure was followed again. After differentiation for 7-14 days, the cover glass was carefully removed, because cells were not only attached to the bottom of the well but sometimes also to the underside of the cover glass. The cells on the bottom of the well were fixed in 1% FA for 15 min and processed for immunohistochemistry. Fixed cells were stored at 4°C for a maximum period of 2 weeks.

Glial differentiation of HFBSCs

After expansion, a volume of 500 µl of BGM (without FBS) containing 1 × 10^5 cells was pipetted into each well of a 12-well plate. The cells were seeded via the side into uncoated wells which contained PDL-coated cover glasses. During culture, the cover glass should not stick to the bottom of the well. On the next day, half of the medium was replaced with serum-free BGM [24]. Cells were observed every other day to follow settlement and changes in morphology. The medium was exchanged with serum-free medium every other day until an average density of 10-20 cells per FOV underneath the cover glass was reached. Then half of the medium was replaced by IM. The cells underneath the cover glass usually adopt glial-like morphologies after 3-4 days of induction. After induction, the medium was exchanged once a week with IM. Cultures were maintained until networks of cells were observed. Because the networks were attached to the underside of the cover glass, the cover glasses were

removed and placed upside down in another well of a 12-well dish. The cells were fixed in 1% FA for 15 min.

Immunohistochemistry

Prior to immunohistochemistry, the cells were washed with 0.05% Tween-20 in PBS for 5 min and permeabilized in 0.1% Triton X-100 in PBS for 10 min. Cells were treated with blocking solution consisting of 5% non-immune serum in 0.05% Tween-20 in PBS for 30 min. Afterwards, the cells were incubated with the primary antibodies in blocking solution at 4°C overnight [25]. The primary antibodies used were: anti-Nestin (1:500, Biosensis, Thebarton, South Australia), anti-SLUG (1:125, Abcam, Cambridge, U.K., ab 27568), anti-AP-2α (1:100, Santa Cruz Biotechnology, Santa Cruz, CA, USA, sc-53164), anti-SOX9 (1:500, Millipore, Billerica, MA, USA, AB5535), anti-SOX10 (1:200, Santa Cruz, sc-17342), anti-β-III-tubulin (1:200, Abcam, ab18207), anti-synapsin-1 (1:200, Abcam, ab8), anti-myelin protein zero (MPZ; 1:200, Neuromics, Minneapolis, MN, USA, Ch23009), and anti-Krox20 (1:100, Covance, New York, NY, USA). The secondary fluorochrome-conjugated antibodies were diluted 1:500 in blocking buffer, and the cells were incubated at room temperature for 1 h. The secondary antibodies were conjugated with either Alexa Fluor 488 or Alexa Fluor 555 (Life Technologies). Nuclear counterstaining was performed with 1:1000 DAPI (Life Technologies, D3571) in PBS. The cells were covered with Vectashield (Vector Laboratories, Burlingame, CA, USA). Omission of the primary antibody served as a control for false cross-reactivity of the secondary antibody. Pertinent positive cell or tissue controls were used: RT4-D6P2T, a rat Schwann cell line (ATCC, Manassas, VA, USA) for anti-nestin, -SOX9, -Krox20, and -MPZ, the Melan-Ink4a cell line (Wellcome Trust Functional Genomics Cell Bank, London, UK) for anti-SOX10 and -β-III-tubulin [26], the SKBR3-breast cancer cell line for anti-SLUG and AP-2α, and mouse brain for anti-synapsin-1. Fluorescence imaging was performed using fluorescence microscopy (Olympus IX70) in combination with the LAS AF microscope software (Version 1.9.0 build 1633, Leica Microsystems). The data were corrected for background staining and normalized using the quantification method of the software. Only those immunostainings showing a peak maximum at emission of at least two times higher than the background were considered to be significantly positive. Pictures were processed using Adobe Photoshop CS6 Extended (Version: 13.0 x64, Adobe Systems Incorporated, San Jose, CA, USA).

Results

Isolation and cultivation of HFBSCs

In our experience, more than 60% of the bulges remained attached and produced cellular outgrowth (Table 1). However, outgrowth did not always yield the desired phenotype of HFBSCs with spindle-like morphology (Fig. 1B); tightly clustered cells with an epithelial appearance were also seen (sheets of flattened polyhedral cells, Fig. 1C). Both cell phenotypes emigrated from bulge explants at 8-10 days of culture. Based on morphology and immunohistochemistry (results not shown), the flattened cells were identified as keratinocytes. Therefore, cultures containing those cells were discarded (Table 1).

Table 1: Outgrowth, adhesion and morphology of cells from the HF bulge explant.

Cultures	HFs planted (n)	Cultures with outgrowth (%)	Cultures with polyhedral cell outgrowth (%)	Cultures with spindle-like cell outgrowth (%)
905E1P0	12	58	33	57
906E1P0	12	58	57	43
916E1P0	12	67	37	63
932E1P0	12	67	100	0
934E1P0	30	67	75	25
Average	–	63	Discarded	34

In vitro NCSC-characteristic protein expression profile

The majority of HFBSCs express the neural crest cell markers SOX9, SLUG, and AP-2α as determined by indirect immunohistochemistry [26]. SOX10 expression was below the level of detection. The neural progenitor cell marker nestin was present in all cells (Fig. 2).

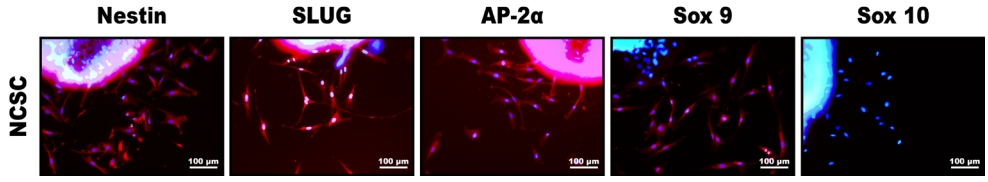

Fig. 2: HFBSCs at day 2 of outgrowth. The NCSC markers nestin (red), SLUG (red), AP-2α (red) and SOX9 (red) are positive. SOX10 (red) is negative. Nuclei are stained with DAPI (blue; scale bar 100 µm).

Expansion and cryopreservation

The selected primary (P0) cultures reached 60-70% confluence after 15-19 days. The P1 cultures reached 80% confluence after 1 week and those from P2, 1 week later. The total yield of cells per HF was approximately 1×10^4. The mean doubling time, calculated from the P2 and P3 cultures, was 3.3 (± 1.5) days (Table 2).

Table 2: Doubling times of HFBSCs after passaging.

Cultures	Cells at start of culture (n)	Cells at end of culture(n)	Doubling Time (days)
905P1 to P2	199.000	1.872.000	2.8
916P1 to P2	328.000	2.128.000	5.6
934P1 to P2	60.000	1.000.000	2.7
1011P2 to P3	350.000	3.800.000	2.9
1012P1 to P3	350.000	4.400.000	2.7
Avg ± SD			3.3 ± 1.5

Simulation of the transplantation procedure: ejection of cells

Shear stress caused by injection through a syringe needle did not change the viability of the cells significantly, whether the cells were freshly cultured or frozen ($p = 0.2401$ and $p = 0.6306$, respectively). However, a small but significant difference in viability was found between cells which were only cultured and those which were cryopreserved ($p = 0.009$). Nevertheless, after cryopreservation, 82.2 % ± 2.33% of the cells were still viable. These results show that HFBSCs can be expanded and kept frozen until needed.

Neural differentiation

For neural differentiation, we used the principle of the ‘sandwich method’. The rationale for this method is, that neuronal survival is improved if the cells are grown on a substrate-coated surface and covered by a cover glass [27]. In general, a density of about 8 cells per FOV (~3.5 mm^2) underneath the cover glass gave the highest

number of surviving neuron-like cells during neuronal induction. A considerable number of cells on top of the cover glass could not endure neuronal induction and died, resulting in cellular debris. Too much of this debris appeared to be destructive to neurons, because it covered the developing neuron-like cells and their projections, vacuoles were formed and the neurons subsequently deteriorated. Under the condition that cells were not covered by cellular debris, different neuron-like cells with elongated, branched projections developed over time. These projections could grow to a length ranging between 100 and 500 µm (Fig. 3A). Neuron-like cells were found mainly on the bottom of the well.

Glial differentiation

After seeding many cells attached within a few minutes to the PDL matrix, but a considerable number of HFBSCs remained motile. A considerable number of these cells migrated underneath the cover glass, sometimes in globular cell aggregates (Fig. 3C) [24]. These cells were mainly bipolar, with a distinct bulbous soma and small projections. After 2 or 3 days, most of these cells showed premature glial-like morphologies. A few days later, their soma became spherical and the first projections appeared, all very different in length. These glia-like cells quickly formed spacious, structured networks. With further culturing, the cells and networks did not alter noticeably.

Immunohistochemistry

In general, many cells were β-III-tubulin-positive early during neural induction, and synapsin-1-positivity was detectable a few days later (Fig. 3A). Glial induction yielded cells which were β-III-tubulin-negative, but positive for MPZ and Krox20 (Fig. 3B).

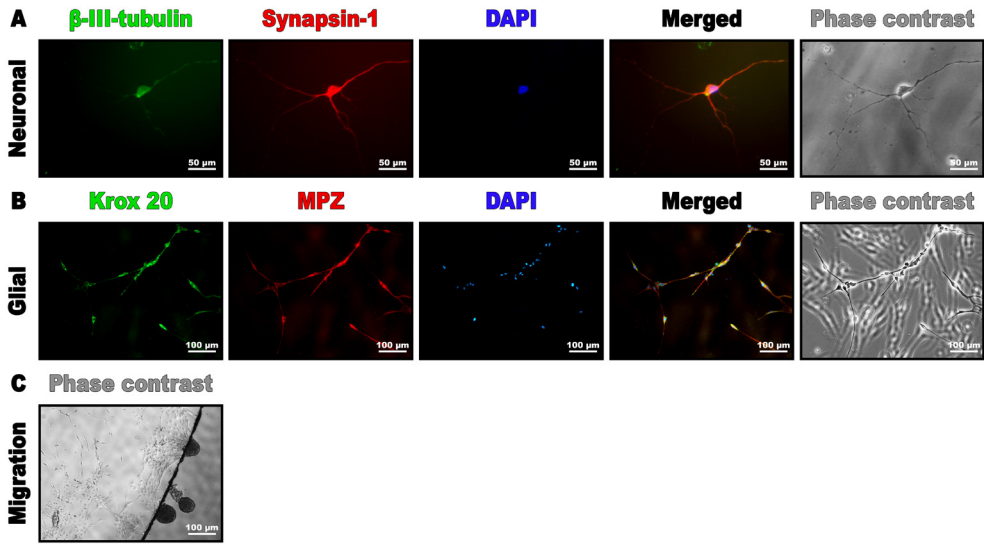

Fig. 3: **A:** Representative HFBSCs 14 days after neuronal induction. Cells at the bottom of the well stained positive for β-III-tubulin (green) as well as synapsin-1 (red). The cell nucleus is stained with DAPI (blue). Merged image reveals overlay of β-III-Tubulin (green) as well as synapsin-1 (red) localization. The phase contrast image shows differences in long dendritic projections and thicker axon (scale bar 50 µm). **B:** HFBSCs 15 days after glial induction. Glial cells were at the underside of the cover glass, therefore cells on the top of the glass are also faintly visible, but out of focus. Cells stained positive for the glial markers Krox20 (green) and MPZ (red). Nuclei are stained with DAPI (blue). Cells with a yellow color in the merged image co-express MPZ (red) and Krox20 (green). The phase contrast image depicts spindle-shaped morphologies of the glial cells (scale bar 100 µm). **C:** Migration of glial cells underneath the cover glass.

Discussion

We isolated, expanded and cryopreserved nestin-positive stem cells, derived from the bulge area from plucked human hairs. We showed that these stem cells, which are also positive for the neural crest markers SOX9, SLUG and AP-2α, are suitable for transplantation purposes because they easily survive cryopreservation and needle shear stress, while conserving their neuronal differentiation capacities.

The technique used to harvest the HF is virtually painless and allows the collection of hundreds of HF per patient. The culture technique to expand the cells is simple and straightforward and usually yields 1×10^4 cells per HF. Only three to four passages are required for this high yield, so cellular senescence is not an issue. Moreover, cellular damage by frequent protease treatments is restricted to a minimum. We do not consider the series of conditions mentioned in this report as imperative protocols, prerequisite to stimulating these cells towards differentiation into neurons and glia cells. There are some critical points in the procedures, however, such as the selection of intact hair follicles, rejection of cultures with undesired cell outgrowth, and the sandwich differentiation culture method. Rigorous rejection of cultures based on critical observations and knowledge of contaminating cell types allowed us to perform a ‘‘selection at the gate’’ of the desired cell type. Obviously, the group of cells which are most prominently present in the hair follicle are keratinocytes. These cultures were immediately discarded. Other cells present in the hair follicle are fibroblasts, which possess in the migrating phase – like many other cells – a spindle-like morphology. However, cultures containing fibroblasts will soon be overgrown by this contaminating cell type, for the doubling time of human dermal fibroblasts is in general 24 h, while the hair follicle bulge stem cells have a doubling time of an average of 3.3 days (see also ‘‘*Results*’’, section *Expansion and cryopreservation*). Fibroblasts will thus overgrow the other cells and form arrays of cells oriented in a curvilinear pattern. These cultures were also discarded. Other cells, which have been reported to be present in the hair follicle are melanocytes, cells from the peripheral nerve ends and some muscle cells [28]. Melanocytes, which in the hair follicle have a similar morphology as the bulge cells (bipolar), do not grow under the culture conditions reported here: they need medium with a relatively low pH, generated by 10% CO_2. We did not consider Schwann cells from the peripheral nerve endings as contaminating, for they are also neural crest-derived. Muscle cells are sometimes present in mouse vibrissae cultures, but we have never demonstrated them in

human hair follicle cultures (using αSMA staining).

Using the sandwich differentiation method, it was possible to vary the culture circumstances in such a way that a different neural cell phenotype was achieved. It is known that a combination of serum deprivation, cell density and substrate can direct neural stem cells to develop towards a neuronal or glial phenotype [29]. In the neuronal differentiation protocol, the surface of the cover glass was soon covered with many cells, due to the relatively high seeding density and proliferative stimulus of FBS. This apparently prevented the attachment of many cells. Thus, different cell types remained floating and finally found a habitat underneath the cover glass. Some of these cells showed a fibroblast-like morphology, while others were neuron-like cells with a small, shining soma and two or more thin projections. In time, the fibroblast-like cells disappeared; they apparently did not survive the differentiation medium. However, there was obviously contact between the small neuron-like cells and the fibroblasts, suggesting paracrine interactions which may stimulate neural differentiation [30]. We assume that, because of the decrease in cell density, neuron-like cells develop long and complex branches in order to seek contact with other cells. It is conceivable that the micro-environment underneath the cover glass, such as a low oxygen pressure and the build-up of autocrine factors, might facilitate neuroglial differentiation and survival of HFBSCs [27]. Interestingly, in both protocols, cells with a shining soma and thin projections preferred migrating underneath the cover glass while other cells apparently preferred to settle on top. This cell type-specific affinity to seek a place in the narrow space between the cover glass and the bottom of the well, or on top of the cover glass, also occurred when HFBSCs were seeded underneath the cover glass (results not shown).

We are convinced that the repertoire of nestin-positive stem cells from the human HF bulge will be of benefit for many different autologous cell-based therapies. Still, there seems to be a difference of opinion about the precise localization of these cells. Clewes *et al*. [31] described nestin-positive cells migrating from the HF bulge in culture, whereas Amoh *et al*. [12, 13] found nestin-positive cells immediately below the sebaceous glands just above the bulge area, i.e., in the isthmus region. In our experience, it is nearly impossible to distinguish the bulge area from the isthmus region in human HFs (Fig. 1A). We therefore assume that the nestin-positive cells in our cultures and those described by Clewes *et al*. [31] do not differ from those described by Amoh *et al*. [12, 13], as was also previously suggested by Djian-

Zaouche *et al*. [32]. Remarkable positive results of neural regeneration and functional improvement have been obtained in animal models of brain, spinal cord, and nerve injury therapy using stem cells derived from hair follicles [16, 12, 13, 17], giving hope for patients suffering from neurodegenerative diseases. Another point of interest, however, is the predisposition of these HFBSCs to repair cranial bone, nerves and tissue of the head, e.g. in patients with severely burnt faces. These patients often have enough remaining hair to perform hair transplantations and to harvest stem cells, which may open possibilities for complete autologous facial repair. This holds true for autologous stem cell therapy in general, as experience with the culturing of stem cells in autologous serum is increasing [33].

Conclusion

We have demonstrated that stem cells from HFs, plucked from human scalps, display a NCSC immune profile and can be cultivated, expanded, and kept frozen until needed. We also showed that differentiation of these stem cells into neurons and glial cells is feasible. The technique used to harvest the HFs is almost painless and allows the collection of hundreds of HFs per patient, which is highly advantageous, making these cells very attractive for autologous transplantation and treatment models for a variety of disorders.

Acknowledgments

The authors acknowledge Suzy Varderesyan, Rianne Läkamp, Fleur ten Tije, and Ierry-Ann Lourens for their assistance in the practical work. TS was supported by MED-EL GmbH (Innsbruck, Austria) and Stichting Het Heinsius-Houbolt Fonds (the Netherlands).

Copyright

This article is distributed under the terms of the Creative Commons Attribution 4.0 International License (http://creativecommons.org/licenses/by/4.0/), which permits unrestricted use, distribution, and reproduction in any medium.

References

1. Prasongchean, W. and Ferretti, P., Autologous stem cells for personalised medicine. N. Biotechnol., 2012. **29**: pp. 641-650.
2. Zhao, T., Zhang, Z.-N., Rong, Z., and Xu, Y., Immunogenicity of induced pluripotent stem cells. Nature, 2011. **474**: pp. 212-215.
3. Zhang, G., Shang, B., Yang, P., Cao, Z., Pan, Y., and Zhou, Q., Induced pluripotent stem cell consensus genes: Implication for the risk of tumorigenesis and cancers in induced pluripotent stem cell therapy. Stem Cells Dev., 2012. **21**: pp. 955-964.
4. Fu, X., The immunogenicity of cells derived from induced pluripotent stem cells. Cell Mol. Immunol., 2014. **11**: pp. 14-16.
5. Kasahara, Y., Ihara, M., and Taguchi, A., Experimental evidence and early translational steps using bone marrow derived stem cells after human stroke. Front. Neurol. Neurosci., 2013. **32**: pp. 69-75.
6. Tian, T., Chen, B., Xiao, Y., Yang, K., and Zhou, X., Intramyocardial autologous bone marrow cell transplantation for ischemic heart disease: A systematic review and meta-analysis of randomized controlled trials. Atherosclerosis, 2014. **233**: pp. 485-492.
7. Grigoriadis, N., Lourbopoulos, A., Lagoudaki, R., Frischer, J.M., Polyzoidou, E., Touloumi, O., Simeonidou, C., Deretzi, G., Kountouras, J., Spandou, E., Kotta, K., Karkavelas, G., Tascos, N., and Lassmann, H., Variable behavior and complications of autologous bone marrow mesenchymal stem cells transplanted in experimental autoimmune encephalomyelitis. Exp. Neurol., 2011. **230**: pp. 78-89.
8. Snyder, E.Y., The risk of putting something where it does not belong: Mesenchymal stem cells produce masses in the brain. Exp. Neurol., 2011. **230**: pp. 75-77.
9. Achilleos, A. and Trainor, P.A., Neural crest stem cells: Discovery, properties and potential for therapy. Cell Res., 2012. 22: pp. 288-304.
10. Huisman, M.A. and Rivolta, M.N., Neural crest stem cells and their potential application in a therapy for deafness. Front. Biosci. (Schol. Ed.), 2012. **4**: pp. 121-132.
11. Sieber-Blum, M., Grim, M., Hu, Y.F., and Szeder, V., Pluripotent neural crest stem cells in the adult hair follicle. Dev. Dyn., 2004. **231**: pp. 258-269.
12. Amoh, Y., Kanoh, M., Niiyama, S., Hamada, Y., Kawahara, K., Sato, Y., Hoffman, R.M., and Katsuoka, K., Human hair follicle pluripotent stem (hfPS) cells promote regeneration of peripheral-nerve injury: An advantageous alternative to ES and iPS cells. J. Cell Biochem., 2009. **107**: pp. 1016-1020.
13. Amoh, Y., Kanoh, M., Niiyama, S., Kawahara, K., Sato, Y., Katsuoka, K., and Hoffman, R.M., Human and mouse hair follicles contain both multipotent and monopotent stem cells. Cell Cycle, 2009. **8**: pp. 176-177.
14. Yu, H., Kumar, S.M., Kossenkov, A.V., Showe, L., and Xu, X., Stem cells with neural crest characteristics derived from the bulge region of cultured human hair follicles. J Invest Dermatol 2010. **130**: pp. 1227-36.
15. Mistriotis, P. and Andreadis, S.T., Hair follicle: A novel source of multipotent stem cells for tissue engineering and regenerative medicine. Tissue Eng. Part B Rev., 2013. **19**: pp. 265-278.
16. Amoh, Y., Li, L., Katsuoka, K., and Hoffman, R.M., Multipotent hair follicle stem cells promote repair of spinal cord injury and recovery of walking function. Cell Cycle, 2008. **7**: pp. 1865-1869.
17. Hu, Y.F., Gourab, K., Wells, C., Clewes, O., Schmit, B.D., and Sieber-Blum, M., Epidermal neural crest stem cell (EPI-NCSC)-mediated recovery of sensory function in a mouse model of spinal cord injury. Stem Cell Rev., 2010. **6**: pp. 186-198.
18. Liu, B., Hunter, D.J., Smith, A.A., Chen, S., and Helms, J.A., The capacity of neural crest-derived stem cells for ocular repair. Birth Defects Res. C Embryo Today, 2014. **102**: pp. 299-308.
19. Aoshiba, K., Yasuda, K., Yasui, S., Tamaoki, J., and Nagai, A., Serine proteases increase oxidative stress in lung cells. Am. J. Physiol. Lung Cell Mol. Physiol., 2001. **281**: pp. L556-564.
20. Kim, M.J., Shin, K.S., Jeon, J.H., Lee, D.R., Shim, S.H., Kim, J.K., Cha, D.H., Yoon, T.K., and Kim, G.J., Human chorionic-plate-derived mesenchymal stem cells and Wharton's jelly-derived mesenchymal stem cells: A comparative analysis of their potential as placenta-derived stem cells. Cell Tissue Res., 2011. **346**: pp. 53-64.
21. Strober, W., Trypan blue exclusion test of cell viability. Curr. Protoc. Immunol., 2001. Appendix **3**: pp. Appendix 3B.
22. Beaudoin, G.M., 3rd, Lee, S.H., Singh, D., Yuan, Y., Ng, Y.G., Reichardt, L.F., and Arikkath, J., Culturing pyramidal neurons from the early postnatal mouse hippocampus and cortex. Nat. Protoc., 2012. **7**: pp. 1741-1754.
23. Jarmalaviciute, A., Tunaitis, V., Strainiene, E., Aldonyte, R., Ramanavicius, A., Venalis, A., Magnusson, K.E., and Pivoriunas, A., A new experimental model for neuronal and glial differentiation using stem cells derived from human exfoliated deciduous teeth. J. Mol. Neurosci., 2013. **51**: pp. 307-317.
24. Pacey, L., Stead, S., Gleave, J., Tomczyk, K., and Doering, L., Neural stem cell culture: Neurosphere generation, microscopical analysis and cryopreservation. 2006.
25. Petersen, K. and Pedersen, H.C., *Detection methods*, in *Immunohistochemical staining methods*, C. Taylor, Editor. 2013, DAKO: Denmark. pp. 78–92.
26. Meulemans, D. and Bronner-Fraser, M., Gene-regulatory interactions in neural crest evolution and development. Dev Cell, 2004. **7**: pp. 291-9.
27. Brewer, G.J. and Cotman, C.W., Survival and growth of hippocampal neurons in defined medium at low density: advantages of a sandwich culture technique or low oxygen. Brain Res., 1989. **494**: pp. 65-74.
28. Locher, H., De Rooij, K.E., De Groot, J.C.M.J., van Doorn, R., Gruis, N.A., Lowik, C.W., Chuva de Sousa Lopes, S.M., Frijns, J.H.M., and Huisman, M.A., Class III beta-tubulin, a novel biomarker in the human melanocyte lineage. Differentiation, 2013. **85**: pp. 173-181.
29. Hung, C.H. and Young, T.H., Differences in the effect on neural stem cells of fetal bovine serum in substrate-coated and soluble form. Biomaterials, 2006. **27**: pp. 5901-5908.
30. Moore, R.N., Cherry, J.F., Mathur, V., Cohen, R., Grumet, M., and Moghe, P.V., E-cadherin-expressing feeder cells promote neural lineage restriction of human embryonic stem cells. Stem Cells Dev., 2012. **21**: pp. 30-41.
31. Clewes, O., Narytnyk, A., Gillinder, K.R., Loughney, A.D., Murdoch, A.P., and Sieber-Blum, M., Human epidermal neural

crest stem cells (hEPI-NCSC)-characterization and directed differentiation into osteocytes and melanocytes. Stem Cell Rev., 2011. **7**: pp. 799-814.
32. Djian-Zaouche, J., Campagne, C., Reyes-Gomez, E., Gadin-Czerw, S., Bernex, F., Louise, A., Relaix, F., Buckingham, M., Panthier, J.J., and Aubin-Houzelstein, G., Pax3 (GFP), a new reporter for the melanocyte lineage, highlights novel aspects of PAX3 expression in the skin. Pigment Cell Melanoma Res., 2012. **25**: pp. 545-554.
33. Duggal, S. and Brinchmann, J.E., Importance of serum source for the *in vitro* replicative senescence of human bone marrow derived mesenchymal stem cells. J. Cell Physiol., 2011. **226**: pp. 2908-2915.

Chapter 3

Lentiviral transduction and subsequent loading with nanoparticles do not affect cell viability and proliferation in hair-follicle-bulge-derived stem cells *in vitro*

Contrast Media and Molecular Imaging, 2016

Vol. **11** (6): pp. 550-560

T. Schomann, L. Mezzanotte, I.M. Lourens, J.C.M.J. de Groot, J.H.M. Frijns, M.A. Huisman

Abstract

The application of stem cells in the treatment of various degenerative diseases is highly promising. However, cell-based therapy could be limited by the problem of low viability of grafted cells and uncertainty about their fate. The combination of molecular imaging and contrast-enhanced MRI may give more insight into the survival and behavior of grafted stem cells. We explore hair-follicle-bulge-derived stem cells (HFBSCs) as a potential candidate for autologous cell-based therapy. HFBSCs are transduced with a lentiviral construct with genes coding for bioluminescent (Luc2) and fluorescent (copGFP) reporter proteins, and subsequently loaded with magnetic nanoparticles to enable MRI visualization. Thus, we investigate for the first time if lentiviral transduction and cellular loading with nanoparticles have a cytotoxic effect upon these stem cells. Transduction efficiency, proliferation rate, cell viability and reporter protein co-expression during long-term culture of transduced HFBSCs were studied using fluorescence and bioluminescence microscopy. In addition, the effect of TMSR50 nanoparticles on proliferation and viability was investigated using the MTS assay and bioluminescence microscopy. The amount of TMSR50-loaded HFBSCs needed to reach signal threshold for MRI was assessed using an agarose phantom. Transduction with the Luc2-copGFP construct did not influence senescence, proliferation, doubling time, and differentiation of the HFBSCs. CopGFP expression was visible immediately after transduction and persisted for at least 15 passages, concomitantly with Luc2 expression. Cellular loading with TMSR50 nanoparticles did not affect cell viability and proliferation. The results imply that combined MRI and bioluminescence imaging may enable *in vivo* localization and long-term monitoring of grafted viable HFBSCs.

Introduction

In regenerative medicine, stem cells are a promising therapeutic tool to treat disorders for which no effective treatments are currently available, such as neurocardiovascular, neurodegenerative, hematologic, immunodeficiency diseases and many more [1-6]. Since low post-transplantation survival rates remain a major problem [7], the assessment of the actual effectiveness of cell-based therapy may be limited by the inability to detect and monitor stem cells after engraftment in the living host. Hence, research has focused on *in vivo* visualization of genetically manipulated (transduced) cells and/or cells containing contrast agents (e.g. magnetic nanoparticles) using a variety of imaging modalities including bioluminescence and fluorescence imaging as well as contrast-enhanced magnetic resonance imaging (MRI). Longitudinal preclinical investigation regarding the cytotoxic effects of genetic manipulation and/or nanoparticle-loading of the stem cells is therefore a prerequisite.

Bioluminescence imaging makes use of firefly or click beetle luciferases which enzymatically convert the substrate D-luciferin into oxyluciferin, resulting in a bioluminescent signal emitting at a wavelength of 425–550 nm [8-10]. Importantly, bioluminescence imaging allows the monitoring of living cells due to the requirement of O_2 and ATP. Since light in this range (blue to green) is particularly well-absorbed by tissue chromophores, such as (oxy-)hemoglobin, melanin and cytochromes, these wildtype luciferases have limited value for in vivo imaging applications [11, 12]. The codon-optimized firefly luciferase Luc2, however, is a good alternative. It couples a high photon flux at its emission peak of 560 nm (at 25 °C) with a thermally induced shift in wavelength (610 nm at 37 °C) – which is beyond the light absorption spectrum of mammalian tissue – and, hence, rendering it a valuable tool for in vivo bioluminescence imaging [13].

An alternative approach is to monitor cells by means of fluorescence imaging using naturally occurring fluorescent proteins, such as green fluorescent protein (GFP) and its numerous variants [14-17]. One of these is copepod green fluorescent protein (copGFP), which occurs in marine planktonic crustaceans belonging to the copepod families Pontellidae and Aetideidae [18, 19]. One of the advantages of copGFP (λ_{ex}: 482 nm, λ_{em}: 502 nm) is that it can be detected in copGFP-expressing cells during cell culture and in histological sections using conventional fluorescence microscopy. In addition, it demonstrates a high fluorescence quantum yield, is more stable at a

wide range of temperatures (including 37 °C, i.e. mammalian body temperature), and features faster folding and faster post-translational maturation rates resulting in rapid availability of the protein after transduction [20].

Bioluminescence and fluorescence imaging, however, do not provide detailed anatomical information. In contrast, MRI of transduced cells loaded with contrast-enhancing nanoparticles allows in vivo monitoring of their exact location and migration within the host after engraftment [21-24]. Recently, multimodal imaging probes that facilitate visualization by means of fluorescence imaging and microscopy as well as MRI have been developed.

NEO-STEM™ TMSR50 nanoparticles are such dual probes, consisting of a magnetic cobalt-ferrite core surrounded by a degradation-resistant silica shell containing the red-fluorescent (625 nm) dye rhodamine B isothiocyanate [25, 26]. TMSR50 nanoparticles are biocompatible with adenocarcinomic A549 cells and human umbilical-cord-blood-derived mesenchymal stem cells [25, 27, 28], but their biocompatibility has not been verified for stem cells from other sources, such as hair-follicle-bulge-derived stem cells (HFBSCs). These stem cells originate from the neural crest [29] and are a promising source of non-embryonic stem cells to be used in autologous cell-based therapy, by virtue of their broad regenerative potential and non-oncogenic properties as well as the fact that they are relatively easy to harvest [30-33].

The present study was designed to test in detail if lentiviral transduction followed by nanoparticle loading have a cytotoxic effect upon HFBSCs intended for grafting. The aim of this study was to get an understanding of the usability of bioluminescence and fluorescence imaging and MRI, in order to visualize and longitudinally monitor viable HFBSCs within live animals after engraftment. Therefore, HFBSCs were transduced with a lentiviral dual-reporter gene construct containing genes that code for Luc2 and copGFP, which are expressed at an equimolar ratio [34], and subsequently loaded with TMSR50 nanoparticles. This allows verification of transduction efficiency and monitoring of the persistence of reporter molecules during culture. Since a possible cytotoxic effect of lentiviral transduction and cellular loading with nanoparticles cannot be excluded [35-37], we have investigated whether or not these treatments affect the proliferation rate, doubling time, cellular senescence, apoptotic pathways and long-term viability of HFBSCs.

Results

Transduced HFBSCs demonstrate stable co-expression of reporter molecules

Expression of the bioluminescent (Luc2) and the fluorescent reporter molecule (copGFP) was monitored over several passages. Expression of copGFP was observed at all selected time points, starting immediately after transduction (P1) and persisting up to P15 (Fig. 1). The majority of targeted cells expressed a green-fluorescent signal (mean ± SEM: 83.6 ± 8.2%).

Transduced HFBSCs stably co-express both reporter molecules as bioluminescence microscopy demonstrated that after addition of D-luciferin a bioluminescent signal indicative of Luc2 activity could be recorded at high passages after transduction (P10 and P15; Fig. 1).

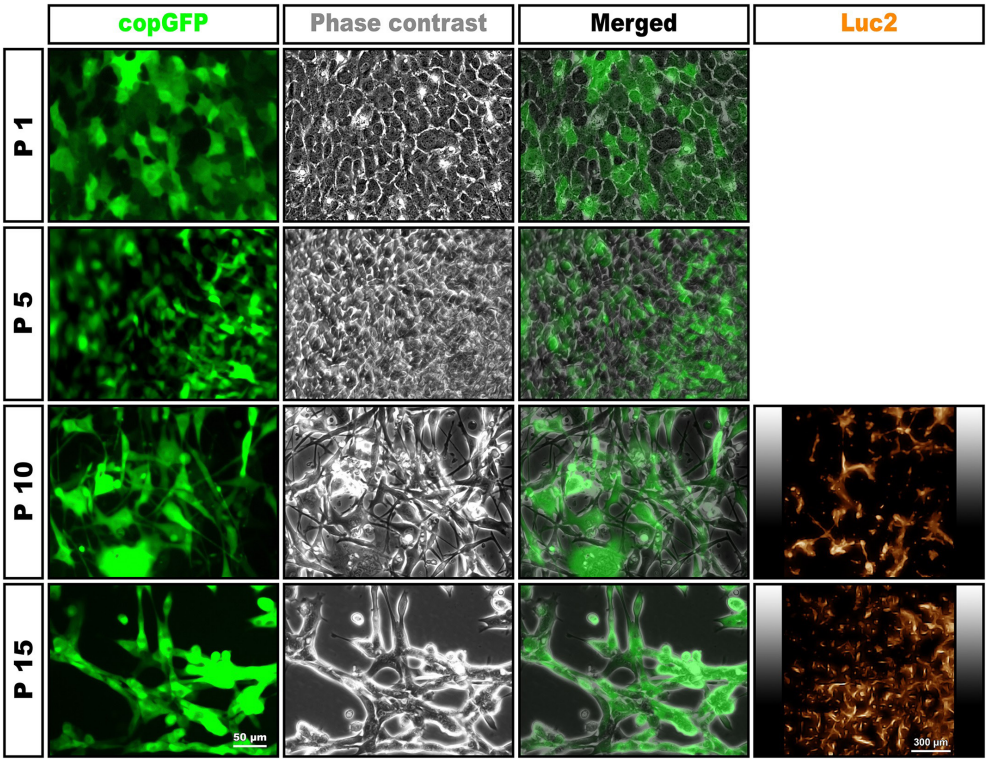

Fig. 1: Stable co-expression of copGFP and Luc2. After lentiviral transduction with the Luc2-copGFP reporter gene construct, the majority of cells exhibit green fluorescence indicating copGFP expression. The fluorescent signal persists for at least 15 passages (P15). Addition of D-luciferin results in a bioluminescent signal due to luciferase activity at P10 and P15, confirming co-expression of Luc2. Scale bar = 50 µm (copGFP, phase contrast, and merged images) or 300 µm (Luc2 images).

Transduction does not inhibit HFBSC proliferation

The proliferation rates of transduced HFBSCs and non-transduced control cells were compared at 1 day, 2 and 3 days (Fig. 2A). Data analysis shows that proliferation curves for the transduced and control cells do not differ in a statistically significant way (p = 0.921, two-tailed, unpaired *t*-test, 95% confidence interval, n = 12 per data point).

The doubling time averages 36.5 ± 3.9 hours for transduced cells and 37.3 ± 6.7 hours for control cells (Fig. 2B), but this difference is statistically not significant (p = 0.894, two-tailed, unpaired *t*-test, 95% confidence interval, n = 9).

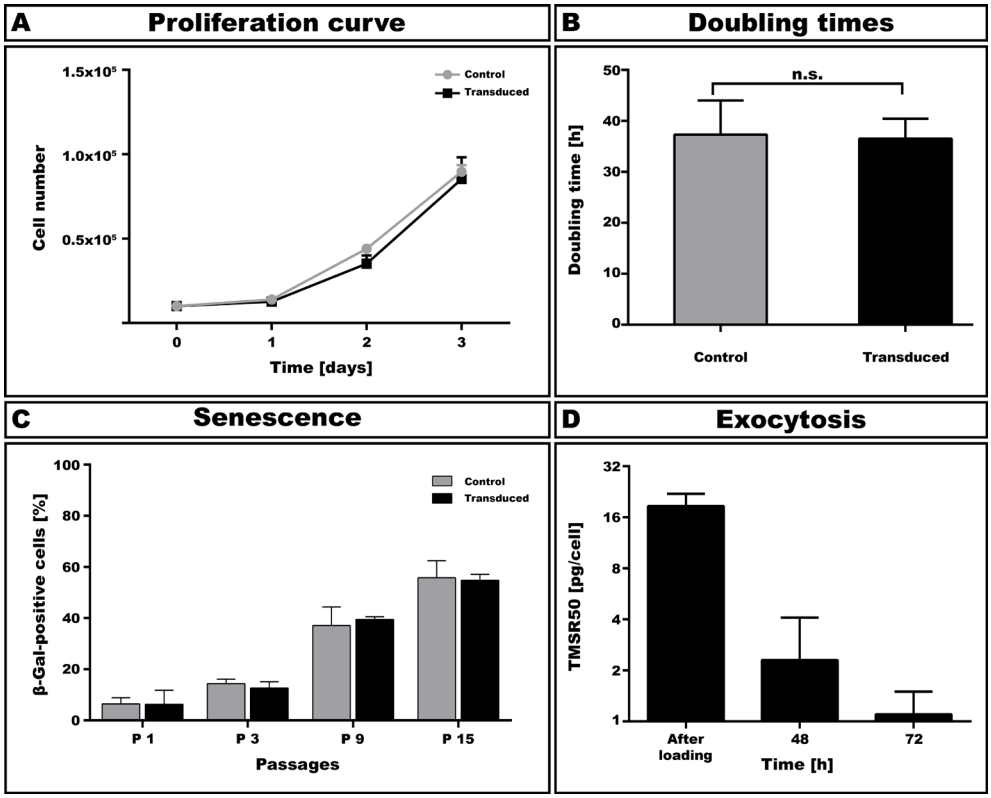

Fig. 2: Transduction does not interfere with HFBSC proliferation and senescence. **A:** The proliferation rate of transduced HFBSCs does not significantly differ from that of non-transduced (control) cells after 1 day, 2 and 3 days (error bars: standard error of the means, SEM). **B:** Comparison of the doubling times of transduced and control cells does not reveal statistically significant differences (error bars: SEM). **C:** Enzyme histochemical staining for lysosomal β-galactosidase reveals that transduced and control cells become senescent alike. The percentage of blue-stained cells increases stably over 15 passages for both the control and transduced cells (error bars: SEM). **D:** Exocytosis and retention of nanoparticles per cell over time reveals robust decrease in TMSR50 concentration per cell within 48 hours. As shown, the concentration of nanoparticles within each cells decreased slightly at 72 hours. At 96 hours after loading, exocytosis of TMSR50 nanoparticles by the cells into the medium was below detectable threshold.

Exocytosis and retention of TMSR50 nanoparticles in transduced HFBSCs

Exocytosis of nanoparticles was followed after loading of transduced HFBSCs. Red fluorescence of TMSR50 nanoparticles in medium was measured directly after loading, 48 hours and 72 hours after loading. Directly after loading, supernatant contained 0.1905 ± 0.0112 mg/ml TMSR50 (Fig. 2D). The nanoparticle concentration in medium was 0.0041± 0.0016 mg/ml after 48 hours and 0.0004 ± 0.0007 mg/ml after 72 hours. At later time points, no fluorescence could be measured.

Knowing the amount of initially seeded cells and the doubling time of 36.5 hours, we were able to calculate the average concentration of uptaken nanoparticles. Directly after loading cells contained 18.6 ± 3.4 pg/cell, while after 48 hours and 72 hours they contained 2.3 ± 1.8 pg/cell and 1.1 ± 0.5 pg/cell, respectively. At 96 hours after loading, fluorescence of exocytosed TMSR50 nanoparticles in the medium was below detectable threshold.

Intracellular retention of nanoparticles was followed in transduced HFBSCs at two different densities (1.0×10^4 and 7.5×10^4 cells/well) over a subsequent period of 7 days. After 1 day, all cells showed red fluorescence indicative of intracellular accumulations of TMSR50 nanoparticles (Fig. 3A–B). Merged images indicate that copGFP and TMSR50 nanoparticles co-exist in the cells. Phase contrast images reveal that the cells remain a normal morphology throughout the 7-day period of observation. Three days after loading, a considerable loss of the red-fluorescent signal was observed in cultures seeded at a density of 1.0×10^4 cells/well (Fig. 3C), whereas cells seeded at 7.5×10^4 cells/well did retain a strong red-fluorescent signal (Fig. 3D). After seven days, the red-fluorescent signal had declined for both densities (Fig. 3E–F), although the cells seeded at 7.5×10^4 cells/well demonstrated a higher signal.

TMSR50 nanoparticles do not induce apoptosis-related caspase activity

We investigated the possible cytotoxic effect of the TMSR50 nanoparticles upon transduced HFBSCs by monitoring caspase-3/7 and caspase-9 activities during the initial 24 hours of cell loading with TMSR50 nanoparticles (Fig. 4A). Caspase-3/7 and caspase-9 activities in TMSR50-loaded cells were not different in a statistically

significant way from those in non-loaded transduced cells (caspase-3/7: p = 0.072, caspase-9: p = 0.699; two-tailed, paired *t*-tests, 95% confidence interval, n = 6). These results demonstrate that TMSR50 nanoparticles do not activate caspase-3/7-mediated or caspase-9-mediated apoptosis in HFBSCs.

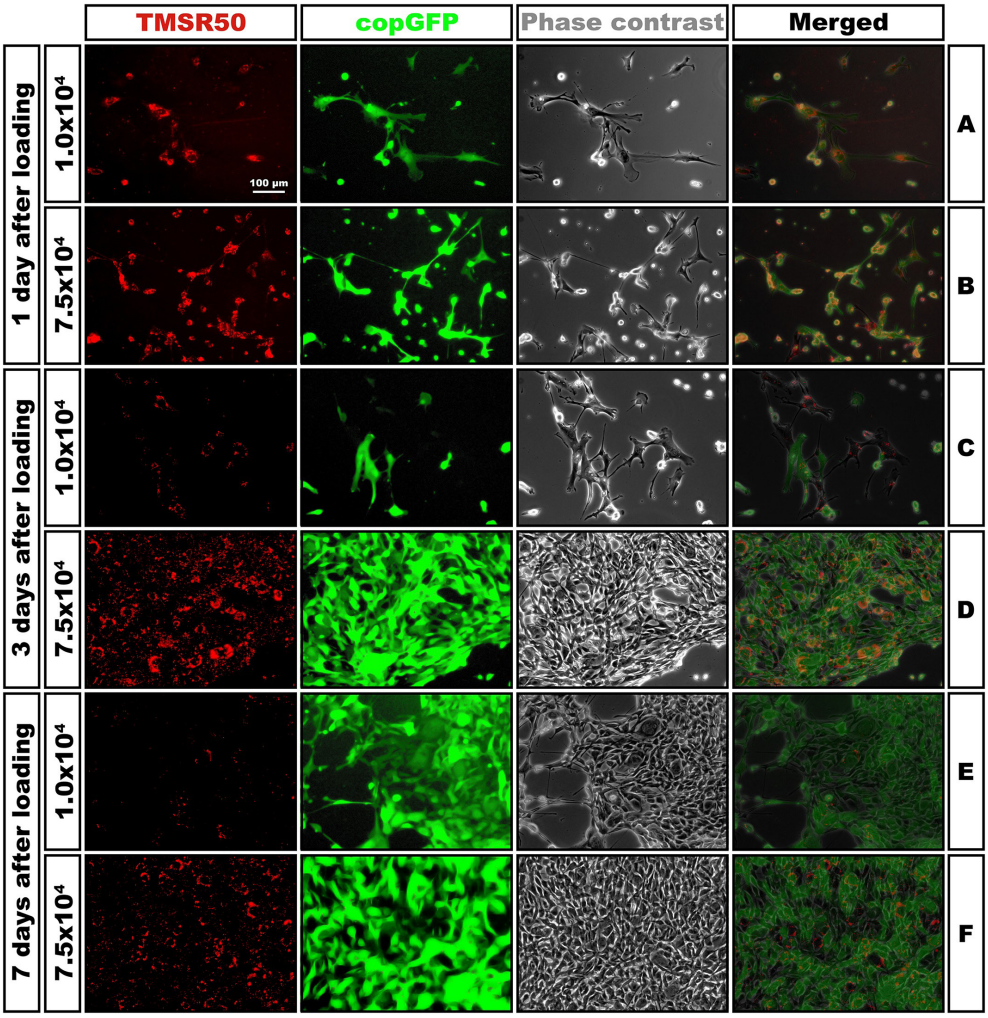

Fig. 3: Intracellular retention of TMSR50 nanoparticles in transduced HFBSCs. Intracellular retention of red-fluorescent TMSR50 nanoparticles was monitored in transduced HFBSCs at seeding densities of 1 × 10^4 (**A**, **C**, **E**) and 7.5 × 10^4 cells/well (**B**, **D**, **F**) for up to seven days. From the merged images it is evident that copGFP and TMSR50 co-exist in the cells. Loss of red fluorescence was observed in cultures at 1 × 10^4 cells/well after three and seven days (**C**, **E**). Red-fluorescent signal was retained in cultures seeded at 7.5 × 10^4 cells/well for up to seven days (**D**, **F**). Scale bar = 100 µm.

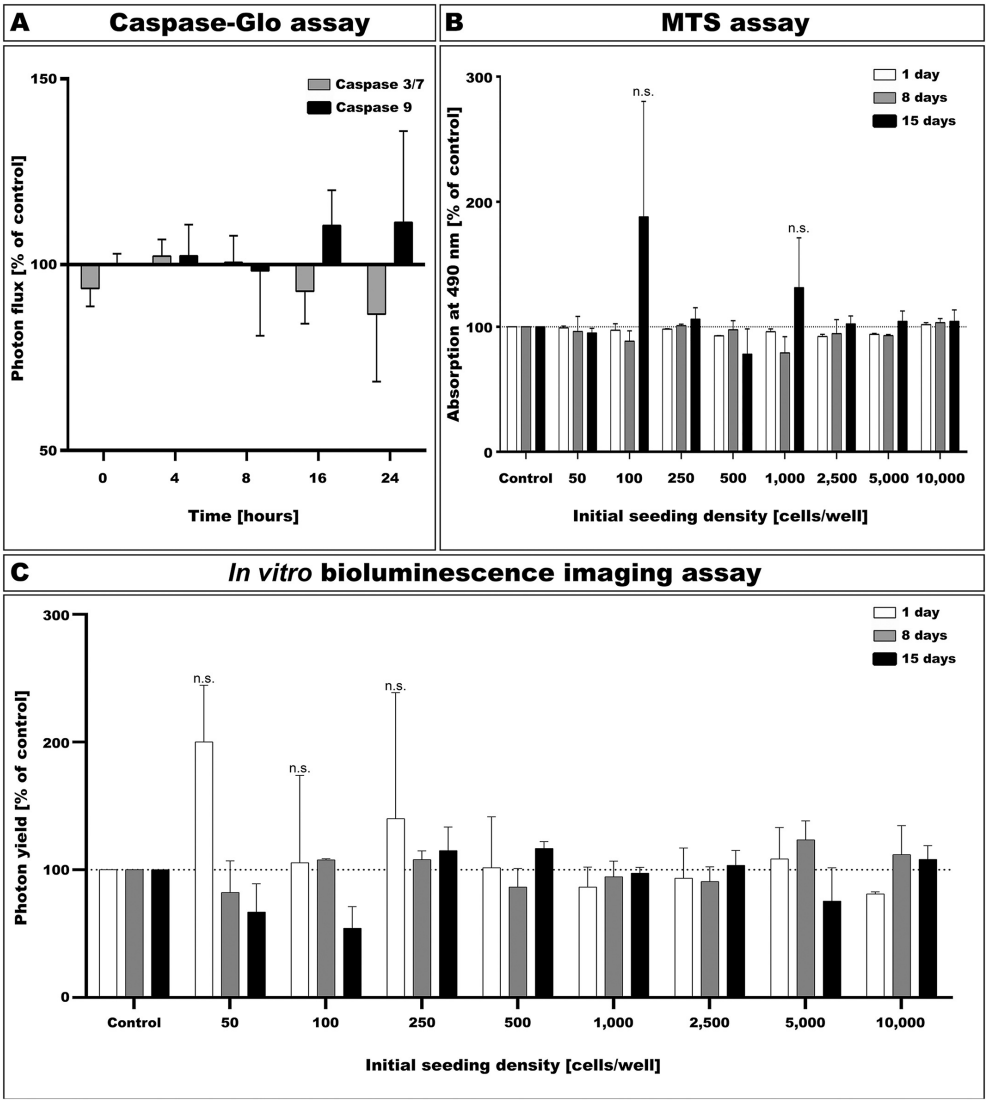

Fig. 4: TMSR50 nanoparticles do not reduce HFBSC viability. **A:** Loading with TMSR50 nanoparticles does not result in significant increases in caspase-3/7 or caspase-9 activities in HFBSCs over a period of up to 24 hours. Bioluminescence of the cells is expressed as a percentage of the photon flux normalized to that of non-loaded transduced cells (100% line; error bars: SEM). **B:** MTS assay demonstrates that viability of transduced HFBSCs is not significantly reduced by TMSR50 nanoparticles after one day or after eight and 15 days. Data are expressed as percentage of absorption at 490 nm and normalized to that of non-loaded transduced cells (control: dotted line; error bars: SEM). **C:** Results with *in vitro* bioluminescence imaging are similar to those obtained with the MTS assay. Data are expressed as percentage of photon yield normalized to the non-loaded transduced cells (control: dotted line; error bars: SEM).

Intracellular TMSR50 nanoparticles do not reduce HFBSC viability

Viability of transduced HFBSCs loaded with TMSR50 nanoparticles was investigated at different densities (range: 0.5×10^2 thru 1.0×10^4 cells/well) over a period of 15 days using the MTS assay and *in vitro* bioluminescence imaging.

Statistical analysis of the data obtained with the MTS assay (Fig. 4B) could not demonstrate any statistically significant changes between the different cell densities as compared to non-loaded transduced HFBSCs, not even after prolonged incubation for up to 15 days ($p = 0.379$, 3-way ANOVA, one-sample *t*-test, 95% confidence interval, n = 6 per data point).

Fig. 4C graphs the normalized data after bioluminescence imaging for the different densities of transduced HFBSCs loaded with TMSR50 nanoparticles. Similar to the MTS data, no statistically significant differences could be observed ($p = 0.531$, 3-way ANOVA, one-sample *t*-test, 95% confidence interval; error bars: SEM, n = 6 per data point).

TMSR50-loaded and non-loaded HFBSCs differentiate alike

Following the differentiation protocol established by Gho *et al*. [38], different neuron-like cells with elongated, branched projections developed over time (Fig. 5). In comparison, no differences were observed regarding the differentiation potential between TMSR50-loaded and non-loaded HFBSCs regarding their morphology. While all cells contain nanoparticles after differentiation (e.g. Fig. 5, arrowhead), not all cells are transduced. However, differentiated transduced cells were also loaded with TMSR50 nanoparticles as indicated by red fluorescence (Fig. 5, circle).

MRI of agarose-embedded TMSR50-loaded HFBSCs

Transduced HFBSCs loaded with TMSR50 nanoparticles were embedded in a multi-layered agarose phantom containing a cell gradient (1.0×10^6, 1.0×10^5, 1.0×10^4, and 1.0×10^3 cells/layer) and investigated using *in vitro* fluorescence imaging and MRI.

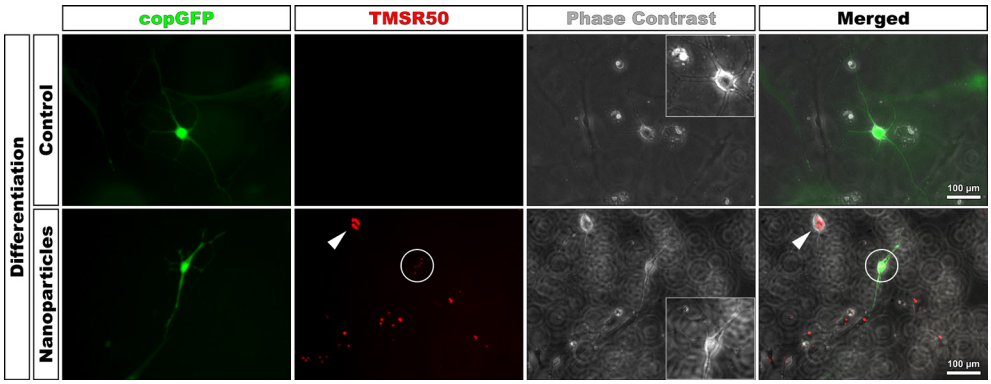

Fig. 5: TMSR50-loaded and non-loaded HFBSCs differentiate alike. Non-loaded (control) and TMSR50-loaded (nanoparticles) HFBSCs were differentiated. After differentiation, both groups developed the same morphologies. The neuronal differentiation process occurred similarly in cells with and without nanoparticles. In both cultures the cells formed networks (see magnified phase contrast). While no red fluorescence was observed in control cells, TMSR50-loaded cells contain red-fluorescent nanoparticles. Scale bar = 100 µm.

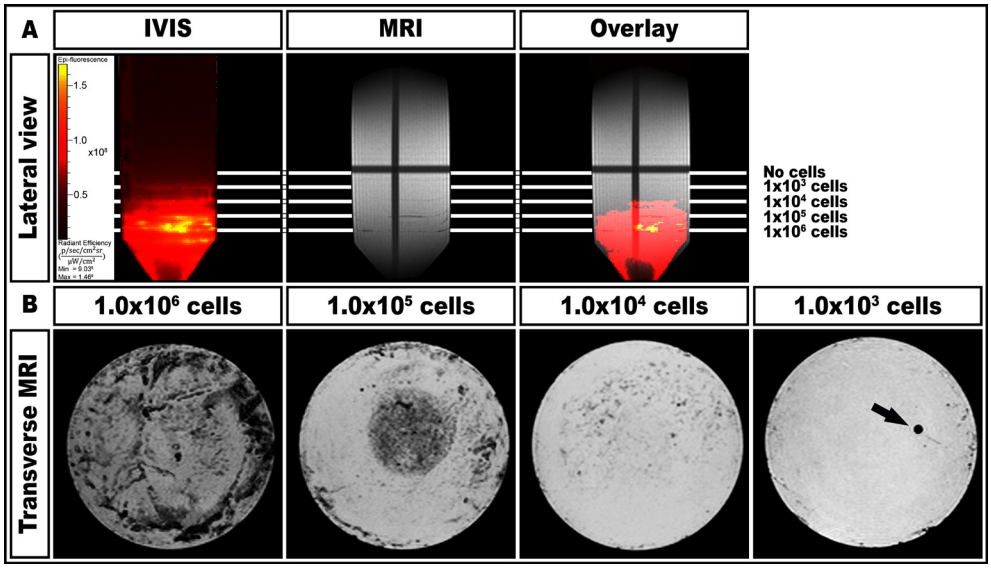

Fig. 6: Visualization of different amounts of TMSR50-loaded HFBSCs. **A:** Images (lateral view) of the 0.5% agarose phantom show layers containing different amounts of TMSR50-loaded HFBSCs (1×10^3 to 1×10^6 cells/layer). Left image: cells visualized by epi-fluorescence imaging with the IVIS® Spectrum multimodal imaging system (min = 9.036, max = 1.468); middle image: cells visualized by contrast-enhanced MRI; and right image: overlay of both. With fluorescence imaging a signal emerges from all cell-containing layers. The layer without TMRS50-loaded HFBSCs does not exhibit fluorescence. MRI displays three distinct layers (1×10^6, 1×10^5 and 1×10^4 cells/layer). The layer containing 1×10^3 cells does not yield sufficient contrast, nor does the layer without cells. **B:** Transverse MRI view of the phantom layers containing TMSR50-loaded HFBSCs. For each image, three consecutive transverse MRI slices of the respective layers were merged. The layers containing 1×10^5 cells and, especially, 1×10^6 cells were clearly above the detection limit, whereas 1×10^4 cells only gave faint contrast. While 1×10^3 cells/layer could be visualized by fluorescence imaging, this amount revealed few hypointense spots (apart from an air bubble right from the center: arrow) at the periphery of the agarose phantom using MRI.

Fluorescence imaging revealed a strong, red-fluorescent signal in the layers containing 1.0×10^6 and 1.0×10^5 cells, whereas the intensity of the signal was distinctly visible in the layers with 1.0×10^4 and 1.0×10^3 cells (Fig. 6A, IVIS).

The agarose phantom was also subjected to MRI and in the lateral view the layers containing 1.0×10^6, 1.0×10^5 and 1.0×10^4 cells show sufficient contrast to allow visualization of the different cell layers (Fig. 6A, MRI). In the transverse view of the MRI (Fig. 6B), the layers containing the higher amounts of cells (1.0×10^6 and 1.0×10^5, respectively) showed clear hypointense spots, whereas the layer with 1.0×10^4 cells was only faintly visible. The layer containing 1.0×10^3 cells shows few hypointense spots at the periphery of the phantom.

Autofluorescence or false-positive MRI signal can be ruled out for the imaged layers, since the layer without cells did not give any signal, either with IVIS or with MRI (Fig. 6A).

Discussion

In this study, we demonstrated that the stem cell population derived from the hair follicle bulge of mouse whisker pads can be stably transduced with the Luc2-copGFP reporter gene construct using a lentiviral vector, allowing fluorescence and bioluminescence imaging. In addition, cells retained the ability to express these reporter molecules after cryopreservation. Furthermore, cells can be efficiently loaded with TMSR50 nanoparticles enabling visualization in an agarose phantom using contrast-enhanced MRI indicating suitability for longitudinal preclinical studies *in vivo*.

The stable integration of the lentiviral construct within the genome of the HFBSCs was evidenced by equimolar co-expression of Luc2 and copGFP for at least 15 passages after transduction. Unlike previous studies [35-37], we did not observe any effect of the transduction upon cell morphology, proliferation, including doubling times, and degree of senescence during these long-term cultures. This discrepancy could be explained by the use of different (stem) cell types. In our study, we have used HFBSCs, whereas in the other papers other cell types and cell lines have been used, such as fibroblasts [32], neuroblastoma cells [35] and mesenchymal stem cells [36]. Alternative explanations could be the use of different GFP variants (GFP versus copGFP) and different viral transduction methods.

After excluding possible inhibitory effects of viral transduction with Luc2-copGFP, we investigated if additional loading with silica-coated nanoparticles triggers the apoptosis-related caspase-3/7 or caspase-9 pathways, as reported previously by Kai *et al*. [39]. Our results have shown that neither caspase-3/7 nor caspase-9 activities are significantly increased when compared to control cells within 24 hours, not even in the first 8 hours after the start of the loading procedure.

Also, we investigated uptake and exocytosis of TMSR50 nanoparticles by HFBSCs. We found that the initial concentration of nanoparticles is in average 18.6 pg/cell and steeply decreases in the following 48 hours. However, the amount of exocytosed nanoparticles stabilized thereafter. After this the amount of exocytosed nanoparticles is not measurable anymore, making cell proliferation the main factor for decrease of nanoparticle concentration in the cells.

In addition, we checked if TMSR50 nanoparticles persist in transduced HFBSCs during 7-day culturing, by monitoring the cell cultures with *in vitro* fluorescence microscopy. After 3 days, cultures containing 1.0×10^4 cells demonstrated slightly less red fluorescence than the cultures containing 7.5×10^4 cells. The 7-day cultures with 7.5×10^4 cells demonstrated a distinct red-fluorescent signal, while the corresponding culture with 1.0×10^4 cells revealed only a faint signal. It is generally known from pulse-chase studies that the amount of intracellular nanoparticles decreases due to dilution during proliferation. In addition, the total amount of nanoparticles in the culture containing 1.0×10^4 cells further decreases due to exocytosis and subsequent medium changes and this explains the pronounced reduction of fluorescent signal in these cultures as compared to the ones containing 7.5×10^4 cells. Therefore, future *in vitro* and *in vivo* nanoparticle-loading experiments should be done at relatively high seeding densities. Our results further indicate that MRI of TMSR50-loaded stem cells needs to be performed within seven days after transplantation, although Kallur *et al*. showed longer *in vivo* retention using different cells and nanoparticles [24]. It should be noted that there are more sensitive methods to detect iron oxide-loaded cells than the method described in this report. It has recently been shown that it is even possible to detect a small number of cells or even single cells, such as Kircher *et al*. following injection of nanoparticle-loaded sensitized T cells to tumor antigens [40]. Furthermore, Foster-Gareau *et al*. showed that single cells loaded with iron oxide nanoparticles could be imaged with a 1.5 T clinical scanner [41]. The sensitivity of detection in vivo depends on many factors, such as hardware, resolution of acquired images, the type of cell and its uptake of iron-oxide nanoparticles. However, we have chosen to perform a feasibility study to combine of Luc2-copGFP-transduced cells with fluorescent, magnetic nanoparticles because the technique is easy, does not require transfection reagents and the detection limit is sufficient for our future *in vivo* experiments. We, like many others, will transplant $>1 \times 10^6$ cells and if only 1% of these cells survive we will still be able to visualize them by means of MRI as demonstrated by Yeum *et al*. [42]. Taking these factors into account, our next goal was to investigate if these nanoparticles negatively affect HFBSC viability in long-term cultures. Statistically, there were no significant differences in viability between nanoparticle-loaded transduced cells and the respective control cells. Three-way ANOVA did not reveal any statistically significant differences between the various virus batches used (data not shown), the different initial seeding densities, and the different individual mice (data not shown), nor did we find differences due to duration of the culture period. Therefore, we pooled all data and performed a one-sample

t-test, which confirmed that the observed outliers in MTS assay and BLI assay are not statistically significant. In contrast to previous studies on the cytotoxic effects of nanoparticles [43, 44], the silica-coated TMSR50 nanoparticles used in this study do not affect HFBSC viability in the short run as well as on the long term. Our finding that amounts as low as 1×10^4 nanoparticle-loaded HFBSCs can be visualized in an agarose phantom indicates that engrafted HFBSCs may be visualized and monitored *in vivo* by means of contrast-enhanced MRI.

In order to longitudinally monitor viable HFBSCs *in vivo*, bioluminescence imaging and MRI represent viable tools for non-invasive visualization after engraftment. These techniques enable exact localization of grafted cells in the living animal in combination with long-term monitoring of their survival and fate. Our group intends to apply BLI and MRI to non-invasively monitor grafted stem cells and longitudinally follow their survival and fate in the cochleas of deafened animals.

Conclusion

We conclude that HFBSCs can be efficiently and stably transduced with the Luc2-copGFP construct, followed by subsequent nanoparticle loading, without affecting cell viability, proliferation and differentiation. This implies that a combined approach using bioluminescence imaging and MRI may enable *in vivo* localization of grafted cells. This multimodal visualization system makes it feasible to monitor transplanted stem cells and simultaneously obtain anatomical information.

Experimental

Animals

Healthy wildtype mice (C57Bl/6) were bred and housed in the Central Animal Facility of Leiden University Medical Center (LUMC). Male and female surplus animals (n = 7) of varying age served as a source for whisker pads, from which HFBSCs were isolated. The use of the animals was approved by the LUMC Animal Experiments Committee (DEC permit 10172).

Animal care and handling was in accordance with the guidelines and regulations as stipulated by the Dutch Experiments on Animals Act (WoD) and the European Directive on the Protection of Animals Used for Scientific Purposes (2010/63/EU).

Culture of hair follicle bulge explants

Hair follicles were dissected out from the whisker pads and the bulge region was excised as previously described [45, 38].

Cell-culture-treated 12-well plates (TPP Techno Plastic Products AG, Trasadingen, Austria) were coated with poly-D-lysine (PDL; Sigma-Aldrich, St. Louis, MO, USA; 0.01 mg/ml in distilled water) at 37°C for 30 minutes. After drying, plates were rehydrated with basic growth medium (BGM) at 37°C for 30 minutes. BGM consists of DMEM/Ham's F-12 1:1 (Biochrom AG, Berlin, Germany), 1% GlutaMax™ (100x; Gibco, Bleiswijk, The Netherlands) and 1% antibiotic/antimycotic solution (100x; Sigma-Aldrich) supplemented with 10% fetal bovine serum (FBS; Gibco), 2% B-27® supplement without vitamin A (50x; Gibco), 1% N-2 MAX media supplement (100x; R&D Systems™, Minneapolis, MN, USA), recombinant human basic fibroblast growth factor (20 ng/mL; R&D Systems), and recombinant human epidermal growth factor (20 ng/mL; R&D Systems).

After rehydration, medium was discarded and in each well one hair follicle bulge explant was placed. To prevent drying, a 20-µL drop of BGM was gently placed on top of the explants, which were then allowed to adhere to the bottom of the well in a humidified incubator at 37°C and 5% CO_2. After 60 minutes, another 20-µL drop

of BGM was carefully added to the moist explants, followed by adding 500 µL of the same medium to each well after another 60 minutes. Plates were incubated in a humidified incubator at 37°C and 5% CO_2 and, after four days, the cultures were examined on a daily basis to detect any outgrowth of cells from the explants. At the first sign of cell outgrowth, the medium was replaced with fresh medium followed by removal of the explants after three days.

Passaging and cryopreservation of HFBSCs

HFBSCs were continuously cultured until 70-80% confluence for each passage [38]. After each passage and proliferation cycle, the cells were washed with phosphate-buffered saline (PBS) and treated with a pre-warmed (37°C) balanced salt solution containing 0.05% trypsin and 0.02% EDTA.4Na (Gibco), for exactly two minutes. After centrifugation, the cells were counted and seeded at a proliferation density of approximately 2.5 × 10^3 cells/cm^2 in PDL-coated cell-culture-treated plates. Passaged cells were processed either directly for transduction or frozen and stored.

Prior to cryopreservation, cells were centrifuged and the pellet was resuspended in FBS (Gibco) containing 10% dimethyl sulfoxide (Sigma-Aldrich) at a concentration of 1 × 10^6 cells/mL and immediately frozen. The vitrified samples were stored either at -80°C for short periods of time or in liquid nitrogen for long-term storage. Prior to use, the vitrified samples were thawed in a water bath (37°C) followed by dilution in an excess volume of BGM.

Lentiviral transduction with the Luc2-copGFP reporter gene construct

HFBSCs were genetically engineered by genomic integration of the Luc2-copGFP reporter gene construct using lentiviral transduction. Vector production and transduction procedures have been described in detail previously [34]. We have used the third-generation lentiviral vector pCDH-EF1-MCS-T2A-copGFP (SBI System Biosciences, Mountain View, CA, USA) containing the elongation factor 1α (EF1α) promoter and the T2A sequences, resulting in equimolar expression of the Luc2 and copGFP genes. Lentiviral particles were produced by transfection of HEK-293 T packaging cells with three packaging plasmids (pCMV-VSVG, pMDLg-RRE, pRSV-

REV; Addgene, Cambridge, MA, USA) and the lentiviral vector plasmid. Supernatant containing lentiviral particles were collected after 48 and 72 hours. Subsequent quantification of virus was performed using a standard antigen-capture HIV p24 ELISA (ZeptoMetrix Corporation, NY, USA). Vector production and cell transduction were performed under appropriate biosafety level conditions (ML-II) in accordance with the National Biosafety Guidelines and Regulations for Research on Genetically Modified Organisms. Procedures and protocols were reviewed and approved by the LUMC Biosafety Committee (GMO permit 08-129).

HFBSCs were seeded in PDL-coated 12-well plates at a cell density of 2.5×10^4 cells/well and maintained in a humidified incubator at 37°C and 5% CO_2. After attachment was accomplished, the cells were transduced using a MOI (multiplicity of infection) of 10. HFBSC transduction was performed under appropriate biosafety level conditions (ML-II) in accordance with the National Biosafety Guidelines and Regulations for Research on Genetically Modified Organisms. Procedures and protocols were reviewed and approved by the LUMC Biosafety Committee (GMO permit 08-129).

Light microscopical detection of Luc2 and copGFP co-expression

Luc2 expression in transduced HFBSCs was assessed in real time using a purpose-built bioluminescence microscope, at P10 and P15. D-luciferin (potassium salt; Synchem, Felsberg, Germany) was added at a final concentration of 0.1 mM. The bioluminescent signal was recorded for 15 minutes and digital images were acquired using Image-Pro® Plus software, followed by conversion of the grayscale images into pseudocolor images.

Cellular copGFP expression was examined immediately following transduction (P1) and at P5, P10 and P15 using an Olympus IX70 fluorescence microscope (FITC filter settings) equipped with a Leica DFC340 FX digital camera. Digital images were acquired and stored using Leica Application Suite Advanced Fluorescence (LAS AF) software (version 1.9.0). All images were subsequently processed using Adobe® Photoshop® CS6 Extended software (version 13.0 x64).

Proliferation curve

To determine if transduction inhibits cell division and growth, the proliferation rate and doubling time of transduced cells were compared with those of non-transduced control cells during the same passage. Cells were seeded at a density of 1×10^4 cells/well in a PDL-coated 12-well plate and counted after 1 day, 2 and 3 days, using a Luna™ automated cell counter (Logos Biosystems, Anyang City, South Korea). The data were statistically analyzed and plotted in graphs using GraphPad Prism version 6.02 software (GraphPad Software, La Jolla, CA, USA).

Senescence assay

To verify if transduction results in cell immortalization or senescence, the proportion of senescent cells in cultures of transduced HFBSCs was determined using the Senescence Cells Histochemical Staining Kit (Sigma-Aldrich), which is based upon histochemical detection of senescence-associated lysosomal β-galactosidase activity. The assay was performed according to the manufacturer's guidelines.

Cells from P1 (directly after transduction), P3, P9 and P15 were seeded at a density of 1×10^4 cells/well in PDL-coated 12-well plates and allowed to attach. After 24 hours, medium was aspirated and cells were washed twice with PBS and fixed in 2% formaldehyde and 0.2% glutaraldehyde in PBS at room temperature for 7 minutes. Next, the cells were rinsed thrice with PBS and incubated in staining solution at pH 6.0 and 37°C for 24 hours, after which it was replaced with PBS. The staining solution contained 5-bromo-4-chloro-3-indolyl-β-D-galactopyranoside (X-gal; 1 mg/mL). Cells expressing β-galactosidase activity (blue staining) as well as the total number of cells were counted, and the percentage of senescent cells was calculated.

Loading of HFBSCs with NEO-STEM™ TMSR50 nanoparticles

Transduced HFBSCs were loaded with NEO-STEM™ TMSR50 nanoparticles (Biterials, Seoul, South Korea) according to the manufacturer's protocol. Nanoparticles were concentrated by centrifugation (12,700×*g*, 10 minutes), dispersed in BGM solution at a concentration of 0.2 mg/mL and, then, sonicated in a bath-type sonicator

(30 kHz, 10 minutes) in order to prevent particle aggregation.

Cells were seeded in PDL-coated 12-well plates at densities of 1×10^4 and 7.5×10^4 cells/well, and incubated with the suspension of TMSR50 nanoparticles for 24 hours, followed by washing with PBS three times and adding fresh pre-warmed (37°C) BGM solution. To investigate the amount of exocytosed nanoparticles over time, medium was collected directly after loading, after 48 hours, 72 hours and 96 hours. Levels of red fluorescence were measured using the SpectraMax Gemini microplate reader (λ_{ex}: 544 nm; λ_{em}: 590 nm; Molecular Devices, Sunnyvale, CA, USA) and analyzed by comparison to a calibration curve.

For prolonged retention, cells were cultured for 7 days, and on alternate days half of the medium was replaced with fresh pre-warmed medium. The cells were examined after 1 day, 3 and 7 days for red fluorescence, due to the rhodamine B isothiocyanate dye from the TMSR50 nanoparticles, with an Olympus IX70 fluorescence microscope (Cy3 filter settings). Images were acquired and digitally stored using LAS AF software. All images were processed using Adobe® Photoshop® CS6 Extended software (version13.0 x64).

Bioluminescent caspase activity assays

To exclude that TMSR50 nanoparticles induce apoptosis in transduced HFBSCs, caspase-3/7 and caspase-9 activities were determined using the Caspase-Glo® 3/7 and Caspase-Glo® 9 bioluminescence-based assay kits, respectively (Promega Corporation, Madison, WI, USA). The assays were performed according to the manufacturer's guidelines with slight modifications.

After centrifugation, transduced HFBSCs were resuspended in BGM containing TMSR50 nanoparticles (0.2 mg/mL) and seeded at a density of 5×10^3 cells/well in a PDL-coated black-walled 96-well microplate (Greiner Bio-One, Kremsmünster, Austria) and allowed to attach for 30 minutes followed by incubation with the respective Caspase-Glo® substrates (caspase-3/7: Z-DEVD-aminoluciferin; caspase-9: Z-LEHD-aminoluciferin) according to the manufacturer's instructions. Bioluminescence was measured directly after seeding and after 4, 8, 16, and 24 hours. Images were acquired for 30 seconds using an IVIS® Spectrum multimodal

imaging system (PerkinElmer, Waltham, MA, USA) with the following settings: open filter, field of view (FOV) C (default setting), f/stop = 1, and medium binning. Image acquisition and analysis were performed with Living Image® version 3.1 software (PerkinElmer). A linear mixed model was fitted to compensate for missing values using SPSS Statistics version 20.0.0.1 software (IBM Corporation, Armonk, NY, USA). GraphPad Prism 6.02 was utilized for additional analysis of the data and plotting of the corresponding graphs.

MTS tetrazolium reduction assay

Cell viability of transduced, nanoparticle-loaded HFBSCs was determined using the colorimetric MTS assay. This assay is based upon the one-step reduction of the colorless tetrazolium compound MTS (3-(4,5-dimethylthiazol-2-yl)-5-(3-carboxymethophenyl)-2-(4-sulfophenyl)-2H-tetrazolium) to a water-soluble colored formazan (blue) in the presence of phenazine ethosulphate. Transduced HFBSCs loaded with TMSR50 nanoparticles and non-loaded control cells were seeded in PDL-coated Corning® Costar® 96-well cell culture plates. After 1 day, 8 and 15 days, cell viability was determined using the CellTiter® 96 AQueous One Solution Cell Proliferation Assay (Promega Corporation) according to the manufacturer's protocol. Colorimetric measurements were performed after a 90-minute incubation period, and 5 seconds shaking, using a VersaMax™ ELISA microplate reader (Molecular Devices, Sunnyvale, CA, USA) at 490 nm. Data acquisition and analysis were performed with SoftMax™ Pro version 5.4.1 software (Molecular Devices).

Differentiation of TMSR50-loaded HFBSCs

Both, transduced HFBSCs loaded with TMSR50 nanoparticles and untreated control cells, were differentiated according to the protocol by Gho *et al*. [38]. Briefly, 2.5 × 10^5 cells were seeded via the side into PDL-coated wells containing PDL-coated cover glasses (Thermo Scientific, Waltham, MA, USA). Differentiation was induced by removal of 250 µL medium and replacement with 300 µL induction medium (IM) consisting of DMEM/Ham's F-12 1:1 supplemented with 1.5 mM cAMP (Sigma-Aldrich), 1% glutamax (Life Technologies), 10 ng/mL NGF, 10 ng/mL GDNF, 10 ng/mL BDNF (all from R&D Systems) and 2% B27 + VitA (Life Technologies).

Subsequently, cultures were allowed to differentiate for at least 60 hours without disturbance followed by removal of 250 µL medium and again substituted with 300 µL IM.

In vitro bioluminescence imaging

The bioluminescent signal of luciferase-expressing cells can be used as a proxy for cell viability, by reason of the fact that the luciferase reaction requires O_2 and ATP. Transduced HFBSCs with and without TMSR50 nanoparticles were seeded in PDL-coated black-walled 96-well microplates (Greiner Bio-One). After 1 day, 8 and 15 days, bioluminescence was recorded after addition of D-luciferin at a final concentration of 0.5 mM. Bioluminescence was measured with an IVIS® Spectrum multimodal imaging system (PerkinElmer) using 30-second acquisition times, open filter, field of view C (default setting), f/stop = 1, and medium binning. Image acquisition and analysis were performed with Living Image® version 3.1 software (PerkinElmer). All images were subsequently processed using Adobe® Photoshop® CS6.

MRI of agarose-embedded TMSR50-loaded HFBSCs

A cell dilution series was done to establish the amount of TMSR50-loaded HFBSCs needed to reach signal threshold for MRI. For this purpose, a multi-layered cell-gradient agarose phantom was fabricated consisting of four layers of agarose-embedded cells at different concentrations, with each cell layer being sandwiched between two acellular agarose layers. Different amounts of cells (5×10^7, 5×10^6, 5×10^5, and 5×10^4 cells/ml) were suspended in a solution of 0.5% agarose (molecular grade; Bioline, London, UK) in PBS. Warm agarose was pipetted, free of air bubbles, into a 50-mL tube. After gelation at -20°C, 20 µL of a cell suspension was mixed with an equal volume of warm agarose and pipetted on top of the solidified agarose bottom layer and left to solidify followed by pipetting 2 mL of agarose on top of the agarose-embedded cell layer. This procedure was repeated several times resulting in four layers containing 1×10^6, 1×10^5, 1×10^4, and 1×10^3 cells/layer. Next, another two layers of 2 mL acellular agarose were created, before filling up the 50-mL tube with agarose. Finally, it was sealed with a layer of Parafilm® M sealing film

before affixing the lid. The phantom was examined for red fluorescence due to the TMSR50 nanoparticles using an IVIS® Spectrum multimodal imaging system at a minimal acquisition time of 1 second (λ_{ex}: 535 nm; λ_{em}: 580 nm). Image acquisition and analysis were performed with Living Image® version 3.1 software.

MRI was performed with a 7-T Bruker PharmaScan® 70/16 (Bruker Biospin, Ettlingen, Germany) equipped with a BGA-9S 300 mT/m gradient system and a conventional 38-mm birdcage transmit-and-receive radio-frequency (RF) coil (Bruker Biospin).

The cell-loaded agarose phantom was placed in the RF coil assembly fixed at the scanner's isocenter and, after an initial localization scan, T2*-weighted three-dimensional fast low-angle shot (FLASH) sequences were used to visualize the different cell layers within the phantom. Optimal sequence parameters were as follows: recovery time (TR): 100 ms; effective echo time (TE): 13 ms; imaging matrix size: 128 x 128 x 64; final voxel resolution of: 0.219 x 0.219 x 25 µm; and a FOV of: 28 x 28 x 16 mm. Data acquisition, image reconstruction and visualization were done with Paravision® 5.1 software (Bruker Biospin).

Statistical analyses

Statistical analyses of the data were performed using GraphPad Prism 6.02 and SPSS Statistics version 20.0.0.1 software (IBM Corporation).

Acknowledgments

The project is financially supported by grants from MED-EL (Innsbruck, Austria) and is also supported by Molecular Imaging of Brain Pathophysiology (BRAINPATH) under grant agreement number 612360 within the Marie Curie Actions-Industry-Academia Partnerships and Pathways (IAPP) program. We gratefully acknowledge Renate Buijink and Stephan Michel (Laboratory for Neurophysiology, LUMC, Leiden, The Netherlands) for the use of their bioluminescence microscope, and Louise van der Weerd and Ernst Suidgeest (Molecular Imaging Laboratories, Department of Radiology, LUMC, Leiden, The Netherlands) for their help with the MR imaging. We thank Alan Chan (Percuros, Enschede, The Netherlands) for supplying the TSMR50 nanoparticles and Ron Wolterbeek (Department of Medical Statistics and Bio-Informatics, LUMC, Leiden, The Netherlands) for his statistical analyses.

Declaration of interest

No conflict of interest has been declared.

Copyright

The content of this article is reproduced on basis of the terms and conditions provided by John Wiley and Sons and Copyright Clearance Center (License Number: 4231310786038; License date: Nov 17, 2017; Licensed Content Publisher: John Wiley and Sons; Licensed Content Publication: Contrast Media & Molecular Imaging).

References

1. Kassem, M., Mesenchymal stem cells: Biological characteristics and potential clinical applications. Cloning Stem Cells, 2004. **6**: pp. 369-374.
2. Schilling, T., Noth, U., Klein-Hitpass, L., Jakob, F., and Schutze, N., Plasticity in adipogenesis and osteogenesis of human mesenchymal stem cells. Mol. Cell Endocrinol., 2007. **271**: pp. 1-17.
3. Andrews, E.M., Tsai, S.Y., Johnson, S.C., Farrer, J.R., Wagner, J.P., Kopen, G.C., and Kartje, G.L., Human adult bone marrow-derived somatic cell therapy results in functional recovery and axonal plasticity following stroke in the rat. Exp. Neurol., 2008. **211**: pp. 588-592.
4. Kim, S.S., Yoo, S.W., Park, T.S., Ahn, S.C., Jeong, H.S., Kim, J.W., Chang, D.Y., Cho, K.G., Kim, S.U., Huh, Y., Lee, J.E., Lee, S.Y., Lee, Y.D., and Suh-Kim, H., Neural induction with neurogenin1 increases the therapeutic effects of mesenchymal stem cells in the ischemic brain. Stem Cells, 2008. **26**: pp. 2217-2228.
5. Muller, J., Ossig, C., Greiner, J.F., Hauser, S., Fauser, M., Widera, D., Kaltschmidt, C., Storch, A., and Kaltschmidt, B., Intrastriatal transplantation of adult human neural crest-derived stem cells improves functional outcome in Parkinsonian rats. Stem Cells Transl. Med., 2015. **4**: pp. 31-43.
6. Sato, T. and Clevers, H., Growing organoids from stem cells. Cell, 2015. **161**: pp. 1700-1701.
7. Lee, S., Choi, E., Cha, M.-J., and Hwang, K.-C., Cell adhesion and long-term survival of transplanted mesenchymal stem cells: A prerequisite for cell therapy. Oxid. Med. Cell. Longev., 2015. **2015**: pp. 632902.
8. Green, A.A. and McElroy, W.D., Crystalline firefly luciferase. Biochim. Biophys. Acta, 1956. **20**: pp. 170-176.
9. Contag, C.H. and Bachmann, M.H., Advances in *in vivo* bioluminescence imaging of gene expression. Annu. Rev. Biomed. Eng., 2002. **4**: pp. 235-260.
10. Mezzanotte, L., Que, I., Kaijzel, E., Branchini, B., Roda, A., and Löwik, C., Sensitive dual color *in vivo* bioluminescence imaging using a new red codon optimized firefly luciferase and a green click beetle luciferase. PLoS ONE, 2011. **6**: pp. e19277.
11. Wilson, B.C., Jeeves, W.P., and Lowe, D.M., *In vivo* and *post mortem* measurements of the attenuation spectra of light in mammalian tissues. Photochem. Photobiol., 1985. **42**: pp. 153-162.
12. Mezzanotte, L., Fazzina, R., Michelini, E., Tonelli, R., Pession, A., Branchini, B., and Roda, A., *In vivo* bioluminescence imaging of murine xenograft cancer models with a red-shifted thermostable luciferase. Mol. Imaging Biol., 2010. **12**: pp. 406-414.
13. Welsh, D.K. and Noguchi, T., Cellular bioluminescence imaging. Cold Spring Harb. Protoc., 2012. **2012**: pp. 852-866.
14. Shimomura, O., Johnson, F.H., and Saiga, Y., Extraction, purification and properties of aequorin, a bioluminescent protein from the luminous hydromedusan, *Aequorea*. J. Cell. Comp. Physiol., 1962. **59**: pp. 223-239.
15. Tsien, R.Y., The green fluorescent protein. Annu. Rev. Biochem., 1998. **67**: pp. 509-544.
16. Shaner, N.C., Steinbach, P.A., and Tsien, R.Y., A guide to choosing fluorescent proteins. Nat. Methods, 2005. **2**: pp. 905-909.
17. Chudakov, D.M., Matz, M.V., Lukyanov, S., and Lukyanov, K.A., Fluorescent proteins and their applications in imaging living cells and tissues. Physiol. Rev., 2010. **90**: pp. 1103-1163.
18. Shagin, D.A., Barsova, E.V., Yanushevich, Y.G., Fradkov, A.F., Lukyanov, K.A., Labas, Y.A., Semenova, T.N., Ugalde, J.A., Meyers, A., Nunez, J.M., Widder, E.A., Lukyanov, S.A., and Matz, M.V., GFP-like proteins as ubiquitous metazoan superfamily: Evolution of functional features and structural complexity. Mol. Biol. Evol., 2004. **21**: pp. 841-850.
19. Hunt, M.E., Scherrer, M.P., Ferrari, F.D., and Matz, M.V., Very bright green fluorescent proteins from the pontellid copepod *Pontella mimocerami*. PLoS ONE, 2010. **5**: pp. e11517.
20. Evdokimov, A.G., Pokross, M.E., Egorov, N.S., Zaraisky, A.G., Yampolsky, I.V., Merzlyak, E.M., Shkoporov, A.N., Sander, I., Lukyanov, K.A., and Chudakov, D.M., Structural basis for the fast maturation of *Arthropoda* green fluorescent protein. EMBO Rep., 2006. **7**: pp. 1006-1012.
21. Jendelova, P., Herynek, V., DeCroos, J., Glogarova, K., Andersson, B., Hajek, M., and Sykova, E., Imaging the fate of implanted bone marrow stromal cells labeled with superparamagnetic nanoparticles. Magn. Reson. Med., 2003. **50**: pp. 767-776.
22. Bulte, J.W. and Kraitchman, D.L., Iron oxide MR contrast agents for molecular and cellular imaging. NMR Biomed., 2004. **17**: pp. 484-499.
23. Sykova, E. and Jendelova, P., In vivo *tracking of stem cells in brain and spinal cord injury*, in *Progr. Brain Res.*, T.W. John and I.R.M. Andrew, Editors. 2007, Elsevier. pp. 367-383.
24. Kallur, T., Farr, T.D., Bohm-Sturm, P., Kokaia, Z., and Hoehn, M., Spatio-temporal dynamics, differentiation and viability of human neural stem cells after implantation into neonatal rat brain. Eur. J. Neurosci., 2011. **34**: pp. 382-393.
25. Kim, J.S., Yoon, T.J., Yu, K.N., Noh, M.S., Woo, M., Kim, B.G., Lee, K.H., Sohn, B.H., Park, S.B., Lee, J.K., and Cho, M.H., Cellular uptake of magnetic nanoparticle is mediated through energy-dependent endocytosis in A549 cells. J. Vet. Sci., 2006. **7**: pp. 321-326.
26. Yoon, T.J., Yu, K.N., Kim, E., Kim, J.S., Kim, B.G., Yun, S.H., Sohn, B.H., Cho, M.H., Lee, J.K., and Park, S.B., Specific targeting, cell sorting, and bioimaging with smart magnetic silica core-shell nanomaterials. Small, 2006. **2**: pp. 209-215.
27. Hwang do, W., Ko, H.Y., Kim, S.K., Kim, D., Lee, D.S., and Kim, S., Development of a quadruple imaging modality by using nanoparticles. Chemistry, 2009. **15**: pp. 9387-9393.
28. Park, K.S., Tae, J., Choi, B., Kim, Y.S., Moon, C., Kim, S.H., Lee, H.S., Kim, J., Kim, J., Park, J., Lee, J.H., Lee, J.E., Joh, J.W., and Kim, S., Characterization, *in vitro* cytotoxicity assessment, and *in vivo* visualization of multimodal, RITC-labeled, silica-coated magnetic nanoparticles for labeling human cord blood-derived mesenchymal stem cells. Int. J. Nanomedicine, 2010. **6**: pp. 263-276.
29. Sieber-Blum, M., Grim, M., Hu, Y.F., and Szeder, V., Pluripotent neural crest stem cells in the adult hair follicle. Dev. Dyn., 2004. **231**: pp. 258-269.

30. Yu, H., Fang, D., Kumar, S.M., Li, L., Nguyen, T.K., Acs, G., Herlyn, M., and Xu, X., Isolation of a novel population of multipotent adult stem cells from human hair follicles. Am. J. Pathol., 2006. **168**: pp. 1879-1888.
31. Krejci, E. and Grim, M., Isolation and characterization of neural crest stem cells from adult human hair follicles. Folia. Biol. (Praha), 2010. **56**: pp. 149-157.
32. Yu, H., Kumar, S.M., Kossenkov, A.V., Showe, L., and Xu, X., Stem cells with neural crest characteristics derived from the bulge region of cultured human hair follicles. J Invest Dermatol 2010. **130**: pp. 1227-36.
33. Liu, F., Zhang, C., and Hoffman, R.M., Nestin-expressing stem cells from the hair follicle can differentiate into motor neurons and reduce muscle atrophy after transplantation to injured nerves. Tissue Eng. Part A, 2014. **20**: pp. 656-662.
34. Mezzanotte, L., Aswendt, M., Tennstaedt, A., Hoeben, R., Hoehn, M., and Löwik, C., Evaluating reporter genes of different luciferases for optimized *in vivo* bioluminescence imaging of transplanted neural stem cells in the brain. Contrast Media Mol. Imaging, 2013. **8**: pp. 505-513.
35. Liu, H.S., Jan, M.S., Chou, C.K., Chen, P.H., and Ke, N.J., Is green fluorescent protein toxic to the living cells? Biochem. Biophys. Res. Commun., 1999. **260**: pp. 712-717.
36. Goto, H., Yang, B., Petersen, D., Pepper, K.A., Alfaro, P.A., Kohn, D.B., and Reynolds, C.P., Transduction of green fluorescent protein increased oxidative stress and enhanced sensitivity to cytotoxic drugs in neuroblastoma cell lines. Mol. Cancer Ther., 2003. **2**: pp. 911-917.
37. McGinley, L., McMahon, J., Strappe, P., Barry, F., Murphy, M., O'Toole, D., and O'Brien, T., Lentiviral vector mediated modification of mesenchymal stem cells & enhanced survival in an *in vitro* model of ischaemia. Stem Cell Res. Ther., 2011. **2**: pp. 12.
38. Gho, C.G., Schomann, T., De Groot, S.C., Frijns, J.H.M., Rivolta, M.N., Neumann, M.H., and Huisman, M.A., Isolation, expansion and neural differentiation of stem cells from human plucked hair: A further step towards autologous nerve recovery. Cytotechnology, 2016. **68**: pp. 1849-1858.
39. Kai, W., Xiaojun, X., Ximing, P., Zhenqing, H., and Qiqing, Z., Cytotoxic effects and the mechanism of three types of magnetic nanoparticles on human hepatoma BEL-7402 cells. Nanoscale Res. Lett., 2011. **6**: pp. 480.
40. Kircher, M.F., Allport, J.R., Graves, E.E., Love, V., Josephson, L., Lichtman, A.H., and Weissleder, R., *In vivo* high resolution three-dimensional imaging of antigen-specific cytotoxic T-lymphocyte trafficking to tumors. Cancer Res., 2003. **63**: pp. 6838-6846.
41. Foster-Gareau, P., Heyn, C., Alejski, A., and Rutt, B.K., Imaging single mammalian cells with a 1.5 T clinical MRI scanner. Magn. Reson. Med., 2003. **49**: pp. 968-971.
42. Yeum, C.E., Park, E.Y., Lee, S.B., Chun, H.J., and Chae, G.T., Quantification of MSCs involved in wound healing: Use of SIS to transfer MSCs to wound site and quantification of MSCs involved in skin wound healing. J. Tissue Eng. Regen. Med., 2013. **7**: pp. 279-291.
43. Okazaki, Y., Rao, S., Asao, S., Tateishi, T., Katsuda, S.-i., and Furuki, Y., Effects of Ti, Al and V concentrations on cell viability. Mater. Trans., 1998. **39**: pp. 1053-1062.
44. Brunner, T.J., Wick, P., Manser, P., Spohn, P., Grass, R.N., Limbach, L.K., Bruinink, A., and Stark, W.J., *In vitro* cytotoxicity of oxide nanoparticles: Comparison to asbestos, silica, and the effect of particle solubility. Environ. Sci. Technol., 2006. **40**: pp. 4374-4381.
45. El Seady, R., Huisman, M.A., Löwik, C.W., and Frijns, J.H.M., Uncomplicated differentiation of stem cells into bipolar neurons and myelinating glia. Biochem. Biophys. Res. Commun., 2008. **376**: pp. 358-362.

Lentiviral transduction and subsequent loading with nanoparticles do not affect cell viability and proliferation in hair-follicle-bulge-derived stem cells *in vitro*

Chapter 4

Neuronal differentiation of hair-follicle-bulge-derived stem cells co-cultured with mouse cochlear modiolus explants

PLOS ONE, 2017

Vol. **12** (10): Article# e0187183

T. Schomann, L. Mezzanotte, J.C.M.J. De Groot, M.N. Rivolta, S.H. Hendriks, J.H.M. Frijns, M.A. Huisman

Abstract

Stem-cell-based repair of auditory neurons may represent an attractive therapeutic option to restore sensorineural hearing loss. Hair-follicle-bulge-derived stem cells (HFBSCs) are promising candidates for this type of therapy, because they (1) have migratory properties, enabling migration after transplantation, (2) can differentiate into sensory neurons and glial cells, and (3) can easily be harvested in relatively high numbers. However, HFBSCs have never been used for this purpose. We hypothesized that HFBSCs can be used for cell-based repair of the auditory nerve and we have examined their migration and incorporation into cochlear modiolus explants and their subsequent differentiation. Modiolus explants obtained from adult wild-type mice were cultured in the presence of EF1α-copGFP-transduced HFBSCs, constitutively expressing copepod green fluorescent protein (copGFP). Also, modiolus explants without hair cells were co-cultured with DCX-copGFP-transduced HFBSCs, which demonstrate copGFP upon doublecortin expression during neuronal differentiation. Velocity of HFBSC migration towards modiolus explants was calculated, and after two weeks, co-cultures were fixed and processed for immunohistochemical staining. EF1α-copGFP HFBSC migration velocity was fast: 80.5 ± 6.1 μm/h. After arrival in the explant, the cells formed a fascicular pattern and changed their phenotype into an ATOH1-positive neuronal cell type. DCX-copGFP HFBSCs became green-fluorescent after integration into the explants, confirming neuronal differentiation of the cells. These results show that HFBSC-derived neuronal progenitors are migratory and can integrate into cochlear modiolus explants, while adapting their phenotype depending on this micro-environment. Thus, HFBSCs show potential to be employed in cell-based therapies for auditory nerve repair.

Introduction

Sensorineural hearing loss (SNHL) can be induced by a variety of causes, such as genetic mutations, prolonged exposure to loud noise, ototoxic drug treatment, or simply as a result of ageing, and is frequently the result of irreversible damage to, and subsequent loss of, hair cells and auditory neurons [1]. The degree of neuron loss is of significance for hearing-impaired patients using a cochlear implant (CI), because this device directly stimulates auditory neurons. Stem cells may counteract the effect of neuronal degeneration and the ensuing neuron loss [2]. Here, stem cells may serve different purposes: their descendants can replace spiral ganglion cells and/or glial cells, but regeneration may also be stimulated by stem-cell-driven paracrine secretion of cytokines and growth factors [3]. This could be of interest in clinical applications, because it can be surmised that in deaf patients stem cells will lack trophic support from hair cells and perhaps also from non-sensory cells.

In 2012, Chen *et al*. reported that human embryonic stem-cell-derived otic progenitors could be successfully incorporated into inner ear tissue in an animal model of SNHL and differentiated into neurons which subsequently innervated the hair cells [4]. Nevertheless, it would be ideal for future clinical applications to have suitable autologous stem cells in order to avoid the risk of graft rejection. Cell-based therapy using autologous neural-crest-derived stem cells (NCSCs) may represent such an attractive therapeutic option. During embryogenesis, neural crest cells delaminate from the dorsal neural tube and migrate laterally towards the otic placode, where they develop in close association with cells from the otic placode [5-7]. Moreover, during embryogenesis, the neural crest and the otic placode develop and differentiate in a similar way, especially since both originate from the lateral border of the neural plate [8-12, 5, 13, 7]. Hence, NCSCs may easily be directed towards an appropriate neuronal or glial phenotype, which is necessary for auditory nerve repair [5]. Another attractive characteristic of NCSCs is that they are migratory by nature. Given this property, it may be surmised that stem cells implanted into the basal cochlear turn will move from the transplantation site further into the damaged area, or will migrate to more apically located cochlear turns. In the adult body, niches with residing NCSCs, such as the hair follicle bulge, can be easily accessed. Only minimally invasive surgery is necessary to harvest hair-follicle-bulge-derived stem cells (HFBSCs), which opens the way to autologous transplantations. Taken together, HFBSCs would be well suited to study cell-based therapy in animal models of SNHL. However, HFBSCs

have never been used in inner ear regeneration research. Therefore, before starting transplantation studies, it is important that a number of prerequisites are met *in vitro*. The current study aimed on establishing if HFBSCs demonstrate three key factors to ensure successful auditory nerve repair in CI users: (1) retention of the nature as a migrating neural crest cell, (2) their incorporation into damaged cochlear tissue (i.e., without hair cells) and (3) their capability to differentiate into auditory neuronal or glial precursor phenotypes after incorporation – without the support of growth factors from hair cells.

To mimic the situation in hearing-impaired patients, we used cochlear modiolus explants – devoid of sensory hair cells – from adult mice and co-cultured the explants with genetically manipulated HFBSCs to investigate the aforementioned key factors [14]. We used stem cells which express copepod green fluorescent protein (copGFP) under the control of either the constitutively active elongation factor 1α (EF1α) or the promotor of doublecortin (DCX), the neuronal migration protein [15].

Material and methods

Animals

Healthy, adult (> 23 days) male and female mice (strain C57Bl/6) were bred and housed in the Animal Care Facility of Leiden University Medical Center (LUMC, the Netherlands). Animal care and handling were in accordance with the guidelines and regulations as stipulated by the Dutch Experiments on Animals Act (WoD) and the European Directive on the Protection of Animals Used for Scientific Purposes (2010/63/EU) and approved by the Animal Experiments Committee of the LUMC (DEC permit 10172).

Culture and transduction of HFBSCs

Mouse whisker pads were taken out within 10 minutes after euthanasia by cervical dislocation and stored in DMEM/Ham's F-12 (Biochrom AG, Berlin, Germany) containing 1% Glutamax (100x; Gibco, Bleiswijk, the Netherlands) and 1% antibiotic/antimycotic solution (100x; Sigma-Aldrich, St. Louis, MO, USA). Hair follicles were dissected from the whisker pads and the bulge region was excised as previously described [16, 17]. Each hair follicle bulge was placed in one well of a 12-well plate (TPP Techno Plastic Products AG, Trasadingen, Austria) pre-coated with an aqueous poly-D-lysine (PDL) solution (0.01 mg/ml; Sigma-Aldrich) and cultured in basic growth medium (BGM) until an outgrowth of 200-400 cells was reached. BGM consists of DMEM/Ham's F-12 1:1 (Biochrom AG, Berlin, Germany), 1% GlutaMax™ (100x; Gibco, Bleiswijk, the Netherlands) and 1% antibiotic/antimycotic solution supplemented with 10% fetal bovine serum (FBS; Gibco), 2% B-27® supplement without vitamin A (50x; Gibco), 1% N-2 MAX media supplement (100x; R&D Systems™, Minneapolis, MN, USA), recombinant human basic fibroblast growth factor (20 ng/ml; R&D Systems), and recombinant human epidermal growth factor (20 ng/ml; R&D Systems). The cultures were maintained in a humidified incubator at 37°C and 5% CO_2. Cells were enzymatically detached, counted, pooled and seeded at a density of 2.5 x 10^3 cells/cm^2 in PDL-coated dishes. At a confluence of 60%-70%, the cultures were passaged according to the procedure mentioned above [16, 17]. At a yield of 4 x 10^5 cells, usually after 4-5 passages, HFBSCs were frozen in 10% DMSO in FBS and stored at -80°C until use. After thawing, HFBSCs were cultured in

BGM on PDL-coated dishes until 80% confluence and subsequently transduced with a third-generation lentiviral vector. To monitor HFBSCs, the lentiviral vector pCDH-EF1α-Luc2-T2A-copGFP (EF1α-copGFP) [18], containing the constitutively-active elongation factor-1α (EF1α) promoter and a T2A-linking sequence, was used. The T2A-linking sequence results in equimolar expression of firefly luciferase (Luc2) and copepod green fluorescent protein (copGFP). In addition, HFBSCs were transduced with the lentiviral vector pCDH-DCX-Fer-P2A-Luc2-T2A-copGFP (DCX-copGFP) [15], Vector production and transduction procedures have been described in detail previously [11]. HFBSCs were seeded in PDL-coated 12-well plates at a cell density of 2.5 x 10^4 cells/well and maintained in a humidified incubator at 37°C and 5% CO_2. After attachment, the cells were transduced using a MOI (multiplicity of infection) of 10 as previously described with an efficiency of 83.6 ± 8.2% (mean ± SEM) [14]. Vector production and HFBSC transduction were performed under appropriate biosafety level conditions (ML-II) in accordance with the National Biosafety Guidelines and Regulations for Research on Genetically Modified Organisms. Procedures and protocols were reviewed and approved by the LUMC Biosafety Committee (GMO permit 08-129). Transduced cells were cryopreserved in FBS containing 10% DMSO until used.

Isolation and dissection of adult mouse modiolus and quarter-turn explants

Auditory bullae were dissected from the adult mouse skull (>23 days) within 10 minutes after euthanasia of the mice and the cochleas were removed and placed in sterile DMEM/Ham's F-12 1:1 containing 1% GlutaMax™ (100x) and 1% antibiotic/antimycotic solution supplemented with 10% FBS. The bony capsule of the cochlea was gently peeled off, the lateral wall tissue was discarded and the whole modiolus taken out using a dissection microscope. The modiolus with the organ of Corti still attached was placed in sterile BGM in a humidified incubator until further processing (within two hours).

Some of the specimens were directly co-cultured with HFBSCs in order to investigate the migration of transduced HFBSCs towards whole modioli. Another portion of the specimens was used to prepare quarter-turn explants. These were prepared by gently cutting the isolated modiolus along a transverse plane and removing the central core of auditory neurons and any excess bone from the inner rim of the osseous

spiral lamina followed by dissection, resulting in whole-turn explants containing the osseous spiral lamina and the organ of Corti. Next, the explants were cut into four and these quarter-turn explants were placed in PDL-coated wells.

Degeneration of hair cells

To mimic a sensory epithelium devoid of hair cells, comparable to the damaged epithelium in deaf patients, we had to ascertain the absence of hair cells under our culture conditions. Therefore, instead of culturing the explants in artificial perilymph, the modioli were kept in BGM for two hours or cultured in PDL-coated dishes for 36 hours and subsequently fixed for immunohistochemistry (Fig. 1).

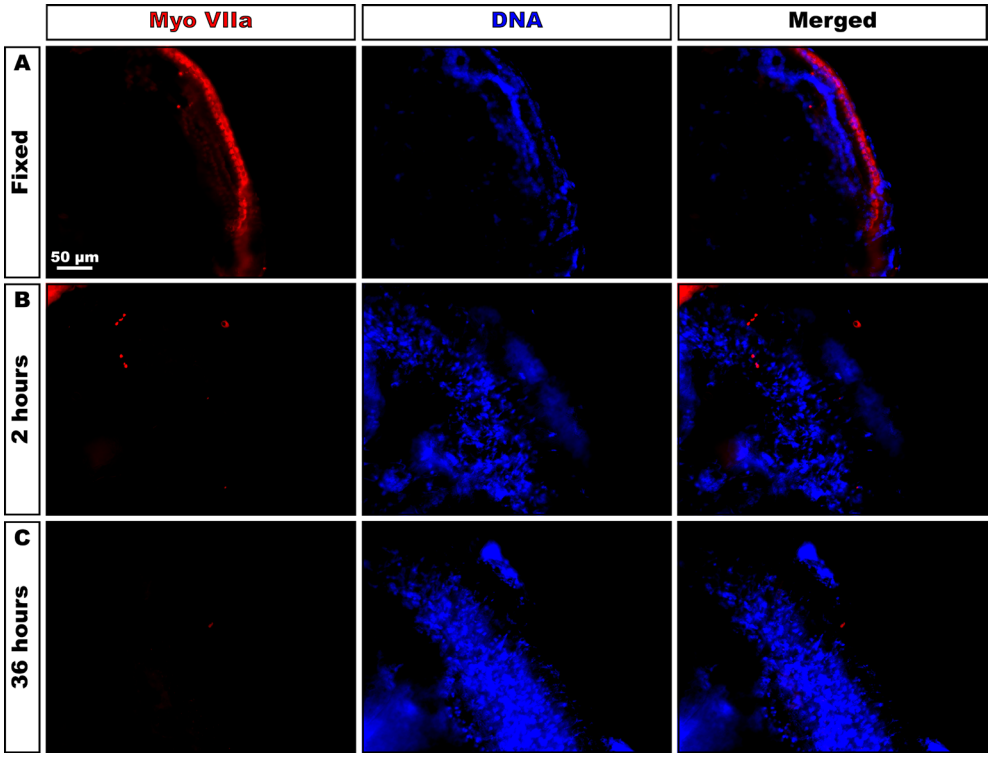

Fig. 1: Degeneration of hair cells in cultured explants. **A:** Staining for myosin VIIa shows the presence of hair cells in cochleas immediately fixed in formaldehyde prior to microdissection (upper lane; Fixed). **B-C:** Quarter-turn explants stored in BGM for 2 hours (B) or 36 hours (C) prior to formaldehyde fixation do not stain for the myosin VIIa, indicating that all hair cells have been lost during culturing.

Migration of HFBSCs

The migratory potential of EF1α-copGFP-transduced HFBSCs (Fig. 2A) was investigated by seeding the cells alongside the border of a well in a PDL-coated 12-well dish, while a whole modiolus explant was placed in the center (for a schematic set-up, see Fig. 2B). Cells and modiolus explant were allowed to attach at 37°C for 60 minutes, after which 500 µl BGM were added carefully (Fig. 2B'). Cell migration velocity was calculated by dividing the migration distance by the time (hours) at various time points (Figs. 2B' - 2D'). Cell migration distance (in mm) was the distance between the border of the area occupied by the cells after seeding and the position of the cells towards the brim of the explant. Measurements continued until the first fluorescent cells were visible underneath the modiolus explant (Fig 2D). Migration was monitored using an Olympus IX70 fluorescence microscope (FITC filter settings) equipped with a Leica DFC340 FX digital camera. Digital images were acquired and stored using Leica Application Suite Advanced Fluorescence (LAS AF) software (version 1.9.0). All images were subsequently processed using Adobe® Photoshop® CC software (version 2014.2.1).

Co-culture of HFBSCs

To start the co-culture experiment, 10 µl BGM containing 2 x 10^4 HFBSCs were pipetted on top of quarter-turn explants. The co-cultures were incubated at 37°C for 60 minutes, allowing attachment of both cells and explants to the bottom of the PDL-coated well, after which 500 µl BGM were added carefully. Parallel cultures were performed with the same HFBSCs cells of the co-culture, in order to establish immunophenotypic changes of the cells. Every other day, half of the medium was refreshed. After 7 days in culture, the explants were taken out of the culture and fixed with pre-warmed (37°C) 1% formaldehyde in PBS. To protect copGFP from photobleaching, the explants were stored in 1.5 ml amber-colored Eppendorf® Safe-Lock microcentrifuge tubes (Sigma-Aldrich) at 4°C.

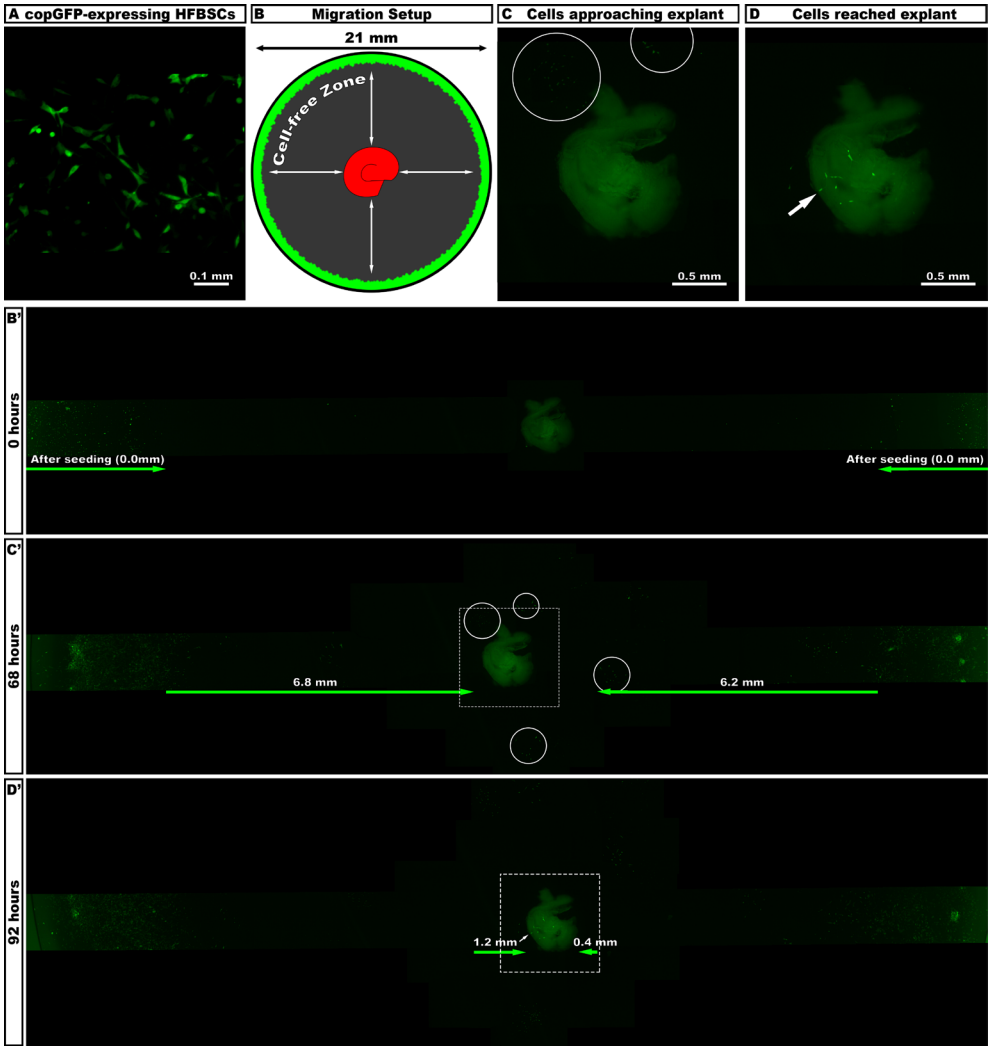

Fig. 2: Migration of copGFP-expressing cells. **A:** Green fluorescent HFBSCs before co-culture expressed copGFP. **B:** Schematic set-up of the migration experiment. At the border of the well (bottom diameter 21 mm), cells were seeded (green) and a modiolus was placed in the middle. **B':** Light-microscope image illustrating the situation directly after seeding and addition of medium (0 h). Fluorescent cells are located at the border of the well, while the modiolus is located in the center as indicated by faint background fluorescence. **C:** Groups of cells approached the modiolus (circles) after 68 hours, as is demonstrated at high magnification. **C':** Overview of area depicted in C (boxed area) reveals that brightly fluorescent HFBSCs radially migrated up to 6.8 mm and 6.2 mm, respectively, from their point of origin (i.e., the border of the well) towards the modiolus. **D:** After 96 hours, HFBSCs reached the modiolus. The arrow indicates the position of the cells located underneath the modiolus. **D':** Overview of area depicted in D (boxed area) illustrating how the first cells reached the modiolus after migrating another 1.2 mm and 0.4 mm, respectively (arrow), after 92 hours. Cells migrated over a cell-free zone (gray) towards the modiolus. In control experiments, i.e. wells without a modiolus in the center, cells proliferated at the border of the well, but did not migrate towards the center of the well (data not shown).

Immunohistochemistry

The fixed quarter-turn explants and control cells were washed with phosphate-buffered saline (PBS) containing 0.05% Tween-20 (Promega, Madison, WI, USA) for 5 minutes and permeabilized with 0.3% Triton X-100 (Sigma-Aldrich) in PBS containing 5% normal goat serum (Dako, Glostrup, Denmark) for 60 minutes. After washing with PBS/Tween-20, the specimens were incubated in blocking solution containing 0.1% Triton X-100 and 5% normal goat serum in PBS for 30 minutes. The specimens were incubated overnight with primary antibodies at room temperature. Primary antibodies used in this study are listed in Table 1. After washing, the specimens were incubated in blocking solution for 10 minutes followed by incubation with goat anti-mouse or goat anti-rabbit fluorochrome-conjugated (Alexa® Fluor 555, 1:300; Alexa® Fluor 750, 1:50) secondary antibodies, at room temperature for 90 minutes. Nuclei were counterstained with DAPI (Invitrogen) at a dilution of 1:1000 in PBS for 15 minutes. The specimens were mounted in a drop of Roti®-Mount FluorCare (Carl Roth GmbH + Co. KG, Karlsruhe, Germany) under a cover glass. All specimens were examined with a Leica DM5500 B fluorescence microscope (filter settings: TXR, Cy7, FITC and DAPI), equipped with a Leica DFC365 FX digital camera. Digital images were acquired and stored using Leica Application Suite X (LAS X) software. All images were subsequently processed using Adobe® Photoshop® CC software (version 2014.2.1).

Phalloidin staining

The presence of F-actin in quarter-turn explants was demonstrated with Alexa® Fluor 555-conjugated phalloidin (Invitrogen, Carlsbad, CA, USA). F-actin is a cytoskeleton marker and used to stain extant cells in the quarter-turn explant. Fixed specimens were washed three times with PBS and incubated with phalloidin (diluted in PBS containing 0.05% Tween-20) for 60 minutes followed by three washing steps with PBS. Next, nuclei of the specimens were counterstained with DAPI (diluted 1:1000 in PBS) for 15 minutes followed by washing with PBS and covered with Roti®-Mount FluorCare and a cover glass.

Table 1: Primary antibodies used for immunohistochemistry (in alphabetical order).

Antibody	Dilution	Manufacturer	Catalogue Number	Positive control	Marker specific for
ATOH1	1:100	Acris	AP-00308PU-N	Developing hair cells	neurons, hair cells and supporting cells in the developing cochlea
TUBB3	1:100	Abcam	AB78078	Mouse sciatic nerve	developing and young neurons
GFAP	1:100	Abcam	AB10062	Human astrocytes	glial cells
KROX-20	1:100	Covance	PRB-236P	RT4-D6P2T cells	myelinating Schwann cells
MPZ	1:100	Prof. Dies Meijer		RT4-D6P2T cells	myelinating Schwann cells, myelinated spiral ganglion neurons
Myosin VIIa	1:100o	Proteus	25-6790	Mouse organ of Corti	adult hair cells
Nestin	1:200	Biosensis	M-1385-100	C17.2 neural stem cells	neural crest cells and neural progenitors
NF-H	1:100	Abcam	AB8135	Mouse brain	mature neurons
NF-M	1:100	DSHB	2H3	Mouse brain	mature neurons
S100	1:100	DAKO	ZO311	RT4-D6P2T cells	Schwann cells
SOX2	1:1000	Abcam	AB97959	M14 melanoma cells	developing hair cells
SOX9	1:500	Millipore	AB5535	M14 melanoma cells	neural crest stem cells

Statistical analyses

Data of the migration experiment were processed in Microsoft Excel 2010 (Microsoft Corporation, Redmond, WA, USA) and expressed as mean ± SD. Statistically analysis was performed using GraphPad Prism version 6.02 software (GraphPad Software, La Jolla, CA, USA).

Results

Adult hair cells degenerate in BGM within 2 hours

Quarter-turn explants, which were fixed in formaldehyde immediately after dissection, stain for the adult hair cell marker myosin VIIa (n=6, Fig. 1A). When cultured in BGM for 2 hours – not in artificial perilymph – only some diffuse, pectinate staining for myosin VIIa could be observed, indicating that already most hair cells had been lost during such a short period of culture (n=3, Fig. 1B). After incubation in BGM for 36 hours, the specimens were completely devoid of staining for myosin VIIa (n=3, Fig. 1C).

Transduced HFBSCs migrate towards modiolus explant

EF1α-copGFP HFBSCs crossed the cell-free zone (radius: 7.5 ± 0.6 mm µm) with a velocity of 80.5 ± 6.1 µm/h (n=4) towards the modiolus explant and arrived, often in groups, at the explant within 2-3 days (Figs. 2C and 2C'). Cells located underneath the explant could clearly be distinguished from the modiolus tissue by adjusting the focus level during observation, i.e., to verify whether fluorescent cells arrived at the tissue (Fig. 2D). In control experiments, i.e. wells without a modiolus explant in the center, cells proliferated at the border of the well, but did not migrate towards the center of the well (data not shown).

Stem cells form a distinct fascicular pattern

In all cultures of the migration experiment, fluorescent HFBSCs invaded the explants within 2 days (2.2 ± 1.6 days) after arrival. Within the next 5 days (5.2 ± 1.6 days), the cells formed a distinct fascicular pattern (n=10). To shorten culture time, the protocol was adapted by seeding 2 x 10^4 EF1α-copGFP HFBSCs directly onto quarter-turn explants (n=50). We did not observe differences in fascicular organization of HFBSCs in the explants between both approaches.

The time course of the fascicular pattern formation by HFBSCs is depicted in Fig. 3. At day 1, cells are visible underneath the tissue, attached to the bottom of the well

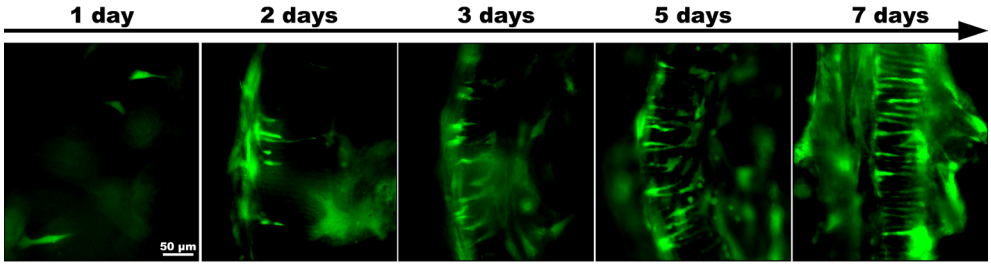

Fig. 3: Distinct fascicular pattern visible within 5 days. One day after seeding, fluorescent HFBSCs migrated under the quarter-turn explant and began migrating into the explant within the next day (2 days). Over time, more EF1α-copGFP HFBSCs settled in the explant (3 days) forming a distinct fascicular pattern after 5 days. Within the next two days the pattern enhanced as the number of HFBSCs within the explant increased.

and invaded the explant after 2 days of co-culture. At day 3, the number of HFBSCs increased within the tissue and cells formed a distinct fascicular pattern within 5 days. This pattern became more enhanced over the next two days, up to day 7.

Similar distinct fascicular pattern formation of HFBSCs transduced with EF1α-copGFP and DCX-copGFP

After obtaining a fascicular pattern of EF1α-copGFP HFBSCs in quarter-turn explants of adult mice (Fig. 4A), we investigated the role of the neuronal migration protein DCX in the process of pattern formation and seeded DCX-copGFP HFBSCs onto quarter-turn explants. During the next 4 days (4.1 ± 0.9 days), different cells became fluorescent and at day 5 (5.3 ± 0.9 days after seeding; n=7), the fluorescent HFBSCs were organized in a distinct fascicular pattern (Fig. 4B), similar to the pattern displayed by EF1α-copGFP HFBSCs. Therefore, the formation of a fascicular pattern is not related to the use of a specific promoter ($p=0.862$, two-tailed, unpaired *t*-test, 95% confidence interval).

Fluorescent EF1α-copGFP HFBSCs, in the fascicular pattern, immunostain for (auditory) neuronal markers

Fluorescent (copGFP-containing) cells in the modiolus explants showed immunostaining for the NCSC marker SOX9 (Fig. 5A). Nestin, a marker for NCSCs and neural progenitors, was weakly positive in most copGFP-expressing and SOX9-positive HFBSCs (Fig. 5A). TUBB3, a marker for young neurons, was

weakly positive, not only in fluorescent HFBSCs but also in some non-fluorescent (endogenous) cells (Fig. 5B). Medium-chain neurofilament protein (NF-M), generally expressed early during neuronal maturation, was exclusively positive in fluorescent HFBSCs (Fig. 5C), while the marker for mature neurons, heavy-chain neurofilament protein (NF-H), was negative (Fig. 5D). Most copGFP-positive cells arranged in the fascicular pattern immunostained for ATOH1, a marker for neurons and hair cells in the developing cochlea (Fig. 5C). The majority of ATOH1-positive cells was also

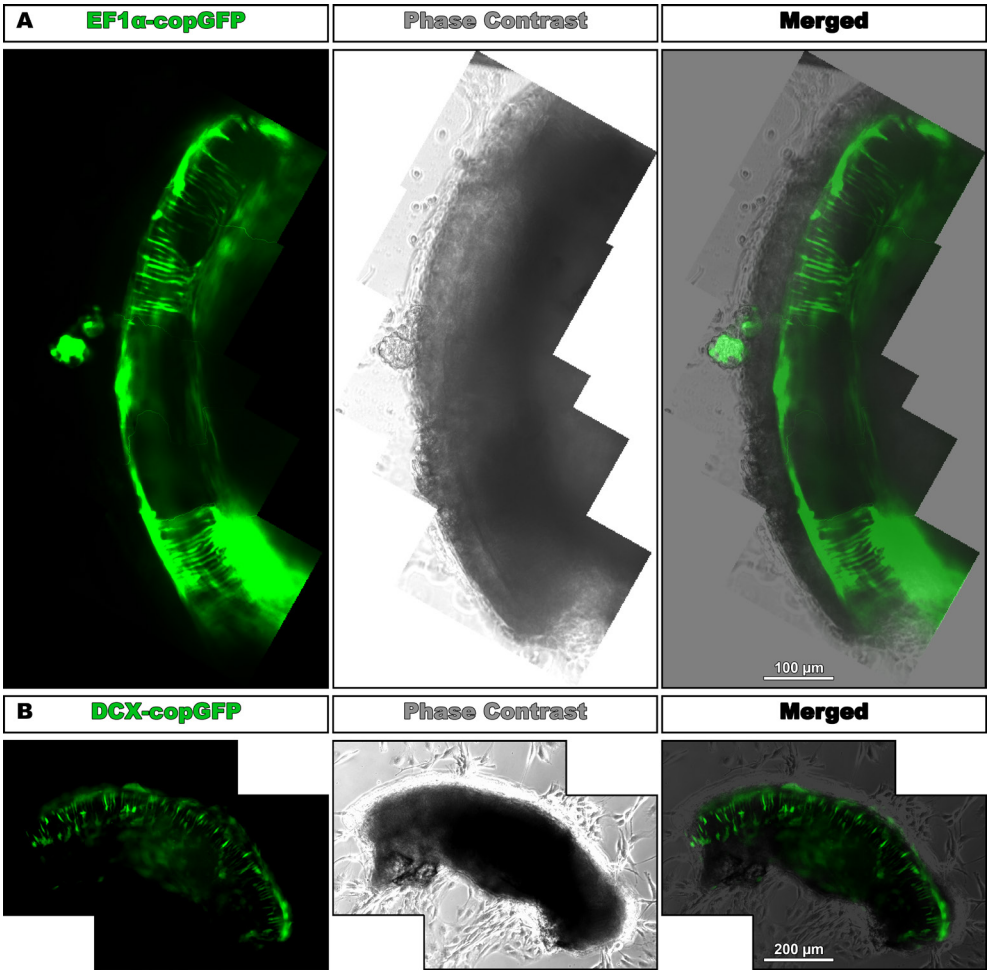

Fig. 4: EF1α-copGFP HFBSCs and DCX-copGFP HFBSCs form a similar distinct fascicular pattern. **A:** Set of stitched fluorescence images showing the distinct fascicular pattern that is formed by the copGFP-expressing cells (green). The stitched phase-contrast images depict the morphology of the quarter-turn explant (gray) and the merged set of images reveals the position of the green fluorescent cells within the explant. **B:** DCX-copGFP cells formed a similar fascicular pattern of fluorescent cells within the explant (green). The merged image of phase-contrast (gray) and fluorescence images depicts the location of DCX-copGFP-expressing cells within the explant.

positive for NF-M. Since hair cells are not present in the explant, the single ATOH1-positive, copGFP-negative cell is most likely a HFBSC that has not been successfully transduced (transduction efficiency is ± 84%). The immunostaining for SOX2, a marker for developing hair cells, was negative. In the pattern, some copGFP-positive HFBSCs, but also many non-fluorescent cells, were immunopositive for F-actin (Fig. 5E). The non-GFP-fluorescent, F-actin-positive cells demonstrate a morphology reminiscent of interdental cells [19].

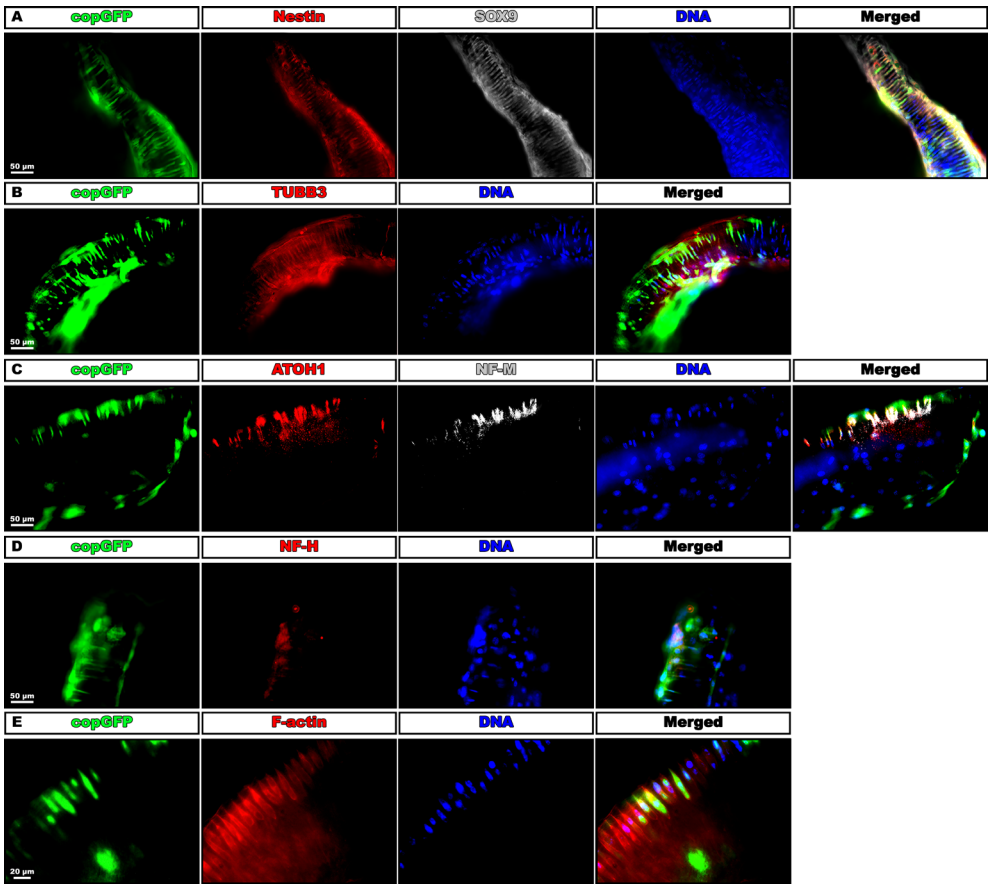

Fig. 5: HFBSCs within quarter-turn explants stain for nestin, SOX9, TUBB3, NF-M, ATOH1 and F-actin. **A:** Cop-GFP-expressing cells (green) in the explants stain for nestin (red) and SOX9 (gray). Nuclear DNA is counterstained with DAPI (blue). Merged images show co-localization of nestin and SOX9 in copGFP-expressing cells. **B:** All green-fluorescent cells and some non-fluorescent cells co-localize with TUBB3 (red) in the explants. **C:** Most copGFP-expressing cells (green) stain positive for ATOH1 (red) and NF-M (gray) was exclusively positive in fluorescent HFBSCs. **D:** NF-H (red) was negative in co-cultured HFBSCs. **E:** In the same row of cells, some transduced HFBSCs (green) were positive for F-actin (red) within the explant. In the explant also many non-fluorescent F-actin-positive cells are present.

Immunostaining for the adult hair cell marker myosin VIIa was negative, both in the hair cell survival experiment (Fig. 1) and in the co-cultures, indicating that the outer and inner hair cells were lost from the explants, even in short-term cultures. None of the glial markers (GFAP, S100, KROX-20 and MPZ) were immunopositive in copGFP-positive HFBSCs. The immunoprofile of the HFBSCs in the pattern compared to non-co-cultured HFBSCs are listed in Table 2. This table shows that HFBSCs changed their phenotype after incorporation in the explants and that they became positive for several (young) neuronal markers and negative for all glial markers. All pertinent positive and negative controls showed appropriate results.

Table 2: Immunoprofile of HFBSCs in the pattern as compared to non-co-cultured HFBSCs.

	Antibody	HFBSCs	HFBSCs in pattern
Neural Crest	SOX9	weakly positive	positive
	Nestin	positive	weakly positive
Neuron	TUBB3	negative	weakly positive
	NF-M	weakly positive	positive
	NF-H	negative	negative
Hair Cell	ATOH1	weakly positive	positive
	SOX2	weakly positive	negative
	Myo VIIa	negative	negative
Glial Cell	GFAP	negative	negative
	S100	negative	negative
	KROX20	negative	negative
	MPZ	negative	negative

Discussion

The results show that our population of HFBSCs meets three important requirements to enable their contribution to successful inner ear regeneration: they are migratory, they integrate into cochlear tissue, and have the capability to adapt a neuronal phenotype depending on the microenvironment.

The cell migration velocity of HFBSCs was relatively fast (80.5 ± 6.1 μm/h) as compared to other cell types as determined in wound-healing migration assays [20-23], indicating that they conserved the migratory nature of NCSCs. Migration of cells is to a large extent dependent on the type of extracellular matrix (ECM) and the presence of chemical attractants, such as growth factors. The cells in this experiment were seeded on a poly-D-lysine matrix, which allows migration of neural crest descendants [24, 25]. On the other hand, we considered it unlikely that chemotactic factors were present in the tissue, because the cultured explants were devoid of hair cells.

However, the remaining non-sensory cells may have expressed growth factors, which could function as a chemoattractant for HFBSCs [26]. In addition, it is generally known that certain growth factors can directly bind to ECM proteins [27]. Hence, it is possible that neural growth factors are present in the ECM of the explants, i.e. in the spiral limbus, the osseous spiral lamina and the basilar membrane. In the co-culture experiment, growth factors from the non-sensory cells and the ECM may therefore have attracted the HFBSCs.

Within five days upon arrival into the explant, the HFBSCs formed a distinctly fascicular pattern while co-localizing with F-actin-positive, non-GFP-fluorescent cells (Fig. 3E). Within seven days after their settlement, HFBSCs developed a neuronal phenotype corresponding to the expression of copGFP under regulation of the DCX promoter. This is an unusually rapid neuronal differentiation, for it has been reported that neuronal progenitors generally need three weeks to achieve NF-M positivity [28]. We hypothesize that there are several biochemical cues present in the explants, probably working in synergy, promoting a neuronal phenotype of the locally present HFBSCs. Firstly, although hair cells have disappeared, neural growth factors could still be present in supporting cells or be bound to ECM proteins. Secondly, the type of ECM proteins may be of importance: among the different classes of ECM molecules

that are present in the cochlea, laminin has been shown to be particularly effective in stimulating neuronal differentiation [29-31, 25]. Thirdly, given the fasciscular pattern of HFBSCs within the explants, the cells are probably dwelling in or near Huschke's teeth, i.e, in the upper region of the spiral limbus. This seems a plausible assumption, for the non-copGFP-fluorescent cells near the F-actin-positive, copGFP-fluorescent HFBSCs (Fig. 3E) are morphologically similar to interdental cells. It is known that a columnar-shaped ECM stimulates neuronal differentiation of cells [32, 33]. Hence, the columnar plates of the spiral limbus matrix (Huschke's teeth) [34] may well have stimulated HFBSCs to differentiate into a neuronal phenotype.

In our opinion, our experiments show that HFBSCs are tolerated in inner ear tissue from adult animals. Indeed, HFBSCs do intermingle with extant cells of the modiolus and can subsequently adapt to the microenvironment. Furthermore, in spite of the absence of trophic factors from hair cells, HFBSCs changed their phenotype into that of young neuronal cells (Fig. 5). Various studies have shown that stems cells isolated from the bulge area of mouse and human hair follicles express nestin, a marker for NCSCs and neural progenitors [35-45]. In these reports, it was established that nestin-positive HFBSCs can differentiate towards a variety of cells such as neurons, glia cells, melanocytes, keratinocytes as well as smooth and cardiac muscle cells. This broad differentiation capacity illustrates the potential of HFBSCs to serve many regenerative purposes. Our finding that nestin-positive HFBSCs differentiate towards a neuronal lineage, corroborates the pertinent above-mentioned reports (Table 2).

Hence, our report presents clear evidence that these cells may be good candidates for *in vivo* regenerative experiments in an animal model of SNHL. In upcoming studies we will use HFBSCs in CI-implanted guinea pigs, deafened by means of concomitant administration of kanamycin and furosemide. In this model no hair cells are present, similar to deaf patients and to our *in vitro* experiments.

Conclusion

In conclusion, the present observations show that HFBSCs are migratory and can successfully integrate into inner ear tissue, i.e., into the modiolus, while adapting a neuronal phenotype. Hence, the results of this study show the potential of HFBSCs for auditory nerve repair. Our next step will be to investigate *in vivo* if HFBSCs after transplantation into the spiral ganglion receive the appropriate biochemical stimuli to differentiate into auditory neurons and/or glial cells.

Acknowledgements

The project is financially supported by grants from MED-EL (Innsbruck, Austria). The authors have no other funding, financial relationships, or conflicts of interest to disclose. We greatly acknowledge Yuedan Li (Department of Immunohematology and Blood Transfusion, LUMC, Leiden, the Netherlands) for performing transduction of the HFBSCs and Martijn Rabelink (Department of Molecular Cell Biology, LUMC, Leiden, the Netherlands) for the production of the lentivirus.

Copyright

This is an open access article distributed under the terms of the Creative Commons Attribution License, which permits unrestricted use, distribution, and reproduction in any medium.

References

1. Lang, H., *Loss, degeneration, and preservation of the spiral ganglion neurons and their processes*, in *The primary auditory neurons of the mammalian cochlea*, A. Dabdoub, *et al*., Editors. 2016, Springer New York: New York, U.S.A. pp. 229-262.
2. Nayagam, B.A., Human stem cells ameliorate auditory evoked responses in a model of neuropathy. Stem Cell Res. Ther., 2012. **3**: pp. 44.
3. Baraniak, P.R. and McDevitt, T.C., Stem cell paracrine actions and tissue regeneration. Regen. Med., 2010. **5**: pp. 121-143.
4. Chen, W., Jongkamonwiwat, N., Abbas, L., Eshtan, S.J., Johnson, S.L., Kuhn, S., Milo, M., Thurlow, J.K., Andrews, P.W., Marcotti, W., Moore, H.D., and Rivolta, M.N., Restoration of auditory evoked responses by human ES-cell-derived otic progenitors. Nature, 2012. **490**: pp. 278-282.
5. Huisman, M.A. and Rivolta, M.N., Neural crest stem cells and their potential application in a therapy for deafness. Front. Biosci. (Schol. Ed.), 2012. **4**: pp. 121-132.
6. Theveneau, E., Steventon, B., Scarpa, E., Garcia, S., Trepat, X., Streit, A., and Mayor, R., Chase-and-run between adjacent cell populations promotes directional collective migration. Nat. Cell Biol., 2013. **15**: pp. 763-772.
7. Steventon, B., Mayor, R., and Streit, A., Neural crest and placode interaction during the development of the cranial sensory system. Dev. Biol., 2014. **389**: pp. 28-38.
8. Verwoerd, C.D., van Oostrom, C.G., and Verwoerd-Verhoef, H.L., Otic placode and cephalic neural crest. Acta Otolaryngol., 1981. **91**: pp. 431-435.
9. Streit, A., Extensive cell movements accompany formation of the otic placode. Dev. Biol., 2002. **249**: pp. 237-254.
10. Bhattacharyya, S. and Bronner-Fraser, M., Hierarchy of regulatory events in sensory placode development. Curr. Opin. Genet. Dev., 2004. **14**: pp. 520-526.
11. Kuriyama, S. and Mayor, R., Molecular analysis of neural crest migration. Philos. Trans. R. Soc. Lond., B, Biol. Sci., 2008. **363**: pp. 1349-1362.
12. Ladher, R.K., O'Neill, P., and Begbie, J., From shared lineage to distinct functions: The development of the inner ear and epibranchial placodes. Development, 2010. **137**: pp. 1777-1785.
13. Groves, A.K. and LaBonne, C., Setting appropriate boundaries: Fate, patterning and competence at the neural plate border. Dev. Biol., 2014. **389**: pp. 2-12.
14. Schomann, T., Mezzanotte, L., Lourens, I.M., De Groot, J.C.M.J., Frijns, J.H.M., and Huisman, M.A., Lentiviral transduction and subsequent loading with nanoparticles do not affect cell viability and proliferation in hair-follicle-bulge-derived stem cells *in vitro*. Contrast Media Mol. Imaging, 2016. **11**: pp. 550-560.
15. Tennstaedt, A., Aswendt, M., Adamczak, J., Collienne, U., Selt, M., Schneider, G., Henn, N., Schaefer, C., Lagouge, M., Wiedermann, D., Kloppenburg, P., and Hoehn, M., Human neural stem cell intracerebral grafts show spontaneous early neuronal differentiation after several weeks. Biomaterials, 2015. **44**: pp. 143-154.
16. El Seady, R., Huisman, M.A., Löwik, C.W., and Frijns, J.H.M., Uncomplicated differentiation of stem cells into bipolar neurons and myelinating glia. Biochem. Biophys. Res. Commun., 2008. **376**: pp. 358-362.
17. Gho, C.G., Schomann, T., De Groot, S.C., Frijns, J.H.M., Rivolta, M.N., Neumann, M.H., and Huisman, M.A., Isolation, expansion and neural differentiation of stem cells from human plucked hair: A further step towards autologous nerve recovery. Cytotechnology, 2016. **68**: pp. 1849-1858.
18. Mezzanotte, L., Aswendt, M., Tennstaedt, A., Hoeben, R., Hoehn, M., and Löwik, C., Evaluating reporter genes of different luciferases for optimized *in vivo* bioluminescence imaging of transplanted neural stem cells in the brain. Contrast Media Mol. Imaging, 2013. **8**: pp. 505-513.
19. Wang, L., Bresee, C.S., Jiang, H., He, W., Ren, T., Schweitzer, R., and Brigande, J.V., *Scleraxis* is required for differentiation of the stapedius and tensor tympani tendons of the middle ear. J. Assoc. Res. Otolaryngol., 2011. **12**: pp. 407-421.
20. Sandulache, V.C., Parekh, A., Dohar, J.E., and Hebda, P.A., Fetal dermal fibroblasts retain a hyperactive migratory and contractile phenotype under 2-and 3-dimensional constraints compared to normal adult fibroblasts. Tissue Eng., 2007. **13**: pp. 2791-2801.
21. Baudoin, J.P., Alvarez, C., Gaspar, P., and Metin, C., Nocodazole-induced changes in microtubule dynamics impair the morphology and directionality of migrating medial ganglionic eminence cells. Dev. Neurosci., 2008. **30**: pp. 132-143.
22. Schiraldi, C., Stellavato, A., D'Agostino, A., Tirino, V., D'Aquino, R., Woloszyk, A., De Rosa, A., Laino, L., Papaccio, G., and Mitsiadis, T.A., Fighting for territories: Time-lapse analysis of dental pulp and dental follicle stem cells in co-culture reveals specific migratory capabilities. Eur. Cell. Mater., 2012. **24**: pp. 426-440.
23. Gu, S.Q., Gallego-Perez, D., McClory, S.P., Shi, J., Han, J., Lee, L.J., and Schoenberg, D.R., The human PMR1 endonuclease stimulates cell motility by down regulating miR-200 family microRNAs. Nucleic Acids Res., 2016. **44**: pp. 5811–5819.
24. Martin, I., Nguyen, T.D., Krell, V., Greiner, J.F.W., Müller, J., Hauser, S., Heimann, P., and Widera, D., Generation of Schwann cell-derived multipotent neurospheres isolated from intact sciatic nerve. Stem Cell Rev., 2012. **8**: pp. 1178-1187.
25. Joo, S., Kim, J.Y., Lee, E., Hong, N., Sun, W., and Nam, Y., Effects of ECM protein micropatterns on the migration and differentiation of adult neural stem cells. Sci. Rep., 2015. **5**: pp. 13043.
26. Sugawara, M., Murtie, J.C., Stankovic, K.M., Liberman, M.C., and Corfas, G., Dynamic patterns of neurotrophin 3

expression in the postnatal mouse inner ear. J. Comp. Neurol., 2007. **501**: pp. 30-37.
27. Schultz, G.S. and Wysocki, A., Interactions between extracellular matrix and growth factors in wound healing. Wound Repair Regen., 2009. **17**: pp. 153-162.
28. Fournier, B.P., Loison-Robert, L.S., Ferre, F.C., Owen, G.R., Larjava, H., and Hakkinen, L., Characterisation of human gingival neural crest-derived stem cells in monolayer and neurosphere cultures. Eur. Cell. Mater., 2016. **31**: pp. 40-58.
29. Maxwell, G.D., Reid, K., Elefanty, A., Bartlett, P.F., and Murphy, M., Glial cell line-derived neurotrophic factor promotes the development of adrenergic neurons in mouse neural crest cultures. Proc. Natl. Acad. Sci. USA, 1996. **93**: pp. 13274-13279.
30. Desban, N., Lissitzky, J.C., Rousselle, P., and Duband, J.L., Alpha1beta1-integrin engagement to distinct laminin-1 domains orchestrates spreading, migration and survival of neural crest cells through independent signaling pathways. J. Cell Sci., 2006. **119**: pp. 3206-3218.
31. Ma, W., Tavakoli, T., Derby, E., Serebryakova, Y., Rao, M.S., and Mattson, M.P., Cell-extracellular matrix interactions regulate neural differentiation of human embryonic stem cells. BMC Dev. Biol., 2008. **8**: pp. 90.
32. Su, W.-T., Liao, Y.-F., Wu, T.-W., Wang, B.-J., and Shih, Y.-Y., Microgrooved patterns enhanced PC12 cell growth, orientation, neurite elongation, and neuritogenesis. J. Biomed. Mater. Res. Part A, 2013. **101A**: pp. 185-194.
33. Mattotti, M., Micholt, L., Braeken, D., and Kovacic, D., Characterization of spiral ganglion neurons cultured on silicon micro-pillar substrates for new auditory neuro-electronic interfaces. J. Neural. Eng., 2015. **12**: pp. 026001.
34. Santi, P.A., Aldaya, R., Brown, A., Johnson, S., Stromback, T., Cureoglu, S., and Rask-Andersen, H., Scanning electron microscopic examination of the extracellular matrix in the decellularized mouse and human cochlea. J. Assoc. Res. Otolaryngol., 2016. **17**: pp. 159-171.
35. Li, L., Mignone, J., Yang, M., Matic, M., Penman, S., Enikolopov, G., and Hoffman, R.M., Nestin expression in hair follicle sheath progenitor cells. Proc. Natl. Acad. Sci. USA, 2003. **100**: pp. 9958-9961.
36. Amoh, Y., Li, L., Yang, M., Moossa, A.R., Katsuoka, K., Penman, S., and Hoffman, R.M., Nascent blood vessels in the skin arise from nestin-expressing hair-follicle cells. Proc. Natl. Acad. Sci. USA, 2004. **101**: pp. 13291-13295.
37. Amoh, Y., Li, L., Campillo, R., Kawahara, K., Katsuoka, K., Penman, S., and Hoffman, R.M., Implanted hair follicle stem cells form Schwann cells that support repair of severed peripheral nerves. Proc. Natl. Acad. Sci. USA, 2005. **102**: pp. 17734-17738.
38. Amoh, Y., Li, L., Katsuoka, K., Penman, S., and Hoffman, R.M., Multipotent nestin-positive, keratin-negative hair-follicle bulge stem cells can form neurons. Proc. Natl. Acad. Sci. USA, 2005. **102**: pp. 5530-5534.
39. Amoh, Y., Li, L., Katsuoka, K., and Hoffman, R.M., Multipotent hair follicle stem cells promote repair of spinal cord injury and recovery of walking function. Cell Cycle, 2008. **7**: pp. 1865-1869.
40. Amoh, Y., Kanoh, M., Niiyama, S., Hamada, Y., Kawahara, K., Sato, Y., Hoffman, R.M., and Katsuoka, K., Human hair follicle pluripotent stem (hfPS) cells promote regeneration of peripheral-nerve injury: An advantageous alternative to ES and iPS cells. J. Cell Biochem., 2009. **107**: pp. 1016-1020.
41. Liu, F., Uchugonova, A., Kimura, H., Zhang, C., Zhao, M., Zhang, L., Koenig, K., Duong, J., Aki, R., Saito, N., Mii, S., Amoh, Y., Katsuoka, K., and Hoffman, R.M., The bulge area is the major hair follicle source of nestin-expressing pluripotent stem cells which can repair the spinal cord compared to the dermal papilla. Cell Cycle, 2011. **10**: pp. 830-839.
42. Uchugonova, A., Duong, J., Zhang, N., Konig, K., and Hoffman, R.M., The bulge area is the origin of nestin-expressing pluripotent stem cells of the hair follicle. J. Cell Biochem., 2011. **112**: pp. 2046-2050.
43. Uchugonova, A., Hoffman, R.M., Weinigel, M., and Koenig, K., Watching stem cells in the skin of living mice noninvasively. Cell Cycle, 2011. **10**: pp. 2017-2020.
44. Mii, S., Duong, J., Tome, Y., Uchugonova, A., Liu, F., Amoh, Y., Saito, N., Katsuoka, K., and Hoffman, R.M., The role of hair follicle nestin-expressing stem cells during whisker sensory-nerve growth in long-term 3D culture. J. Cell Biochem., 2013. **114**: pp. 1674-1684.
45. Yashiro, M., Mii, S., Aki, R., Hamada, Y., Arakawa, N., Kawahara, K., Hoffman, R.M., and Amoh, Y., From hair to heart: Nestin-expressing hair-follicle-associated pluripotent (HAP) stem cells differentiate to beating cardiac muscle cells. Cell Cycle, 2015. **14**: pp. 2362-2366.

Chapter 5

Imaging bioluminescent exogenous stem cells in the intact guinea pig cochlea

The Anatomical Record, 2019

DOI: 10.1002/ar.24068

T. Schomann, L. Mezzanotte, J.C.M.J. De Groot, C.W.G.M. Löwik, J.H.M. Frijns, M.A. Huisman

Abstract

Stem-cell-based therapy may be used to replace damaged or lost neurons in the cochlear nerve of patients suffering from severe-to-profound sensorineural hearing loss. In order to achieve functional recovery in future clinical trials, knowledge about survival of grafted cells and their differentiation into functional neurons is a prerequisite. This calls for non-invasive *in vivo* visualization of cells and long-term monitoring of their survival and fate after cochlear transplantation.

We have investigated if molecular optical imaging enables visualization of exogenous cells in the intact cochlea of guinea pig cadaver heads. Transduced (stem) cells, stably co-expressing fluorescent (copGFP) and bioluminescent (Luc2) reporter molecules, were injected into the internal auditory meatus or directly into the cochlea through the round window.

After injection of the cells into the internal auditory meatus, a bright bioluminescent signal was observed in the cavum conchae of the auricle, indicating that light generated by Luc2 is passing through the tympanic membrane and the external auditory meatus. Similar results were obtained after injection of the cells through the round window membrane, either directly into the scala tympani or in Rosenthal's canal within the modiolus of the basal cochlear turn. Imaging of the auditory bulla demonstrated that the bioluminescent signal passes through the tympanic membrane and crevices in the bony wall of the bulla. After opening the auditory bulla, the bioluminescent signal was emanating from the round window.

This is the first study demonstrating that bioluminescence imaging enables visualization of luciferase-expressing cells injected into the intact guinea pig cochlea.

Introduction

The inner ear in Mammals contains the sense organs for hearing (cochlea) and balance (vestibular system). Within the cochlea, the sensory epithelium or organ of Corti houses, two different types of sensory cells: the outer and inner hair cells. The former function as acoustical pre-amplifiers, whereas the latter are the actual sound receptor cells. Inner hair cells are responsible for the mechano-electric transduction process in the cochlea; they transduce sound-induced vibrations into a chemical signal leading to an electric signal which is delivered by the auditory nerve to the brain, where auditory information is finally processed.

Degeneration of the hair cells and spiral ganglion neurons (SGNs) in the cochlea leads ultimately to sensorineural hearing loss (SNHL). The World Health Organization has estimated that approximately 5% of the world's population suffer from some form of disabling SNHL [1]. In humans and other mammalian species, the cochlea itself is not able to spontaneously replace lost hair cells and SGNs.

SNHL currently cannot be treated by means of either pharmaceutical or surgical intervention, but auditory function can be partially restored with conventional hearing aids or – in case of severe-to-profound SNHL – with a cochlear implant, which electrically stimulates the residual SGNs in the modiolus directly. Since the first application of this kind of cochlear prosthesis, technology has progressed significantly and this has led to advanced electrode and speech processor strategies resulting in higher performance levels [2, 3]. There nevertheless exists considerable interindividual variability in performance, especially in noisy listening environments. This variability can be explained by regional variations in the distance between the sites of action potential initiation and the electrodes of the cochlear implant resulting from regression of the dendrites of the SGNs [2, 3]. Alternatively, it may be due to neurocellular changes creating variation in the sensitivity of SGNs [4].

It is now generally accepted that the preservation of functional SGNs in sufficiently high numbers along the entire cochlear spiral is crucial with regard to cochlear implant performance [5-7]. Besides local loss of SGN dendrites after prolonged deafness and neural degeneration, variation in electrode position within the cochlea and/or tissue growth (fibrosis and ossification) can also reduce the performance of the cochlear implant [4, 2]. In adults, not much is known about the precise histological

status in the cochlea and the time course of SGN degeneration in deafness and reports are contradictory (cf., [7]). Even less is known about the neural status in deaf children, and probably much depends on the etiology causing the deafness. A growing body of evidence from animal studies suggests that cell-based therapy using stem cells and/or neural progenitor cells may be applied to replace damaged or lost SGNs, and this may eventually result in enhanced cochlear implant performance in patients [8-18]. However, survival of grafted stem cells or neural progenitor cells and their differentiation into SGNs and glial (Schwann) cells as well as their functional integration into extant peripheral auditory structures are a prerequisite to achieve functional repair of the cochlear nerve. This calls for non-invasive *in vivo* visualization of grafted stem cells and longitudinal monitoring of their survival and fate in the cochleas of deafened animals.

Molecular optical imaging based on reporter gene expression is a highly sensitive and versatile imaging modality and is gaining popularity in small animal research, because it allows for real-time tracking of different kinds of grafted cells as well as *in vivo* monitoring of the migration, proliferation and persistence of exogenous cells within the host (for reviews, see [19-21]). In order to track grafted cells by means of whole-body molecular optical imaging, it is essential that these cells stably express reporter molecules that can be visualized. Genetic modification of cells using a lentiviral construct carrying a foreign gene that codes for a fluorescent, or bioluminescent, reporter molecule is a usual approach and results in stable expression of the reporter molecule, which can then be detected by means of either fluorescence or bioluminescence imaging (Fig. 1). Fluorescence imaging is based upon the phenomenon that a fluorophore absorbs energy from a light source and emits light at a different wavelength [22, 23]. Bioluminescence imaging, in contrast, is based upon the emission of light generated during the enzymatic conversion of D-luciferin into oxyluciferin by luciferase enzymes.

We have designed a lentiviral gene construct resulting in stable, equimolar co-expression of a fluorescent (copGFP) and bioluminescent reporter molecule (Luc2), because such a dual-reporter approach exploits the different but complementary advantages of both reporter molecules. Whereas the fluorescent reporter is advantageous for *in vitro* light-microscopical detection of transduced cells and post-mortem visualization of grafted cells in histological sections of the cochlea, the bioluminescent reporter is more suitable for detection of grafted cells using

optical whole-body molecular optical imaging, because of its high sensitivity, a high signal-to-noise ratio – due to low background luminescence levels – and the higher penetration depth, as compared to fluorescence imaging [24-27]. Furthermore, as enzymatic conversion of D-luciferin into oxyluciferin is dependent on ATP and O_2, the bioluminescent signal can be used as a proxy for cell viability and, hence, to confirm the viability of the injected cells.

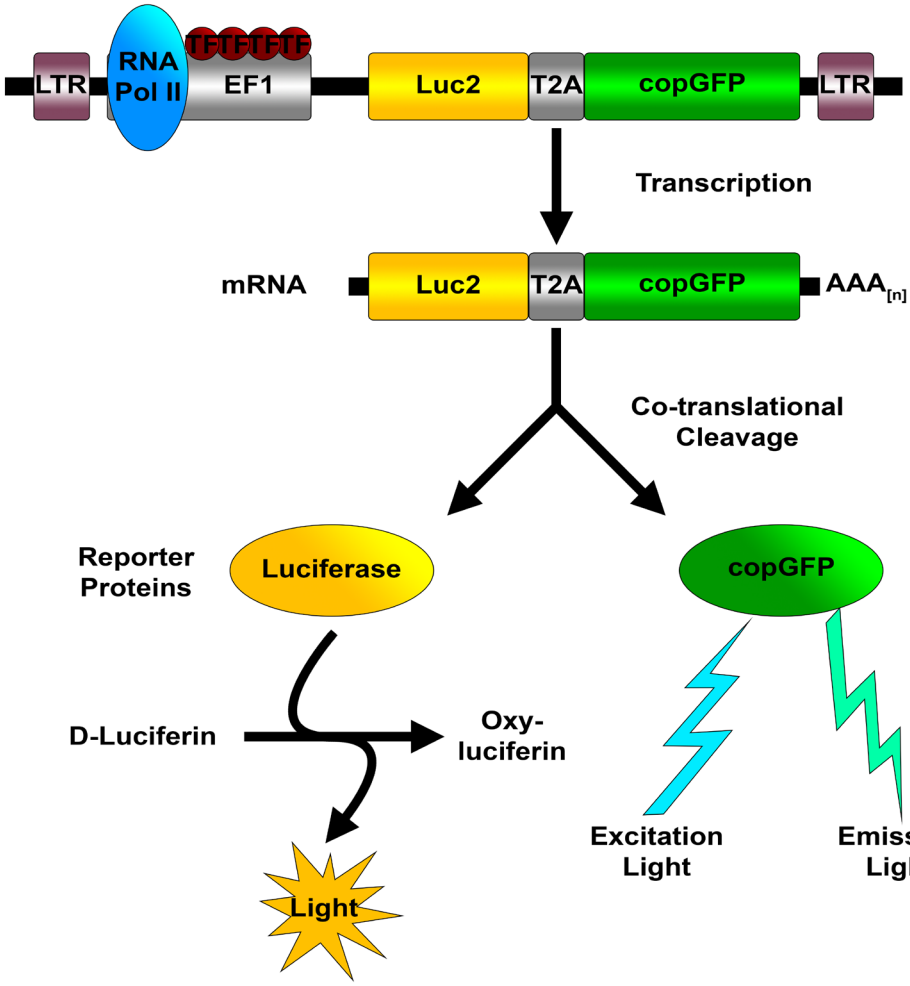

Fig. 1: Schematic drawing explaining the basic principles of dual-reporter gene expression in genetically engineered cells. The lentiviral gene construct is designed to stably co-express copepod green fluorescent protein (copGFP; emitting at ~502 nm) and codon-optimized firefly luciferase Luc2 (emitting at ~560 nm). The copGFP-Luc2 construct is composed of the EF1 promotor and genes coding for copGFP and Luc2. Both genes are coupled via a T2A-like sequence, which mediates co-translational cleavage (ribosome skipping) and, hence, results in bicistronic expression. The inserts are flanked by long terminal repeats (LTR). TF: transcription factors; RNA Pol II: RNA polymerase II.

The objective of this study was to investigate if visualization of exogenous stem cells within the intact cochlea of cadaver guinea pig, using molecular optical imaging, is feasible for future *in vivo* stem cell transplantation experiments. We have used the guinea pig because it is the most commonly used animal model of deafness. However, molecular imaging in the guinea pig is particularly challenging since this species is a newcomer to the field of molecular optical imaging and because the cochlea is embedded within the auditory bulla consisting of compact bone with a high mineral density, which may block signal detection during molecular optical imaging.

Material and methods

Animals

In order to avoid the unnecessary use of living animals, and in compliance with the 3Rs guiding principles for animal experimentation, we have only used cadavers from animals used in non-related experiments.

Cadaver heads (n=26; i.e. 52 cochleas) from adult female guinea pigs (strain: Dunkin Hartley) were obtained from the Department of Pharmaceutical Sciences (Utrecht University, the Netherlands). Animals had been used for non-related experiments. Approval for their use was obtained from the respective Animal Welfare Officers of Utrecht University and Leiden University Medical Center (LUMC).

Surplus C57BL/6 mice served as a source for whisker pads and were obtained from the LUMC Central Animal Facility. The use of surplus mice was approved by the LUMC Animal Experiments Committee (DEC permit 10172).

Cell cultures

Two different types of cells were used in this study: (1) HEK293-copGFP-CBG99 cells, a recently established cell line that stably expresses copGFP and the CBG99 luciferase at an equimolar ratio [23]; and (2) hair-follicle-bulge-derived stem cells (HFBSCs), which have been proved to be multipotent and may differentiate into neurons and glial cells, both *in vitro* and in living animals [28, 29]. HEK293-copGFP-CBG99 cells were used in a series of experiments to determine the implantation approach of first choice (cf., section “Whole-head imaging after cochlear implantation of transduced cells”), because these cells are routinely cultured and abundantly available at our laboratories, in contrast to the HFBSCs. We used HFBSCs, because we aim to use these stem cells in future transplantation experiments.

HEK293-copGFP-CBG99 cells were cultured in Dulbecco’s modified Eagle’s medium (DMEM; Sigma-Aldrich, St. Louis, MO, USA) supplemented with 10% fetal bovine serum (FBS), 2 mM L-glutamine and penicillin/streptomycin solution (diluted 1:100; PAA Laboratories, Pasching, Austria). The cell cultures were maintained in a

humidified incubator with 5% CO_2 at a temperature of 37°C.

HFBSCs were isolated from mouse whiskers according to a previously described protocol [30]. Hair follicles were dissected out from the whisker pads and the bulge region was removed. Explants were transferred to 12-well cell culture plates pre-coated with poly-D-lysine (PDL; Sima-Aldrich, St. Louis, MO, USA), stem cell culture medium was added and stem cells were allowed to migrate from the explant. Stem cell culture medium, modified from Nguyen *et al*. [31], consisted of DMEM/F12 (Biochrom AG, Berlin, Germany) supplemented with Gibco® GlutaMax™-I (Life Technologies™), to which 10% FBS, Gibco® B-27® serum-free supplement (Life Technologies™), N2 supplement (R&D Systems, Minneapolis, MN, USA), epidermal growth factor (20 ng/ml; R&D Systems), basic fibroblast growth factor (20 ng/ml; R&D Systems) and antibiotic/antimycotic solution (diluted 1:100; Sigma-Aldrich) were added.

After one week in culture, the explants were removed, culture medium was changed and cells were allowed to grow until they reached 70-80% confluency. Culture medium was changed twice weekly. Cell cultures were maintained in a humidified incubator with 5% CO_2 at a temperature of 37°C. After several cycles of passage and expansion, cells were trypsinized (0.05% trypsin and 0.02% EDTA.4Na in PBS) for 2 minutes, pelleted by centrifugation at ~280 x *g* for 10 minutes, resuspended (cell density: 1 x 10^6 cells/ml) in FBS containing 10% DMSO and immediately frozen, and stored at -80°C.

Lentiviral vector production and transduction of HFBSCs

We designed a lentiviral gene construct (Fig. 1) that allows stable, equimolar co-expression of copGFP and Luc2. Details on cloning and recombination procedures have been reported previously [23]. In brief, the gene coding for Luc2 is inserted into the multiple cloning site (MCS) of the lentiviral expression vector pCDH-EF1-MCS-T2A-copGFP (SBI System Biosciences, Mountain View, CA, USA), which contains the elongation factor 1α (EF1) promoter and a T2A-like sequence. The T2A peptide mediates co-translational cleavage allowing bicistronic expression [32].

Lentivirus particles were generated by means of calcium-phosphate-mediated

transfection in HEK293 cells [33]. Virus was quantified by antigen-capture ELISA, measuring HIV p24 levels (ZeptoMetrix Corporation, NY, USA). These values were converted to an infectious titer using the approximation that 1 ng of p24 equals 2,500 infectious units. HFBSCs were resuspended in medium and subsequently transduced with pseudoviral particles containing the copGFP-Luc2 construct, using 40 ng virus per 1 x 10^5 cells, followed by storage at -80°C.

Lentiviral vector production and stem cell transduction were performed under appropriate biosafety level conditions (ML-II) in accordance with the National Biosafety Guidelines and Regulations for Research on Genetically Modified Organisms. Procedures and protocols were reviewed and approved by the LUMC Biosafety Committee (GMO permit 00-026).

Loading of transduced HFBSCs with iron oxide nanoparticles

HFBSCs containing the copGFP-Luc2 construct were loaded with superparamagnetic iron oxide nanoparticles (ferumoxytol) according to the procedure of Thu *et al*. [34]. An amount of 4 x 10^6 cells were resuspended in serum-free basic growth medium (BGM) containing 2 IU/ml sodium heparin (LEO Pharma, Amsterdam, the Netherlands), 60 µg/ml protamine hydrochloride (MEDA Pharma BV, Amstelveen, the Netherlands) and 50 µg/ml ferumoxytol (Takeda Pharma A/S, Roskilde, Denmark) followed by incubation at 37°C for 2 hours. An equal amount of BGM containing 20% FBS was added, upon which the cells were transferred to PDL-coated dishes and incubated in a humidified incubator with 5% CO_2 at a temperature of 37°C. After 24 hours, the cells were washed with PBS and then with PBS containing heparin (10 IU/ml). The cells were passaged by adding pre-warmed (37°C) balanced salt solution containing 0.05% trypsin and 0.02% EDTA.4Na (Gibco Life Technologies) to the culture dish and incubation for 2 minutes. Cells were collected and resuspended in PBS at a concentration of 5 x 10^4 cells/µl and stored at 4°C until transplantation.

In vitro light-microscopical detection of reporter molecule expression in transduced HFBSCs

Fluorescence microscopy

Transduced HFBSCs containing the copGFP-Luc2 construct were plated and allowed to attach in PDL-coated 12-well cell culture plates. Real-time observation of copGFP expression was performed using an Olympus IX70 epi-illumination fluorescence microscope (FITC filter settings) equipped with a Leica DFC340 FX digital color camera. Images were acquired and digitally stored using Leica Application Suite Advanced Fluorescence (LASAF) version 1.9 software.

Bioluminescence microscopy

HFBSCs with the copGFP-Luc2 construct were plated and allowed to attach in PDL-coated glass-bottom microwell dishes (MatTek Corporation, Ashland, MA, USA) containing 3 ml of stem cell culture medium. Luc2 expression was assessed in real time using bioluminescence microscopy [35]. For this purpose, an Olympus BX51WIF microscope was fitted with a V240 XY-shifting table (Luigs & Neumann, Ratingen, Germany) and a Hamamatsu ORCA UU-BT-1024G high-resolution, back-thinned CCD camera, and the microscope's main body was enclosed by a custom-made dark box to block external light. D-luciferin (potassium salt; Synchem, Felsberg, Germany) was added at a final concentration of 0.1 mM, i.e. 10-fold lower than that used by Ogoh *et al*. [36]. The bioluminescent signal was recorded over a course of 15 minutes, during which the cells were kept at a temperature of 37°C. Images were acquired and digitally stored using Image-Pro® Plus software, followed by conversion of the grayscale images into pseudocolor images.

In vitro imaging of luciferase expression in transduced HFBSCs

In order to determine the time window for optimal signal measurement, transduced HFBSCs containing the copGFP-Luc2 construct were resuspended in PBS and plated in different amounts (2.5 x 10^4/100 µl or 5 x 10^4 cells/100 µl per well) in black-walled 96-well plates (NUNC™, Rochester, NY, USA). D-luciferin was added at a final concentration of 0.5 mM and bioluminescence was recorded by consecutive 30-second acquisitions during 30 minutes. All images were taken with the IVIS® Spectrum multimodal imaging system (Xenogen, Caliper Life Sciences, Hopkinton,

MA, USA) using an open filter, field of view C (default setting), f/stop=1, and medium binning for all bioluminescence measurements. Image acquisition and analysis were done with Living Image version 4.2.1 software (Caliper Life Sciences, Hopkinton, MA, USA).

Whole-head imaging after cochlear implantation of transduced cells

Real-time observations were performed either on intact auditory bullae after removal from the cadaver heads or on auditory bullae left *in situ* within the cadaver heads. Cells were resuspended in PBS at a density of 1 x 10^6 cells/100 µl. After dilution and addition of D-luciferin (at a final concentration of 15 mg/ml), 5 µl of the cell suspension was injected using a 20-µl Hamilton syringe with a 25-gauge needle. The volume of the perilymphatic injections is less than the total volume (8-10 µl) of perilymph in the guinea pig cochlea [37, 38]. Cell suspensions were also injected into the internal auditory meatus (volume: 10 µl) and into the cochlear modiolus at a volume of ≤5 µl [11, 39, 14].

All imaging measurements were performed with the IVIS® Spectrum multimodal imaging system. Digital images were acquired immediately after injection of the cell suspensions into the cochlea, approximately 15 minutes after addition of D-luciferin to the cell suspension. A grayscale image of the cadaver head was first collected, using the laser scan surface topography modality, followed by the acquisition and overlay of the pseudocolor bioluminescent images. Image acquisition and analysis were done with Living Image version 4.2.1 software using a 30-second acquisition time, open filter, field of view C (default setting), f/stop=1, and medium binning for all bioluminescence measurements.

The imaging experiments were performed at the Small Animal Imaging Unit of the LUMC Central Animal Facility under appropriate biosafety level conditions (DM-II) in accordance with the National Biosafety Guidelines and Regulations for Research on Genetically Modified Organisms.

Validation of cochlear implantation of transduced cells

To determine if the reporter signal passes through the bony capsule of the cochlea, auditory bullae (n=4) were removed from the cadaver heads and HEK293-copGFP-CBG99 cells (5 x 10^4 cells in 10 µl luciferin-containing PBS) were injected directly into the internal auditory meatus followed by imaging of the intact bullae. Next, the auditory bullae were opened to reveal its internal structures and the cochleas were viewed by imaging.

In order to confirm if cells injected into the internal auditory meatus actually reach Rosenthal's canal in the cochlear modiolus, 10 µl of a 1% aqueous solution of methylene blue were injected into the internal auditory meatus. After 30 minutes, the cochleas (n=2) were removed from the auditory bulla, fixed in 2.5% glutaraldehyde in 0.1 M sodium cacodylate/HCl buffer (pH 7.4) for 1 hour, rinsed in the same buffer and decalcified in 10% EDTA.2Na (pH 7.4) at room temperature for one week. Next, the decalcified cochleas were dehydrated in an ascending ethanol series and treated according to the Spalteholz clearing method using methyl salicylate and benzyl benzoate [40] to render the tissues and decalcified bone transparent. Specimens were examined with a Leica M205C stereomicroscope equipped with a Leica IC80 HD color camera. Digital images were acquired and stored using Leica Application Suite (LAS V4.5; Leica Camera AG, Wetzlar, Germany) software.

Comparison of application routes for cochlear implantation

Three different application routes were compared, in order to determine the most convenient approach to introduce transduced cells into the cochlea (Fig. 2). To this end, the auditory bullae were left *in situ* in the cadaver heads.

With the first approach (Fig. 2A), the foramen magnum was opened and widened to expose the internal auditory meatus located in the medial aspect of the auditory bulla. HEK293-copGFP-CBG99 cells (5 x 10^4 cells in 10 µl PBS containing D-luciferin at a final concentration of 15 mg/ml) were injected directly into the internal auditory meatus of the right ear (n=4). The left ear (n=4) was not injected and served as control.

During the second approach (Fig. 2B), a retro-auricular surgical incision was made to expose the skull bone and the right auditory bulla (n=4) was opened with a diamond burr to obtain easy access to the round window niche. HEK293-copGFP-GCB99 cells (5 x 10^4 cells in 5 µl luciferin-containing PBS) were injected directly into the scala tympani through the round window membrane. The left ear (n=4) served as control.

With the third approach (Fig. 2C), HEK293-copGFP-CBG99 cells (5 x 10^4 cells in 5 µl luciferin-containing PBS) were injected into Rosenthal's canal through the round window membrane of the right cochlea (n=4). The left ear (n=4) served as control. As an additional control for all approaches, cells were injected into the left masseter muscle.

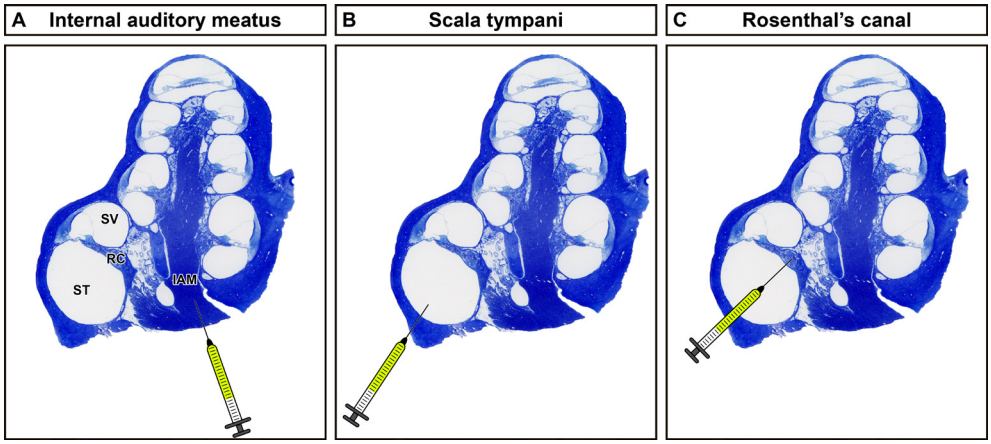

Fig. 2. Illustration of the three different injection routes. **(A)** Injection into the internal auditory meatus. **(B)** Injection into the scala tympani via the round window membrane. **(C)** Injection into Rosenthal's canal via the round window membrane. IAM: internal auditory meatus; ST: scala tympani; SV: scala vestibuli; RC: Rosenthal's canal.

Cell dilution series

In addition, a cell dilution series was performed to determine the amount of cells needed to reach signal threshold for bioluminescent imaging. Transduced HFBSCs containing the copGFP-Luc2 construct were resuspended in PBS at a density of 1 x 10^6 cells per 100 µl. After appropriate dilution and addition of D-luciferin (at a final concentration of 15 mg/ml), different volumes (10 µl, 5 µl, 2.5 µl, and 1 µl) containing 5 x 10^4 cells, 2.5 x 10^4 cells, 1.25 x 10^4 cells and 0.5 x 10^4 cells, respectively, were injected into Rosenthal's canal through the round window membrane (cf., section "Comparison of application routes for cochlear implantation"). Both the right (n=8)

and left cochleas (n=8) were injected, but the left cochleas received the lower amount of cells.

Detection of transduced iron-containing HFBSCs in histological sections of cochleas

To visualize HFBSCs in histological sections of the cochlea, auditory bullae (n=6) were used to inject transduced HFBSCs containing iron oxide nanoparticles (5 x 10^4 cells in 5 µl luciferin-containing PBS) into the scala tympani through the round window membrane (cf., section “Comparison of application routes for cochlear implantation”).

Immediately following imaging, the cochleas were removed from the auditory bullae and fixed by intralabyrinthine perfusion with 4% formaldehyde in 0.1 M sodium cacodylate buffer (pH 7.4) and overnight immersion in the same fixative at 4°C. Next, the cochleas were rinsed in the same buffer and decalcified in 10% EDTA.2Na (pH 7.4) at room temperature for one week. Decalcified cochleas were dehydrated in an ascending ethanol series and xylene followed by paraffin embedding. Serial sections were cut at a thickness of 8 µm along a plane parallel to the central axis of the modiolus, mounted on gelatin-coated glass slides, dewaxed in xylene and rehydrated in a descending ethanol series.

Sections were pre-treated with 3% H_2O_2 in methanol for 30 minutes to inhibit endogenous peroxidase activity and washed in distilled water (30 minutes). Iron-containing nanoparticles were visualized using Perls’ Prussian blue method followed by DAB intensification [41]. Incubation in 1% potassium ferrocyanide ($K_4Fe(CN)_6.3H_2O$) in 1% aqueous hydrochloric acid for 30 minutes was followed by several washes in distilled water (3 x 10 minutes). Next, the sections were incubated in a solution containing 0.1% 3,3’-diaminobenzidine.4HCl and 0.03% H_2O_2 in PBS in the dark for 10 minutes, followed by 3 washes in distilled water (5 minutes each) to stop the reaction. The sections were subsequently mounted in Roti®-Mount FluorCare (Carl Roth GmbH + Co. KG, Karlsruhe, Germany) mounting medium and examined with a Leica DM5500B microscope equipped with a Leica DFC 450C color camera. Digital images were acquired and stored using Leica Application Suite (LAS V4.5; Leica Camera AG, Wetzlar, Germany) software.

Results

Detection of light emanating from the cochlea

In order to determine if it is possible to detect bioluminescent signals emanating from the cochlea *in situ*, HEK293-copGFP-CBG99 cells were injected into the internal auditory meatus of intact auditory bullae. A bright and distinctly localized bioluminescent signal could be seen passing through the tympanic membrane and crevices in the bony wall of the auditory bulla (Fig. 3A). The signal was observed emanating from the round window after opening the bulla and exposing the cochlea (Fig. 3B). This observation indicates that HEK293-copGFP-CBG99 cells, after injection into the cochlea, retain enough luciferase activity to yield detectable bioluminescence.

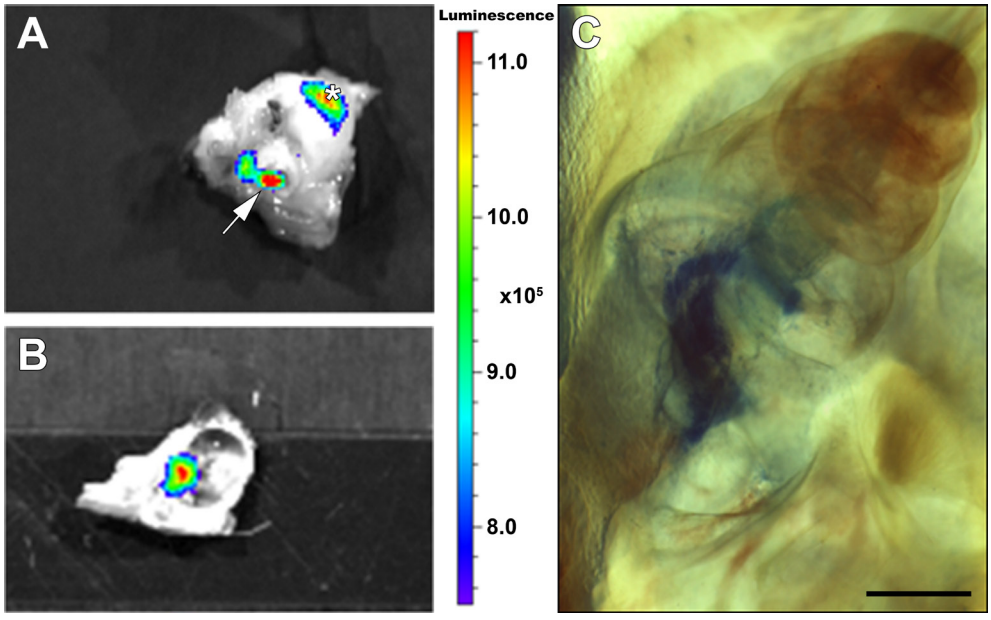

Fig. 3: Detection of bioluminescent signals emanating from the cochlea *in situ* and verification of injection. **(A-B)** Pseudocolor light emission images of an auditory bulla after injection of HEK293-copGFP-CBG99 cells (5 x 10^4 cells in 10 µl PBS containing D-luciferin at a final concentration of 15 mg/ml) directly into the internal auditory meatus. Bioluminescence is expressed as radiance (photons/second/cm^2/steradian). Optical imaging of the auditory bulla after its removal from the skull demonstrates that the bioluminescent signal can pass through the tympanic membrane (arrow) and crevices (*) in the bony wall of the auditory bulla **(A)**. After removing part of the bony wall of the auditory bulla **(B)**, the cochlea can be discerned and a bright bioluminescent signal is observed at the basal cochlear turn, localized near the round window. **(C)** Photomicrograph of a cleared cochlea after injection of a methylene blue solution directly into the internal auditory meatus. Myelin sheaths of the neurons in the basal and middle turns are stained blue, allowing visualization of Rosenthal's canal (scale bar: 1 mm).

In order to confirm if cells injected into the internal auditory meatus actually reach Rosenthal's canal in the modiolus, we injected cochleas with methylene blue. In cleared specimens a distinct blue staining of the myelin sheath of the auditory neurons was present in the basal and middle turns (Fig. 3C).

Comparison of the different application routes

Approach via the internal auditory meatus

The auditory bullae were left *in situ* in the cadaver heads and the foramen magnum was widened to allow easy access to the internal auditory meatus. After injection of HEK293-copGFP-CBG99 cells into the internal auditory meatus of the right auditory bulla, a bright bioluminescent signal was observed in the cavum conchae of the auricle (Fig. 4A), indicating that light generated by enzymatic (luciferase) conversion of D-luciferin is passing through the tympanic membrane and the external auditory meatus.

Approach via the round window: Direct injection into the scala tympani

In this experiment, both auditory bullae were left *in situ* in the cadaver heads. After opening the auditory bulla, HEK293-copGFP-CBG99 cells were injected through the round window membrane directly into the scala tympani. The bioluminescent signal was invariably located near the cavum conchae of the auricle (Fig. 4C), indicating that the light emitted by the cochlea was passing through the tympanic membrane and the external auditory meatus. Control injection into the masseter muscle resulted in much less bioluminescent signal, due to light absorption by tissue chromophores such as oxyhemoglobin, myoglobin and cytochromes (Fig. 4D).

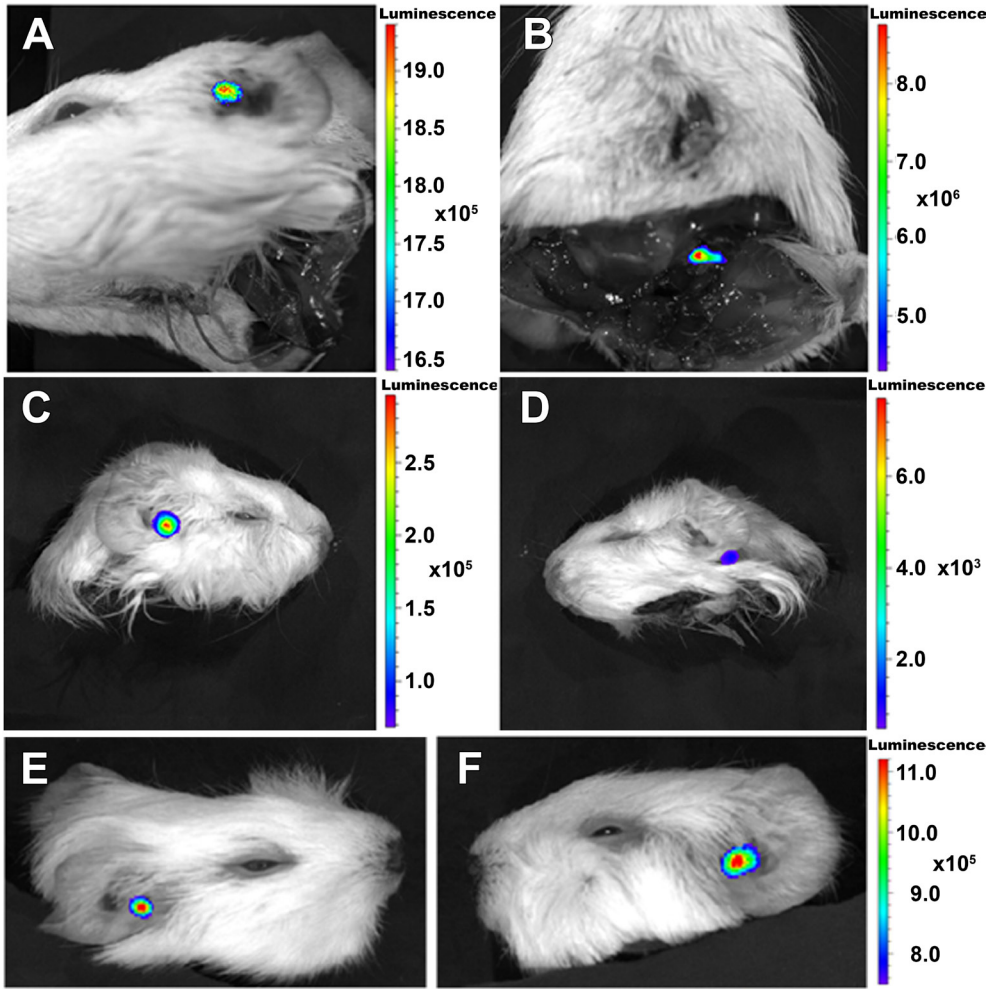

Fig. 4: Comparison of the different application routes. **(A-B)** Pseudocolor light emission images of guinea pig cadaver heads after injection of HEK293-copGFP-CBG99 cells (5 x 10^4 cells in 10 µl PBS containing D-luciferin at a final concentration of 15 mg/ml) into the internal auditory meatus. **(A)** Ventrolateral view of the cadaver head from the left side. Bioluminescent signal is located at the cavum conchae of the auricle. **B:** Ventral view of the same head seen from the rear. A distinct bioluminescent signal is seen emanating from the injection site, i.e. the internal auditory meatus. **(C-D)** Injection of HEK293-copGFP-CBG99 cells (5 x 10^4 cells in 5 µl PBS containing D-luciferin) directly into the scala tympani via the round window membrane. **(C)** Lateral view from the right side showing bioluminescent signal located at the cavum conchae of the auricle. **(D)** Injection of transduced cells into the left masseter muscle results in a considerably lower signal, due to light absorption by tissue chromophores. **(E-F)** Injection of HEK293-copGFP-CBG99 cells (5 x 10^4 cells in 5 µl PBS containing D-luciferin) directly into the modiolus of the basal cochlear turn. After an initial injection in the right ear **(E)** followed by a second injection in the left ear **(F)**, in both ears a bright bioluminescent signal was invariably located near the cavum conchae of the auricle, indicating that the light emanating from the cochlea is passing through the tympanic membrane and the external auditory meatus. Bioluminescence is expressed as radiance (photons/second/cm2/steradian).

Approach via the round window: Direct injection into Rosenthal's canal

Similar results were obtained after injection of HEK293-copGFP-CBG99 cells through the round window membrane, directly into the modiolus of the basal cochlear turn (Figs. 4E-F). Molecular optical imaging of the auditory bullae following their removal from the skull demonstrated that the bioluminescent signal is passing through the tympanic membrane and crevices in the bony wall of the bullae. After opening the auditory bulla to show its internal structures, a distinct bioluminescent signal was seen emanating from the area near the round window, i.e. the site of injection (data not shown; cf., Fig. 3). The finding that the bioluminescent signal was restricted to a small area – rather than being dispersed more widely – indicates that leakage of the fluid after intracochlear injection does not occur.

In future transplantation experiments we aim to introduce transduced stem cells into the spiral ganglion and for that reason injection into Rosenthal's canal is the approach of first choice.

***In vitro* light-microscopical detection of reporter molecule expression in HFBSCs with copGFP-Luc2**

Cultures of transduced HFBSCs containing the copGFP-Luc2 construct were tested for copGFP expression using fluorescence microscopy. Fluorescence micrographs and the corresponding bright-field overlays demonstrate that nearly all cells express copGFP (Figs. 5A-C).

Luc2 expression was verified by means of bioluminescence microscopy. Close examination of the bioluminescent images and the bright-field overlays reveals that the majority of cells express the bioluminescent reporter molecule, implying that the transduced cells have retained their viability (Figs. 5D-F).

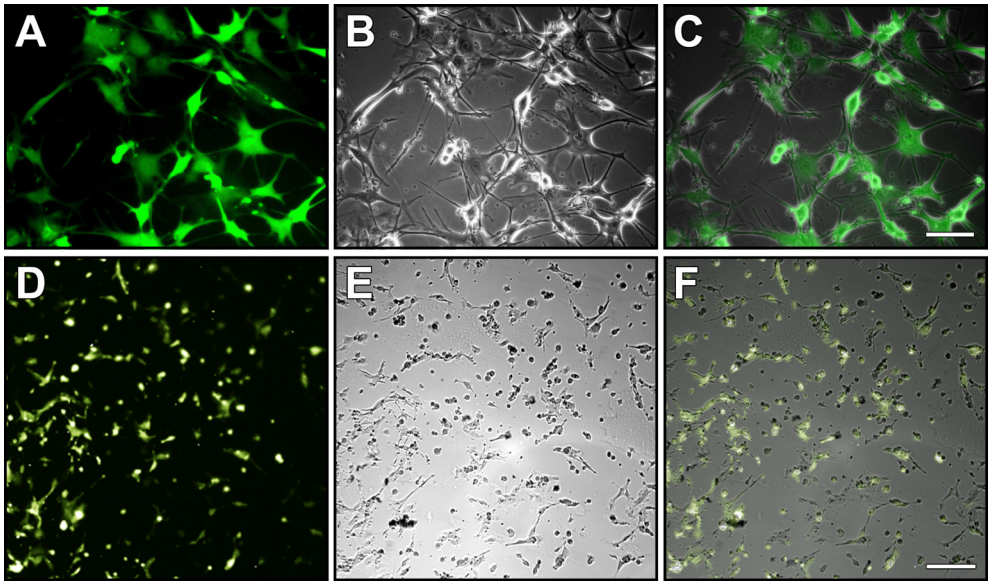

Fig. 5: Detection of reporter molecule expression in HFBSCs expressing copGFP-Luc2. Light micrographs showing reporter molecule expression in cultures of transduced HFBSCs containing the copGFP-Luc2 construct. **(A-C)** Fluorescence microscopy: Fluorescence **(A)** and bright-field **(B)** images of a representative area in the culture were merged and the resulting overlay **(C)** shows that nearly all cells express the fluorescent reporter molecule copGFP (scale bar: 100 µm). **(D-F)** Bioluminescence microscopy: From the overlay **(F)** of the bioluminescence **(D)** and bright-field **(E)** images it is clear that most (i.e., viable) cells express the bioluminescent reporter molecule Luc2 (scale bar: 200 µm).

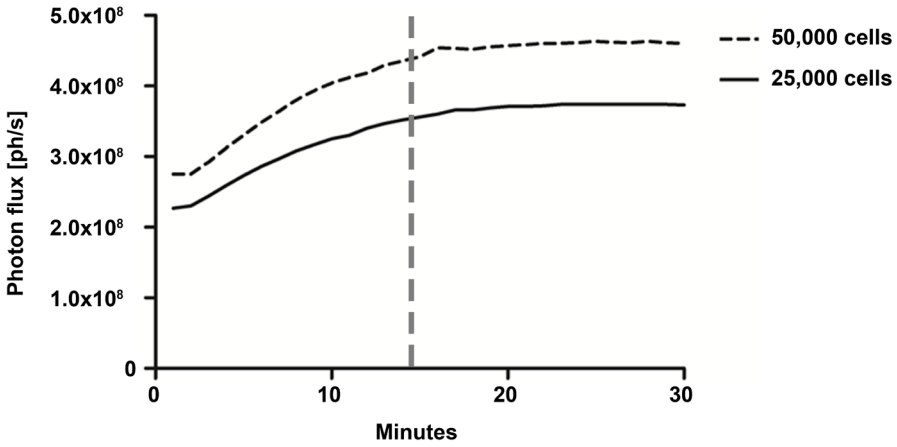

Fig. 6: Time course of the bioluminescent signal observed in cultures of transduced HFBSCs. The signal of transduced HFBSCs containing the copGFP-Luc2 construct gradually increases after addition of D-luciferin (final concentration: 0.5 mM) and reaches its plateau phase after approximately 15 minutes (red line), irrespective of the amount of plated cells (dotted line: 5 x 10^4 cells; solid line: 2.5 x 10^4 cells) studied. Values for each time point and cell amount represent the averaged data sets from 6 wells. Bioluminescence is expressed as photon flux (ph/s: photons/second).

In vitro imaging of luciferase expression in cultures of HFBSCs with copGFP-Luc2

Luc2 emission kinetics were measured in cultures of transduced HFBSCs containing the copGFP-Luc2 construct. Quantitative measurement of Luc2 emission kinetics demonstrates that approximately 15 minutes after addition of D-luciferin the bioluminescent signal reaches its plateau phase (Fig. 6), irrespective of the amount of cells (2.5 x 10^4 cells/100 µl or 5 x 10^4 cells/100 µl) studied. This image acquisition window was used in all subsequent imaging experiments.

Cell dilution series to determine the limit of detection

A cell dilution series was performed to determine the limit of detection for the bioluminescent signal using transduced HFBSCs containing the copGFP-Luc2 construct. A bioluminescent signal of 4.3 ± 0.5 x 10^5 photons/second was detected after round window membrane injection of an amount of 5 x 10^4 cells, while lower signals amounting to 2.0 ± 0.3 x 10^5 and 1.2 ± 0.3 x 10^5 photons/second were detected after injection of 2.5 x 10^4 and 1.25 x 10^4 cells, respectively (cf., Figs. 7A-C). Injection of 0.5 x 10^4 cells did not result in a detectable bioluminescent signal (Fig. 7D). Quantitative analysis shows that the threshold for bioluminescence imaging lies between 0.5 x 10^4 cells and 1.25 x 10^4 cells (Fig. 7E).

Detection of iron-containing HFBSCs in histological sections of cochleas

Transduced HFBSCs containing iron oxide nanoparticles could be visualized in dewaxed histological sections of the cochlea using the Perls' Prussian blue method and DAB intensification (Fig. 8A).

CopGFP-expressing cells in deparaffinized histological sections of the cochlea showed a green-fluorescent signal. However, most probably due to formaldehyde fixation, several cochlear structures (bony capsule, bony modiolus) and tissues (e.g., spiral ganglion cells and myelin sheaths of the auditory neurons) showed a high cellular autofluorescence in the same range of the spectrum, at which copGFP emits light (Fig. 8B). Therefore, our strategy to load the transduced cells also with

iron oxide nanoparticles proved to be prudent. Immunohistochemical detection with specific antibodies to copGFP was therefore not necessary.

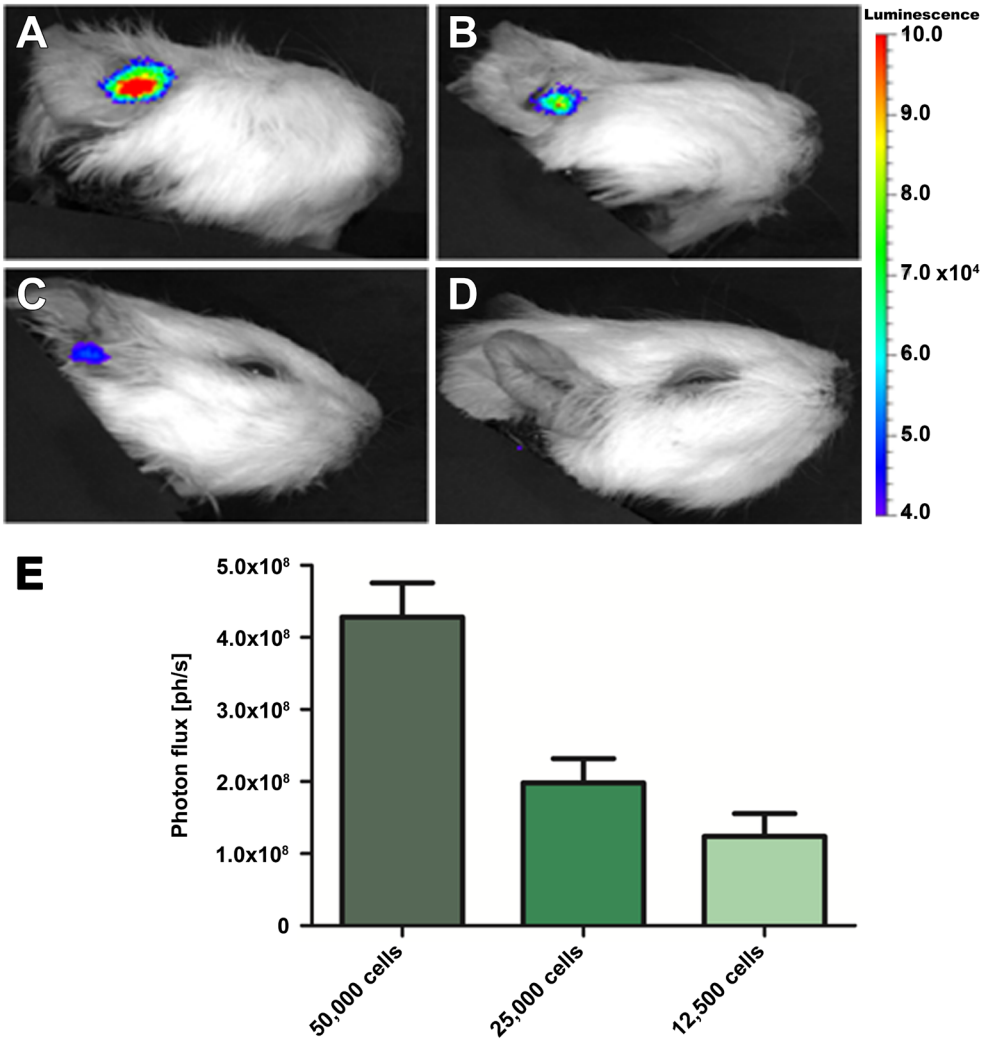

Fig. 7: Cell dilution series. **(A-D)** To determine the amount of transduced HFBSCs (containing the copGFP-Luc2 construct) needed to reach signal threshold for bioluminescence imaging a cell dilution series was performed. Bioluminescence is expressed as radiance (photons/second/cm^2/steradian). Cells were resuspended in PBS at a concentration of 1 x 10^6 cells/100 µl followed by addition of D-luciferin (final concentration: 15 mg/ml). Different amounts of cells were injected into the modiolus of the basal cochlear turn in the right ear. A bright bioluminescent signal was seen after injection of 5 x 10^4 cells **(A)**. Considerably lower signals were detected after injection of 2.5 x 10^4 cells **(B)** and 1.25 x 10^4 cells **(C)**. Injection of 0.5 x 10^4 cells **(D)** did not result in a detectable bioluminescent signal. **(E)** Quantitative measurement of the bioluminescent signal shows that the threshold for bioluminescence imaging lies between 0.5 x 10^4 cells and 1.25 x 10^4 cells. Bioluminescence is expressed as photon flux (ph/s: photons/second).

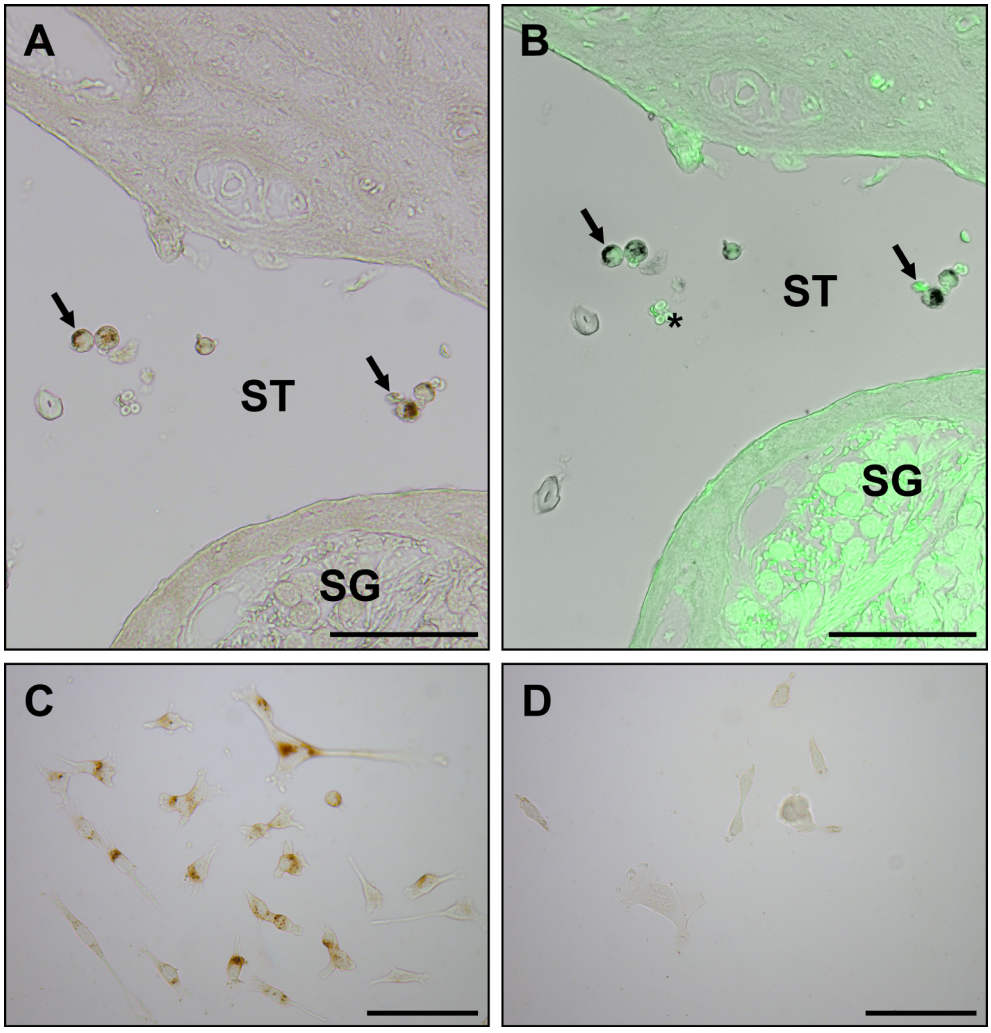

Fig. 8: Perls' Prussian blue staining of transduced HFBSCs containing ferumoxytol. Histochemical visualization of non-heme iron in transduced HFBSCs containing iron oxide nanoparticles (ferumoxytol) using the method with DAB intensification. Dark brown precipitates represent the presence of intracellular iron accumulations. **(A)** Iron accumulations in transduced iron-containing HFBSCs (arrows) after injection into the scala tympani (ST) of the cochlea. The spiral ganglion (SG) does not contain iron accumulations. **(B)** Same section, but with overlay of grayscale bright field image with the green-fluorescent signal, demonstrating that iron-containing HFBSCs also express copGFP (arrows). However, spiral ganglion cells, myelin sheath, bone matrix, and erythrocytes (*) demonstrate autofluorescence at the same wavelengths. **(C)** Iron accumulations in transduced HFBSCs in culture dishes after uploading with ferumoxytol nanoparticles. **(D)** Transduced HFBSCs (control) that have not been uploaded with ferumoxytol nanoparticles do not demonstrate any intracellular deposits after treatment with the Perls' Prussian blue method and DAB intensification (scale bar: 100 µm).

Discussion

The objective of this study was to investigate if visualization of exogenous stem cells within the intact guinea pig cochlea, using molecular optical imaging, is feasible for future *in vivo* stem cell transplantation experiments. To the best of our knowledge, this is the first study that has been undertaken to detect luciferase-expressing cells in the intact cochlea of guinea pigs using bioluminescence imaging. Although other authors have tracked green-fluorescent stem cells in histological sections of the cochlea from various rodent species using fluorescence microscopy [9, 12, 42, 43, 39, 44], the present study is the first that uses molecular optical imaging for the non-destructive *in situ* detection of bioluminescent stem cells injected into an anatomically complex structure such as the cochlea.

Whole-specimen imaging has been used to make three-dimensional reconstructions of rodent cochleas using digitized optical sections obtained from a variety of fluorescence-based microscopical techniques, such as orthogonal-plane fluorescence optical sectioning microscopy [40, 45], confocal laser scanning microscopy [46-48], thin-sheet laser imaging microscopy [49] and, more recently, two-photon excitation fluorescence microscopy which uses near-infrared excitation wavelengths [50, 51]. However, none of these approaches can be used in sedated animals as they require *post-mortem* removal of the cochlea from the auditory bulla and rigorous preparatory steps, involving chemical fixation, decalcification, dehydration and clearing. Non-destructive or minimally invasive *in vivo* imaging modalities – such as fluorescence intravital microscopy [52], fluorescence microendoscopy, optical coherence tomography [53], and magnetic resonance imaging – can be used to study cochlear blood flow and anatomy in sedated animals, but do not allow real-time tracking of cells in living animals. However, recent studies have shown that bioluminescence imaging is a valid and efficient imaging technique, in particular in small rodents [54-57].

Our results demonstrate that light emanating from the cochlea can be detected using bioluminescence imaging. We assume that the light does not penetrate the bony capsule of the cochlea nor the thick bone of the auditory bulla, but emanates from the round window membrane and is then reflected by the inner wall of the bulla and escapes through the tympanic membrane and the external auditory meatus. The spatial resolution of bioluminescence imaging is 3-5 mm with a penetration

depth of 1-3 cm [25, 26]. The distance from round window to tympanic membrane in the guinea pig measures approximately 2 mm, whereas the distance from the round window to the distal end of the bony part of the external auditory meatus is approximately 5 mm [40]. The external auditory meatus, measured from its proximal end at the tympanic membrane to its distal opening, i.e. cavum conchae, including the bony and cartilaginous walls, is approximately 4.45-7.45 mm long, with an average length of 5.77 mm [58]. These considerations suggest that fluorescence imaging with a spatial resolution of 2-3 mm and a penetration depth of only 5-7 mm [26] cannot be used to visualize cells in the cochlea of guinea pigs. Moreover, it should be emphasized that not only is penetration depth a limiting factor, but also absorbance of light due to tissue chromophores, such as oxyhemoglobin, myoglobin and cytochromes, may result in a reduction of photon yield at or near the site of injection (cf., Fig. 4B).

Bioluminescence imaging is a highly sensitive technique, detecting amounts of the reporter molecule as low as 10^{-15}-10^{-17} M [27]. In contrast, fluorescence imaging detects reporter molecule amounts that are in the range of 10^{-9}-10^{-12} M [27]. Also in favor of bioluminescence is its signal-to-noise ratio which is high for luciferase-based systems, but low for fluorescent proteins [24, 27]. Furthermore, as a result of codon optimization, the expression of Luc2, is considerably higher than that of the commonly used wild-type firefly luciferase. *In vivo*, its photon yield is higher than that of the green-emitting click beetle luciferase CBG99 [23] and its spectrum of emission is more red-shifted, thus allowing injection of a 10-fold lower amount of cells, i.e. 10^5 cells instead of 10^6 cells.

Temporal resolution of bioluminescence imaging is in the range of minutes, with average image acquisition times of 10 minutes [24]. With the settings as used in our study, the bioluminescent signal reaches plateau phase approximately 10-15 minutes after addition of D-luciferin to the cell suspension. The plateau phase lasts for approximately 30-40 minutes. This allows data and image acquisition within a temporal window during which signal emission remains stable. Nevertheless, it should be emphasized that luciferase emission kinetics after injection of the luciferin-containing cell suspension in the cadaver head will be different from that after intravenous or intraperitoneal injection of D-luciferin alone in a living animal.

In small animals, such as mice and rats, D-luciferin at a dose of 150 mg/kg is typically

used and this is adequate for bioluminescence imaging of most organs. However, higher concentrations of D-luciferin resulting in higher signal emission [59] and new luciferase substrates (e.g., CycLuc1) to maximize photon emission [60] have been recently used to improve bioluminescence imaging in specific applications. In the guinea pig, we cannot inject D-luciferin by means of intravenous injections – because of the absence of a tail (vein) – and shall have to resort to other application routes, such as intraperitoneal injection. In future *in vivo* experiments, longitudinal monitoring of grafted stem cells requires repeated bioluminescence imaging sessions in the same individual and, hence, repeated injections with D-luciferin. For that purpose, D-luciferin can be applied either via repeated middle ear instillation – as used by Kanzaki *et al*. [54] to demonstrate GFAP-expressing cells in cochleas of transgenic GFAP-Luc mice – or chronically by means of an osmotic minipump with a large infusion reservoir or by repeated intraperitoneal injections.

The advantage of using the construct coding for Luc2 and copGFP is that both proteins are translated as single proteins in an equimolar ratio as a result of co-translational cleavage ('ribosome skipping') mediated by the T2A-like sequence in the bicistronic construct [32]. Efficiency of transduction can then easily be estimated by using fluorescence microscopy.

We have chosen for copGFP, as it has a higher photon yield as compared to other naturally occurring fluorescent proteins and because of the varied availability of antibodies against this protein, enabling *post-mortem* immunohistochemical demonstration of injected cells in histological sections.

Alternatively, injected stem cells containing iron oxide nanoparticles (e.g., ferumoxytol) can be detected in histological sections using the Perls' Prussian blue method with DAB intensification. With this method we were able to identify ferumoxytol-containing HFBSCs after injection in the scala tympani, avoiding autofluorescence of cochlear tissues. However, we did not find iron-containing HFBSCs within the spiral ganglion in histological sections of the cochleas. Apparently, proper engraftment of cells into the modiolus was not achieved, since we injected the cells in non-viable tissue of guinea pig cadaver heads. We cannot conclude other than that most cells got flushed out during injection and subsequent tissue fixation and processing steps. In addition, we expect that iron oxide-containing cells will be easily detectable in living animals by means of magnetic resonance imaging (cf., [30]. However, the aim of this study

was to visualize luciferase-expressing cells within the intact guinea pig cochlea, and in this we succeeded.

In this study we have used guinea pig cadavers, but we are confident that the transduced cells will also express a high level of bioluminescence in a living animal. This is supported by the *in vitro* finding that transduced HFBSCs express luciferase activity after multiple proliferation cycles over a period of 15 weeks [30], which makes us confident to assume that these cells are capable to retain their ability to express luciferase after cochlear injection in living animals. For implantation purposes, the number of cells that is injected into the cochlear modiolus varies between 5 x 10^4 and 2 x 10^5 [11, 39, 14]. Our cell dilution experiment shows that the limit of detection for bioluminescence of the transduced HFBSCs is between 0.5 x 10^4 and 1.25 x 10^4 cells after injection into Rosenthal's canal in the basal turn of the cochlea. Based upon an initial amount of 2 x 10^5 cells, this would mean that approximately 5% of the population of grafted cells would suffice for detection. However, one may ask if such a low percentage of surviving cells may ultimately result in a sufficient degree of regeneration, taking into account the massive amount of cell debris and dead cells. This will be studied in a series of stem cell transplantation experiments in living, deafened guinea pigs.

In conclusion, this feasibility study demonstrates that bioluminescence imaging enables visualization of luciferase-expressing, exogenous stem cells in the intact guinea pig cochlea.

Acknowledgements

We are grateful to Hans Sturkenboom (Department of Pharmacological Sciences, Utrecht University, the Netherlands) for kindly providing the guinea pig cadaver heads. We thank Renate Buijink and Stephan Michel (Laboratory for Neurophysiology, LUMC, Leiden, the Netherlands) for technical assistance and the use of their bioluminescence microscope.

This project is financially supported by grants from Stichting Het Heinsius-Houbolt Fonds, the Netherlands. Timo Schomann was financially supported by MED-EL (Innsbruck, Austria) and Percuros B.V. (Alan Chan and Ronny Fassnacht) through funding from the European Commission of the H2020-MSCA-RISE-2014 award through the PRISAR project (grant number 644373) and the H2020-MSCA-RISE-2016 award through the CHARMED project (grant number 734684).

Copyright

This is an open access article under the terms of the Creative Commons Attribution License, which permits use, distribution and reproduction in any medium.

References

1. WHO. Deafness and hearing loss. WHO Fact Sheet No. 300; http://www.who.int/mediacentre/factsheets/fs300/en/index.html 2017 [cited 2017/05/22]; Available from: http://www.who.int/mediacentre/factsheets/fs300/en/index.html.
2. Bierer, J.A., Faulkner, K.F., and Tremblay, K.L., Identifying cochlear implant channels with poor electrode-neuron interfaces: Electrically evoked auditory brain stem responses measured with the partial tripolar configuration. Ear Hear., 2011. **32**: pp. 436-444.
3. Kalkman, R.K., Briaire, J.J., and Frijns, J.H.M., Current focussing in cochlear implants: An analysis of neural recruitment in a computational model. Hear. Res., 2015. **322**: pp. 89-98.
4. Briaire, J.J. and Frijns, J.H.M., The consequences of neural degeneration regarding optimal cochlear implant position in scala tympani: A model approach. Hear. Res., 2006. **214**: pp. 17-27.
5. Gantz, B.J., Woodworth, G.G., Knutson, J.F., Abbas, P.J., and Tyler, R.S., Multivariate predictors of audiological success with multichannel cochlear implants. Ann. Otol. Rhinol. Laryngol., 1993. 102: pp. 909-916.
6. 6. Eppsteiner, R.W., Shearer, A.E., Hildebrand, M.S., DeLuca, A.P., Ji, H., Dunn, C.C., Black-Ziegelbein, E.A., Casavant, T.L., Braun, T.A., Scheetz, T.E., Scherer, S.E., Hansen, M.R., Gantz, B.J., and Smith, R.J.H., Prediction of cochlear implant performance by genetic mutation: The spiral ganglion hypothesis. Hear. Res., 2012. **292**: pp. 51-58.
7. Snel-Bongers, J., Briaire, J.J., van der Veen, E.H., Kalkman, R.K., and Frijns, J.H., Threshold levels of dual electrode stimulation in cochlear implants. J. Assoc. Res. Otolaryngol., 2013. **14**: pp. 781-790.
8. Rask-Andersen, H., Bostrom, M., Gerdin, B., Kinnefors, A., Nyberg, G., Engstrand, T., Miller, J.M., and Lindholm, D., Regeneration of human auditory nerve. *In vitro*/*in video* demonstration of neural progenitor cells in adult human and guinea pig spiral ganglion. Hear. Res., 2005. **203**: pp. 180-191.
9. Regala, C., Duan, M., Zou, J., Salminen, M., and Olivius, P., Xenografted fetal dorsal root ganglion, embryonic stem cell and adult neural stem cell survival following implantation into the adult vestibulocochlear nerve. Exp. Neurol., 2005. **193**: pp. 326-333.
10. Coleman, B., Hardman, J., Coco, A., Epp, S., De Silva, M., Crook, J., and Shepherd, R., Fate of embryonic stem cells transplanted into the deafened mammalian cochlea. Cell Transplant., 2006. **15**: pp. 369-380.
11. Corrales, C.E., Pan, L., Li, H., Liberman, M.C., Heller, S., and Edge, A.S., Engraftment and differentiation of embryonic stem cell-derived neural progenitor cells in the cochlear nerve trunk: Growth of processes into the organ of Corti. J. Neurobiol., 2006. **66**: pp. 1489-1500.
12. Hu, Z. and Ulfendahl, M., Cell replacement therapy in the inner ear. Stem Cells Dev., 2006. **15**: pp. 449-459.
13. Sekiya, T., Kojima, K., Matsumoto, M., Holley, M.C., and Ito, J., Rebuilding lost hearing using cell transplantation. Neurosurgery, 2007. **60**: pp. 417-433.
14. Chen, W., Jongkamonwiwat, N., Abbas, L., Eshtan, S.J., Johnson, S.L., Kuhn, S., Milo, M., Thurlow, J.K., Andrews, P.W., Marcotti, W., Moore, H.D., and Rivolta, M.N., Restoration of auditory evoked responses by human ES-cell-derived otic progenitors. Nature, 2012. **490**: pp. 278-282.
15. Gunewardene, N., Dottori, M., and Nayagam, B.A., The convergence of cochlear implantation with induced pluripotent stem cell therapy. Stem Cell Rev., 2012. **8**: pp. 741-754.
16. Huisman, M.A. and Rivolta, M.N., Neural crest stem cells and their potential application in a therapy for deafness. Front. Biosci. (Schol. Ed.), 2012. **4**: pp. 121-132.
17. Needham, K., Minter, R.L., Shepherd, R.K., and Nayagam, B.A., Challenges for stem cells to functionally repair the damaged auditory nerve. Expert Opin. Biol. Ther., 2013. **13**: pp. 85-101.
18. Shi, F. and Edge, A.S., Prospects for replacement of auditory neurons by stem cells. Hear. Res., 2013. **297**: pp. 106-112.
19. De Almeida, P.E., Van Rappard, J.R., and Wu, J.C., *In vivo* bioluminescence for tracking cell fate and function. Am. J. Physiol. Heart Circ. Physiol., 2011. **301**: pp. H663-671.
20. Welsh, D.K. and Noguchi, T., Cellular bioluminescence imaging. Cold Spring Harb. Protoc., 2012. **2012**: pp. 852-866.
21. Mezzanotte, L., Van 't Root, M., Karatas, H., Goun, E.A., and Lowik, C., *In vivo* molecular bioluminescence imaging: New tools and applications. Trends Biotechnol., 2017. **35**: pp. 640-652.
22. Shagin, D.A., Barsova, E.V., Yanushevich, Y.G., Fradkov, A.F., Lukyanov, K.A., Labas, Y.A., Semenova, T.N., Ugalde, J.A., Meyers, A., Nunez, J.M., Widder, E.A., Lukyanov, S.A., and Matz, M.V., GFP-like proteins as ubiquitous metazoan superfamily: Evolution of functional features and structural complexity. Mol. Biol. Evol., 2004. **21**: pp. 841-850.
23. Mezzanotte, L., Aswendt, M., Tennstaedt, A., Hoeben, R., Hoehn, M., and Löwik, C., Evaluating reporter genes of different luciferases for optimized *in vivo* bioluminescence imaging of transplanted neural stem cells in the brain. Contrast Media Mol. Imaging, 2013. **8**: pp. 505-513.
24. Choy, G., O'Connor, S., Diehn, F.E., Costouros, N., Alexander, H.R., Choyke, P., and Libutti, S.K., Comparison of noninvasive fluorescent and bioluminescent small animal optical imaging. BioTechniques., 2003. **35**: pp. 1022-1026, 1028-1030.
25. Massoud, T.F. and Gambhir, S.S., Molecular imaging in living subjects: Seeing fundamental biological processes in a new light. Genes Dev., 2003. **17**: pp. 545-580.
26. Shah, K. and Weissleder, R., Molecular optical imaging: Applications leading to the development of present day therapeutics. NeuroRx, 2005. **2**: pp. 215-225.
27. Zhao, C., Tian, M., and Zhang, H., *In vivo* stem cell imaging. Open Nucl. Med. J., 2010. **2**: pp. 171-177.
28. Liu, F., Uchugonova, A., Kimura, H., Zhang, C., Zhao, M., Zhang, L., Koenig, K., Duong, J., Aki, R., Saito, N., Mii, S., Amoh, Y., Katsuoka, K., and Hoffman, R.M., The bulge area is the major hair follicle source of nestin-expressing pluripotent stem cells which can repair the spinal cord compared to the dermal papilla. Cell Cycle, 2011. **10**: pp. 830-839.
29. Gho, C.G., Schomann, T., De Groot, S.C., Frijns, J.H.M., Rivolta, M.N., Neumann, M.H., and Huisman, M.A., Isolation, expansion and neural differentiation of stem cells from human plucked hair: A further step towards autologous nerve recovery. Cytotechnology, 2016. **68**: pp. 1849-1858.

30. Schomann, T., Mezzanotte, L., Lourens, I.-A.-L.M., de Groot, J.C.M.J., Frijns, J.H.M., and Huisman, M.A., Lentiviral transduction and subsequent loading with nanoparticles do not affect cell viability and proliferation in hair-follicle-bulge-derived stem cells *in vitro*. Contrast Media Mol. Imaging, 2016. **11**: pp. 550-560.
31. Nguyen, T.D., Widera, D., Greiner, J., Muller, J., Martin, I., Slotta, C., Hauser, S., Kaltschmidt, C., and Kaltschmidt, B., Prolonged cultivation of hippocampal neural precursor cells shifts their differentiation potential and selects for aneuploid cells. Biol. Chem., 2013. **394**: pp. 1623-1636.
32. Szymczak, A.L. and Vignali, D.A., Development of 2A peptide-based strategies in the design of multicistronic vectors. Expert Opin. Biol. Ther., 2005. **5**: pp. 627-638.
33. Abbas, L., Seppen, J., Barry, S.C., Klinkspoor, J.H., Katen, L.J., Lee, S.P., Garcia, J.V., and Osborne, W.R.A., Apical gene transfer into quiescent human and canine polarized intestinal epithelial cells by lentivirus vectors. J. Virol., 2000. **74**: pp. 7642-7645.
34. Thu, M.S., Bryant, L.H., Coppola, T., Jordan, E.K., Budde, M.D., Lewis, B.K., Chaudhry, A., Ren, J., Varma, N.R., Arbab, A.S., and Frank, J.A., Self-assembling nanocomplexes by combining ferumoxytol, heparin and protamine for cell tracking by magnetic resonance imaging. Nat. Med., 2012. **18**: pp. 463-467.
35. Buijink, M.R., Almog, A., Wit, C.B., Roethler, O., Olde Engberink, A.H.O., Meijer, J.H., Garlaschelli, D., Rohling, J.H.T., and Michel, S., Evidence for weakened intercellular coupling in the mammalian circadian clock under long photoperiod. PLoS ONE, 2016. **11**: pp. e0168954.
36. Ogoh, K., Akiyoshi, R., May Maw, T., Sugiyama, T., Dosaka, S., Hatta-Ohashi, Y., and Suzuki, H., Bioluminescence microscopy using a short focal-length imaging lens. J. Microsc., 2014. **253**: pp. 191-197.
37. Thorne, M., Salt, A.N., DeMott, J.E., Henson, M.M., Henson, O.W., Jr., and Gewalt, S.L., Cochlear fluid space dimensions for six species derived from reconstructions of three-dimensional magnetic resonance images. Laryngoscope, 1999. **109**: pp. 1661-1668.
38. Shinomori, Y., Jones, D.d., Spack, D.S., and Kimura, R.S., Volumetric and dimensional analysis of the guinea pig inner ear. Ann. Otol. Rhinol. Laryngol., 2001. **110**: pp. 91-98.
39. Ogita, H., Nakagawa, T., Lee, K.Y., Inaoka, T., Okano, T., Kikkawa, Y.S., Sakamoto, T., and Ito, J., Surgical invasiveness of cell transplantation into the guinea pig cochlear modiolus. ORL J. Otorhinolaryngol. Relat. Spec., 2009. **71**: pp. 32-39.
40. Voie, A.H., Imaging the intact guinea pig tympanic bulla by orthogonal-plane fluorescence optical sectioning microscopy. Hear. Res., 2002. **171**: pp. 119-128.
41. Meguro, R., Asano, Y., Odagiri, S., Li, C., Iwatsuki, H., and Shoumura, K., Nonheme-iron histochemistry for light and electron microscopy: A historical, theoretical and technical review. Arch. Histol. Cytol., 2007. **70**: pp. 1-19.
42. Sekiya, T., Kojima, K., Matsumoto, M., Kim, T.S., Tamura, T., and Ito, J., Cell transplantation to the auditory nerve and cochlear duct. Exp. Neurol., 2006. **198**: pp. 12-24.
43. Bogaerts, S., Douglas, S., Corlette, T., Pau, H., Saunders, D., McKay, S., and Oleskevich, S., Microsurgical access for cell injection into the mammalian cochlea. J. Neurosci. Methods, 2008. **168**: pp. 156-163.
44. Kasagi, H., Kuhara, T., Okada, H., Sueyoshi, N., and Kurihara, H., Mesenchymal stem cell transplantation to the mouse cochlea as a treatment for childhood sensorineural hearing loss. Int. J. Pediatr. Otorhinolaryngol., 2013. **77**: pp. 936-942.
45. Hofman, R., Segenhout, J.M., and Wit, H.P., Three-dimensional reconstruction of the guinea pig inner ear, comparison of OPFOS and light microscopy, applications of 3D reconstruction. J. Microsc., 2009. **233**: pp. 251-257.
46. MacDonald, G.H. and Rubel, E.W., Three-dimensional imaging of the intact mouse cochlea by fluorescent laser scanning confocal microscopy. Hear. Res., 2008. **243**: pp. 1-10.
47. Kopecky, B.J., Duncan, J.S., Elliott, K.L., and Fritzsch, B., Three-dimensional reconstructions from optical sections of thick mouse inner ears using confocal microscopy. J. Microsc., 2012. **248**: pp. 292-298.
48. Wrzeszcz, A., Reuter, G., Nolte, I., Lenarz, T., and Scheper, V., Spiral ganglion neuron quantification in the guinea pig cochlea using confocal laser scanning microscopy compared to embedding methods. Hear. Res., 2013. **306**: pp. 145-155.
49. Santi, P.A., Light sheet fluorescence microscopy: A review. J. Histochem. Cytochem., 2011. **59**: pp. 129-138.
50. Yuan, T., Gao, S.S., Saggau, P., and Oghalai, J.S., Calcium imaging of inner ear hair cells within the cochlear epithelium of mice using two-photon microscopy. J. Biomed. Opt., 2010. **15**: pp. 016002.
51. Yang, X., Pu, Y., Hsieh, C.L., Ong, C.A., Psaltis, D., and Stankovic, K.M., Two-photon microscopy of the mouse cochlea in situ for cellular diagnosis. J. Biomed. Opt., 2013. **18**: pp. 31104.
52. Shi, X., Zhang, F., Urdang, Z., Dai, M., Neng, L., Zhang, J., Chen, S., Ramamoorthy, S., and Nuttall, A.L., Thin and open vessel windows for intra-vital fluorescence imaging of murine cochlear blood flow. Hear. Res., 2014. **313**: pp. 38-46.
53. Tona, Y., Sakamoto, T., Nakagawa, T., Adachi, T., Taniguchi, M., Torii, H., Hamaguchi, K., Kitajiri, S., and Ito, J., *In vivo* imaging of mouse cochlea by optical coherence tomography. Otol. Neurotol., 2014. **35**: pp. e84-89.
54. Kanzaki, S., Fujioka, M., Yasuda, A., Shibata, S., Nakamura, M., Okano, H.J., Ogawa, K., and Okano, H., Novel *in vivo* imaging analysis of an inner ear drug delivery system in mice: Comparison of inner ear drug concentrations over time after transtympanic and systemic injections. PLoS ONE, 2012. **7**: pp. e48480.
55. Meltser, I., Cederroth, C.R., Basinou, V., Savelyev, S., Lundkvist, G.S., and Canlon, B., TrkB-mediated protection against circadian sensitivity to noise trauma in the murine cochlea. Curr. Biol., 2014. **24**: pp. 658-663.
56. Kanzaki, S., Watanabe, K., Fujioka, M., Shibata, S., Nakamura, M., Okano, H.J., Okano, H., and Ogawa, K., Novel *in vivo* imaging analysis of an inner ear drug delivery system: Drug availability in inner ear following different dose of systemic drug injections. Hear. Res., 2015. 330: pp. 142-146.
57. Park, J.S., Cederroth, C.R., Basinou, V., Meltser, I., Lundkvist, G., and Canlon, B., Identification of a circadian clock in the inferior colliculus and its dysregulation by noise exposure. J. Neurosci., 2016. **36**: pp. 5509-5519.
58. Wysocki, J. and Sharifi, M., Measurements of selected parameters of the guinea pig temporal bone. Folia Morphol. (Warsz), 2005. **64**: pp. 145-150.
59. Aswendt, M., Adamczak, J., Couillard-Despres, S., and Hoehn, M., Boosting bioluminescence neuroimaging: An optimized protocol for brain studies. PLoS One, 2013. **8**: pp. e55662.
60. Evans, M.S., Chaurette, J.P., Adams, S.T., Jr., Reddy, G.R., Paley, M.A., Aronin, N., Prescher, J.A., and Miller, S.C., A synthetic luciferin improves bioluminescence imaging in live mice. Nat. Methods, 2014. **11**: pp. 393-395.

Chapter 6

Ouabain does not induce selective spiral ganglion cell degeneration in guinea pigs

BioMed Research International, 2018

Article# 1568414

T. Schomann, D. Ramekers, J.C.M.J. De Groot, C.H. van der Ploeg, F.G.J. Hendriksen, S. Böhringer, S.F.L. Klis, J.H.M. Frijns, M.A. Huisman

Abstract

Round window membrane (RWM) application of ouabain is known to selectively destroy type-I spiral ganglion cells (SGCs) in cochleas of several rodent species, while leaving hair cells intact. This protocol has been used in rats and Mongolian gerbils, but observations in the guinea pig are conflicting This is why we re-investigated the effect of ouabain on the guinea pig cochlea.

Ouabain solutions of different concentrations (0.01 mM, 0.1 mM, 1 mM and 10 mM) were placed, in a piece of gelfoam, upon the RWM of the right cochleas. The left cochleas served as controls. Auditory function was assessed using acoustically evoked auditory brainstem responses (aABR). Finally, cochleas were fixed and processed for histological examination. Due to variability within treatment groups, histological data was pooled and three categories based upon general histological observations were defined: Cochleas without outer hair cell (OHC) and SGC loss (Category 1), cochleas with OHC loss only (Category 2), and cochleas with OHC and SGC loss (Category 3).

Animals treated with 1 mM or 10 mM ouabain showed shifts in hearing thresholds, corresponding to varying histological changes in their cochleas. Most cochleas exhibited complete outer hair cells loss in the basal and middle turns, while some had no changes, together with either moderate or near-complete loss of SGCs. Neither loss of inner hair cells nor histological changes of the stria vascularis were observed in any of the animals. Cochleas in Category 1 had normal aABRs and morphology. On average, in Category 2 OHC loss was 46.0 ± 5.7% and below-threshold SGC loss, a 44.9 ± 2.7 dB wave II threshold shift and a 17.1 ± 3.8 dB wave II amplitude decrease, and in Category 3 with 68.3 ± 6.9% OHC loss, 49.4 ± 4.3% SGC loss, 39.0 ± 2.4 dB threshold shift, and 15.8 ± 1.6 dB amplitude decrease.

Our results show that ouabain does not solely destroy type-I SGCs in the guinea pig cochlea.

Introduction

In the last decades cochlear implant (CI) technology has progressed considerably, resulting in a variety of improvements such as advanced electrode and speech-processor strategies associated with high performance levels. However, crucial for CI efficacy is the preservation of a critical number of auditory neurons [1, 2]. In this perspective, CI users could benefit from stem-cell-based therapy, especially since stem cells may introduce a healthy, additive population of neurons and glial cells that is necessary for interaction with and repair of the damaged auditory nerve [3, 4]. Several studies have already investigated the use of stem cells in auditory neuron regeneration, showing that various types of stem cells have the capacity to migrate either centrally or peripherally to functionally appropriate locations in the inner ear [5-7, 3, 4].

In future transplantation experiments, we intend to study the potential of hair-follicle-bulge-derived stem cells to repair the damaged auditory nerve in a guinea pig model. Such a study calls for partial denervation of the auditory nerve without inflicting damage to the organ of Corti – in particular, loss of inner hair cells and supporting cells. The approach of our choice is round window membrane application of ouabain, a selective and potent Na^+/K^+-ATPase inhibitor, which has been reported to result in selective degeneration and subsequent loss of type-I spiral ganglion cells (SGCs) without affecting the type-II SGCs and the hair cells in the organ of Corti ([8, 9]; for a review, see [10]). The advantage of a protocol that selectively destroys (type-I) SGCs would be that the remaining hair cells and supporting cells may continue to produce chemotactic growth factors, supporting transplanted stem cells and directing the peripheral projections of newly formed neurons to the hair cells in the organ of Corti [11-13].

The denervatory effect of ouabain was originally observed in the cochlea of Mongolian gerbils by Schmiedt and co-workers [8, 9], and corroborated by other authors [14-16]. It was subsequently demonstrated to occur as well in the cochlea of other rodent species, such as mouse [17-22] and rat [23-25], mostly in a dose-dependent way. It has also been reported that ouabain destroys SGCs in the cochlea of the cat without causing any hair cell loss [26].

Ouabain has been used in a number of stem cell transplantation studies as an agent to induce selective loss of type-I SGCs in the cochlea prior to transplantation of stem cells, mostly in Mongolian gerbils [7, 27-29, 12], but also in mice [30], rats [31] as well as in guinea pigs [11].

Only two reports have described the morphological effect of local application of ouabain upon the SGCs in the guinea pig cochlea. Hamada and Kimura [32] investigated the effect of ouabain after round window application upon cochlear histology and observed that ouabain causes, in a dose-dependent way, shrinkage (and loss) of type-I SGCs, loss of primarily outer hair cells (OHCs), degeneration of the nerve endings at the base of the inner hair cells (IHCs), and, in the most severely affected cases, edema in the stria vascularis. This is in stark contrast to the paper by Cho *et al*. [11] who found that the effect of round window membrane application of ouabain in the guinea pig cochlea is similar to that observed in other rodents, i.e., that it selectively destroys the type-I SGCs without affecting the number of hair cells and the morphological appearance of the stria vascularis.

These conflicting papers led us to re-investigate the effects of ouabain application via the round window membrane of the guinea pig cochlea and to study the validity of this protocol in the guinea pig.

Material and methods

Animals and experimental design

Twenty healthy albino guinea pigs (*Cavia porcellus*; strain: Dunkin Hartley; weighing 250-350 g; 4 males and 16 females) were obtained from Envigo RMS B.V. (Horst, the Netherlands). The animals were housed in the Animal Care Facility of Utrecht University (the Netherlands) under standard housing conditions (group cages with enriched environment; diurnal light cycle (12 h light, 12 h dark); temperature 21°C; relative humidity 60%) and had free access to food and water.

Table 1: Overview of the five experimental groups.

Group	Treatment	n	ABR Threshold	IHC	OHC	SGC
1	10 mM ouabain	2	elevated	normal	loss (n=2)	no loss (n=1)
						loss (n=1)
2	1 mM ouabain	8	normal (n=2)	normal	no loss (n=2)	no loss (n=2)
			elevated (n=6)	normal	no loss (n=2)	no loss (n=2)
					loss (n=4)	no loss (n=2)
						loss (n=2)
3	0.1 mM ouabain	4	normal	normal	normal	normal
4	0.01 mM ouabain	4	normal	normal	normal	normal
5	PBS	2	normal	normal	normal	normal

The animals underwent surgery during which a piece of gelfoam soaked in ouabain solutions of different concentrations (groups I-IV) was placed upon the round window membrane of the right cochleas. Group I (n=2) was treated with a 10 mM solution; Group II (n=8) with a 1 mM solution; Group III (n=4) with a 0.1 mM solution, and Group IV (n=4) with a 0.01 mM solution (Table 1). A control group (Group V; n=2) was treated with a piece of gelfoam soaked in sterile phosphate-buffered saline (PBS). Due to the unexpected variability of the effects with 1 mM ouabain we decided to investigate also the effect of 10 mM ouabain, which was our stock solution, since we expected the electrophysiological and histological effect of ouabain to be unambiguous. However, the number of animals in our animal experimental permit was limited due to ethical

issues and redesign during the course of the experiments. The left cochleas were not treated and served as normal-hearing controls. Auditory brainstem responses were recorded to determine the baseline (pre-treatment) hearing thresholds (Day 0) and post-treatment hearing thresholds (Days 2, 4, and 7). Animals were euthanized at either Day 4 (group I) or Day 7 (groups II-V).

The surgical and experimental procedures used in this study were approved by the Animal Experiments Committees of both Leiden University Medical Center (DEC permit 13224) and the University Medical Center Utrecht (DEC 2015.I.03.004). Animal care and handling were in accordance with the guidelines and regulations as stipulated by the Dutch Experiments on Animals Act (WoD) and the European Directive on the Protection of Animals Used for Scientific Purposes (2010/63/EU).

Ouabain preparation

Ouabain octahydrate (Sigma Aldrich, St. Louis, MO, USA) was dissolved in sterile PBS at a concentration of 10 mM. This stock solution was aliquoted and stored at 4°C, shielded from the light. Prior to use, aliquots were diluted in PBS to prepare working solutions with a final concentration of either 10 mM, 1 mM, 0.1 mM or 0.01 mM. Immediately before surgery, small pieces (1 mm3) of gelfoam (Willospon® Special; Will-Pharma, Zwanenburg, the Netherlands) were soaked in 10 µl of working solution [33]. The gelfoam carrier was used once the fluid was completely absorbed. Deafening procedure

Animals were anesthetized by combined intramuscular (i.m.) injection of (S)-ketamine (Narketan®; Vétoquinol, France; 40 mg/kg) and dexmedetomidine (Dexdomitor®; Orion Pharma, Finland; 0.25 mg/kg).

Both pre-emptive analgesia and antibiotic prophylaxis were administered pre operatively and consisted of subcutaneous (s.c.) injections of the non-steroidal anti-inflammatory drug carprofen (Rimadyl®; Zoetis B.V., Capelle a/d IJssel, the Netherlands; 5 mg/kg) and the non-ototoxic antibiotic enrofloxacine (Baytril® 5%; Bayer AG, Leverkusen, Germany; 5 mg/kg), respectively. No adverse interactions between these drugs and ouabain have been reported in the pharmaceutical databases (cf., www.drugbank.ca).

Prior to surgery, the site of incision was infiltrated subcutaneously with 0.3 ml of a local anesthetic mixture containing 2% xylocaine and adrenaline 1:200,000 (AstraZeneca, London, UK). A retroauricular incision was made in order to expose and open the auditory bulla. A hole was made ventrolaterally in the posterior portion of the right auditory bulla (Fig. 1) using a #15 surgical blade under the operating microscope to reveal the round window. A piece of gelfoam soaked with ouabain or PBS was placed into the round window niche [33]. The hole in the bulla was fully closed with self-curing glass ionomer restorative dental cement (GC Fuji PLUS® II; GC Corporation, Tokyo, Japan) followed by suturing the wound with either Safil® 5/0 (B. Braun Melsungen AG, Melsung, Germany) or Vicryl® 5/0 (Ethicon, Somerville, NJ, USA) absorbable surgical suture. Immediately after surgery, atipamezole (Antisedan®; Orion Pharma; 1 mg/kg) was injected subcutaneously to abolish the clinical effects of dexmedetomidine. One day after surgery, a second s.c. injection of carprofen (4 mg/kg) was given.

Auditory brainstem responses

Auditory function of the right and left ears was separately assessed using acoustically evoked auditory brainstem responses (aABRs) before surgery (Day 0) and at 2, 4, and 7 days after gelfoam placement.

Prior to auditory testing on Days 2, 4 and 7, anesthesia was induced by combined i.m. injection of (S)-ketamine (Narketan®; 40 mg/kg) and dexmedetomidine (Dexdomitor®; 0.25 mg/kg) and maintained for approximately 30-60 min. Immediately after measurements, atipamezole (1 mg/kg) was injected subcutaneously. To perform aABR recordings animals were placed in a custom-designed sound-attenuating box, and disposable 27-gauge subdermal needle electrodes (Rochester Electro-Medical Inc., Lutz, FL, USA) were placed behind the pinna of the right ear (active) and at the vertex (reference). The ground electrode was placed in the right flank of the animal. The aABR recordings were performed using the procedure described previously by Ramekers *et al*. [34] with some slight modifications. Broadband acoustic clicks (20 µs monophasic rectangular alternating pulses; interstimulus interval 99 ms; n=75 pairs) were generated and attenuated using an RZ6-A-P1 Auditory Processor (Tucker-Davis Technologies Inc., Alachua, FL, USA). The responses were differentially amplified (×5,000), band-pass filtered (0.1-10 kHz) using a PAR-5113 pre-amplifier

(EG&G Instruments, Gaithersburg, MD, USA), digitized, sampled at 195 kHz and stored on a personal computer for off-line analysis. Stimulus generation and signal acquisition were controlled with custom-made software (Department of Medical Engineering and Clinical Physiology, University Medical Center Utrecht).

Acoustic clicks were delivered monaurally using ER-2 Tubephone™ Insert Earphones (Etymotic Research Inc., Elk Grove Village, IL, USA) and 3.5 mm E-A-RLink Infant Eartips (E-A-R® Auditory Systems, Indianapolis, IN, USA), first to the right ear and next to the left ear. Hearing thresholds were obtained by starting at approximately 100 dB peak-equivalent sound pressure level (SPL) and decreasing the sound level in steps of 10 dB until the response had disappeared. Peak thresholds were then defined as the interpolated sound level at which the aABR peak was 0.3 μV. Only waves I and II were analyzed, since these are more discernable than later peaks. Data were processed using MATLAB software (MathWorks, Natick, MA, USA) and MS Excel (Microsoft, Redmond, WA, USA).

Histology

Fixation and tissue processing

Immediately after the final aABR measurements, the animals were euthanized by an intracardial injection with sodium pentobarbital (Euthasol®; AST Farma, Oudewater, the Netherlands). After decapitation, both cochleas were removed and fixed by means of intralabyrinthine perfusion with a fixative containing 3% glutaraldehyde, 2% formaldehyde, 1% acrolein and 2.5% dimethyl sulfoxide in 0.08 M sodium cacodylate buffer, pH 7.4 [35]. Perfusion was followed by overnight immersion in the same fixative at 4°C, after which the cochleas were rinsed several times in 0.1 M sodium cacodylate buffer (pH 7.4). Cochleas were decalcified in a 10% aqueous EDTA.2Na solution (pH 7.4) at room temperature for 5-7 days and postfixed in a 1% aqueous OsO4 solution containing 1% $K_4Ru(CN)_6$ at 4°C for 2 h followed by several rinses in distilled water. Dehydration was performed in a graded ethanol (50-100%) and propylene oxide series. Cochleas were embedded in Spurr's low-viscosity resin which was allowed to polymerize at 70°C overnight. Next, the cochleas were divided into two halves along a standardized midmodiolar plane [36] and re-embedded in fresh resin. For histological evaluation, 5 consecutive semithin (1 μm) sections were cut with a diamond knife on a Leica RM2265 microtome, collected on gelatin-coated

glass slides, stained with an aqueous solution of 1% methylene blue, 1% azur B and 1% sodium tetraborate, and mounted in Entellan® (Merck KGaA, Darmstadt, Germany) mounting medium under a glass coverslip.

Sections were examined with a Leica DM5500B microscope equipped with a Leica DFC 450C digital color camera. Digital images of each transection of Rosenthal's canal (two basal, two middle, and three apical transections) as well as the corresponding sections of the organ of Corti were acquired and stored using Leica Application Suite software (LAS V4.5; Leica Microsystems GmbH, Wetzlar, Germany).

Hair cell counts

From base to apex the guinea pig cochlea spirals upwards in approximately 4 turns. The number of hair cells (OHCs and IHCs) was counted in a semi-quantitative way as described by Van Ruijven *et al*. [36]. This protocol does not involve the time-consuming preparation of cytocochleograms by counting all (remaining) hair cells within the cochlea, but limits itself to 7 different locations along the cochlear spiral at a half-turn spacing, as seen in semithin sections of cochleas divided along a standardized midmodiolar plane (B1, B2, M1, M2, A1, A2, and A3; Fig. 1).

Hair cell counts are expressed as the mean percentage of remaining hair cells per individual transection of the respective half turn (two transections each for the basal [B1, B2] and middle [M1, M2] turns and three transections for the apical [A1, A2, A3] turn).

In oblique transections of the organ of Corti, either one of the following features was used for the identification of OHCs: (1) the presence of the reticular lamina and/or stereocilia; (2) the degree of cytoplasmic staining characteristic for OHCs; and (3) the presence of the basal part of the hair cell. All remaining OHCs were counted irrespective of their histological appearance. OHCs and IHCs were counted at each location using the Cell Counter plugin of ImageJ (https://imagej.nih.gov/ij/plugins/cell-counter.html). Counted hair cells were marked in the images of the histological sections to prevent double counting. For statistical analysis, OHC counts were averaged for each cochlear turn (basal, middle and apical) within each treatment group and compared to a dataset of averaged OHC counts from the left (non-treated) cochleas.

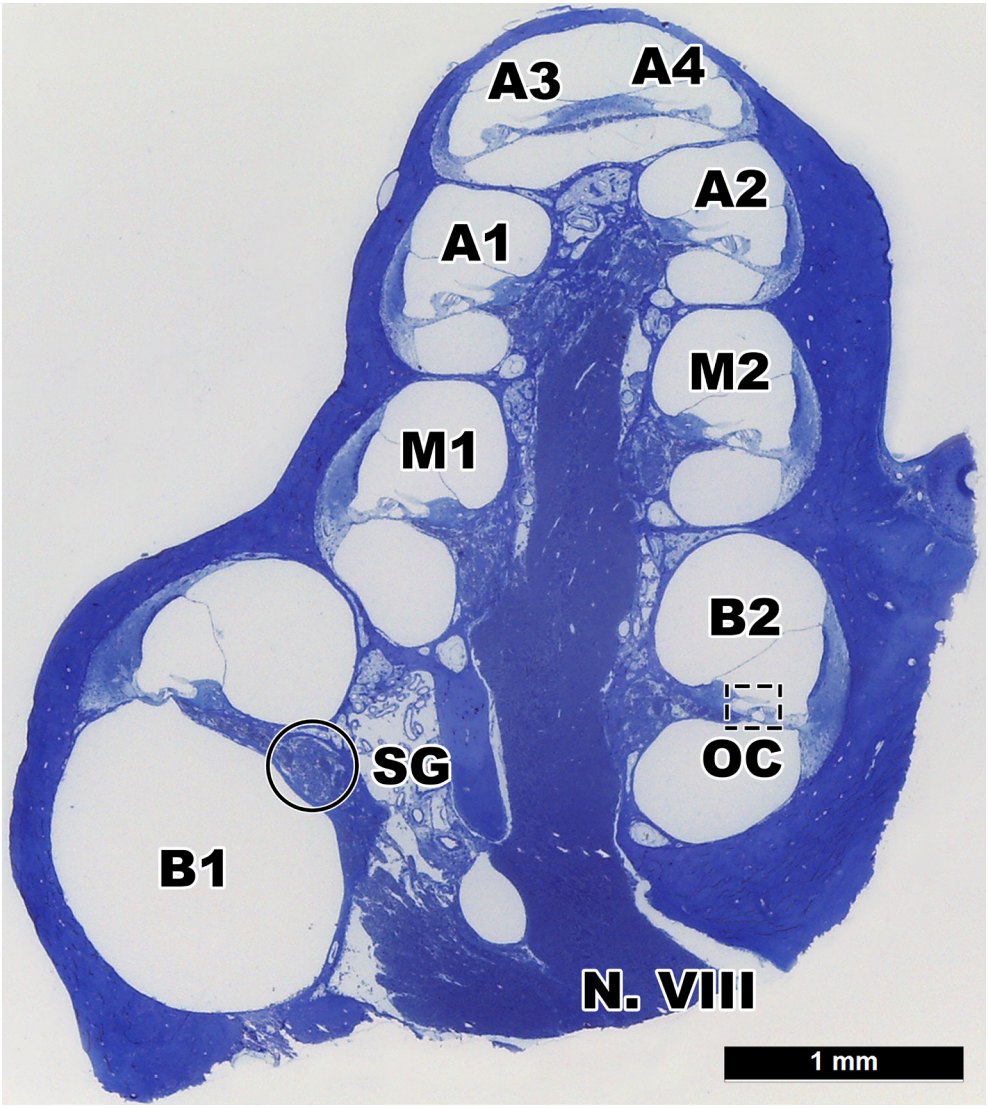

Fig. 1: Histology of the guinea pig cochlea. The midmodiolar section of a guinea pig cochlea shows 8 different locations (basal = B1, B2; middle = M1, M2; apical = A1, A2, A3, and A4) along the cochlear spiral at a half-turn spacing (not showing the helicotrema). The number of SGCs in the spiral ganglion (SG) were counted and the number of hair cells (IHCs and OHCs) in the organ of Corti (OC) was determined for each location, except A4.

Spiral ganglion cell packing densities

SGC packing densities were determined in digital images (acquired at a fixed objective lens magnification of x20) of Rosenthal's canal taken from 5 different cochlear locations (B1, B2, M1, M2, and A1) as previously described by Versnel *et al*. [37] and Agterberg *et al*. [38]. Using ImageJ image analysis software (version 1.47; US National Institutes of Health, Bethesda, MD, USA), the bony boundaries of Rosenthal's canal were outlined and its cross-sectional area (in μm^2) was calculated.

SGC perikarya were counted at each location using the Cell Counter plugin of ImageJ (https://imagej.nih.gov/ij/plugins/cell-counter.html), including: (1) all perikarya demonstrating the morphological determinants typical of type-I and type-II SGCs (no distinction was made between type-I and type-II SGCs; for details, see Romand and Romand [39]); (2) partial and complete profiles of perikarya; and (3) perikaya with and without evident nucleus or nucleoli. The SGC packing density was calculated by dividing the number of SGCs by the cross-sectional area of Rosenthal's canal and expressed as the mean number of SGCs per mm^2.

For statistical analysis, SGC packing densities for each cochlear turn (basal, middle and apical) were averaged within each treatment group and compared to a dataset of averaged SGC packing densities from the left (non-treated) cochleas.

Stria vascularis

We evaluated in a qualitative manner the following morphological features: shrinkage and/or swelling of the marginal and intermediate cells, edema, loss of intermediate cells (resulting in flattening of the stria vascularis), and the degree of azurophilic staining of the marginal and intermediate cells (intracellular density).

Data analysis

For both aABR wave I and wave II separately, the thresholds and amplitudes were grouped first by treatment (10 mM, 1 mM, 0.1 mM, 0.01 mM ouabain, and PBS alone) and subsequently by histological appearance. The threshold was defined as the interpolated sound level at which a 0.3 μV signal was evoked. The aABR amplitude before treatment (Day 0) was defined as the largest amplitude recorded for that particular wave; at subsequent time points the amplitude was determined at

the same sound level (typically ~90 dB SPL). Changes in threshold and amplitude after ouabain treatment were both expressed in dB relative to pre-treatment values. Statistical analyses of the data were performed using MS Excel and GraphPad Prism 7.00 software (GraphPad Software, La Jolla, CA, USA). Data were expressed as mean ± standard deviation (SD). A one-way ANOVA with Tukey's multiple comparison test and 95% confidence interval was applied to the data. Correlations between aABR measures and OHC counts were assessed with the non-parametric Spearman's rank correlation coefficient; for correlations between aABR measures and SGC packing densities the parametric Pearson's correlation coefficient was used. Groups I-V were compared using ANOVA. Due to small group sizes (i.e., group I and group V) it is difficult to check assumptions, and therefore an additional statistical analysis (sensitivity analysis) was performed by pooling groups into three final groups (low treatment dose [L]: 0 mM (i.e., PBS alone), 0.01 mM; medium treatment dose [M]: 0.1 mM; high treatment dose [H]: 1 mM, 10 mM) to achieve minimum group size of four animals. Gender was included in a two-way ANOVA to test for possible gender effects.

Results

Auditory brainstem responses

All animals showed normal hearing thresholds prior to surgery (Day 0) without significant differences among the treatment groups (wave I: $p = 0.52$; wave II: $p = 0.25$; one-way ANOVA, Tukey's multiple comparison test, 95% confidence interval). This was evaluated by comparison to normative data from previous studies from our group [40, 41]. In addition, no significant differences were found between waves I and wave II within the different treatment groups at the different days (Days 0, 2, 4, and 7). Since wave II was more robust and less prone to random fluctuation than wave I in our measurements, we predominantly focus on the wave II data as described previously [42]. Figs. 2A-D depict representative aABRs of the left (non-treated) and right (treated) ears, 4 days after treatment with ouabain.

After treatment with 10 mM ouabain (Group I) the right ears showed a substantial and statistically significant 43-dB increase in the wave II thresholds, already within 4 days ($p < 0.005$; one-way ANOVA; Fig. 2G), whereas the left (non-treated) ears, as expected, did not show any threshold shift. The left ear showed a normal aABR (Fig. 2A), while the right ear revealed substantial hearing loss that resulted in one-sided deafness after treatment with 10 mM ouabain (Fig. 2B).

After 1 mM ouabain, the left (non-treated) ear was not affected (Fig. 2C), but the right (treated) ear exhibited a hearing loss of 30 dB (Fig. 2D). Of the 8 animals treated with 1 mM ouabain (Group II), 2 animals did not show any changes in their aABR thresholds of both wave I and wave II (i.e., non-responders). The remaining 6 animals expressed pronounced changes in wave II thresholds. On average, the 8 animals in Group II demonstrated an increase in wave II threshold of the right ears, already within 4 days (25 dB; $p = 0.585$; one-way ANOVA; Fig. 2G), and did not change at Day 7 (24 dB). The left (non-treated) ears showed normal hearing thresholds.

The decreases in wave II amplitudes were significantly different in Groups I and II ($p = 0.007$ and $p = 0.015$, respectively; one-way ANOVA), 4 days after deafening (Fig. 2H). The pattern of amplitude decrease across treatment groups resembles the increase in threshold as shown in Fig. 2G.

Animals treated with lower concentrations of ouabain, i.e. 0.1 mM (Group III) and 0.01 mM (Group IV) or PBS alone (Group V), did not show any significant changes in the threshold and amplitude of wave II. The left (non-treated) ears also showed normal hearing thresholds. aABR latencies were unaffected in any of the groups at any time point after ouabain treatment (data not shown).

Including gender in the ANOVA did not change the results (e.g. p = 0.7 for the model amplitude of wave II at day 4 against treatment groups I-V). The p values for gender were larger than 0.7 in all analyses. Concerning the additional sensitivity analysis, using the pooled groups (L and H) also did not change the results in most analyses (e.g. p = 0.0058 no pooling [I-V], p = 0.0047 pooled [L, M, and H] treatment groups, amplitude of wave II at day 4 against treatment groups). For analyses of wave I, the

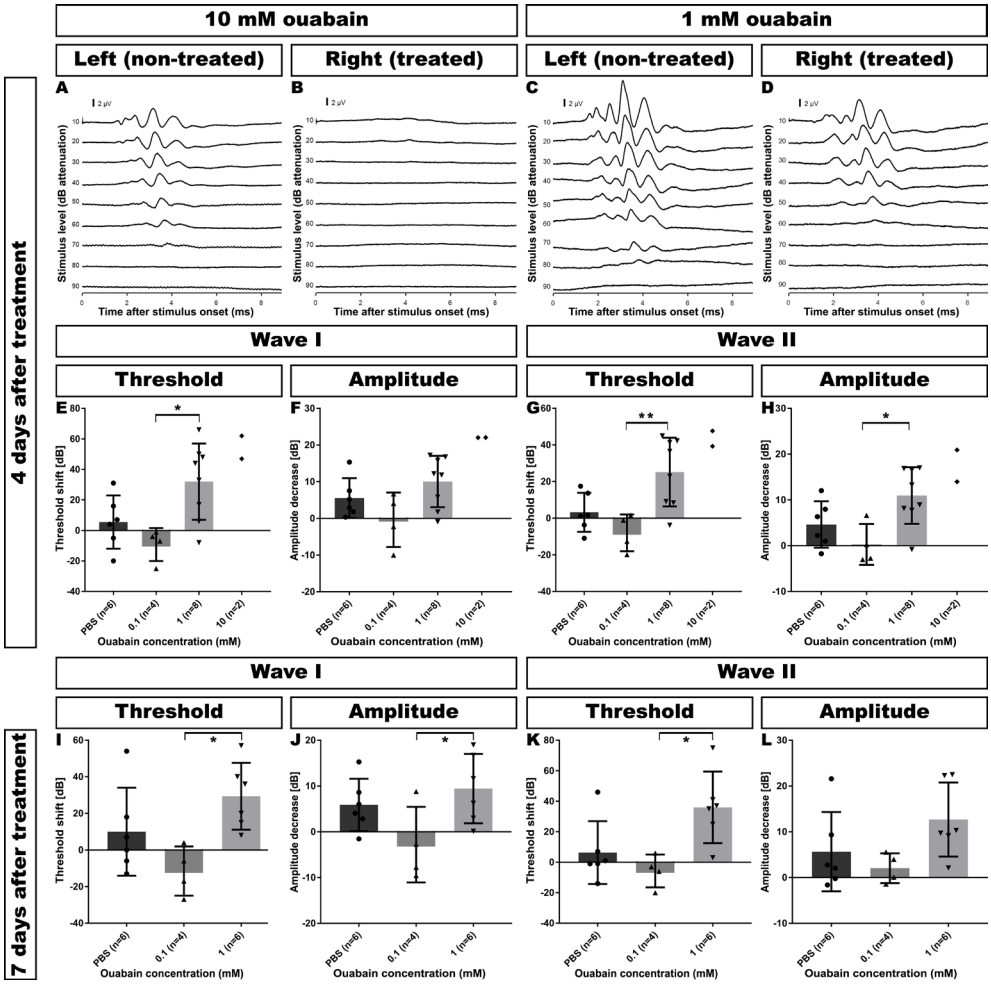

significance of the sensitivity analysis for the pooled treatment groups increased as compared to the original group allocation (e.g. p = 0.02 no pooling [I-V], p = 0.0056 pooled [L, M, and H] treatment groups, amplitude of wave I at day 4 against treatment groups). This can be explained by the fact that the effects for low treatment concentrations are similar and pooled into the same pooled group. In all cases p values for the sensitivity analysis of the pooled treatment groups were lower than for the original group allocation. This implies that the analyses presented above are robust with respect to group size.

Fig. 2: Acoustically evoked auditory brainstem responses (aABRs) were recorded before and after treatment with ouabain. **(A+B)** Example of an animal treated with 1 mM ouabain showing a moderate increase of the aABR threshold in the right (treated) cochlea **(B)**, while the aABR threshold in the left (untreated) cochlea **(D)** remained normal. **(C+D)** Example of an animal treated with 1 mM ouabain revealing a dramatic aABR threshold shift in the right (treated) cochlea **(D)**, while the responses in the left (untreated) cochlea **(C)** remained normal. **(E)** Wave I threshold increased substantially after treatment with 1 mM and 10 mM ouabain. There was no significant threshold shift after treatment with lower concentrations (0.1 mM and 0.01 mM). Left (untreated) ears and right ears treated with PBS alone served as control. **(F)** Four days after treatment, wave I amplitudes had also decreased substantially in the cochleas treated with 1 mM and 10 mM ouabain, but not with lower concentrations (0.1 mM and 0.01 mM). Left (untreated) ears and right ears treated with PBS alone served as control. **(G)** Within 4 days after treatment with 1 mM and 10 mM ouabain, wave II threshold increased substantially. There was no significant threshold shift after treatment with lower concentrations (0.1 mM and 0.01 mM). Left (untreated) ears and right ears treated with PBS alone served as control. **(H)** Wave II amplitudes also decreased substantially in the cochleas treated with 1 mM and 10 mM ouabain 4 days after treatment, but not with lower concentrations (0.1 mM and 0.01 mM). Left (untreated) ears and right ears treated with PBS alone served as control. **(I)** Seven days after treatment, wave I thresholds were still substantially elevated in animals treated with 1 mM ouabain. There was no significant threshold shift after treatment with lower concentrations (0.1 mM and 0.01 mM). Left (untreated) ears and right ears treated with PBS alone served as control. **(J)** Wave I amplitudes remained substantially decreased in cochleas 7 days after treatment with 1 mM ouabain. Animals treated with lower concentrations (0.1 mM and 0.01 mM) did not display significant decrease in wave I amplitude. Left (untreated) ears and right ears treated with PBS alone served as control. **(K)** Wave II thresholds remained substantially elevated in animals 7 days after treatment with 1 mM ouabain. There was no significant threshold shift after treatment with lower concentrations (0.1 mM and 0.01 mM). Left (untreated) ears and right ears treated with PBS alone served as control. **(L)** Seven days after treatment with 1 mM ouabain, wave II amplitudes remained substantially decreased in these animals. Animals treated with lower concentrations (0.1 mM and 0.01 mM) did not display significant decrease in wave II amplitude. Left (untreated) ears and right ears treated with PBS alone served as control. Thresholds (E, G, I and K) and amplitudes (F, H, J and L) are expressed as change (in dB) from pre-treatment levels. Differences in amplitudes of contralateral ears between animals treated with 1 mM and 10 mM are within the normal range of the animals. Error bars represent SD; * = $p \leq 0.05$, ** = $p \leq 0.01$, *** = $p \leq 0.001$.

Histology

General findings

Table 1 summarizes the general histological findings. We found OHC loss and SGC loss in animals from Group I and in some of Group II, but none of the animals demonstrated loss of IHCs or morphological changes in the stria vascularis, such as swelling, shrinkage, edema or gross changes in intracellular density.

In the right cochleas of both animals in Group I (10 mM ouabain) a near-complete loss of OHCs was seen in the basal and middle turns and in the lower region of the apical turn, either with (n=1) or without (n=1) SGC loss. The average number of OHCs present in all turns of the cochlea amounted to 38.1 ± 4.8% ($p < 0.001$, one-way ANOVA; Fig. 3A) and 64.6 ± 17.2% of the SGCs were present on average (Fig. 3B).

Of the 8 animals treated with 1 mM ouabain (Group II), 2 animals did not show any changes in their aABR thresholds. In addition, these non-responding animals did not show any morphological changes in the right (treated) cochleas. The remaining 6 animals demonstrated a significant increase of their wave II thresholds as well as varying degrees of histological changes in their right cochleas.

Fig. 3: Quantification of OHC loss and SGC loss after ouabain treatment. Data are normalized and expressed as percentages of an averaged dataset from the left (untreated) cochleas (normal). **(A)** OHC loss accrues with increasing ouabain concentrations (1 mM: 72.6 ± 11.0% of OHCs remaining; 10 mM: 38.1 ± 4.8% of OHCs remaining). IHCs are not affected. Control (0 mM) includes right ears treated with PBS alone. Normal (100%) is 21 OHCs, the sum of OHCs counted at B1, B2, M1, M2, A1, A2, and A3. **(B)** SGC loss also progresses with increased ouabain concentrations. Compared to SGC packing densities in the left (non-treated) cochleas, near-normal numbers (95.3 ± 2.8%) of the SGC perikarya are present in cochleas treated with 0.01 mM and 0.1 mM ouabain. Control (0 mM) includes right ears treated with PBS alone. Normal (100%) is 1362 SGCs, the average of perikarya counted at B1, B2, M1, M2, and A1. Cochleas treated with 1 mM ouabain show a moderate loss with an average of 87.4 ± 8.7% of SGC perikarya remaining, whereas in cochleas treated with 10 mM ouabain the average number of SGC perikarya present in Rosenthal's canal decreases to 64.6 ± 17.2%. Error bars represent SD; ** = $p \leq 0.01$, *** = $p \leq 0.001$. **(C)** OHC counts in the basal, middle and apical turns at 1 mM and 10 mM ouabain and the average OHC count (cf., Fig. 3A). For basal and middle turns, normal (100%) is 6 OHCs per turn, i.e., the sum of OHCs counted at B1+B2 and M1+M2, respectively, and for the apical turn normal (100%) is 9 OHCs, the sum of OHCs counted at A1+A2+A3. At a concentration of 1 mM, ouabain causes OHC loss in the basal (50.0 ± 18.9%) and middle (35.4 ± 15.6%) turns. In the apical turn, OHC counts are almost normal (93.1 ± 7.0%). A concentration of 10 mM ouabain results in loss of OHCs in all turns. In the basal turn 91.7 ± 8.4% and in the middle turn 83.3% of the OHCs are lost. In the apical turn, approximately 27.8 ± 5.5% of the OHCs is lost. **(D)** SGC packing densities in the basal, middle and apical turns at 1 mM and 10 mM ouabain and the average SGC packing density (cf., Fig. 3B). Normal (100%) is 1293 SGCs for the basal turns, 1470 SGCs for the middle turns and 1325 SGCs for the apical turn. In the basal turn, SGC packing densities are reduced to 66.9 ± 12.6%, while they are near-normal in the middle (96.2 ± 9.2%) and apical (111.0 ± 6.5%) turns. At a concentration of 10 mM ouabain, SGC packing densities are reduced to 40.5 ± 17.0% in the basal turn and 73.1 ± 20.1% in the middle turn. The packing density in the apical turn is normal (95.8 ± 8.1%).

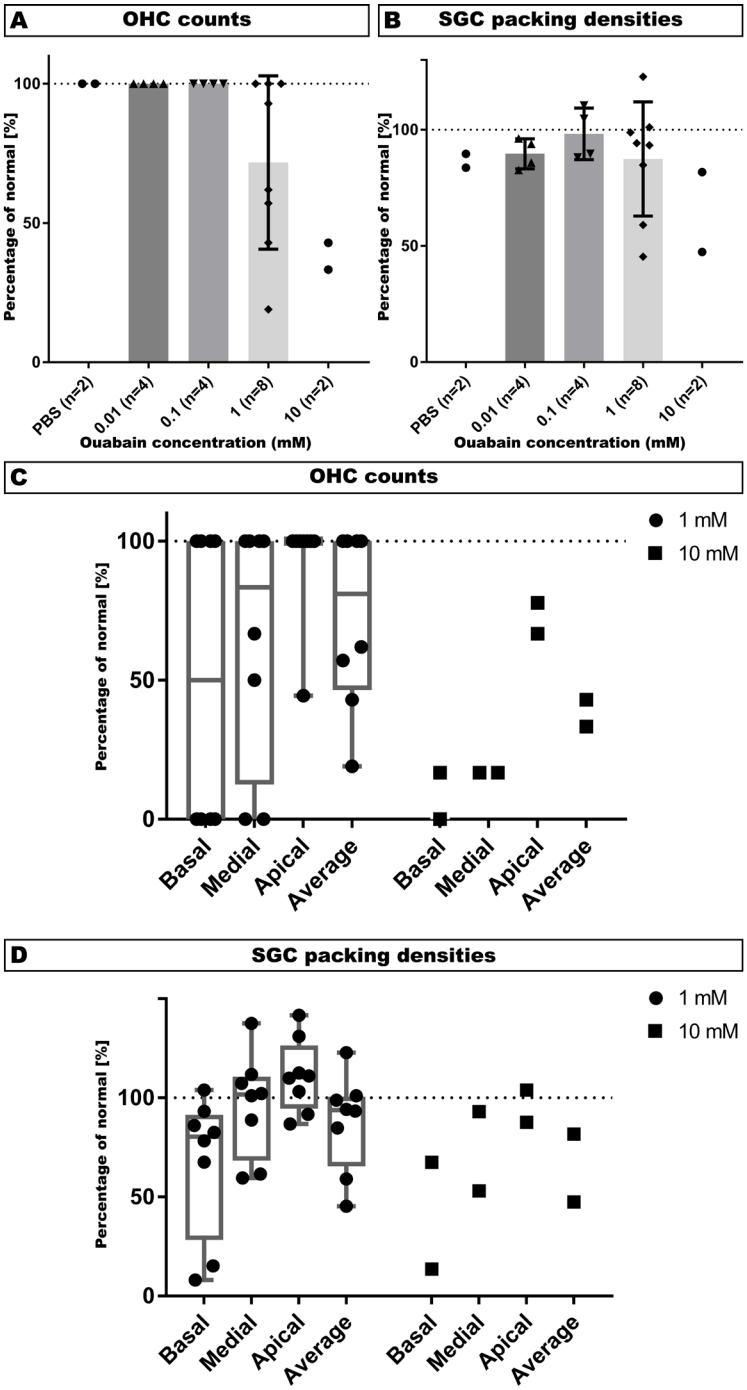
A
OHC counts
Percentage of normal [%]
100
50
0
PBS (n=2)
0.01 (n=4)
0.1 (n=4)
1 (n=8)
10 (n=2)
Ouabain concentration (mM)
B
SGC packing densities
Percentage of normal [%]
100
50
0
PBS (n=2)
0.01 (n=4)
0.1 (n=4)
1 (n=8)
10 (n=2)
Ouabain concentration (mM)
C
OHC counts
1 mM
10 mM
Percentage of normal [%]
100
50
0
Basal
Medial
Apical
Average
Basal
Medial
Apical
Average
D
SGC packing densities
1 mM
10 mM
Percentage of normal [%]
100
50
0
Basal
Medial
Apical
Average
Basal
Medial
Apical
Average

Two animals did not show any histological changes, despite the observed threshold shift in wave II. Another 2 animals demonstrated complete OHC loss (but no loss of IHCs) in the basal (B1, B2) and middle (M1, M2) turns of the right cochleas. Although there was no obvious loss of SGC perikarya, the number of peripheral processes in the osseous spiral lamina appears diminished (see Fig. 4D) or the peripheral processes seem to have been substituted by fibroblasts (Fig. 4G). In the remaining 2 animals, OHC loss was seen in all turns of the right cochleas (complete loss in the basal (B1, B2) and middle (M1, M2) turns, and partial loss in the apical (A1, A2) turn) together with loss of peripheral processes in the osseous spiral lamina as well as a complete loss of SGC perikarya (type-I and type-II) in the basal (B1, B2) turn and partial loss in the lower middle (M1) turn.

Statistical analysis of the averaged OHC counts and SGC packing densities demonstrates that the cochleas in Group II exhibit a significant OHC loss (28.3 ± 11.0%; $p = 0.004$, one-way ANOVA; Fig. 3A) together with minor loss of SGCs (12.6 ± 8.7%; Fig. 3B).
Animals in Groups III to V did not show any obvious morphological changes 7 days after treatment with ouabain, or decreased OHC counts or SGC packing densities (Figs. 3A-B). The left (non-treated) cochleas all demonstrated a normal morphology.

To investigate the longitudinal (basal-apical) gradient of the cochleotoxic effect of ouabain, we analyzed the OHC counts of animals treated with 1 mM and 10 mM ouabain from the basal, middle and apical turns. At 1 mM (group II), ouabain caused OHC loss in the basal (50.0 ± 18.9%) and middle (35.4 ± 15.6%) turns, whereas in the apical turn OHC counts were close to normal (93.1 ± 7.0%; Fig. 3C). At a concentration of 10 mM ouabain OHC loss was seen in all turns: in the basal turn 91.7 ± 8.4% of the OHCs were lost, in the middle turn 83.3%, and in the apical turn 27.8 ± 5.5% of the OHCs were lost (Fig. 3C).

SGC packing densities were reduced primarily in the basal turn (66.9 ± 12.6%), but were near-normal in the middle and apical turns of guinea pigs treated with 1 mM ouabain (Fig. 3D). At a concentration of 10 mM ouabain, SGC packing densities were reduced to 40.5 ± 17.0% in the basal turn and 73.1 ± 20.1% in the middle turn. In contrast to the OHC counts at 10 mM ouabain, the SGC packing density in the apical turn remained normal (95.8 ± 8.1%).

Categorization based upon histological findings

Variability within Groups I and II was substantial, and the observed loss of both OHCs and SGCs was often bimodal; whereas some animals showed substantial losses, others in the same group did not. Therefore, we pooled all histological data of the right cochleas in all groups and defined three categories based upon the general histological observations (Fig. 4; Table 2): Category 1 (n=14) contains cochleas that do not demonstrate any loss of OHCs (Fig. 4A) and SGCs (Fig. 4B); in Category 2 (n=3) the cochleas show OHC loss only (Fig. 4D-E); and in Category 3 (n=3) the cochleas exhibit both OHC and SGC loss (Fig. 4G-H). OHC loss was defined as the absence of any of the 3 OHCs in any of the 7 transections of the organ of Corti.

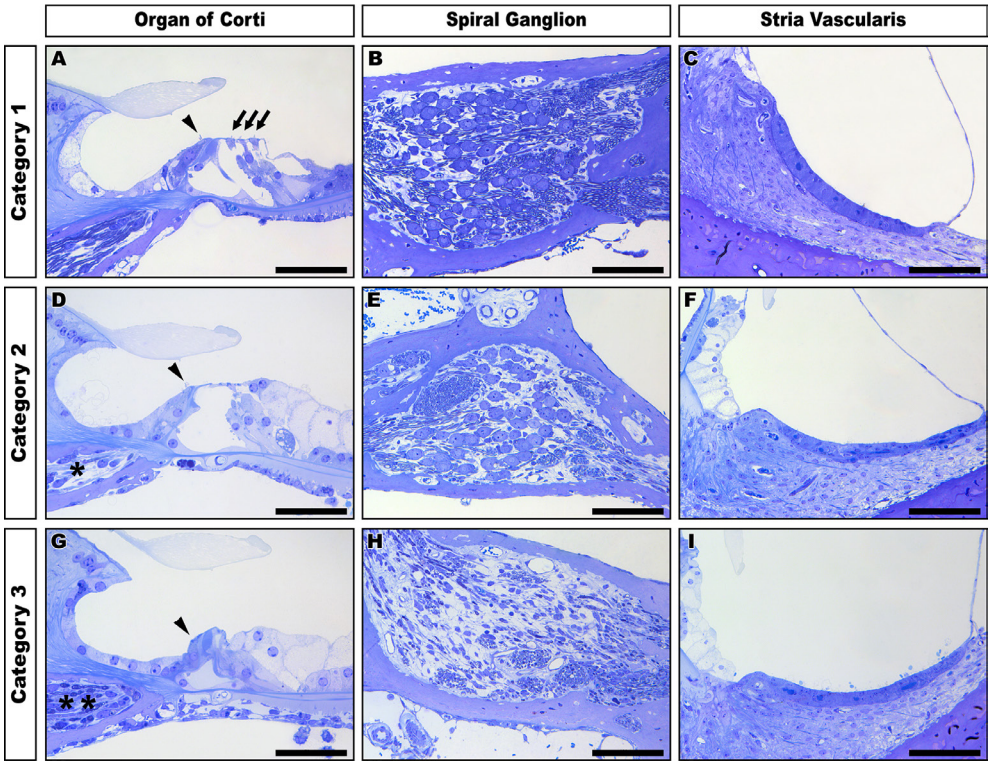

Fig. 4: Examples of the variety in histological changes in the cochlea after round window membrane application of ouabain in guinea pigs. Cochleas in Category 1 do not demonstrate any effect of ouabain upon the OHCs (arrows), IHCs (arrow heads), SGCs, or the stria vascularis. These cochleas do not appear different from the left (non-treated) cochleas or from the right cochleas treated with lower ouabain concentrations (0.1 mM and 0.01 mM) or PBS alone. Category 2 contains cochleas with complete OHC loss, with apparent loss of peripheral processes in the osseous spiral lamina (*), but without obvious loss of SGCs, in the basal and middle turns, while cochleas in Category 3 show complete OHC loss in all turns together with loss of peripheral processes in the osseous spiral lamina, which seem to be substituted with fibroblasts (**), and extensive loss of SGCs in the basal and middle turns. In none of the animals, any loss of IHCs or histological changes in the stria vascularis are obvious. Scale bars: 50 µm (organ of Corti) and 100 µm (spiral ganglion and stria vascularis).

Table 2. Distribution of the cochleas from the 5 experimental groups among the three histological categories and corresponding averages.

Category 1	N1	Category 2	N2	Category 3	N3
No OHC and SGC loss		OHC loss only		Both OHC and SGC loss	
Group II	4	Group I	1	Group I	1
Group III	4	Group II	2	Group II	2
Group IV	4				
Group V	2				
Total	14		3		3
OHC loss	0%		46.0 ± 5.7%		68.3 ± 6.9%
SGC loss	4.7 ± 3.0%		10.8 ± 6.0%		49.4 ± 4.3%
Threshold shift	1.7 ± 11.9 dB		44.9 ± 2.7 dB		39.0 ± 2.4 dB
Amplitude	3.8 ± 5.0 dB		17.1±3.8 dB		15.8 ± 1.6 dB

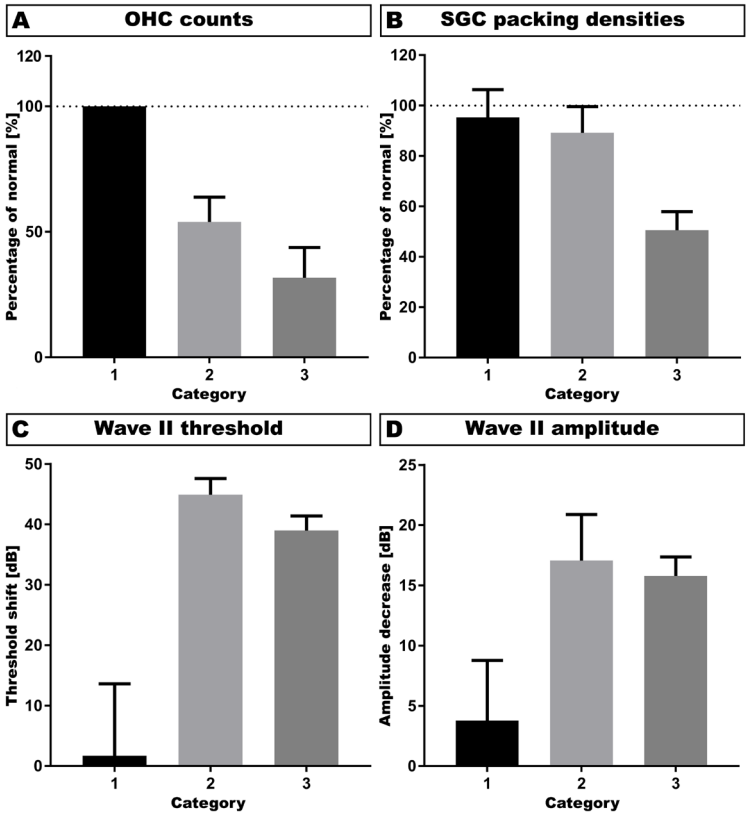

SGC loss was defined as a loss of ≥20% as compared to the averaged SGC packing densities of the left (non-treated) cochleas (n=12). In none of the animals IHC loss (Fig. 4A, 4D, 4G) or any morphological changes in the stria vascularis (Fig. 4C, 4F, 4I) were obvious.

Re-evaluation based upon the averaged OHC counts and SGC packing densities shows that cochleas in Category 1 exhibit normal numbers of OHCs (100%) and SGCs (95.3 ± 3.0%), comparable to the left (non-treated) cochleas, together with near-normal wave II amplitudes and normal hearing thresholds (Fig. 5).

Cochleas of Category 2 showed considerable OHC loss (46.0 ± 5.7%; Fig. 5A) and on average minor loss of SGCs (10.8 ± 6.0%; Fig. 5B), whilst the animals displayed substantial threshold shifts and substantially decreased wave II amplitudes as compared to those in Category 1 (Figs. 5C-D).

In the cochleas of Category 3 a substantial number of the OHCs (68.3 ± 6.9%) was lost, as compared to Categories 1 and 2 (Fig. 5A), and SGC loss was considerably higher (49.4 ± 4.3%) than that in Categories 1 and 2 (Fig. 5B). Animals in Category 3 showed a substantial decrease in wave II amplitudes as well as a substantial threshold shift, similar to those in Category 2 (Figs. 5C-D).

Although the right cochleas of animals in Category 2 had, on average, near-normal SGC packing densities, their ABR thresholds had increased and their ABR amplitudes had decreased. It seems that, in this particular category, OHC loss is a more sensitive measure to determine hearing loss. Therefore, we investigated how the quantitative histological data correlate with the aABR data (Fig. 6). The results

Fig. 5: Re-evaluation of results using post-hoc histological categorization. **(A)** Category 1 consists of cochleas without any OHC loss. In Category 2, average OHC loss is moderate and in Category 3 the average number of remaining OHC has even decreased more. Normal (100%) is 21 OHCs, the sum of OHCs counted at B1, B2, M1, M2, A1, A2, and A3. **(B)** Average SGC packing density in Category 1 cochleas is near-normal. There is on average minor loss of SGCs (i.e., <20%) in Category 2, whereas the average SGC packing density in Category 3 cochleas is approximately half of that in normal-hearing controls, i.e. the left (non-treated) cochleas. Normal (100%) is 1362 SGCs, the average of perikarya counted at B1, B2, M1, M2, and A1. **(C)** The wave II threshold of Category 1 remains normal, while animals in Categories 2 and 3 showed a substantial shift in wave II threshold, 4 days after treatment with ouabain. The wave II threshold shifts do not differ between Categories 2 and 3. **(D)** Animals in Category 1 show a slight decrease in their wave II amplitude, whereas animals in both Categories 2 and 3 show a much larger decrease, 4 days after ouabain treatment. The wave II amplitudes in Categories 2 and 3 do not significantly differ from one another. OHC counts (A) and SGC packing densities (B) are normalized and expressed as percentages of an averaged dataset from the left (untreated) cochleas (normal). Thresholds (C) and amplitudes (D) are normalized and expressed as change (in dB) from pre-treatment levels. Error bars represent SEM.

show a moderately positive correlation between the variance in threshold shift after ouabain treatment and OHC loss (Fig. 6A; $R2 = 0.44$, $p < 0.001$); the decrease in wave II amplitude correlated to a similar extent with OHC loss (Fig. 6B; $R2 = 0.45$, $p < 0.001$). However, in both cases the relationship between the two variables clearly deviated from a linear one; these data should therefore be treated with caution. The positive correlations between threshold shift and SGC loss and between amplitude decrease and SGC loss (Fig. 6C-D; for both $R2 = 0.30$; $p < 0.001$) is weak and indicates that the number of SGCs is not primarily related to threshold shifts of pure tone audiometry. We confirmed that throughout all experiments, correlations between aABR wave II measurements (threshold/amplitude) and histological quantifications (OHC/SGC counts) were highly similar to those for wave I (data not shown).

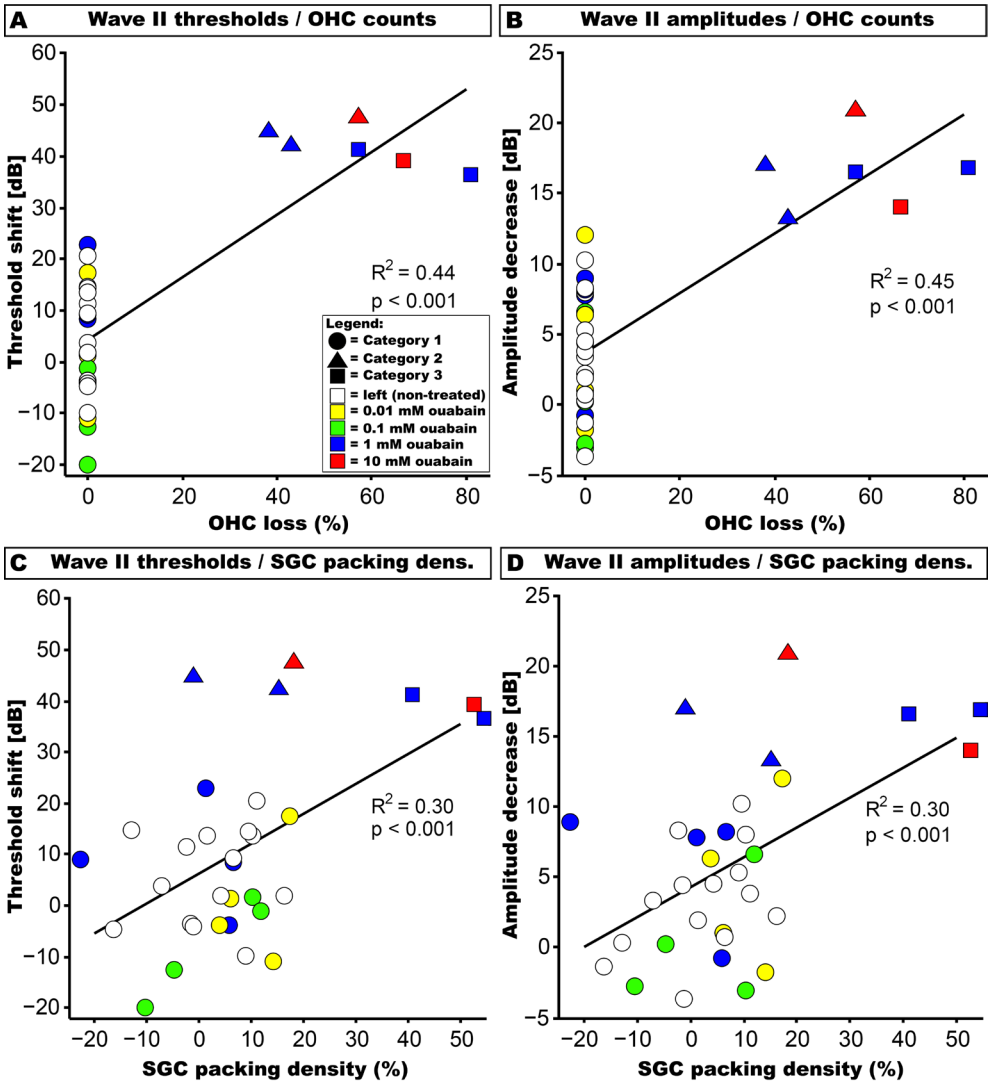

Fig. 6: Scatter plots of aABR data and OHC loss and SGC packing densities. OHC counts and SGC packing densities are normalized and expressed as percentages of an averaged dataset from the left (untreated) cochleas. Thresholds and amplitudes are normalized and expressed as change (in dB) from pre-treatment levels. **(A)** The variance in wave II threshold shift after ouabain treatment can be explained for 44% by OHC loss ($p < 0.001$). **(B)** The decrease in wave II amplitude is positively correlated with OHC loss. The explained variance (R2) is 45% ($p < 0.001$). **(C)** The aABR wave II threshold shift and SGC loss are moderately correlated ($p < 0.001$). **(D)** There is also a moderate positive correlation between wave II amplitude decrease and SGC packing densities ($p < 0.001$). Colors indicate treatment group: open symbols are left (non-treated) cochleas; right ears are shown in closed symbols colored yellow (0.01 mM ouabain), green (0.1 mM), blue (1 mM), and red (10 mM). Post-hoc categorization is visualized using circles (Category 1), triangles (Category 2) and squares (Category 3).

Discussion

We found that, within days, locally applied ouabain, in a dose-dependent fashion, results in a loss of OHCs, either with or without concomitant SGC loss. Both OHC loss and SGC loss demonstrated a longitudinal gradient with a preference for the basal and middle turns, similar to the effect of various other cochleotoxic drugs. Loss of IHCs and morphological changes in the stria vascularis were not seen. These results are largely in line with the observations of Hamada and Kimura [32], who reported that round window application of ouabain results in morphological damage to three main targets in the guinea pig cochlea, i.e. the organ of Corti, the spiral ganglion, and the stria vascularis. Similar to our results, degeneration of OHCs was one of their most consistent findings. In addition, they reported that IHC often remained intact after ouabain treatment, and that in some cochleas severe shrinkage of type-I SGCs was present; there are even indications of loss of SGC perikarya (their Fig. 1E).

The stria vascularis in our samples did not demonstrate any gross morphological changes, such as cell swelling or shrinkage of the marginal and intermediate cells, as previously reported after perilymphatic perfusion of 2 mM ouabain [43]. Nor did we observe an increase in the intercellular spaces (edema) as seen by Hamada and Kimura [32] after round window application of 2 mM ouabain, which they describe as ‘cystic stria vascularis’ (their Figure 1D). It should be noted that they only found this strial edema in the most severely affected cases. Neither did we observe intracellular vacuolation of the marginal cells as reported in guinea pigs after cochlear perfusion of 1 mM ouabain using a glass perfusion pipette [44].

After round window membrane application, ouabain directly enters into the perilymph of the scala tympani. The observed ouabain-induced degeneration of OHCs can be explained by one or more of the following mechanisms.

Ouabain could exert direct effect upon the Na^+/K^+-ATPase present in the basolateral membranes of the OHCs. Their main body is immersed in cortilymph, which communicates with the scala tympani. Perilymphatic ouabain may diffuse into the cortilymph [45] and subsequently bind to the Na^+/K^+-ATPase in the basolateral membranes of the OHCs, resulting in either inhibition of its ion transporter function or disturbance of its signal receptor function [46]. Ouabain-induced degeneration of OHCs may therefore be attributed to a direct effect upon these cells, although,

alternatively, OHC loss may be the result of a direct effect upon the stria vascularis resulting in changed electrolyte composition of the endolymph and, hence, of the endocochlear potential [47, 43, 48].

It has been shown that perilymphatic perfusion of ouabain interferes with strial function resulting in a changed electrolyte composition of the endolymph and reduced cochlear potentials [43, 44]. It has generally been assumed that this effect is based upon direct binding of ouabain to the Na^+/K^+-ATPase located at the basolateral membranes of the marginal cells, which are involved in secretion of K^+ into the endolymph, and thus maintain endolymph homeostasis and generation of the endocochlear potential. For this to take place, it is necessary that perilymphatic ouabain enters the stria vascularis after diffusion through the loosely arranged collagen network of the spiral ligament (cf., [45, 49]), although there is no experimental evidence for such a diffusion route. A recent paper by Adachi *et al*. [50] concludes that fibrocytes in the spiral ligament play a pivotal role in the transport of K^+ to the stria vascularis and, hence, are involved in the maintenance of the endocochlear potential. From their data it seems likely to propose that ouabain exerts a direct effect upon the Na^+/K^+-ATPase present in the type II spiral ligament fibrocytes rather than upon the strial Na^+/K^+-ATPase.

The subsequent change in endolymph composition could then (indirectly) impair the function of the OHCs. Although no visible morphological changes in the stria vascularis (and the spiral ligament) could be observed in our animals, it cannot be excluded that ouabain has interfered with both tissues at a subcellular level.

We observed that treatment with ouabain resulted in complete loss of the OHCs, primarily in the basal and middle turns, already within 4-7 days after round window membrane application of ouabain. This rapid loss of OHCs is similar to that observed after concomitant administration of kanamycin and furosemide [37], which results in a complete loss of OHCs in all cochlear turns within 7 days.

Loss of IHCs was not observed in any of the responding animals. This is in line with a myriad of earlier publications, indicating that IHCs are less vulnerable to most ototoxic drugs. Although we did not observe any morphological changes at the light microscopical level, it cannot be excluded that cellular changes may have occurred in the IHCs, as illustrated by the observation that ouabain-induced loss of SGCs eventually results in loss of the synaptic ribbons in the IHC [21]. This so-called

hidden hearing loss has been recently demonstrated to occur in noise-exposed or aged cochleas in mouse models [51].

The effect of ouabain upon the SGCs may be taking place parallel to that upon the OHCs, but loss of SGCs seems to be a later event, as illustrated by our observation that SGCs are still present in a number of animals in which complete OHC loss had occurred. On the other hand, we observed that in some animals loss of OHCs was accompanied by SGC loss. This implies that ouabain may act simultaneously upon the perikarya of the SGCs and/or the surrounding satellite glial cells or Schwann cells, which has also been reported for cisplatin-induced cochleotoxicity [36]. Ouabain can directly affect the Na^+/K^+-ATPase present in the nerve fibres, the perikarya of the SGCs and/or the satellite glial cells leading to depolarization of the cell and eventually neuronal cell death [52], because ouabain can enter Rosenthal's canal through the canaliculi perforantes which are located in the osseous spiral lamina and the lateral wall of the bony modiolus [53, 45]. The observed effect of ouabain upon the SGCs is more acute than that after combined administration of kanamycin and furosemide. With ouabain concentrations of ≥1 mM, already within 7 days a complete loss of SGCs can be observed, whereas with the kanamycin and furosemide deafening protocol it takes 4-6 weeks to obtain such a dramatic loss [37, 54].

Our data clearly show that ouabain interferes with auditory function in guinea pigs, as both the aABR amplitude and threshold were affected, seemingly in a dose-dependent fashion, already within 2 days after round window membrane application and did not recover during the course of the experiment (cf., Fig. 2). However, since the histological damage varied considerably within these treatment groups, it is difficult to identify the main cause for the observed hearing loss. The high variability in histological damage observed in the (affected) animals (Groups I and II) may be due to the fact that gelfoam was used as a carrier to apply ouabain to the cochlea. It is not certain if with this means of application ouabain concentrations have reached equal intracochlear levels among the different animals. However, especially the results of Group I (10 mM) have to be handled with caution, since this group only consist of two animals and thus displays results of a group with limited sample size. The small number of animals causes high uncertainty about the variability in this group. Some variability in our method might also be the result of outbred albino Dunkin Hartley guinea pigs, which are commonly used in inner ear biology. One method to possibly reduce this variability is to use inbred strains, such as strain 2 or strain 13, for future

experiments [55]. Our sensitivity analyses suggest that the groups treated with PBS and 0.01 mM ouabain are similar as well as the groups treated with 1 mM and 10 mM ouabain as pooling these pairs of groups did not cause a dilution of effect in either the ANOVA or the linear regression. Nonetheless, the histological results of group I (10 mM) and group II (1 mM) suggest that ouabain, when used in the guinea pig to induce selective degeneration of (type-I) SGCs, is contrary to the observations in other rodent species since it also results in loss of OHCs.

The *post-hoc* categorization of the data based upon our histological observations reveals that cochleas exhibiting only moderate OHC loss without any significant SGC loss (Category 2) displayed a degree of hearing loss that is rather similar to that observed in cochleas with both severe OHC and SGC loss (i.e., Category 3; see Fig. 5). In both categories the threshold shift is substantial and amounts to 39-45 dB, which is accordance with the 40-45 dB increase in threshold known to be associated with complete OHC loss [56]. The fact that approximately 50% of the OHCs were present in Category 2 and 30% of the OHCs still remained in Category 3, and the remaining OHCs did not show any light microscopical changes, may indicate that the function of these remaining OHCs was impaired or that there were just not enough functional OHCs left to perform effective tuning of the basilar membrane. The substantial SGC loss observed in cochleas of Category 3 is not likely to have contributed to the threshold increase, as it would have augmented the difference between the threshold shifts in Category 2 and Category 3 cochleas. Furthermore, thresholds of (electrically evoked) ABRs and compound action potentials do not tend to increase with progressing SGC loss after deafening [42, 34], indicating that a degenerating SGC population in itself does not imply higher excitation thresholds.

The aABR amplitude was substantially lower in the two categories exhibiting OHC loss (Categories 2 and 3; see Fig. 5). As with the aABR threshold, the amplitude obviously collapsed with moderate OHC loss, but did hardly change with increasing OHC loss and additional SGC loss. Since the aABR amplitude essentially reflects population size, recruitment and synchrony – and given that the IHCs remained intact – we can therefore conclude that such a substantial decrease in amplitude is likely the result of reduced recruitment caused by OHC loss. It is at this point worthwhile to repeat that our findings were very similar for the ABR wave I and wave II. Despite the histological differences between Categories 2 and 3, the similarity in aABR amplitude and threshold are striking. This discrepancy may partly be explained

by histologically intact, but non-functional, cells that therefore do not contribute to the mechano-electric transduction process. With up to 7 days, the time frame of our study was similar to that of the deafening procedure of guinea pigs described by Cho *et al*. [11]. They found that application of ouabain results in severe decrease in SGC numbers within 7 days. In our study, this histological effect can be observed within the same time frame, including loss of OHCs. However, we only studied the effect of ouabain on OHCs, SGCs and stria vascularis over a time frame of up to 7 days. Consequently, we can only draw conclusions about the short-term effect of ouabain upon the OHCs and SGCs, but not about any long-term effects on, for instance, the stria vascularis. In addition, it may be possible that animals treated with 0.1 mM ouabain (Group III) after an extended period, i.e. 14 days or 21 days, do show histological effect. However, regarding the loss of SGCs, a previous study showed that there is no long-term SGC regeneration after systemic deafening [57]. From our experiments we can conclude that ouabain does result in a rapid loss of SGCs in the guinea pig cochlea; in the responding animals already within 7 days a complete loss of SGCs can be observed.

Therefore, in theory, ouabain deafening should be suitable for stem cell therapy in the inner ear since supporting cells and IHCs are preserved. However, the observation that affected aABRs do not automatically implicate an underlying loss of SGCs, makes us conclude that locally applied ouabain is not a reliable model to investigate cell-based auditory nerve therapy in the guinea pig.

Acknowledgements

The authors would like to thank René van de Vosse (Department of Medical Engineering and Clinical Physics, University Medical Center Utrecht, the Netherlands) for technical support and the animal caretakers of the Animal Care Facility of the Utrecht University (Utrecht, the Netherlands). This work was supported by grants from MED-EL (Innsbruck, Austria) and Stichting Het Heinsius-Houbolt Fonds (the Netherlands). Timo Schomann was financially supported by Percuros B.V. (Alan Chan and Ronny Fassnacht) through funding from the European Commission of the H2020-MSCA-RISE-2014 award through the PRISAR project (Grant no. 644373) and the H2020-MSCA-RISE-2016 award through the CHARMED project (Grant no. 734684).

Declaration of interest

No conflict of interest has been declared.

Copyright

This article is distributed under the terms of the Creative Commons Attribution License (http://creativecommons.org/licenses/by/4.0/), which permits unrestricted use, distribution, and reproduction in any medium.

References

1. Gantz, B.J., Woodworth, G.G., Knutson, J.F., Abbas, P.J., and Tyler, R.S., Multivariate predictors of audiological success with multichannel cochlear implants. Ann. Otol. Rhinol. Laryngol., 1993. **102**: pp. 909-916.
2. Briaire, J.J. and Frijns, J.H.M., The consequences of neural degeneration regarding optimal cochlear implant position in scala tympani: A model approach. Hear. Res., 2006. **214**: pp. 17-27.
3. Ulfendahl, M., Hu, Z., Olivius, P., Duan, M., and Wei, D., A cell therapy approach to substitute neural elements in the inner ear. Physiol. Behav., 2007. **92**: pp. 75-79.
4. Sekiya, T., Kojima, K., Matsumoto, M., and Ito, J., Replacement of diseased auditory neurons by cell transplantation. Front. Biosci., 2008. **13**: pp. 2165-2176.
5. Hu, Z., Ulfendahl, M., and Olivius, N.P., Central migration of neuronal tissue and embryonic stem cells following transplantation along the adult auditory nerve. Brain Res., 2004. **1026**: pp. 68-73.
6. Coleman, B., Hardman, J., Coco, A., Epp, S., De Silva, M., Crook, J., and Shepherd, R., Fate of embryonic stem cells transplanted into the deafened mammalian cochlea. Cell Transplant., 2006. **15**: pp. 369-380.
7. Corrales, C.E., Pan, L., Li, H., Liberman, M.C., Heller, S., and Edge, A.S., Engraftment and differentiation of embryonic stem cell-derived neural progenitor cells in the cochlear nerve trunk: Growth of processes into the organ of Corti. J. Neurobiol., 2006. **66**: pp. 1489-1500.
8. Schmiedt, R.A., Okamura, H.O., Lang, H., and Schulte, B.A., Ouabain application to the round window of the gerbil cochlea: A model of auditory neuropathy and apoptosis. J. Assoc. Res. Otolaryngol., 2002. **3**: pp. 223-233.
9. Lang, H., Schulte, B.A., and Schmiedt, R.A., Ouabain induces apoptotic cell death in type I spiral ganglion neurons, but not type II neurons. J. Assoc. Res. Otolaryngol., 2005. **6**: pp. 63-74.
10. Lang, H., *Loss, degeneration, and preservation of the spiral ganglion neurons and their processes*, in *The primary auditory neurons of the mammalian cochlea*, A. Dabdoub, *et al.*, Editors. 2016, Springer New York: New York, U.S.A. pp. 229-262.
11. Cho, Y.B., Cho, H.H., Jang, S., Jeong, H.S., and Park, J.S., Transplantation of neural differentiated human mesenchymal stem cells into the cochlea of an auditory-neuropathy guinea pig model. J. Korean Med. Sci., 2011. **26**: pp. 492-498.
12. Chen, W., Jongkamonwiwat, N., Abbas, L., Eshtan, S.J., Johnson, S.L., Kuhn, S., Milo, M., Thurlow, J.K., Andrews, P.W., Marcotti, W., Moore, H.D., and Rivolta, M.N., Restoration of auditory evoked responses by human ES-cell-derived otic progenitors. Nature, 2012. **490**: pp. 278-282.
13. Ramekers, D., Versnel, H., Grolman, W., and Klis, S.F.L., Neurotrophins and their role in the cochlea. Hear. Res., 2012. **288**: pp. 19-33.
14. Wang, L.E., Cao, K.L., Yin, S.K., Wang, Z., and Chen, Z.N., Cochlear function after selective spiral ganglion cells degeneration induced by ouabain. Chin. Med. J., 2006. **119**: pp. 974-979.
15. Qu, J., Gan, Y.N., Xie, K.L., Liu, W.B., Wang, Y.F., Hei, R.Y., Mi, W.J., and Qiu, J.H., Inhalation of hydrogen gas attenuates ouabain-induced auditory neuropathy in gerbils. Acta Pharmacol. Sin., 2012. **33**: pp. 445-451.
16. Bourien, J., Tang, Y., Batrel, C., Huet, A., Lenoir, M., Ladrech, S., Desmadryl, G., Nouvian, R., Puel, J.L., and Wang, J., Contribution of auditory nerve fibers to compound action potential of the auditory nerve. J. Neurophysiol., 2014. **112**: pp. 1025-1039.
17. Kilpatrick, L.A., Samuvel, D.J., Zhu, J., Smythe, N., and Lang, H., Ouabain-induced auditory nerve degeneration in congenic Ly5.1 mice. J. Otol., 2011. **6**: pp. 19-28.
18. Kilpatrick, L.A., Zhu, J., Lee, F.S., and Lang, H., Role of stromal cell-derived factor-1 expression in the injured mouse auditory nerve. Otolaryngol. Head Neck Surg., 2011. **145**: pp. 1007-1015.
19. Lang, H., Li, M., Kilpatrick, L.A., Zhu, J., Samuvel, D.J., Krug, E.L., and Goddard, J.C., Sox2 up-regulation and glial cell proliferation following degeneration of spiral ganglion neurons in the adult mouse inner ear. J. Assoc. Res. Otolaryngol., 2011. **12**: pp. 151-171.
20. Yuan, Y. and Chi, F., Dynamic changes in hair cell ribbon synapse induced by loss of spiral ganglion neurons in mice. Chin. Med. J. (Engl), 2014. **127**: pp. 1941-1946.
21. Yuan, Y., Shi, F., Yin, Y., Tong, M., Lang, H., Polley, D.B., Liberman, M.C., and Edge, A.S., Ouabain-induced cochlear nerve degeneration: Synaptic loss and plasticity in a mouse model of auditory neuropathy. J. Assoc. Res. Otolaryngol., 2014. **15**: pp. 31-43.
22. Zhang, Z.J., Guan, H.X., Yang, K., Xiao, B.K., Liao, H., Jiang, Y., Zhou, T., and Hua, Q.Q., Dose-dependent effects of ouabain on spiral ganglion neurons and Schwann cells in mouse cochlea. Acta Otolaryngol., 2017. **137**: pp. 1017-1023.
23. Fu, Y., Ding, D., Jiang, H., and Salvi, R., Ouabain-induced cochlear degeneration in rat. Neurotox. Res., 2012. **22**: pp. 158-169.
24. Qu, J., Huang, H., Wang, J., Mi, W.J., Qiao, L., and Qiu, J.H., Detrimental effects of ouabain on cochlear spiral ganglion cells in rats. Chin. J. Otorhinolaryngol. Head Neck Surg., 2012. **47**: pp. 926-930.
25. Wang, X., Wang, Y., Ding, Z.J., Yue, B., Zhang, P.Z., Chen, X.D., Chen, X., Chen, J., Chen, F.Q., Chen, Y., Wang, R.F., Mi, W.J., Lin, Y., Wang, J., and Qiu, J.H., The role of RIP3 mediated necroptosis in ouabain-induced spiral ganglion neurons injuries. Neurosci. Lett., 2014. **578**: pp. 111-116.
26. Kim, B.Y., Bae, W.Y., Kim, J.-R., and Lee, T.H., Damage of spiral ganglion cell induced by ouabain application in cat. Korean J. Otorhinolaryngol.-Head Neck Surg., 2014. **57**: pp. 589-595.
27. Matsuoka, A.J., Kondo, T., Miyamoto, R.T., and Hashino, E., Enhanced survival of bone-marrow-derived pluripotent stem cells in an animal model of auditory neuropathy. Laryngoscope, 2007. **117**: pp. 1629-1635.
28. Lang, H., Schulte, B.A., Goddard, J.C., Hedrick, M., Schulte, J.B., Wei, L., and Schmiedt, R.A., Transplantation of mouse embryonic stem cells into the cochlea of an auditory-neuropathy animal model: Effects of timing after injury. J. Assoc. Res. Otolaryngol., 2008. **9**: pp. 225-240.
29. Hashino, E. and Fritsch, M.H., *Embryonic stem cell-derived neurons for inner ear therapy*, in *Embryonic stem cells - Recent advances in pluripotent stem cell-based regenerative medicine*, C. Atwood, Editor. 2011, InTech. pp. 189-202.

30. Yuan, Y., Mizutari, K., Cheng, Y., Lang, H., Liberman, M.C., Shi, F., and Edge, A.S., Reinnervation of hair cells and cochlear nucleus by engrafted neurons derived from stem cells, in Abstract Book Association for Research in Otolaryngology. 2012: San Diego,. pp. 124-125.
31. Zhang, P.Z., He, Y., Jiang, X.W., Chen, F.Q., Chen, Y., Shi, L., Chen, J., Chen, X., Li, X., Xue, T., Wang, Y., Mi, W.J., and Qiu, J.H., Stem cell transplantation via the cochlear lateral wall for replacement of degenerated spiral ganglion neurons. Hear. Res., 2013. **298**: pp. 1-9.
32. Hamada, M. and Kimura, R.S., Morphological changes induced by administration of a Na^+,K^+-ATPase inhibitor in normal and hydropic inner ears of the guinea pig. Acta Otolaryngol., 1999. **119**: pp. 778-786.
33. Havenith, S., Versnel, H., Agterberg, M.J.H., De Groot, J.C.M.J., Sedee, R.J., Grolman, W., and Klis, S.F.L., Spiral ganglion cell survival after round window membrane application of brain-derived neurotrophic factor using gelfoam as carrier. Hear. Res., 2011. **272**: pp. 168-177.
34. Ramekers, D., Versnel, H., Strahl, S.B., Smeets, E.M., Klis, S.F.L., and Grolman, W., Auditory-nerve responses to varied inter-phase gap and phase duration of the electric pulse stimulus as predictors for neuronal degeneration. J. Assoc. Res. Otolaryngol., 2014. **15**: pp. 187-202.
35. De Groot, J.C.M.J., Veldman, J.E., and Huizing, E.H., An improved fixation method for guinea pig cochlear tissues. Acta Otolaryngol., 1987. **104**: pp. 234-242.
36. Van Ruijven, M.W.M., De Groot, J.C.M.J., and Smoorenburg, G.F., Time sequence of degeneration pattern in the guinea pig cochlea during cisplatin administration. A quantitative histological study. Hear. Res., 2004. **197**: pp. 44-54.
37. Versnel, H., Agterberg, M.J.H., De Groot, J.C.M.J., Smoorenburg, G.F., and Klis, S.F.L., Time course of cochlear electrophysiology and morphology after combined administration of kanamycin and furosemide. Hear. Res., 2007. **231**: pp. 1-12.
38. Agterberg, M.J.H., Versnel, H., De Groot, J.C.M.J., Smoorenburg, G.F., Albers, F.W.J., and Klis, S.F.L., Morphological changes in spiral ganglion cells after intracochlear application of brain-derived neurotrophic factor in deafened guinea pigs. Hear. Res., 2008. **244**: pp. 25-34.
39. Romand, R. and Romand, M.R., The ontogenesis of pseudomonopolar cells in spiral ganglion of cat and rat. Acta Otolaryngol., 1984. **97**: pp. 239-249.
40. Havenith, S., Klis, S.F.L., Versnel, H., and Grolman, W., A guinea pig model of selective severe high-frequency hearing loss. Otol. Neurotol., 2013. **34**: pp. 1510-1518.
41. Havenith, S., Versnel, H., Klis, S.F., and Grolman, W., Local delivery of brain-derived neurotrophic factor on the perforated round window membrane in guinea pigs: A possible clinical application. Otol. Neurotol., 2015. **36**: pp. 705-713.
42. Agterberg, M.J.H., Versnel, H., Van Dijk, L.M., De Groot, J.C.M.J., and Klis, S.F.L., Enhanced survival of spiral ganglion cells after cessation of treatment with brain-derived neurotrophic factor in deafened guinea pigs. J. Assoc. Res. Otolaryngol., 2009. **10**: pp. 355-367.
43. Bosher, S.K., The effects of inhibition of the strial Na^+-K^+-activated ATPase by perilymphatic ouabain in the guinea pig. Acta Otolaryngol., 1980. **90**: pp. 219-229.
44. Higashiyama, K., Takeuchi, S., Azuma, H., Sawada, S., Kakigi, A., and Takeda, T., Ouabain-induced vacuolar formation in marginal cells in the stria vascularis is dependent on perilymphatic Na(+). ORL J. Otorhinolaryngol. Relat. Spec., 2010. 71 Suppl **1**: pp. 57-66.
45. Rask-Andersen, H., Schrott-Fischer, A., Pfaller, K., and Glueckert, R., Perilymph/modiolar communication routes in the human cochlea. Ear Hear., 2006. **27**: pp. 457-465.
46. Silva, E. and Soares-da-Silva, P., New insights into the regulation of Na^+,K^+-ATPase by ouabain. Int. Rev. Cell Mol. Biol., 2012. **294**: pp. 99-132.
47. Konishi, T. and Mendelsohn, M., Effect of ouabain on cochlear potentials and endolymph composition in guinea pigs. Acta Otolaryngol., 1970. **69**: pp. 192-199.
48. Shugyo, A., Mori, N., and Matsunaga, T., A comparison of the reduction in the K^+ activity of the scala media produced by furosemide and ouabain. Eur. Arch. Otorhinolaryngol., 1990. **248**: pp. 79-81.
49. Salt, A.N., Gill, R.M., and Hartsock, J.J., Perilymph kinetics of FITC-dextran reveals homeostasis dominated by the cochlear aqueduct and cerebrospinal fluid. J. Assoc. Res. Otolaryngol., 2015. **16**: pp. 357-371.
50. Adachi, N., Yoshida, T., Nin, F., Ogata, G., Yamaguchi, S., Suzuki, T., Komune, S., Hisa, Y., Hibino, H., and Kurachi, Y., The mechanism underlying maintenance of the endocochlear potential by the K^+ transport system in fibrocytes of the inner ear. J. Physiol., 2013. **591**: pp. 4459-4472.
51. Kujawa, S.G. and Liberman, M.C., Synaptopathy in the noise-exposed and aging cochlea: Primary neural degeneration in acquired sensorineural hearing loss. Hear. Res., 2015. **330**: pp. 191-199.
52. Xiao, A.Y., Wei, L., Xia, S., Rothman, S., and Yu, S.P., Ionic mechanism of ouabain-induced concurrent apoptosis and necrosis in individual cultured cortical neurons. J. Neurosci., 2002. **22**: pp. 1350-1362.
53. Shepherd, R.K. and Colreavy, M.P., Surface microstructure of the perilymphatic space: Implications for cochlear implants and cell- or drug-based therapies. Arch. Otolaryngol. Head Neck Surg., 2004. **130**: pp. 518-523.
54. Kroon, S., Ramekers, D., Smeets, E.M., Hendriksen, F.G.J., Klis, S.F.L., and Versnel, H., Degeneration of auditory nerve fibers in guinea pigs with severe sensorineural hearing loss. Hear. Res., 2017. **345**: pp. 79-87.
55. Festing, M.F.W., *Inbred strains of guinea pigs*, in *Inbred strains in biomedical research*. 1979, Macmillan Education UK: London. pp. 308-312.
56. Liberman, M.C. and Dodds, L.W., Single-neuron labeling and chronic cochlear pathology. III. Stereocilia damage and alterations of threshold tuning curves. Hear. Res., 1984. **16**: pp. 55-74.
57. Ramekers, D., Versnel, H., Strahl, S.B., Klis, S.F.L., and Grolman, W., Temporary neurotrophin treatment prevents deafness-induced auditory nerve degeneration and preserves function. J. Neurosci., 2015. **35**: pp. 12331-12345.

Chapter 7

Multimodal imaging of hair follicle bulge-derived stem cells in a mouse model of traumatic brain injury

Submitted

T. Schomann, J.D. Iljas, I. Que, Y. Li, E. Suidgeest, L. van der Weerd, L.J. Cruz, J.H.M. Frijns, A.B. Chan, C.M.W.G. Löwik, M.A. Huisman, L. Mezzanotte

Abstract

Traumatic brain injury (TBI) is a devastating event for which current therapies are limited. Stem cell transplantation may lead to recovery of function via different mechanisms, such as cell replacement through differentiation, stimulation of angiogenesis, and support to the microenvironment. Adult hair follicle bulge-derived stem cells (HFBSCs) possess neuronal differentiation capacity, are easy to harvest, and are relatively immune-privileged, which makes them potential candidates for autologous stem cell-based therapy.

In this study, we applied *in vivo* multimodal, optical, and magnetic resonance imaging techniques to investigate the behavior of mouse HFBSCs in a mouse model of TBI. HFBSCs expressed Luc2 and copGFP and were examined for their differentiation capacity *in vitro*. Subsequently, transduced HFBSCs, preloaded with ferumoxytol, were transplanted next to the TBI lesion (cortical region) in nude mice, two days after injury. Brains were fixed for immunohistochemistry 58 days after transplantation.

Luc2- and copGFP-expressing, ferumoxytol-loaded HFBSCs showed adequate neuronal differentiation potential *in vitro*. Bioluminescence of the lesioned brain revealed survival of HFBSCs and magnetic resonance imaging identified their localization in the area of transplantation. Immunohistochemistry showed that transplanted cells stained for nestin and neurofilament protein (NF-pan). Cells also expressed laminin and fibronectin, but extracellular matrix masses were not detected. After 58 days, ferumoxytol could be detected in HFBSCs in brain tissue sections.

These results showed that HFBSCs are able to survive after brain transplantation and suggest that cells may undergo differentiation towards a neuronal cell lineage, which supports their potential use for cell-based therapy for TBI.

Introduction

In recent years, stem cell therapy has attracted huge interest as a new therapeutic method for the treatment of brain injury. Many studies using animal models and even human clinical trials have demonstrated potential of stem cell transplantation for the treatment of neurological disorders [1, 2]. The goal of stem cell therapy is the formation of new tissue to replace damaged tissue by utilizing the regenerative capacity of stem cells [3].

Application of autologous stem cells, such as bone marrow-derived mesenchymal stem cells (BM-MSCs) and human umbilical cord blood cells, could induce neuro-restorative effects in the brain after injury [4]. In general, these effects are mainly attributed to paracrine mechanisms such as the stimulatory effect of stem cells on endogenous cells to release growth and trophic factors. It has been reported that BM-MSCs have the ability to migrate, differentiate, and contribute to neuronal repair [5]. The advantage of BM-MSCs is that they can be harvested from the patient allowing autologous stem cell therapy. Furthermore the latter allows the conduction of clinical trials using BM-MSCs in patients with traumatic brain injury (TBI) [6]. However, their mesodermal potency poses a risk for unwanted differentiation after transplantation [7].

An alternative could be the use of autologous adult neural progenitor stem cells that can be isolated from easily accessible tissues in the adult body such as periodontal ligament surrounding teeth, soft palate, inferior turbinate, or hair follicles [8-11]. These stem cells derive from a rich source of multipotent stem cells called the neural crest. The differentiation of neural crest-derived cells (NCSCs) from adult tissue under neurogenic conditions results in the production of cells that fulfill most criteria for a genuine neuronal differentiation [12]. For cell-based therapy, the use of NCSCs from the hair follicle bulge (or: hair follicle bulge-derived stem cells, HFBSCs) has several advantages above using other stem cell types, such as embryonic stem cells and neural stem cells. These advantages are i) they are abundant and easily accessible, and only minimally invasive surgery is necessary to harvest them; ii) they are suitable candidates for autologous transplantation, which would avoid rejection of the transplant and graft-versus-host disease due to immunomodulation [13]; and iii) there is no evidence for tumor formation [14]. Besides, the hair follicle is an immune-privileged site indicating HFBSC tolerance in xenogeneic and allogeneic

transplantations [13].

However, successful translation of stem cell-based therapies in the clinics will require robust preclinical testing and validation, focusing on consensual definitions of terms and the elucidation of the cells' exact mechanism of action [15]. An integral part of this is the requirement to monitor the extension of the TBI and response to treatment in a non-invasive manner, which could be facilitated by the application of multimodal imaging tools.

In order to regenerate neural tissue, transplanted stem cells have to survive, differentiate into neurons and/or glial cells, and seek appropriate neuronal connections in order to achieve functional neuronal repair. Visualization of the migration and the fate of the transplanted stem cells in the injured brain in living animals could provide direct monitoring of the cells' behaviour after transplantation.

The aim of this study is to combine multimodality imaging technologies, such as optical imaging by means of bioluminescence imaging (BLI) and magnetic resonance imaging (MRI), to investigate *in vivo* the behavior of transplanted HFBSCs cells in a mouse model of TBI [16, 17]. The ultimate goal is to achieve a better understanding of the mechanism of recovery (e.g., cell replacement, support of the microenvironment, or a combination of both). This may ultimately contribute to a better strategy towards the promotion of neural tissue regeneration.

For this purpose, HFBSCs were transfected with a lentiviral vector containing a construct that is composed of a promoter and genes coding for both codon-optimized firefly luciferase (Luc2) and copepod green fluorescent protein (copGFP), in which the latter demonstrates a high fluorescence quantum yield and is more stable at a wide range of temperatures. Both genes are coupled via a T2A-like sequence, which mediates co-translational cleavage and, hence, results in bicistronic expression of copGFP and Luc2 [18]. The promoter is either the constitutively active elongation factor 1α (EF1α) or the promoter of doublecortin (DCX), which is a neuronal migration protein and early neuronal marker [19].

Additionally, transduced cells were loaded with ferumoxytol, which is a superparamagnetic iron oxide (SPIO) nanoparticle, in order to confirm their anatomical location by means of MRI *in vivo* [20]. Ferumoxytol is an FDA-approved

drug for treatment of iron deficiency anemia, and has been successfully used to image MSCs or macrophages loaded with heparin-protamine-ferumoxytol (HPF) complexes in preclinical studies [21, 22].

Material and methods

Cell culture

Hair follicles were dissected out from the whisker pads of healthy adult (> 23 days) male and female surplus mice (strain C57Bl/6), as previously described [23, 24]. Isolation of HFBSCs from the bulge region of the hair follicle was described elsewhere [14, 24, 25].

Selected HFBSCs were cultured on poly-D-lysine-coated (PDL; Sigma-Aldrich, St. Louis, MO, USA; 0.01 mg/ml in distilled water) cell culture-treated 12-well plates (TPP Techno Plastic Products AG, Trasadingen, Austria) in basic growth medium (BGM), and maintained in a humidified incubator at 37°C and 5% CO_2. BGM, modified from Nguyen *et al*. [26], consists of DMEM/Ham's F-12 1:1 (Biochrom AG, Berlin, Germany), 1% GlutaMax™ (100x; Gibco, Bleiswijk, the Netherlands) and 1% antibiotic/antimycotic solution (100x; Sigma-Aldrich) supplemented with 10% fetal bovine serum (FBS; Gibco), 2% B-27® supplement without vitamin A (50x; Gibco), 1% N-2 MAX media supplement (100x; R&D Systems™, Minneapolis, MN, USA), recombinant human basic fibroblast growth factor (20 ng/ml; R&D Systems), and recombinant human epidermal growth factor (20 ng/ml; R&D Systems). The cultures were passaged as previously described after 60%-70% confluence was reached [24, 25]. HFBSCs were frozen in 10% DMSO in FBS and stored at -80°C until use. After thawing, HFBSCs were cultured in BGM on PDL-coated dishes (TPP Techno Plastic Products AG) and used for subsequent experiments.

Lentiviral vector production and transduction of HFBSCs

HFBSCs were transduced with a third-generation lentiviral vector containing the sequences for Luc2 and copGFP. Details on cloning and recombination procedures have been reported previously [27, 28]. In brief, lentivirus particles were generated by means of transfection of HEK293 cells with packaging plasmids and the plasmid pCDH-EF1-Luc2-T2A-copGFP or pCDH-DCX-Luc2-T2A-copGFP [25]. Virus was quantified by antigen-capture ELISA, measuring HIV p24 levels (ZeptoMetrix Corporation, NY, USA). For transduction, HFBSCs were resuspended in BGM. Pseudoviral particles containing the copGFP-Luc2 constructs, using 40 ng virus per

1 x 10^5, were added to the cells. Transduced HFBSCs were stored at -80°C until use.

Lentiviral vector production and stem cell transduction were performed under the appropriate biosafety level conditions (ML-II) in accordance with the National Biosafety Guidelines and the Regulations for Research on Genetically Modified Organisms. Procedures and protocols were reviewed and approved by the LUMC Biosafety Committee (GMO permit 00-026).

Fluorescence microscopy

Transduced HFBSCs containing the copGFP-Luc2 construct were plated and allowed to attach in PDL-coated 12-well cell culture plates. Expression of copGFP was observed using an Olympus IX70 epi-illumination fluorescence microscope (FITC filter settings) with a Leica DFC340 FX digital color camera (Leica Camera AG, Wetzlar, Germany). Images were acquired and digitally stored using Leica Application Suite Advanced Fluorescence (LAS-AF) version 1.9 software.

In vitro differentiation

Expression of copGFP under regulation of the DCX promoter was investigated by differentiating pCDH-DCX-Luc2-T2A-copGFP-transduced HFBSCs, according to a previously established neural differentiation protocol [24, 25]. pCDH-EF1α-Luc2-T2A-copGFP-transduced HFBSCs served as controls. Briefly, 2.5 x 10^5 cells were seeded via the side into PDL-coated wells containing PDL-coated cover glasses (Thermo Scientific, Waltham, MA, USA) in a total volume of 500 µl BGM. Differentiation was induced by replacing 250 µl medium with 300 µl induction medium (IM). IM consists of DMEM/Ham's F-12 1:1 supplemented with 1.5 mM cAMP (Sigma-Aldrich), 1% GlutaMax (Life Technologies), 10 ng/ml NGF, 10 ng/ml GDNF, 10 ng/ml BDNF (all from R&D Systems), and 2% B27 with vitamin A (Life Technologies). Subsequently, cultures were allowed to differentiate for at least 60 hours without disturbance, followed by an additional substitution of 250 µl medium with 300 µl IM.

Loading of HFBSCs with HPF complexes

HFBSCs containing the copGFP-Luc2 construct were loaded with HPF complexes, according to the procedure of Thu *et al*. [22]. An amount of 4 x 10^6 cells were re-suspended in serum-free BGM containing 2 IU/ml sodium heparin (LEO Pharma, Amsterdam, the Netherlands), 60 µg/ml protamine hydrochloride (MEDA Pharma BV, Amstelveen, the Netherlands), and 50 µg/ml ferumoxytol (Rienso®, Takeda Pharma A/S, Roskilde, Denmark), which was then followed by incubation at 37°C for 2 hours. An equal amount of BGM containing 20% FBS was added, upon which the cells were transferred to PDL-coated dishes and incubated in a humidified incubator with 5% CO_2 at 37°C. After 24 hours, the cells were firstly washed with phosphate-buffered saline (PBS) and then with PBS containing heparin (10 IU/ml). The cells were passaged by adding pre-warmed (37°C) balanced salt solution containing 0.05% trypsin and 0.02% EDTA.4Na (Gibco Life Technologies) to the culture dish, before being incubated for 2 minutes. Cells were collected and re-suspended in PBS at a concentration of 5 x 10^4 cells/µl and stored at 4°C until transplantation.

Detection of ferumoxytol

To visualize HPF complexes that were endocytosed by HFBSCs, cells were fixed with pre-warmed 1% formaldehyde in PBS directly after incubation. Fixed ferumoxytol-loaded HFBSCs and mouse brain cryosections were pre-treated with 3% H_2O_2 in methanol for 30 minutes to inhibit endogenous peroxidase activity. This was followed by washing in distilled water for 30 minutes. Iron oxide-containing ferumoxytol was visualized using Perls' Prussian blue method, followed by 3,3'-diaminobenzidine (DAB) intensification [29]. Cells were then incubated in 1% potassium ferrocyanide ($K_4Fe(CN)_6.3H_2O$) with 1% HCl in distilled water for 30 minutes, which was then followed by several washes in distilled water (3 x 10 minutes). Next, the specimens were incubated in the dark for 10 minutes in a solution containing 0.1% 3,3'-diaminobenzidine, 4% HCl and 0.03% H_2O_2 in PBS. This was followed by 3 washes in distilled water (5 minutes each) to stop the reaction. Specimens were subsequently mounted in Roti®-Mount FluorCare mounting medium (Carl Roth GmbH + Co. KG, Karlsruhe, Germany), and examined with a Leica DM5500B microscope with a Leica DFC 450C color camera. Digital images were acquired and stored using Leica Application Suite (LAS V4.5) software.

Animals and TBI

Animal care and handling were in accordance with the guidelines and regulations as stipulated by the Dutch Experiments on Animals Act (WoD) and the European Directive on the Protection of Animals Used for Scientific Purposes (2010/63/EU). All applicable institutional and national guidelines for the care and use of animals were followed.

Healthy 8-week-old female CD1-nude mice (n=10; Charles River, Chatillon-sur-Chalaronne, France) were used for the transplantation experiments. Mice were housed in the Animal Care Facility of Leiden University Medical Center (LUMC, the Netherlands) under standard housing conditions (group cages with enriched environment, food and water *ad libitum*; diurnal light cycle [12 h light, 12 h dark], temperature 21°C; humidity 60%). The use of the animals was approved by the Animal Experiments Committee of the Leiden University Medical Center (DEC permits 10065, 11198/3, and 13024/1).

Anesthesia was induced for all experiments with 4% isoflurane in air (Teva Pharmachemie BV, Haarlem, the Netherlands), and mice were kept under anesthesia with 1.5% isoflurane in air. TBI was induced using a liquid nitrogen pre-cooled copper conical cylinder with a 3-mm diameter tip. The cylinder was applied to the head of each mouse approximately 3 mm left of the bregma for 40 seconds, so as to induce traumatic brain damage as previously described [30].

Two days after induction of the TBI, mice were anesthetized with 2% isoflurane in air for transplantation of transduced, ferumoxytol-loaded HFBSCs. A motorized, computer-controlled stereotaxic instrument (Neurostar, Tübingen, Germany) with mouse brain atlas integration and real-time visualization of the injection site in the atlas space was used for *in vivo* injections of HFBSCs into the mouse brain. The anesthetized mouse was placed into the stereotaxic instrument which fixes the skull with ear bars, and a clamp system that tightens against the jawbone and the palate. The coordinates for injection were X (-2), Y (2), and Z (1) relative to the anterior bregma. The needle was navigated by a motorized stereotactic frame utilizing StereoDrive software. Each injection was carried out within a standardized time frame, i.e. 1 minute injection time and 2 minutes deposition rest before needle retraction, to prevent potential variations in the effect of shearing forces. A total

volume of 2 µl containing 2 x 10^5 HFBSCs was stereotactically transplanted into the cerebral cortex of the animals.

Bioluminescence imaging

Observation of survival (pCDH-EF1α-Luc2-T2A-copGFP) and differentiation (pCDH-DCX-Luc2-T2A-copGFP) of transplanted HFBSCs were achieved using BLI at 2, 14, 33, and 49 days after transplantation. Prior to imaging, mice received an intraperitoneal injection of D-luciferin potassium salt (Synchem UG & Co. KG, Felsberg, Germany). Anesthesia was induced with 4% isoflurane in air, and mice were kept under anesthesia with 1.5% isoflurane in air. Images were acquired 15 minutes after injection of D-luciferin (150 mg/kg) using 30-second exposure, open filter, field of view C (default setting), f/stop=1, and medium binning for all bioluminescence measurements. All imaging measurements were performed with the IVIS® Spectrum multimodal imaging system (Caliper Life Sciences, Hopkinton, MA, USA), which combines laser scan surface topography with BLI, with the stage warmed to 37°C. Image acquisition and analysis were performed with Living Image version 4.2.1 software (Caliper Life Sciences).

Magnetic resonance imaging

In addition to BLI, ferumoxytol-loaded HFBSCs were imaged after their transplantation into the mouse brain with TBI using MRI to investigate the exact location of the stem cells at 1 and 48 days after transplantation. MRI was performed with a 7-T Bruker PharmaScan® 70/16 (Bruker Biospin, Ettlingen, Germany) equipped with a BGA-9S 300 mT/m gradient system and a conventional 23-mm birdcage transmit-and-receive radio-frequency (RF) coil (Bruker Biospin). Mice were initially anesthetized with 4% isoflurane in air and kept under anesthesia with 1.5% isoflurane in air throughout the imaging procedure. Mice were placed in the RF coil, fixed in the bed with ear bars, and kept warm using a water-heated pad with thermo-coupling to control mouse temperature. Respiration rate and temperature were measured continuously. After an initial localization scan, T2*-weighted three-dimensional fast low-angle shot (FLASH) sequences were used to visualize the mouse. Optimal sequence parameters were as follows: repetition time (TR): 100 ms; effective echo time (TE): 13 ms; imaging

matrix size: 128 x 128 x 64; final voxel resolution of: 219 x 219 x 250 µm; and a FOV of: 28 x 28 x 16 mm. Data acquisition, image reconstruction and visualization were achieved with Paravision® 6.0.1 software (Bruker Biospin, Ettlingen, Germany). Images were processed using ImageJ image analysis software (https://imagej.nih.gov/ij/plugins/cell-counter.html; version 1.47; US National Institutes of Health, Bethesda, MD, USA).

Immunohistochemistry

After 58 days, the anesthetized animals were fixed by means of intracardial perfusion with 4% formaldehyde in PBS. After decapitation, the brains were removed and stored in 1% formaldehyde in PBS at 4°C until further processing. Next, specimens were embedded in Tissue-Tek® O.C.T.™ (Sakura Finetek Europe B.V., Alphen aan den Rijn, the Netherlands) compound and frozen for cryosectioning at -20°C. Frozen mouse brains were cut with the Microtome Cryostat HM 500 OM (MICROM International GmbH, Walldorf, Germany), 10 µm brain sections were transferred onto KP Plus slides (Klinipath B.V., Duiven, the Netherlands), and the slides were stored at -20°C.

For immunohistochemistry, sections were processed as previously described [24]. This procedure was also followed for the cultured cells. Primary and secondary antibodies used in this study are listed in Table 1. For all stainings, proper positive and negative controls were used. Nuclei were counterstained with 1:1000 DAPI (Invitrogen) in PBS for 15 minutes. The specimens were mounted in a drop of Roti®-Mount FluorCare (Carl Rothi GmbH+Co. KG, Karlsruhe, Germany). All specimens were examined with a Leica DM5500 B fluorescence microscope (filter settings: TXR, Cy7, FITC and DAPI), equipped with a Leica DFC365 FX digital camera. Digital images were acquired and stored using Leica Application Suite X (LAS X) software.

Statistical analysis

Statistical analyses of the data were performed using GraphPad Prism 6.02 and SPSS Statistics version 20.0.0.1 software (IBM Corporation, Armonk, NY, USA). A multiple *t*-test was applied to the cytokine assay data, and data were expressed

as mean ± standard error of the mean (SEM). A one-way ANOVA with Bonferroni's multiple comparison test and 95% confidence interval was applied to the BLI data, and data were expressed as mean ± SEM.

Table 1: Antibodies.

Type	Antibody	Host	Clonality	Company	Cat. No.	Localization	Dilution	Control
Primary	CopGFP	Rabbit	polyclonal	Evrogen	AB513	Cytoplasm	1:200	Luc2-copGFP transduced cells
Primary	Doublecortin (DCX)	Rabbit	polyclonal	Abcam	Ab18723	Cytoplasm	1:200	C17.2, Brain (Mouse) Tissue Lysate - normal tissue, 0 days old
Primary	Fibronectin	Rabbit	polyclonal	Sigma-Aldrich	F3648	ECM	1:400	
Primary	GFAP	Rabbit	polyclonal	DAKO	Z0334	Cytoplasm	1:500	RT4-D6PT2
Primary	Ki-67	Rabbit	polyclonal	Abcam	ab15580	Nuclear	1:100	Human dermal fibroblasts
Primary	Laminin	Rabbit	polyclonal	Dako	Z009701	ECM	1:200	RT4-D6P2T, MelbA, HFBSCs
Primary	Luc2	Mouse	monoclonal	DSHB	DSHB-LUC-2	Cytoplasm	25:100	Luc2-copGFP transduced cells
Primary	Nestin 4D11	Mouse	monoclonal	Biosensis	M-1385-100	Cytoplasm	1:300	C17.2 (NSCs), M14, RT4-D6P2T
Primary	NF-Pan	Mouse	monoclonal	EMD Millipore	NE1017	Cytoskeleton	1:1000	Mouse brain slices
Secondary	Alexa Fluor™ 555	Goat	polyclonal	BioLegend	405324		1:200	
Secondary	Alexa Fluor™ 750	Goat	polyclonal	Abcam	ab175733		1:200	

Results

In vitro differentiation of transduced HFBSCs

HFBSCs, transduced with the pCDH-EF1α-Luc2-T2A-copGFP gene construct, constitutively express both Luc2 and copGFP at equimolar ratios. Prior to differentiation, the HFBSCs exhibited a bright greent-fluorescent signal and normal morphologies (Fig. 1A, Day -1). The merged image demonstrates that all cells were successfully transduced with the reporter gene construct. After induction of neuronal differentiation, HFBSCs adopted neuronal morphologies within 7 days as shown in the fluorescence and phase-contrast images (Fig. 1A, Day 7).

Under the regulation of the promoter for the neuronal migration protein DCX, HFBSCs that were transduced with the pCDH-DCX-Luc2-T2A-copGFP construct did not express copGFP (or Luc2) during standard cell culture as marked by the absence of any fluorescent signal (Fig. 1B, Day -1). However, after induction of neuronal differentiation, HFBSCs showed both a neuronal morphologies and copGFP expression under regulation of the DCX promoter within 7 days (Fig. 1B, Day 7).

Confirmation of ferumoxytol uptake by HFBSCs

To confirm that HFBSCs could take up the MRI contrast agent ferumoxytol, we performed a Perls' Prussian blue staining with DAB intensification on transduced cells loaded with HPF complexes. While the cells constitutively expressed copGFP, Perls' Prussian Blue staining with DAB intensification revealed the presence of iron oxide within 92.2 ± 1.1% of the cells as marked by intracellular deposits of a brown precipitate (Fig. 1C).

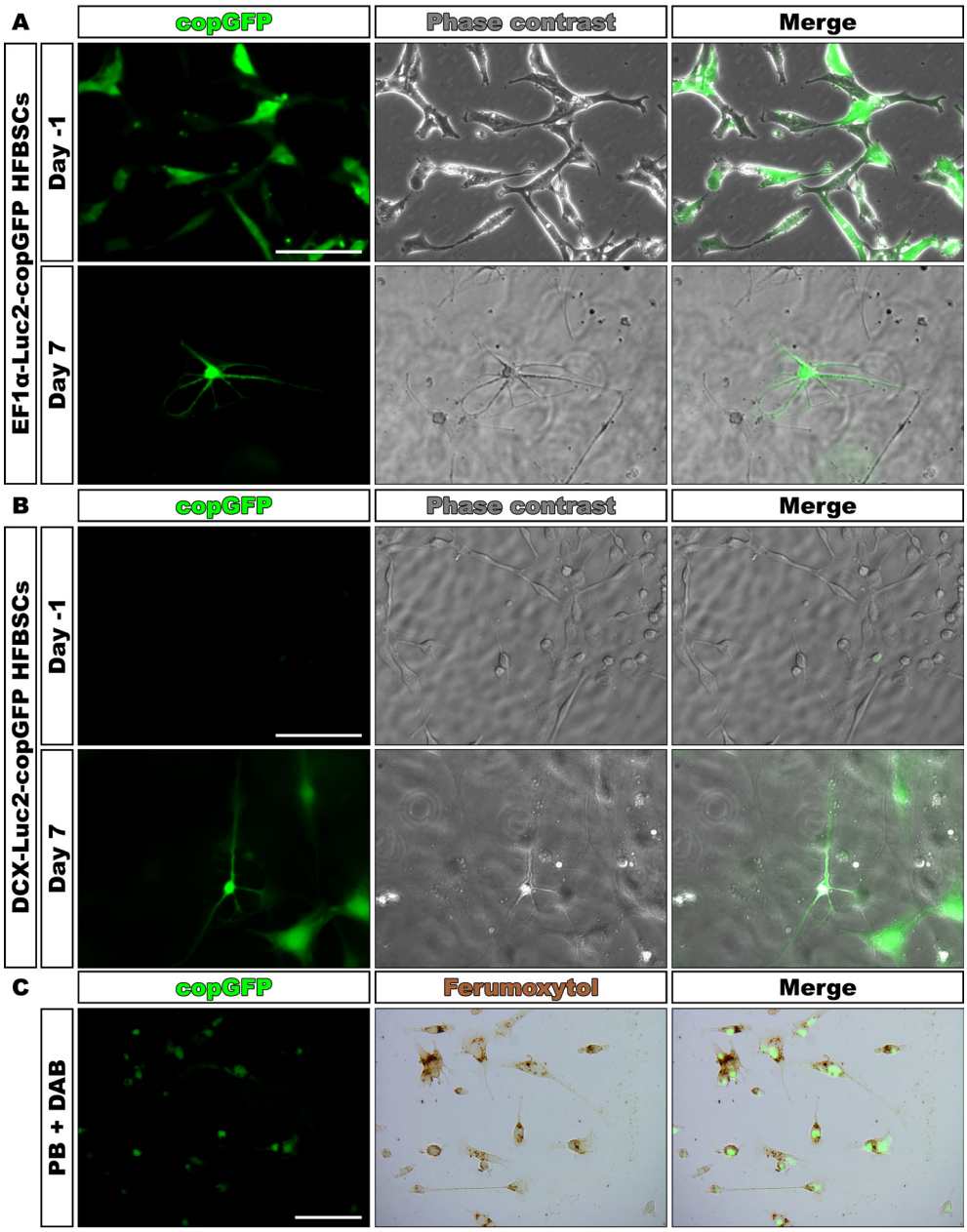
A
copGFP
Phase contrast
Merge
EF1α-Luc2-copGFP HFBSCs
Day -1
Day 7
B
copGFP
Phase contrast
Merge
DCX-Luc2-copGFP HFBSCs
Day -1
Day 7
C
copGFP
Ferumoxytol
Merge
PB + DAB

Fig. 1: *In vitro* differentiation and loading with ferumoxytol of transduced HFBSCs. **(A)** Prior to differentiation (Day -1) pCDH-EF1α-Luc2-T2A-copGFP-transduced cells exhibited a bright green-fluorescent signal of copGFP and had normal morphologies (Phase contrast). The merged image demonstrates that all cells were transduced with the reporter gene construct. Within 7 days, HFBSCs adapted neuronal morphologies (copGFP fluorescence and Phase contrast). Scale bar is 100 µm. **(B)** HFBSCs transduced with the pCDH-DCX-Luc2-T2A-copGFP construct did not express copGFP (or Luc2) prior to differentiation (Day -1) as indicated by the absence of a fluorescent signal. However, cells expressed copGFP under regulation of the DCX promoter as indicated by the green fluorescent signal 7 days after start of the differentiation. HFBSCs also adapted neuronal morphologies (Phase contrast). Scale bar is 100 µm. **(C)** Perls' Prussian blue (PB) staining + DAB intensification stained ferumoxytol within the cells as marked by a brown precipitate. Faint copGFP fluorescence persisted through the staining process as can be observed in the fluorescence and merged images. Scale bar is 100 µm.

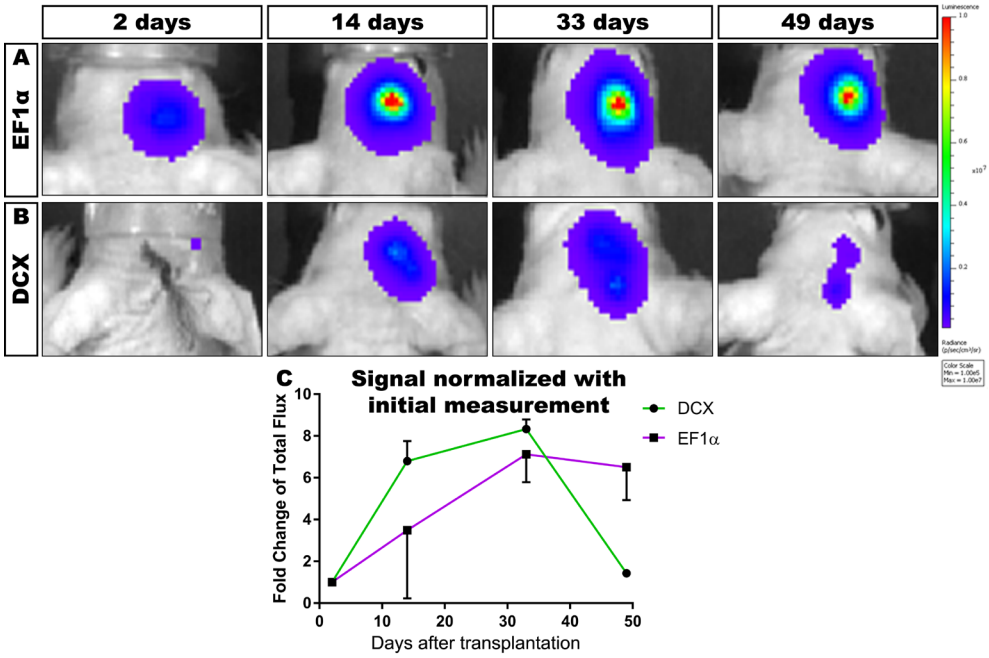

Fig. 2: Observation of Luc2 activity in TBI mice *in vivo*. **(A)** Representative overlays of pCDH-EF1α-Luc2-T2A-copGFP-transduced HFBSCs from 2, 14, 33, and 49 days after transplantation. The bioluminescent signal increased with relative stability over the course of time. **(B)** Representative overlays of HFBSCs transduced with pCDH-DCX-Luc2-T2A-copGFP over the same period of time. No bioluminescent signal was observed 2 days after transplantation. The signal increased between 14 days and 33 days, but almost undetectable after 49 days. **(C)** Analysis of the bioluminescent signal were measured 2, 14, 33, and 49 days after transplantation. The bioluminescence data was normalized with the initial signal, and measured 2 days after transplantation, which depicts the trend of the bioluminescent signal from HFBSCs over time. The bioluminescent signal of pCDH-EF1α-Luc2-T2A-copGFP-transduced HFBSCs increased steadily over the course of time, while the bioluminescence of pCDH-DCX-Luc2-T2A-copGFP-transduced HFBSCs decreased after 33 days and was almost undetectable at 49 days.

Bioluminescence imaging of HFBSCs transduced with pCDH-EF1α- and pCDH-DCX-Luc2-T2A-copGFP in mice with TBI

After transplantation, the bioluminescent signal of pCDH-EF1α-Luc2-T2A-copGFP-transduced HFBSCs showed a slow and stable increase over a period of 49 days (Fig. 2A). Cells transduced with the pCDH-DCX-Luc2-T2A-copGFP gene construct revealed a faint or absent bioluminescence, 2 days after transplantation (Fig. 2B). However, representative overlays show that a distinct bioluminescent signal emanated from the injection site within 14 days, and peaked 33 days after transplantation. Interestingly, the bioluminescent signal dropped below initial levels and almost vanished 49 days after transplantation of transduced HFBSCs. A strong bioluminescent signal was obtained from transplanted HFBSCs containing the pCDH-EF1α-Luc2-T2A-copGFP construct, while it was not significantly different between the days of the measurements (one-way ANOVA, p=0.14) (Fig 2C). The bioluminescent signal from pCDH-DCX-Luc2-T2A-copGFP-transduced HFBSCs initially increased over the period of 33 days and thereafter steadily decreased, which was statistically significant (one-way ANOVA, p=0.048; Fig 2C).

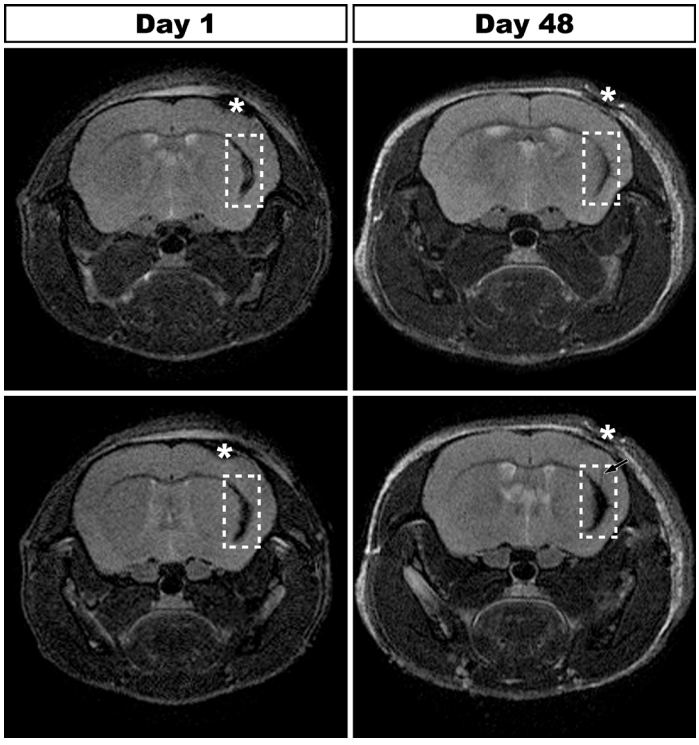

Fig. 3: MRI of ferumoxytol-loaded HFBSCs in TBI mice *in vivo*. The upper panel shows representative scans of the region containing the TBI lesion 1 day and 48 days after transplantation. The scan at Day 1 revealed a hypointense area containing clotted iron-containing erythrocytes (asterisk), which vanished over the course of time. Dotted box: Injected cells. The lower panel shows representative scans of the transplanted ferumoxytol-loaded transduced HFBSCs over the same course of time. The dotted box at day 1 after transplantation shows the location of ferumoxytol-containing cells. Asterisk: Clotted erythrocytes. The hypointense signal of ferumoxytol could also be imaged at the transplantation site at least 48 days after transplantation.

MRI of TBI mice transplanted with ferumoxytol-loaded HFBSCs

In order to enable visualization of the cells by means of MRI, HFBSCs were loaded with ferumoxytol prior to transplantation. The TBI lesion, which was induced 2 days before transplantation of the HFBSCs, was clearly visible on the MRI due to iron-rich, clotted erythrocytes (Fig. 3, asterisks). In addition to the lesion, the transplanted ferumoxytol-loaded HFBSCs (Fig. 3, dotted boxes) were also visible. Over the course of 8 days, the hypo-intense signal from the iron-containing erythrocytes at the site of the TBI lesion completely disappeared (data not shown; cf., Fig. 3, Day 48). Ferumoxytol-loaded HFBSCs were visible as a hypointense area within the mouse brain 1 day after injection (Fig. 3, Day 1, dotted boxes). Subsequent MRI of mice revealed that a hypointense area from ferumoxytol persisted within the brain for at least 48 days and showed migration of the hypointense signal towards the site of TBI (Fig. 3, Day 48, arrow).

Histochemical staining

The stability of copGFP protein enabled visualization of the fluorescent protein in cryosections of mouse brains without additional immunohistological staining for copGFP (Figs. 4A-D and Figs. 5A-C, copGFP protein). However we performed an additional immunostaining of the cryosections for copGFP (Figs. 4A and 4C,) or Luc2 (Figs. 4B, 4D, and 5A-C) to confirm the presence of pCDH-EF1α-Luc2-T2A-copGFP-transduced HFBSCs. Furthermore, all cells that exhibited green fluorescence from copGFP also showed staining for the neural progenitor cell marker nestin. (Fig. 4A). A marker for astrocytes in the central nervous system, GFAP, showed staining in the mouse brain, but not in HFBSCs (Fig. 4B). The depicted GFAP signal originates from glial cells surrounding the copGFP expressing HFBSCs. Staining for the neural marker neurofilament with NF-pan was faint and restricted to individual HFBSCs, but co-localized with copGFP (Fig. 4C). Staining of the transduced HFBSCs for DCX was negative (Fig. 4D). In addition, the surrounding area of some green fluorescent HFBSCs also stained for fibronectin (Fig. 5A) and laminin (Fig. 5B). This indicates secretion of these extracellular matrix proteins by the injected cells. Staining for the proliferation marker Ki-67 was negative in transplanted HFBSCs (Fig. 5C), but positive in HFBSCs *in vitro* (Table 2). Positive and negative controls showed the reliability of the staining performed (data not shown).

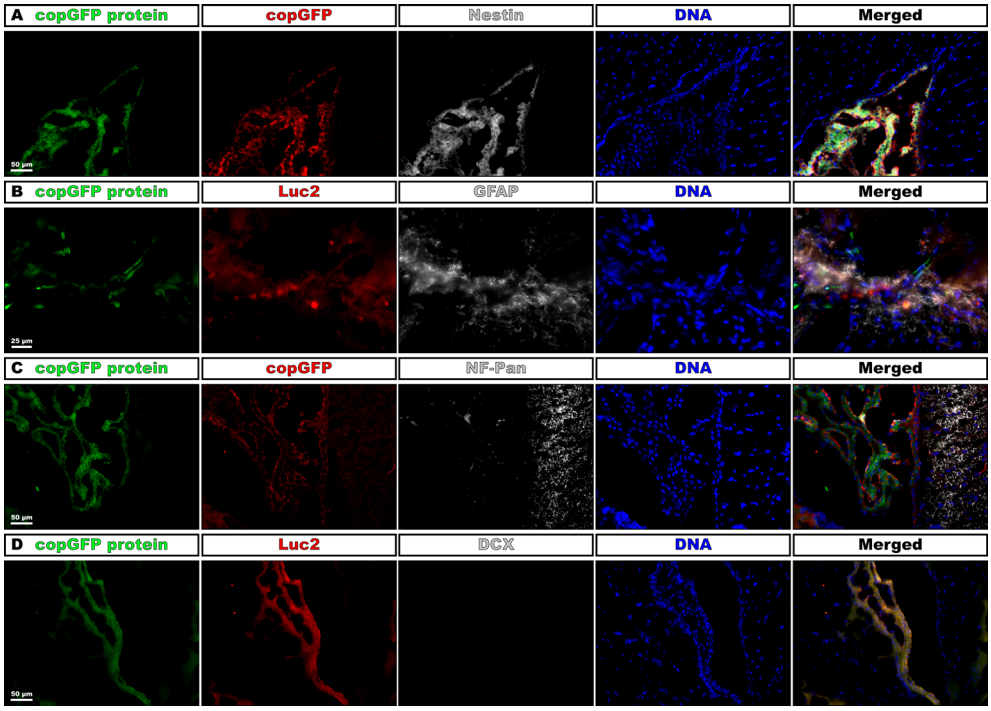

Fig. 4: Immunohistochemical staining of HFBSCs constitutively expressing Luc2 and copG. Sections of mouse brains containing transduced HFBSCs exhibited native green fluorescence emitted by copGFP after fixation, sectioning and staining of the sections (A-D; copGFP protein; green). Sections containing copGFP-expressing HFBSCs were stained for either copGFP (A and C) or Luc2 (B and D). **(A)** CopGFP-expressing HFBSCs stained for copGFP (red) and the neural progenitor cell marker nestin (gray). The merged image shows co-localization of copGFP, nestin, and DNA of copGFP-expressing HFBSCs in the mouse brain. **(B)** HFBSCs, which expressed copGFP (green), also stained for Luc2 (red). GFAP (gray) stained in the mouse brain, but is absent in HFBSCs (green/red). **(C)** Transplanted HFBSCs (green/red) stained for NF-pan (gray). **(D)** None of the copGFP-expressing HFBSCs (green/red) stained for DCX. Scale bar = 50 µm.

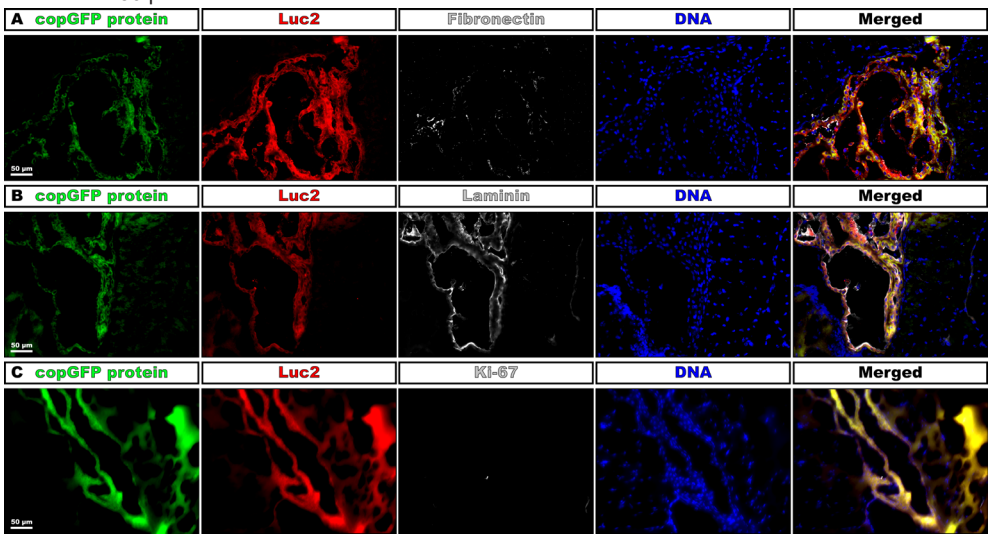

Table 2 compares the immunostaining of cultured HFBSCs and the cryosections of TBI mouse brains. Perls' Prussian blue staining with DAB intensification of cryosections, which were immunohistochemically stained for nestin and laminin, showed that HFBSCs (which also expressed copGFP and stained for copGFP or Luc2) stained for ferumoxytol after 58 days *in vivo* (Fig. 6A). However, iron staining was also positive in the tissue surrounding the graft, which may indicate uptake of iron by other cells, e.g. macrophages, (Fig 6A, merge). Reconstruction of brain sections guided by fluorescence of copGFP (Fig. 6B) reconfirmed that, after transplantation, HFBSCs were present in the superficial cortex (where TBI was imaged by means of MRI; Fig. 6B, Cortex) as well as in the deep cortex and corpus callosum (Fig. 6B, Corpus callosum) next to the injection site as depicted in Fig. 6C.

Table 2: Overview of staining pattern.

	Antibody	Cultured HFBSCs	Transplanted HFBSCs	Specification
HFBSCs	copGFP	positive	positive	Transduced HFBSCs expressing copGFP
	Luc2	positive	positive	Transduced HFBSCs expressing Luc2
Neural Crest	Nestin	positive	positive	Neural crest cells and neuronal progenitors
Neuron	DCX	negative	weakly positive	Early neuronal development
	NF-Pan	weakly positive	positive	Neurons
Glial Cell	GFAP	negative	negative	Glial cells in the peripheral and central nervous system
ECM	Fibronectin	negative	positive	Cell adhesion, growth, migration, differentiation, neuron protection
	Laminin	positive	positive	Cell attachment, stimulates neuronal differentiation, promotion of tissue survival
Other	Ki-67	positive	negative	Proliferating cells

Fig. 5: Immunohistochemical staining for extracellular matrix and proliferating cells. CopGFP-expressing HFBSCs in mouse brain sections remained native fluorescence (A-C; copGFP protein; green). Additionally, sections were stained for Luc2 (A-C; red). **(A)** The surrounding area of some HFBSCs stained for fibronectin (gray). **(B)** The vicinity of transplanted HFBSCs stained for laminin (gray). **(C)** Staining for Ki-67 (gray) was negative in sections containing HFBSCs (green/red). Scale bar = 50 µm.

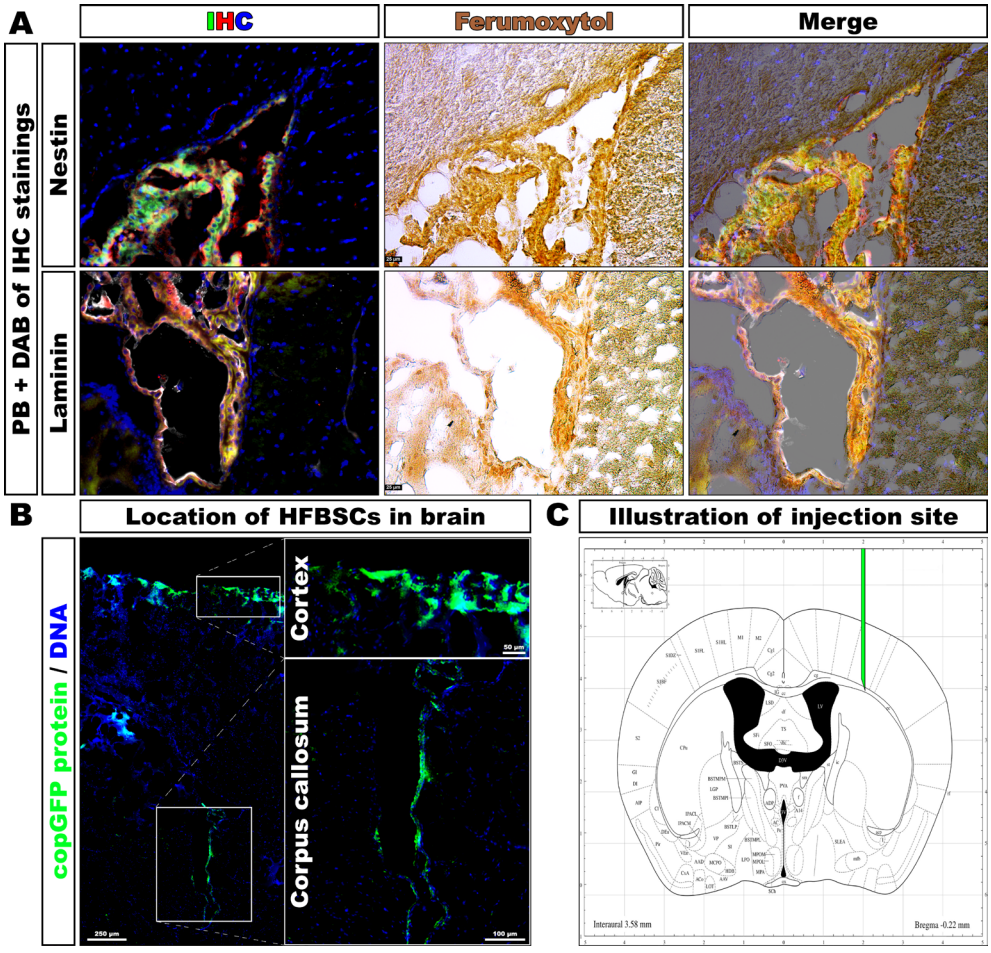

Fig. 6: Perls' Prussian blue staining with DAB intensification of mouse brain sections. **(A)** Immunohistochemically stained sections from Fig. 4A and Fig. 5B (IHC) were also stained with Perls' Prussian blue with DAB intensification. This showed that HFBSCs stain for ferumoxytol 58 days after transplantation in TBI mice (Ferumoxytol). The merged image of the ferumoxytol staining and the corresponding immunofluorescence image reveals co-localization of Fe^{3+} deposits and a fluorescent signal (Merged). **(B)** The native fluorescence of the copGFP, which persists also after the preparation of the brain sections, indicates the location of the HFBSCs within the mouse brain, i.e. the cortex and the corpus callosum (enlarged images of boxes). **(C)** Illustration of the injection site of HFBSCs in the mouse brain (adapted from the Neurostar Robotic Stereotactic Software).

Discussion

We are able to show for the first time that HFBSCs can survive and differentiate towards a neuronal cell lineage after transplantation of these cells into the mouse brain by applying *in vivo* multimodal imaging, i.e., BLI and MRI.

We established that HFBSCs tolerate genetic manipulation and loading with nanoparticles *in vitro* in a previous study [25]. For the present study, we loaded the HFBSCs with the (ultrasmall) SPIO nanoparticle ferumoxytol, which has proven effective for *in vivo* tracking of stem cells with high sensitivity by means of MRI [20, 31-33]. We showed that HFBSCs take up HPF complexes using the Perls' Prussian blue method and DAB intensification, which stains Fe^{3+} deposits within the cells.

In mice with TBI, the bioluminescent signal of HFBSCs transduced with pCDH-EF1α-Luc2-T2A-copGFP remained high over time, while bioluminescence of pCDH-DCX-Luc2-T2A-copGFP-transduced HFBSCs was initially low. It increased over a period of at least 33 days and completely vanished afterwards, which indicated that BLI can be used tracking early differentiation *in vivo*. Tennstaedt *et al*. reported the same bioluminescence pattern of human neural stem cells transduced with Luc2 under regulation of the DCX promoter in their *in vivo* study [19]. Our discovery that the bioluminescent signal vanished within 49 days after injection was also in line with work of Ladewig *et al*., who demonstrated decreased DCX expression during cell maturation, which is likely due to the fact that DCX is a marker expressed early on in neural differentiation [34]. In addition, we could rule out that the decrease in bioluminescent signal was due to cell death since pCDH-EF1α-Luc2-T2A-copGFP-transduced HFBSCs remained visible and constantly expressed Luc2, as shown by BLI over the same period.

We checked for hypointense regions in the mouse brain by means of MRI at 1 day after transplantation of ferumoxytol-loaded transduced HFBSCs, and again 48 days after transplantation. Bryant *et al*. recently demonstrated that formation of FHP complexes (ferumoxytol is the base component and heparin and protamine are added to form the complexes) improved the MRI contrast compared to HPF complexes (ferumoxytol is added as last component) [35]. However, in our case HFBSCs showed high uptake of HPF complexes and could be clearly detected after transplantation next to the TBI lesion (cortical region) in nude mice at both

time points. One day after transplantation the MRI showed hypointense spots in the cortex area, indicating the presence of ferumoxytol. MRI and BLI data were combined to show that cells were transplanted at the correct site, and that they remained viable and present in a detectable amount. The MRI enabled visualization of ferumoxytol at the transplantation site after 48 days and we were able to observe changes in the hypointense regions indicating migration of cells, most likely HFBSCs as indicated by Perls' Prussian blue staining with DAB intensification for iron oxide in cryosections, towards the area of TBI (Fig. 3B, Day 48, arrow). This is in line with the finding of Zheng *et al*. who were able to image neural stem cells for up to 87 days *in vivo* [36].

Transduced HFBSCs maintained fluorescence after fixation, sectioning and (immune)staining. Therefore, we were able to visualize the copGFP expressed by HFBSCs in cryosections of mouse brains. We verified that this green fluorescence was obtained from copGFP and excluded auto-fluorescence by staining the sections with primary antibodies against either copGFP or Luc2, which were both expressed by the transplanted cells. The transplanted HFBSCs showed staining for the neural marker neurofilament (NF-pan), which is in line with previous findings [34, 19], but not for glial fibrillary acidic protein (GFAP), which indicates their differentiation towards a neuronal lineage. In addition, the majority of copGFP-expressing HFBSCs in brain sections of TBI mice were positive for nestin, a marker for NCSCs and neural progenitors, underlining the neural differentiation potential of these stem cells. Staining for DCX, a marker that is expressed early on in neural differentiation, was negative, which confirmed our bioluminescence results that at this time point the cells passed their commitment of neuronal differentiation and progressed towards a more mature neuronal state. Underlining this finding was the fact that the transplanted cells were not positive for cell proliferation marker Ki-67, indicating that HFBSCs did not enter a harmful, tumorigenic state of uncontrolled proliferation. Surprisingly, transplanted cells showed positive staining for the extracellular matrix proteins laminin (all) and fibronectin (some). Laminin and fibronectin have been shown to play important roles in neurite guidance regeneration of tissue after TBI and motility of neural crest cells, which further support the potential role of HFBSCs in tissue regeneration in TBI [37-39].

After identifying transplanted HFBSCs within brain sections of TBI mice, we stained these sections for Fe^{3+}, a component of ferumoxytol. The staining revealed that

HFBSCs still contained ferumoxytol after 58 days *in vivo*. Our results indicate that ferumoxytol was partially excreted by HFBSCs and taken up by cells in the surrounding tissue, e.g. macrophages. However, a substantial part of the hypointense signal on the MRI originates from ferumoxytol-containing HFBSCs.

Moreover, our finding of fluorescent cells, which are localized in the corpus callosum and the site of TBI (in the superficial cortex) in brain sections, may indicate that HFBSCs participate in recovery after neural trauma. The mechanism of how this recovery might occur remains unknown. However, the need to further elucidated potential recovery persists. Recovery may occur by cell replacement due to differentiation, through paracrine effects or combination of both. In case both mechanisms occur, a strategy could be to transplant cells in biologic scaffolds made of brain-derived extracellular matrices in the form of hydrogels with the aim to enhance survival and promote angiogenesis [40]. On the other hand, if the paracrine effect prevails a therapeutic strategy based on the solely administration of exosomes derived from HFBSCs would represent an alternative neurorestorative therapy. Moreover, the exosomes could be tailored to maximize clinical benefits [41].

Conclusion

In conclusion, this first study about HFBSCs transplantation in a mouse model of TBI indicates that HFBSCs are able to survive in mice brain and the procedure is safe in mice. In this relative short time most of the transplanted cells remained nestin positive but some individual cells undergo differentiation towards a neuronal cell lineage and a part could be found in the lesioned area. Because of all this evidence, HFBSCs qualify as possible candidates for cell-based therapy of TBI, although further studies are required to elucidate their ability to enhance repair processes and improve cognitive function.

Acknowledgements

This work was supported by the FP7 European Union Marie Curie IAPP Program, BRAINPATH, under grant number 612360, the project grant H2020-MSCA-RISE PRISAR grant number 644373, and a by grant from MED-EL (Innsbruck, Austria) grant number FK0151/MEDELI001.This project is financially supported by grants from Stichting Het Heinsius-Houbolt Fonds, the Netherlands. Timo Schomann received funding from MED-EL (Innsbruck, Austria). The authors acknowledge Carola van der Ploeg for technical assistance.

Conflict of Interest Statement

No conflict of interest has been declared.

References

1. Lemmens, R. and G.K. Steinberg, Stem cell therapy for acute cerebral injury: What do we know and what will the future bring? Curr. Opin. Neurol., 2013. 26 (**6**): p. 617-625.
2. Hasan, A., G. Deeb, R. Rahal, K. Atwi, S. Mondello, H.E. Marei, A. Gali, and E. Sleiman, Mesenchymal stem cells in the treatment of traumatic brain injury. Front. Neurol., 2017. 8 (**28**): p. 1-15.
3. Kiasatdolatabadi, A., N. Lotfibakhshaiesh, M. Yazdankhah, S. Ebrahimi-Barough, M. Jafarabadi, A. Ai, E. Sadroddiny, and J. Ai, The role of stem cells in the treatment of cerebral palsy: A review. Mol. Neurobiol., 2017. 54 (**7**): p. 4963-4972.
4. Bang, O.Y., E.H. Kim, J.M. Cha, and G.J. Moon, Adult stem cell therapy for stroke: Challenges and progress. J. Stroke, 2016. 18 (**3**): p. 256-266.
5. Chen, J., P. Venkat, A. Zacharek, and M. Chopp, Neurorestorative therapy for stroke. Front. Hum. Neurosci., 2014. 8 (**382**): p. 1-12.
6. Cellvation, I. Cellvation. 2017 [cited 2018/03/31]; Available from: http://cellvation.com/.
7. Grigoriadis, N., A. Lourbopoulos, R. Lagoudaki, J.M. Frischer, E. Polyzoidou, O. Touloumi, C. Simeonidou, G. Deretzi, J. Kountouras, E. Spandou, K. Kotta, G. Karkavelas, N. Tascos, and H. Lassmann, Variable behavior and complications of autologous bone marrow mesenchymal stem cells transplanted in experimental autoimmune encephalomyelitis. Exp. Neurol., 2011. 230 (**1**): p. 78-89.
8. Fernandes, K.J., I.A. McKenzie, P. Mill, K.M. Smith, M. Akhavan, F. Barnabe-Heider, J. Biernaskie, A. Junek, N.R. Kobayashi, J.G. Toma, D.R. Kaplan, P.A. Labosky, V. Rafuse, C.C. Hui, and F.D. Miller, A dermal niche for multipotent adult skin-derived precursor cells. Nat. Cell Biol., 2004. 6 (**11**): p. 1082-1093.
9. Sieber-Blum, M. and M. Grim, The adult hair follicle: Cradle for pluripotent neural crest stem cells. Birth Defects Res. C. Embryo Today, 2004. 72 (**2**): p. 162-172.
10. Techawattanawisal, W., K. Nakahama, M. Komaki, M. Abe, Y. Takagi, and I. Morita, Isolation of multipotent stem cells from adult rat periodontal ligament by neurosphere-forming culture system. Biochem. Biophys. Res. Commun., 2007. 357 (**4**): p. 917-923.
11. Hauser, S., D. Widera, F. Qunneis, J. Müller, C. Zander, J. Greiner, C. Strauss, P. Lüningschrör, P. Heimann, H. Schwarze, J. Ebmeyer, H. Sudhoff, M.J. Araúzo-Bravo, B. Greber, H. Zaehres, H. Schöler, C. Kaltschmidt, and B. Kaltschmidt, Isolation of novel multipotent neural crest-derived stem cells from adult human inferior turbinate. Stem Cells Dev., 2012. 21: p. 742-756.
12. Fernandes, K.J., N.R. Kobayashi, C.J. Gallagher, F. Barnabe-Heider, A. Aumont, D.R. Kaplan, and F.D. Miller, Analysis of the neurogenic potential of multipotent skin-derived precursors. Exp. Neurol., 2006. 201 (**1**): p. 32-48.
13. Paus, R., B.J. Nickoloff, and T. Ito, A 'hairy' privilege. Trends Immunol., 2005. 26 (**1**): p. 32-40.
14. Sieber-Blum, M., M. Grim, Y.F. Hu, and V. Szeder, Pluripotent neural crest stem cells in the adult hair follicle. Dev. Dyn., 2004. 231 (**2**): p. 258-269.
15. Jendelova, P., S. Kubinova, I. Sandvig, S. Erceg, A. Sandvig, and E. Sykova, Current developments in cell- and biomaterial-based approaches for stroke repair. Expert Opin. Biol. Ther., 2016. 16 (**1**): p. 43-56.
16. Mezzanotte, L., I. Que, E. Kaijzel, B. Branchini, A. Roda, and C. Löwik, Sensitive dual color *in vivo* bioluminescence imaging using a new red codon optimized firefly luciferase and a green click beetle luciferase. PLoS ONE, 2011. 6 (**4**): p. e19277.
17. Mezzanotte, L., M. Van 't Root, H. Karatas, E.A. Goun, and C. Lowik, *In vivo* molecular bioluminescence imaging: New tools and applications. Trends Biotechnol., 2017. 35 (**7**): p. 640-652.
18. Abbas, L., J. Seppen, S.C. Barry, J.H. Klinkspoor, L.J. Katen, S.P. Lee, J.V. Garcia, and W.R.A. Osborne, Apical gene transfer into quiescent human and canine polarized intestinal epithelial cells by lentivirus vectors. J. Virol., 2000. 74 (**16**): p. 7642-7645.
19. Tennstaedt, A., M. Aswendt, J. Adamczak, U. Collienne, M. Selt, G. Schneider, N. Henn, C. Schaefer, M. Lagouge, D. Wiedermann, P. Kloppenburg, and M. Hoehn, Human neural stem cell intracerebral grafts show spontaneous early neuronal differentiation after several weeks. Biomaterials, 2015. 44: p. 143-154.
20. Pirko, I., S.T. Fricke, A.J. Johnson, M. Rodriguez, and S.I. Macura, Magnetic resonance imaging, microscopy, and spectroscopy of the central nervous system in experimental animals. NeuroRx, 2005. 2 (**2**): p. 250-264.
21. Khurana, A., H. Nejadnik, R. Gawande, G. Lin, S. Lee, S. Messing, R. Castaneda, N. Derugin, L. Pisani, T.F. Lue, and H.E. Daldrup-Link, Intravenous ferumoxytol allows noninvasive MR imaging monitoring of macrophage migration into stem cell transplants. Radiology, 2012. 264 (**3**): p. 803-811.
22. Thu, M.S., L.H. Bryant, T. Coppola, E.K. Jordan, M.D. Budde, B.K. Lewis, A. Chaudhry, J. Ren, N.R. Varma, A.S. Arbab, and J.A. Frank, Self-assembling nanocomplexes by combining ferumoxytol, heparin and protamine for cell tracking by magnetic resonance imaging. Nat. Med., 2012. 18 (**3**): p. 463-467.
23. El Seady, R., M.A. Huisman, C.W. Löwik, and J.H.M. Frijns, Uncomplicated differentiation of stem cells into bipolar neurons and myelinating glia. Biochem. Biophys. Res. Commun., 2008. 376 (**2**): p. 358-362.
24. Gho, C.G., T. Schomann, S.C. De Groot, J.H.M. Frijns, M.N. Rivolta, M.H. Neumann, and M.A. Huisman, Isolation, expansion and neural differentiation of stem cells from human plucked hair: A further step towards autologous nerve recovery. Cytotechnology, 2016. 68 (**5**): p. 1849-1858.
25. Schomann, T., L. Mezzanotte, I.M. Lourens, J.C.M.J. De Groot, J.H.M. Frijns, and M.A. Huisman, Lentiviral transduction and subsequent loading with nanoparticles do not affect cell viability and proliferation in hair-follicle-bulge-derived stem cells *in vitro*. Contrast Media Mol. Imaging, 2016. 11 (**6**): p. 550-560.
26. Nguyen, T.D., D. Widera, J. Greiner, J. Muller, I. Martin, C. Slotta, S. Hauser, C. Kaltschmidt, and B. Kaltschmidt, Prolonged cultivation of hippocampal neural precursor cells shifts their differentiation potential and selects for aneuploid cells. Biol. Chem., 2013. 394 (**12**): p. 1623-1636.
27. Löw, K., A. Blesch, J. Herrmann, and M.H. Tuszynski, A dual promoter lentiviral vector for the *in vivo* evaluation of gene

therapeutic approaches to axon regeneration after spinal cord injury. Gene Ther., 2010. 17 (5): p. 577-591.
28. Mezzanotte, L., M. Aswendt, A. Tennstaedt, R. Hoeben, M. Hoehn, and C. Löwik, Evaluating reporter genes of different luciferases for optimized *in vivo* bioluminescence imaging of transplanted neural stem cells in the brain. Contrast Media Mol. Imaging, 2013. 8 (**6**): p. 505-513.
29. Meguro, R., Y. Asano, S. Odagiri, C. Li, H. Iwatsuki, and K. Shoumura, Nonheme-iron histochemistry for light and electron microscopy: A historical, theoretical and technical review. Arch. Histol. Cytol., 2007. 70 (**1**): p. 1-19.
30. Smith, B.A., B.-W. Xie, E.R. van Beek, I. Que, V. Blankevoort, S. Xiao, E.L. Cole, M. Hoehn, E.L. Kaijzel, C.W.G.M. Löwik, and B.D. Smith, Multicolor fluorescence imaging of traumatic brain injury in a cryolesion mouse model. ACS Chem. Neurosci., 2012. 3 (**7**): p. 530-537.
31. Gutova, M., J.A. Frank, M. D'Apuzzo, V. Khankaldyyan, M.M. Gilchrist, A.J. Annala, M.Z. Metz, Y. Abramyants, K.A. Herrmann, L.Y. Ghoda, J. Najbauer, C.E. Brown, M.S. Blanchard, M.S. Lesniak, S.U. Kim, M.E. Barish, K.S. Aboody, and R.A. Moats, Magnetic resonance imaging tracking of ferumoxytol-labeled human neural stem cells: Studies leading to clinical use. Stem Cells Transl. Med., 2013. 2 (**10**): p. 766-775.
32. Khurana, A., H. Nejadnik, F. Chapelin, O. Lenkov, R. Gawande, S. Lee, S.N. Gupta, N. Aflakian, N. Derugin, S. Messing, G. Lin, T.F. Lue, L. Pisani, and H.E. Daldrup-Link, Ferumoxytol: A new, clinically applicable label for stem-cell tracking in arthritic joints with MRI. Nanomedicine, 2013. 8 (**12**): p. 1969-1983.
33. Schieda, N., Parenteral ferumoxytol interaction with magnetic resonance imaging: A case report, review of the literature and advisory warning. Insights Imaging, 2013. 4 (**4**): p. 509-512.
34. Ladewig, J., P. Koch, E. Endl, B. Meiners, T. Opitz, S. Couillard-Despres, L. Aigner, and O. Brustle, Lineage selection of functional and cryopreservable human embryonic stem cell-derived neurons. Stem Cells, 2008. 26 (**7**): p. 1705-1712.
35. Bryant, L.H., Jr., S.J. Kim, M. Hobson, B. Milo, Z.I. Kovacs, N. Jikaria, B.K. Lewis, M.A. Aronova, A.A. Sousa, G. Zhang, R.D. Leapman, and J.A. Frank, Physicochemical characterization of ferumoxytol, heparin and protamine nanocomplexes for improved magnetic labeling of stem cells. Nanomedicine, 2017. 13 (**2**): p. 503-513.
36. Zheng, B., T. Vazin, P.W. Goodwill, A. Conway, A. Verma, E. Ulku Saritas, D. Schaffer, and S.M. Conolly, Magnetic particle imaging tracks the long-term fate of *in vivo* neural cell implants with high image contrast. Sci. Rep., 2015. 5: p. 14055.
37. Evans, A.R., S. Euteneuer, E. Chavez, L.M. Mullen, E.E. Hui, S.N. Bhatia, and A.F. Ryan, Laminin and fibronectin modulate inner ear spiral ganglion neurite outgrowth in an *in vitro* alternate choice assay. Dev. Neurobiol., 2007. 67 (**13**): p. 1721-1730.
38. Tate, C.C., M.C. Tate, and M.C. LaPlaca, Fibronectin and laminin increase in the mouse brain after controlled cortical impact injury. J Neurotrauma, 2007. 24 (**1**): p. 226-230.
39. Strachan, L.R. and M.L. Condic, Neural crest motility on fibronectin is regulated by integrin activation. Exp. Cell Res., 2008. 314 (**3**): p. 441-452.
40. Crapo, P.M., S. Tottey, P.F. Slivka, and S.F. Badylak, Effects of biologic scaffolds on human stem cells and implications for CNS tissue engineering. Tissue Eng Part A, 2014. 20 (**1-2**): p. 313-23.
41. Zhang, Z.G., B. Buller, and M. Chopp, Exosomes - beyond stem cells for restorative therapy in stroke and neurological injury. Nat Rev Neurol, 2019.

Chapter 8

General discussion

Summary

The aim of this thesis was to investigate the feasibility of multimodal visualization techniques to observe adult stem cells, in particular HFBSCs, in the living animal. Due to the novelty of HFBSCs in the field of inner ear research, a series of proof-of-principle experiments have been undertaken to investigate if these cells can undergo neuronal differentiation, tolerate genetic modification with lentiviral constructs containing the genes coding for reporter proteins, and tolerate subsequent loading with nanoparticles *in vitro* (Chapters 2 and 3). In addition, it was of importance to examine if HFBSCs do integrate into modiolar tissue and if they can be visualized in the cochlea of the guinea pig (Chapters 4 and 5). Lastly, we performed *in vivo* studies to investigate the ototoxic effect of ouabain in guinea pigs and the behavior of HFBSCs in mice with traumatic brain injury (Chapters 6 and 7). The main outcomes of this research are summarized in the first part of this chapter to give a general overview. In addition, major issues that might have influenced those outcomes will be discussed. The second part will solely focus on future research.

Main outcomes and respective implications

Objective 1: The isolation, expansion and neural differentiation of stem cells from human plucked hair.

In the study described in Chapter 2, the human hair follicle was investigated as a source for autologous SCs [1]. We were able to obtain hair follicles with an easy, minimally invasive technique that is almost painless for the patient. From the harvested hair follicles HFBSCs were isolated, which still possess the immunophenotype of NCSCs, e.g., nestin-positive, SOX9-positive, but SOX10-negative [2], and neural and glial differentiation potential after isolation, expansion and cryopreservation.

However, the isolated and cultured HFBSCs remain a heterogenous population consisting of various cell types. The exact composition of the HFBSC cultures and the various cell types contaminating the cultures, such as fibroblasts, are still not exactly defined. Thus, to obtain a (more) purified stem cell culture, unwanted cells need to be removed. In our studies, this was achieved by “selection at the gate”, during which cultures with obvious unwanted cell outgrowth from the hair follicle,

such as keratinocytes and fibroblasts, were immediately discarded.

A second and next step for purification could be the cultivation in serum-free medium under sphere-forming conditions to eliminate fibroblasts, which require a combination of growth factors and an adhering matrix to survive [3, 4]. Nevertheless, it has to be taken into consideration that the process of purification and multiplication of stem cells derived from adult tissues each have their own specific problems. It could be, for instance, that transdifferentiation is required to achieve the right dermal lineage or that spontaneous differentiation into an unwanted phenotype may play a role.

Regarding induced pluripotent stem cells (iPSCs) as a source for homologous stem cells, the genetic manipulation to reprogram somatic cells into pluripotent stem cells is still not safe and is currently under debate with respect to epigenetic changes that may occur during the process of reprogramming [5, 6].

Therefore, HFBSCs which can be harvested almost painlessly from the patient and which are multipotent in the ectodermal lineage may be a good type of stem cell to be used parallel to iPSCs in neural regeneration studies. In this way, the most favorable source for cell-based regenerative medicine can be evaluated.

Objective 2: Rule out the possible cytotoxic effects of lentiviral transduction and subsequent loading with nanoparticles on cell viability and proliferation of HFBSCs *in vitro*.

We isolated HFBSCs from hair follicles of mouse whisker pads and investigated the possible cytotoxic effects of different labeling techniques in Chapter 3 [7]. HFBSCs were stably transduced with a lentiviral construct containing genes coding for Luc2 and copGFP, enabling visualization by means of FLI and BLI, respectively. After loading HFBSCs with SPIO nanoparticles, we were able to image them by means of MRI. Finally, we could rule out that the applied techniques had any adverse effect upon proliferation and differentiation capacity of HFBSCs.

During this experiment, silica-coated NEO-STEM™ TMSR50 nanoparticles, which contain a magnetic core and a fluorescent dye, were used. Thus, TMSR50 could enable visualization of loaded cells by means of MRI *in vivo* and immunofluorescent

analysis of histological sections. This quite detailed study was necessary to prove that multimodal (in-depth) visualization of HFBSCs is possible, which opens the way to use this technique in animals larger than mice, e.g., guinea pigs.

However, in a later study (Chapter 6) we also used the FDA-approved SPIO suspension ferumoxytol, which is not cytotoxic [8]. We were able to show retention of ferumoxytol in HFBSCs for at least 48 days *in vivo*. Ferumoxytol does not allow FLI and, thus, it cannot be visualized together with specific (cell) markers after immunofluorescent staining. Therefore, after successful immunohistochemistry and FLI, we applied Perls' Prussian blue staining, followed by DAB intensification, on the same tissue sections to visualize ferumoxytol within the cells. Finally, we merged the images obtained from the immunofluorescent staining with the images showing staining for ferumoxytol (and other iron oxide) within the tissue sections revealing retention of ferumoxytol by HFBSCs.

This elaborate procedure would not have been necessary in case of SPIO nanoparticles with a silica coating that contains a fluorescent dye, such as NEO-STEM™ TMSR50. In addition, such a dye would enable *in vivo* visualization when using one of the near-infrared fluorescence imaging windows, in which light absorption and autofluorescence by living tissue is minimal, thus, resulting in an improved penetration depth. However, NEO-STEM™ TMSR50 and other NEO-STEM™ variants as well as NEO-LIVE™, which contains a NIRF dye, are not commercially available anymore. This led to the use of ferumoxytol in Chapters 5 and 7.

Objective 3: Investigate migration, integration, and neural differentiation potential of HFBSCs in co-culture with modiolus explants from adult mice.

HFBSCs were cultured together with modiolus explants to investigate if they would integrate into the tissue and subsequently differentiate into neural (progenitor) cells [9]. In Chapter 4, we showed that HFBSCs migrate towards and into explants of modiolus tissue. The cells incorporated into the explant and formed a distinct fascicular pattern. Depending on this micro-environment, cells adapted a neuronal phenotype as shown with DCX-copGFP-transduced HFBSCs and immunofluorescence.

An improved and/or more mature pattern might have been obtained after a prolonged period, but during co-culture the modiolus tissue tended to be overgrown by cells. In addition, the explant deteriorated with time. Furthermore, image quality could be improved by employing a confocal laser scanning microscope instead of regular fluorescence microscopy. Nevertheless, we showed that HFBSCs are able to differentiate towards a neuronal phenotype when the cells are in contact with modiolar tissue, which makes them advantageous for future cell-based auditory nerve therapy.

Objective 4: The feasibility of BLI for the visualization of transduced cells after engraftment in the intact guinea pig cochlea.

The guinea pig is a commonly used animal model in the field of inner ear research. However, it is rarely used in the field of molecular imaging. In order to investigate the therapeutic potential of SCs in the inner ear it is necessary to combine the field of hearing research with the field of molecular imaging. Therefore, we investigated if it is possible to image transduced cells by means of BLI after transplantation in the inner ear of guinea pigs. This is particularly challenging since the cochlea is embedded within the auditory bulla consisting of compact bone with a high mineral density, which could block signal detection during molecular optical imaging. Our results in Chapter 5 show that we obtained a distinct, quantifiable bioluminescent signal, which emanates from the external auditory meatus of the guinea pig cadavers.

In light of the 3Rs guiding principles, which specify the replacement, reduction, and refinement of the use of animals in research, we decided to use the cadavers of 26 guinea pigs from non-related experiments for this feasibility study to reduce the number of live animals in our experiments. In this *ex vivo* study, D-luciferin was added directly to the HFBSC suspension, which then was injected into several sites in the cochlea. However, for *in vivo* studies the application of D-luciferin has to be adapted, since direct application to the HFBSCs is not possible without an entryway, such as a tube or a minipump [10, 11]. Also, the lack of a tail (vein) complicates and significantly limits intravenous injections of substances in the guinea pig compared to mice and rats. Nonetheless, D-luciferin can be administered intraperitoneally, which should result in sufficient uptake for successful BLI. In addition, signal intensity could be improved by substitution of D-luciferin with the luciferin analogue AkaLumine-

HCl, which – aside from shifting the emitted light towards a near-infrared spectrum wavelength (λ_{max}: 677 nm) – generates a maximal signal at very low concentrations [12]. Furthermore, *in vivo* imaging could significantly enhanced by using the AkaBLI system, which combines AkaLumine-HCl with the newly developed Akaluc [13]. Akaluc is a mutated firefly luciferase that catalyzed AkaLumine-HCl ~7x more effective than wildtype firefly luciferase and emits light in the near-infrared spectrum (λ_{max}: 650 nm). In the near future, we hope to assess this in more detail in future *in vivo* studies.

Objective 5: Determine if the ototoxic drug ouabain results in selective type-I SGN degeneration in guinea pigs.

Ouabain has been reported to selectively destroy type-I SGNs in the cochlea of several rodent species. However, two conflicting papers about the possible effect of ouabain upon the guinea pig cochlea made us to re-investigate this deafening protocol. In Chapter 6 we describe our results and conclude that round window application of ouabain results in a rapid loss of type-I and type-II SGNs as well as OHCs in the guinea pig. In addition, affected aABRs do not implicate loss of SGNs. Thus, we conclude that round window application of ouabain is not limited to degeneration of type-I SGNs and, as a consequence, it is not a reliable model to investigate cell-based auditory nerve therapy in the guinea pig.

This non-selectivity together with a high variability presented an unexpected challenge, since literature on (most) rodents and cats was consistent. Also a recent study in guinea pigs underlined this consistency [14], which was in contrast to an older publication [15]. Since we expected an unambiguous effect of ouabain, this unforeseen situation and a limited number of animals resulted in small group sizes for two groups. We decided to investigate a 10-fold higher concentration of ouabain than initially intended since we expected unambiguous results. Due to a limited number of animals, these animals had to be taken from another group, which resulted in the small group sizes. However, this shortcoming in group size could be circumvented by a statistical analysis. Nevertheless, the effect of ouabain on the SGNs of the auditory nerve and the hair cells in the guinea pig cochlea is intriguing and should be investigated more closely in order to understand the exact mechanism of action.

Objective 6: Multimodality imaging of HFBSCs in a mouse model of traumatic brain injury.

In Chapter 7 we investigated the *in vivo* behavior of labeled HFBSCs in a traumatic brain injury (TBI) mouse model. To achieve this, we first transduced the cells with genes coding for reporter proteins and subsequently loaded them with SPIO ferumoxytol nanoparticles. HFBSCs were able to take up ferumoxytol nanoparticles and differentiate after genetic manipulation using a viral vector to introduce one or more reporter molecules. Finally, labeled HFSBCs were transplanted in mice with TBI and followed by means of BLI and MRI over the course of 49 days and 58 days, respectively. BLI data demonstrated survival and neuronal differentiation of HFBSCs. MRI data showed their exact location within the brain. Immunofluorescent staining underlined the differentiation towards a neuronal lineage after brain transplantation. This feasibility study is a first indication that HFBSCs might be used for cell-based therapy in TBI. Since isolation, expansion and neural differentiation of SCs from hair follicle is possible, these cells are a promising source for autologous cell-based therapy in neuronal degenerative disorders.

Future research

Future experiments have to be undertaken to visualize HFBSCs in the inner ear of guinea pigs in order to observe potential regeneration of the auditory nerve. To improve visualization of transplanted cells *in vivo*, the AkaBLI system could be employed. Due to a shift towards a near-infrared wavelength and an enhanced bioluminescent signal of the two components of this system, i.e. AkaLumine-HCl and Akaluc, cells can also be imaged in deep tissue.

Regarding the deafening of the guinea pigs, systemic administration of kanamycin and furosemide could be applied to observe the behavior of SCs in a model of acute SNHL. In this model no hair cells will be present, which is similar to deaf patients and to our *in vitro* experiments (Chapter 4), and could be used to study the regeneration of damaged tissue by HFBSCs and/or possibly their differentiation into neuronal or glial cells. This model of kanamycin/furosemide-induced deafness could be useful to study SGN regeneration in CI-implanted animals, since a CI circumvents the hair cells, which could present an advance towards clinical application.

The necessary steps to investigate the feasibility of SCs in such a model were performed in this thesis by stable transduction with reporter molecules that enable *in vivo* visualization, tracking of HFBSCs loaded with SPIO nanoparticles *in vivo* and *ex vivo*, and successful integration into tissue *in vitro* and *in vivo*.

In addition, a chemically defined, xeno-free cell culture method should be investigated to better simulate culture conditions of future regenerative therapies and prevent immune response reactions. Severe immune response reactions can be triggered by xenogeneic supplements, such as fetal bovine serum and (mouse) cell feeder layers, which would then lead to rejection of the transplant [16, 17]. Transplant rejection by the immune system of the host organism, a so-called graft-versus-host disease, would lead to inflammation, organ damage, and major health problems. This response of the immune system could also be induced by the transplantation of cells that were cultured in medium containing xenogeneic components. In this case the graft-versus-host reaction is triggered by xenogeneic antigens from the animal serum and/or feeder cells, which are presented to immune system cells, such as T cells, by the major histocompatibility complex class II on the membrane of the cells. Currently, xeno-free alternatives for media are available, which should facilitate the cultivation of stem cells under xeno-free conditions.

In this context, it is worth considering the use of iPSCs, which are autologous and can be cultured towards a defined cellular phenotype. However, although iPSCs are available from stock, the achievement of an iPSC population from each patient remains a challenge. Moreover, on their way from bench to bedside, the potential of iPSCs for regenerative therapy needs to be further investigated in animal models, such as the guinea pig in case of hearing research. Depending on which SC source gives better results for cell-based therapy, the transplantation of patient-derived, possibly pre-differentiated, iPSCs or ectodermal SCs into deafened guinea pigs during cochlear implantation may allow electrical stimulation of the SCs and conceivably facilitate neuronal differentiation, as shown in previous studies [18-20]. However, the optimal source for stem cell-based regenerative therapy needs yet to be evaluated.

References

1. Gho, C.G., Schomann, T., De Groot, S.C., Frijns, J.H.M., Rivolta, M.N., Neumann, M.H., and Huisman, M.A., Isolation, expansion and neural differentiation of stem cells from human plucked hair: A further step towards autologous nerve recovery. Cytotechnology, 2016. **68**: pp. 1849-1858.
2. Liu, J.A. and Cheung, M., Neural crest stem cells and their potential therapeutic applications. Dev. Biol., 2016. **419**: pp. 199-216.
3. Greiner, J.F., Hauser, S., Widera, D., Muller, J., Qunneis, F., Zander, C., Martin, I., Mallah, J., Schuetzmann, D., Prante, C., Schwarze, H., Prohaska, W., Beyer, A., Rott, K., Hutten, A., Golzhauser, A., Sudhoff, H., Kaltschmidt, C., and Kaltschmidt, B., Efficient animal-serum free 3D cultivation method for adult human neural crest-derived stem cell therapeutics. Eur. Cell Mater., 2011. **22**: pp. 403-419.
4. Hauser, S., Widera, D., Qunneis, F., Müller, J., Zander, C., Greiner, J., Strauss, C., Lüningschrör, P., Heimann, P., Schwarze, H., Ebmeyer, J., Sudhoff, H., Araúzo-Bravo, M.J., Greber, B., Zaehres, H., Schöler, H., Kaltschmidt, C., and Kaltschmidt, B., Isolation of novel multipotent neural crest-derived stem cells from adult human inferior turbinate. Stem Cells Dev., 2012. **21**: pp. 742-756.
5. Watanabe, A., Yamada, Y., and Yamanaka, S., Epigenetic regulation in pluripotent stem cells: A key to breaking the epigenetic barrier. Philos. Trans. R. Soc. Lond., B, Biol. Sci., 2013. **368**: pp. 20120292.
6. Hochedlinger, K. and Jaenisch, R., Induced pluripotency and epigenetic reprogramming. Cold Spring Harb. Perspect. Biol., 2015. **7**: pp. a019448.
7. Schomann, T., Mezzanotte, L., Lourens, I.M., De Groot, J.C.M.J., Frijns, J.H.M., and Huisman, M.A., Lentiviral transduction and subsequent loading with nanoparticles do not affect cell viability and proliferation in hair-follicle-bulge-derived stem cells *in vitro*. Contrast Media Mol. Imaging, 2016. **11**: pp. 550-560.
8. Castaneda, R.T., Khurana, A., Khan, R., and Daldrup-Link, H.E., Labeling stem cells with ferumoxytol, an FDA-approved iron oxide nanoparticle. J. Vis. Exp., 2011: pp. e3482.
9. Schomann, T., Mezzanotte, L., De Groot, J.C.M.J., Rivolta, M.N., Hendriks, S.H., Frijns, J.H.M., and Huisman, M.A., Neuronal differentiation of hair-follicle-bulge-derived stem cells co-cultured with mouse cochlear modiolus explants. PLoS ONE, 2017. **12**: pp. e0187183.
10. Waaijer, L., Klis, S.F., Ramekers, D., Van Deurzen, M.H., Hendriksen, F.G., and Grolman, W., The peripheral processes of spiral ganglion cells after intracochlear application of brain-derived neurotrophic factor in deafened guinea pigs. Otol. Neurotol., 2013. **34**: pp. 570-578.
11. Ramekers, D., Versnel, H., Strahl, S.B., Klis, S.F.L., and Grolman, W., Temporary neurotrophin treatment prevents deafness-induced auditory nerve degeneration and preserves function. J. Neurosci., 2015. **35**: pp. 12331-12345.
12. Kuchimaru, T., Iwano, S., Kiyama, M., Mitsumata, S., Kadonosono, T., Niwa, H., Maki, S., and Kizaka-Kondoh, S., A luciferin analogue generating near-infrared bioluminescence achieves highly sensitive deep-tissue imaging. Nat. Commun., 2016. **7**: pp. 11856.
13. Iwano, S., Sugiyama, M., Hama, H., Watakabe, A., Hasegawa, N., Kuchimaru, T., Tanaka, K.Z., Takahashi, M., Ishida, Y., Hata, J., Shimozono, S., Namiki, K., Fukano, T., Kiyama, M., Okano, H., Kizaka-Kondoh, S., McHugh, T.J., Yamamori, T., Hioki, H., Maki, S., and Miyawaki, A., Single-cell bioluminescence imaging of deep tissue in freely moving animals. Science, 2018. **359**: pp. 935-939.
14. Cho, Y.B., Cho, H.H., Jang, S., Jeong, H.S., and Park, J.S., Transplantation of neural differentiated human mesenchymal stem cells into the cochlea of an auditory-neuropathy guinea pig model. J. Korean Med. Sci., 2011. **26**: pp. 492-498.
15. Hamada, M. and Kimura, R.S., Morphological changes induced by administration of a Na^+,K^+-ATPase inhibitor in normal and hydropic inner ears of the guinea pig. Acta Otolaryngol., 1999. **119**: pp. 778-786.
16. Tuschong, L., Soenen, S.L., Blaese, R.M., Candotti, F., and Muul, L.M., Immune response to fetal calf serum by two adenosine deaminase-deficient patients after T cell gene therapy. Hum. Gene Ther., 2002. **13**: pp. 1605-1610.
17. Sundin, M., Ringden, O., Sundberg, B., Nava, S., Gotherstrom, C., and Le Blanc, K., No alloantibodies against mesenchymal stromal cells, but presence of anti-fetal calf serum antibodies, after transplantation in allogeneic hematopoietic stem cell recipients. Haematologica, 2007. **92**: pp. 1208-1215.
18. Yamada, M., Tanemura, K., Okada, S., Iwanami, A., Nakamura, M., Mizuno, H., Ozawa, M., Ohyama-Goto, R., Kitamura, N., Kawano, M., Tan-Takeuchi, K., Ohtsuka, C., Miyawaki, A., Takashima, A., Ogawa, M., Toyama, Y., Okano, H., and Kondo, T., Electrical stimulation modulates fate determination of differentiating embryonic stem cells. Stem Cells, 2007. **25**: pp. 562-570.
19. Tandon, N., Cimetta, E., Taubman, A., Kupferstein, N., Madaan, U., Mighty, J., Redenti, S., and Vunjak-Novakovic, G., Biomimetic electrical stimulation platform for neural differentiation of retinal progenitor cells. Conf. Proc. IEEE Eng. Med. Biol. Soc., 2013. **2013**: pp. 5666-5669.
20. Pires, F., Ferreira, Q., Rodrigues, C.A., Morgado, J., and Ferreira, F.C., Neural stem cell differentiation by electrical stimulation using a cross-linked PEDOT substrate: Expanding the use of biocompatible conjugated conductive polymers for neural tissue engineering. Biochim. Biophys. Acta, 2015. **1850**: pp. 1158-1168.

Appendix

Summary in Dutch

Het doel van dit proefschrift was om de haalbaarheid te onderzoeken van het observeren van volwassen stamcellen, in het bijzonder HFBSC's, met behulp van multimodale visualisatietechnieken in levende dieren. Omdat het gebruik van HFBSC's in het veld van binnenooronderzoek nog nieuw is, zijn er een reeks proof-of-principle experimenten uitgevoerd om te onderzoeken of deze cellen neuronale differentiatie kunnen ondergaan en of ze genetische modificatie met reportermoleculconstructies en het vervolgens beladen met nanodeeltjes in vitro kunnen tolereren (Hoofdstuk 2 en Hoofdstuk 3). Vervolgens was het van belang om te onderzoeken of HFBSC's integreren in modiolair weefsel en of we ze kunnen visualiseren achter het dikke slaapbeen van de cavia (Hoofdstuk 4 en Hoofdstuk 5). Ten slotte hebben we in vivo studies uitgevoerd om het ototoxische effect van ouabain in de cavia en het gedrag van HFBSC's bij muizen met traumatisch hersenletsel te onderzoeken (Hoofdstuk 6 en Hoofdstuk 7). De belangrijkste resultaten van dit onderzoek zullen worden samengevat in de eerste paragraaf van de discussie om een algemeen overzicht te geven. Omstandigheden die deze resultaten hebben kunnen beïnvloeden zullen worden besproken in de tweede paragraaf. De derde paragraaf zal uitsluitend gericht zijn op toekomstig onderzoek.

List of abbreviations

aABR	Acoustically-evoked auditory brainstem response
ALS	Amyotrophic lateral sclerosis
ANOVA	Analysis of variance
AP-2α	Activating protein 2α
ATOH1	Atonal homolog 1
ATP	Aadenosine triphosphate
BDNF	Brain-derived neurotrophic factor
BGM	Basic growth medium
BLI	Bioluminescence imaging
cAMP	Cyclic adenosine monophosphate
CBG	Click beetle green luciferase
CI	Cochlear implant
copGFP	Copepod green fluorescent protein
Cy7	Cyanine 7
DAB	3,3'-Diaminobenzidine
DAPI	4',6-Diamidino-2-phenylindole
dB	Decibel
DC	Deiters' cell
DCX	Doublecortin
DMEM	Dulbecco's modified eagle medium
DMSO	Dimethyl sulfoxide
DNA	Deoxyribonucleic acid
ECM	Extracellular matrix
EDTA	Ethylenediaminetetraacetic acid
EF1α	Elongation factor 1α
Em	Emission
ESC	Embryonic stem cell
Ex	Exitation
FA	Formaldehyde
FBS	Fetal bovine serum
FDA	Food and Drug Administration
FITC	Fluorescein isothiocyanate
FLASH	Fast low-angle shot
FLI	Fluorescence Imaging

FOV	Field of view
GDNF	Glial cell-derived neurotrophic factor
GFAP	Glial fibrillary acidic protein
GFP	Green fluorescent protein
GMO	Genetically modified organism
GvHD	Graft-versus-host disease
HCl	Hydrogen chloride
HDFa	Human dermal fibroblasts, adult
HFBSC	Hair follicle bulge-derived stem cells
HIV	Human immunodeficiency virus
IHC	Inner hair cell
IM	Induction medium
iPSC	Induced pluripotent stem cell
IS	Inner sulcus
IVIS	In vivo imaging system
KROX-20	Early growth response protein 2
LAS AF	Leica Application Suite Advanced Fluorescence
LAS X	Leica Application Suite X
Luc2	Codon-optimized luciferase
LUMC	Leiden University Medical Center
MOI	Multiplicity of infection
MPZ	Myelin protein zero
MRI	Magnetic resonance imaging
MTS	3-(4,5-Dimethylthiazol-2-yl)-5-(3-carboxymethophenyl)-2-(4-sulfophenyl)-2H-tetrazolium
Myo	Myosin
N. VIII	Vestibulocochlear nerve, eighth cranial nerve
NC	Neural crest
NCSC	Neural crest-derived stem cell
NF	Neurofilament
NF-H	Neurofilament heavy
NF-M	Neurofilament middle
NGF	Nerve growth factor
OC	Organ of Corti
OHC	Outer hair cell
OOC	Organ-on-a-chip
OSL	Osseous spiral lamina

OsO_4	Osmium tetroxide
PBS	Phosphate-buffered saline
PDL	Poly-D-lysine
R^2	Coefficient of determination
RF	Radio-frequency
rhEGF	recombinant human epidermal growth factor
rhFGF	recombinant human fibroblast growth factor
RNA	Ribonucleic acid
RWM	Round window membrane
SC	Stem cell
SD	Standard deviation
SEM	Standard error of the mean
SG	Spiral ganglion
SGC	Spiral ganglion cell
SGN	Spiral ganglion neuron
SLUG	Zinc finger protein SNAI2
SMA	Smooth muscle actin
SNHL	Sensorineural hearing loss
SOX10	SRY (sex determining region Y)-related HMG-box 10
SOX2	SRY (sex determining region Y)-related HMG-box 2
SOX9	SRY (sex determining region Y)-related HMG-box 9
SPIO	Superparamagnetic iron oxide
SPL	Sound pressure level
SPSS	Statistical Package for the Social Sciences
TBI	Traumatic brain injury
TE	Echo time
TM	Tectorial membrane
TNF-α	Tumor necrosis factor α
ToC	Tunnel of Corti
TR	Recovery time
TUBB3	Class III β-tubulin
TXR	Texas red
VitA	Vitamin A
X-gal	5-Bromo-4-chloro-3-indolyl-β-D-galactopyranoside
λ_{em}	Emission maximum
λ_{ex}	Exitation maximum

List of publications

1. Greiner, J.F.-W., Müller, J., Zeuner, M.-T., Hauser, S., Seidel, T., Klenke, C., Grunwald, L.-M., Schomann, T., Widera, D., Sudhoff, H., Kaltschmidt, B., and Kaltschmidt, C., 1,8-Cineol inhibits nuclear translocation of NF-κB p65 and NF-κB-dependent transcriptional activity. Biochim. Biophys. Acta, 2013. 1833: pp. 2866-2878.
2. Greiner, J.F., Muller, J., Zeuner, M.T., Hauser, S., Seidel, T., Klenke, C., Grunwald, L.M., Schomann, T., Widera, D., Sudhoff, H., Kaltschmidt, B., and Kaltschmidt, C., 1,8-Cineol inhibits nuclear translocation of NF-kappaB p65 and NF-kappaB-dependent transcriptional activity. Biochim. Biophys. Acta, 2013. 1833: pp. 2866-2878.
3. Schomann, T., Qunneis, F., Widera, D., Kaltschmidt, C., and Kaltschmidt, B., Improved method for ex ovo-cultivation of developing chicken embryos for human stem cell xenografts. Stem Cells Int., 2013. 2013: pp. 1-9.
4. Gho, C.G., Schomann, T., Groot, S.C.d., Frijns, J.H.M., Rivolta, M.N., Neumann, M.H.A., and Huisman, M.A., Isolation, expansion and neural differentiation of stem cells from human plucked hair: A further step towards autologous nerve recovery. Cytotechnology, 2015. 68: pp. 1849-1858.
5. Schomann, T., Mezzanotte, L., Lourens, I.-A.-L.M., de Groot, J.C.M.J., Frijns, J.H.M., and Huisman, M.A., Lentiviral transduction and subsequent loading with nanoparticles do not affect cell viability and proliferation in hair-follicle-bulge-derived stem cells in vitro. Contrast Media Mol. Imaging, 2016. 11: pp. 550-560.
6. Schomann, T., Mezzanotte, L., De Groot, J.C.M.J., Rivolta, M.N., Hendriks, S.H., Frijns, J.H.M., and Huisman, M.A., Neuronal differentiation of hair-follicle-bulge-derived stem cells co-cultured with mouse cochlear modiolus explants. PLoS ONE, 2017. 12: pp. e0187183.
7. Schomann, T., Ramekers, D., de Groot, J.C.M.J., van der Ploeg, C.H., Hendriksen, F.G.J., Boehringer, S., Klis, S.F.L., Frijns, J.H.M., and Huisman, M.A., Ouabain does not induce selective spiral ganglion cell degeneration in guinea pigs. BioMed Res. Int., 2018. 2018: pp. 15.
8. Schomann, T., Mezzanotte, L., de Groot, J.C.M.J., Lowik, C.W.G.M., Frijns, J.H.M., and Huisman, M.A., Imaging bioluminescent exogenous stem cells in the intact guinea pig cochlea. Anat. Rec. (Hoboken), 2019.

Curriculum vitae

Timo Schomann was born on January 1, 1986 in Verl, Germany. In 2010, he received the Bachelor of Science degree in Bioinformatics and Genome Research at Bielefeld University, Bielefeld, Germany. His bachelor thesis titled "*Influence of the pluripotency genes Nanog, Sox2 and Oct4 on NF-κB*" was supervised by Dr. P. Lüningschrör. In the same year, he started the master study Molecular Cell Biology, from which he graduated with a Master of Science with his thesis titled "In vivo *differentiation potential of ITSCs in the developing chicken embryo model*", supervised by Prof. dr. B. Kaltschmidt and Dr. D. Widera, in October 2012.

In January 2013, he started his PhD research under supervision of Prof. dr. ir. J. H. M. Frijns and Dr. M. A. Huisman at the Leiden University Medical Center. The data obtained during this time lead to this thesis. In June 2018, he started working as a researcher at Leiden University Medical Center.

Acknowledgements

I would like to thank my family and friends, my colleagues, and everybody who supported me during the realization of my thesis. Without your support it would have been much more difficult to finish this thesis. Thank you very much!